DTU Nanotech
Department of Micro- and Nanotechnology

Master Thesis, s053179

Taylor dispersion in time dependent flow

Emil Hovad

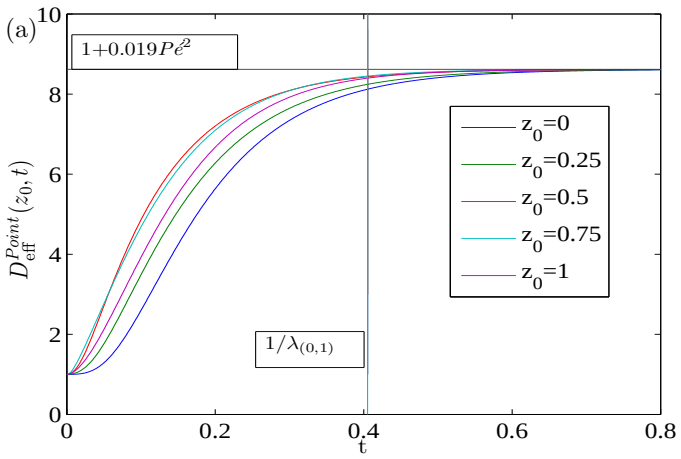

Supervisor: Professor Henrik Bruus

Department of Micro- and Nanotechnology
Technical University of Denmark

5 September 2011

Abstract

Taylor dispersion, is a well known and studied phenomena both in the physical and chemical community. The phenomena occurs in nearly every flow where velocity gradients are present for a solute distribution.
In this thesis the delta function also called the point concentration, will be investigated with respect to the effects of the no flux wall boundary, and other anomalous effect will be seen depending on the transverse placement.
These effects off the transverse placement for the point concentrations, is investigated in the infinite parallel plate channel and a circular channel, for a steady flows, single-frequency pulsating flows and a plus one frequency flow superimposed on the steady flow. This is done by using Vedel and Bruus framework from "Transient Taylor-Aris dispersion in time-dependent flows"[1], to derive the effective diffusion for the point concentration.
The Taylor dispersion for a point concentration is also calculated for the non-Newtonian fluids, The Power law fluid and the Casson fluid. Where these steady velocity fields are implemented in the framework.

Resumé

Taylor spredning, er et velkendt og studeret fænomen både i de fysiske og kemiske akademiske miljø. Dette fænomen optræder i næsten alle flow, hvor hastigheden gradienter er til stede for et opløst stof.

I denne afhandling delta funktionen eller punkt koncentrationen vil blive undersøgt med hensyn til virkningerne af ikke flux randbetingelsen. Andre effekter vil ogsåblive undersøgt med hensyn til tværgående placering af point koncentrationen. Dette sker foregår i en kanal med to uendelige store parallel plader og i en cirkulær kanal. Pulserende strømme og punkt koncentration tværgående placering er ogsåundersøgt, hvor forskellige dynamikker ses afhængig af den tværgående placering. Dette gøres ved hjælp af S. Vedel og H. Bruus formel "Transient Taylor-Aris dispersion in time-dependent flows" [1], til at udlede den effektive diffusion for punkt koncentrationen. Taylor dispersion for punkt koncentrationen beregnes ogsåfor nogle ikke-Newtonske væsker, The Power law fluid og the Casson fluid. Hvor disse stabil hastighed felter er bliver indsat i formlen for dispersionen. Dette er et dansk resumé af afhandlingen

Preface

This thesis is submitted as fulfillment of the prerequisites for obtaining the degree in Master of Science in Engineering at the Technical University of Denmark (DTU). The thesis work is carried out at the Department of Micro- and Nanotechnology (DTU Nanotech) in the Theoretical Microuidics group (TMF) headed by Professor Henrik Bruus. The duration of the thesis work was 7 months from 14 Februar 2011 to 5 September 2011 corresponding to 35 ECTS points.

It has been a pleasure to learn about physics at the Theoretical Microuidics group(TMF). A special thanks to professor Henrik Bruus, who has been a motivating supervisor. Furthermore Henrik has great knowledge and insights in the field of Theoretical Microuidics and excellent overview as a supervisor. Also S. Vedel has been a great help in clarifying his and Bruus' article and helping with different questions in Theoretical Microuidics.

Emil Hovad
Department of Micro- and Nanotechnology
Technical University of Denmark
5 September 2011

Contents

List of Figures

List of Tables

List of symbols

Table 1: List of used quantities alphabetized by symbol.

Quantity	Symbol
Cross-sectional part of the $\boldsymbol{\nabla}$ operator	$\boldsymbol{\nabla}_\perp = \mathbf{e}_y\partial_y + \mathbf{e}_z\partial_z$
Bra of $\bullet$, and ket of $\bullet$	$\langle \bullet \vert$, and $\vert \bullet \rangle$
Complex conjugation	$*$
Cross-sectional area	$\mathcal{A}$
Channel radius/half-height	a
Concentration field of solute	c
pth axial moment of concentration	c_p
nth basis function	f_n
Bessel function, first kind of order s	J_s
Channel length	$\mathcal{L}$
Characteristic length	L_o
pth full moment of concentration	M_p
Cross-sectional position vector	$\boldsymbol{r}_\perp = (y, z)$
Molecular diffusivity	D
Effective diffusivity	D_eff
Effective diffusivity for the circular channel with a point concentration	$D_\mathrm{eff}^\mathrm{Point}(r_0, t)$
Effective diffusivity, time-averaged	$D_\mathrm{eff}^\mathrm{avr}$
Effective diffusivity, steady flow	$D_\mathrm{eff}^\mathrm{steady}$
Effective diffusivity for the infinite parallel plate channel with a point concentration	$D_\mathrm{eff}^\mathrm{Point}(z_0, t)$
Cartesian basis vectors	$\mathbf{e}_x$, $\mathbf{e}_y$,$\mathbf{e}_z$
Surface normal vector	$\vec{n}$
Pressure	p
Characteristic pressure	P_o
Peclet number	Pé $= U_\mathrm{o}L_\mathrm{o}/D$
Channel aspect ratio	$R = w/a$
Position vector	$\boldsymbol{r}$
Initial value for $c(x, \boldsymbol{r}_\perp, t)$	$\tilde{c}(x, \boldsymbol{r}_\perp)$

Quantity	Symbol
Characteristic concentration	C_o
Schmidt number	$\mathrm{Sc} = \nu/D$
Characteristic time	T_o
Time	t
Characteristic velocity	U_o
Axial velocity component of solvent	u
Volume	$\mathcal{V}$
Velocity field of solvent	$\vec{v}$
Channel half-width	w
Womersley number	$\mathrm{Wo} = \sqrt{L_\mathrm{o}^2\tilde{\omega}_\mathrm{o}/\nu}$
Solute center of mass	$\overline{x}$
Cylindrical coordinates	x, r, φ
Cartesian coordinates	x, y, z
Fluid momentum equilibration rate	α_m, α_fl
Kronecker delta	$\delta_{n,m}$
ℓth velocity component amplitude	ϵ_k
Dynamic viscosity	η
nth root of Bessel function J_s	$\xi_{s,n}$
nth diffusion rate eigenvalue	λ_n
pth moment of conc. about the mean	μ_p
Kinematic viscosity of solvent	ν
Density of solvent	ρ
Diffusivity enhancement, Eq. (3.21b)	χ_plate, χ_rect
Cross section	Ω
Base frequency, non-dimensionalized	$\omega_\mathrm{o} = \mathrm{Wo}^2\mathrm{Sc}$
Base frequency, dimensionfull	$\tilde{\omega}_\mathrm{o}$
Strain rate	$\dot{\boldsymbol{\gamma}}$
Deviatoric stress tensor	$\boldsymbol{\tau}$
Deviatoric strain rate	$\dot{\boldsymbol{\gamma}}^\mathrm{dev}$

Chapter 1

Introduction

G.I. Taylor was the first to discover the enhanced solute diffusion due to shear from the solvent flow [2]. He derived the well known result $D_{\text{eff}} = (1 + \text{Pé}^2/48)D$ where the channel has a circular cross section of radius a and $\text{Pé} = aU_{\text{o}}/D$ where the flow was a steady Poiseuille flow. With mathematical finesse Aris gained increased insight by using the method of moments to solve the effective diffusivity [3] for a steady flow. Barton did some further work, by changing some details of Aris [4]. Other work has been done on the shear enhanced dispersion in steady flows[5, 6, 7, 8, 9].

In many circumstances where flows are unsteady and shear is generated by the ever changing gradient of the velocity field, this causes time-dependent changes in the effective diffusivity $D_{\text{eff}}(t)$. Bruus and Vedel derived an expression for the effective diffusivity $D_{\text{eff}}(t)$, that is a general expression for the transient effective Taylor Aris diffusivity for any laminar time dependent flow, in any constant cross-sectional shape [1]. Previous research have been done in transient analysis by Mazumder and coworkers [10, 11].

My thesis will investigate an delta function also called point concentration, were a continuation of Vedel and Bruus article "Transient Taylor-Aris dispersion in time-dependent flows"[1] is used. The mathematical procedures and principles comes from this article.
Earlier work have been done by Latini and Bernoff; Were the anomalous spread of the delta function in the transverse direction was investigated, where they neglected the pipe wall boundary [12]. Camassa investigated the transient behaviour with anomalous diffusion of a steady flow and also applied solid wall boundary conditions, and found a exact evolution [13].
In this thesis the delta function or the point concentration will be investigated with respect to the effects of the no flux wall boundary, and other transients anomalous effect will be seen depending on the transverse placement. A the steady region is found where all the initial point concentrations converges to the value of the uniform distribution in the cross sectional steady effective diffusion $D^{\text{Point}}_{\text{effSteady}}(\boldsymbol{r}_\perp, t) = D^{\text{steady}}_{\text{eff}}$.
These investigations is done in the infinite parallel plate channel and a circular channel, for steady flows, single-frequency pulsating flows and for a plus one frequency flow super-

imposed on the steady flow.

The point concentration is often used in biophysics to simulate an injection of a substance. In medicine a concentration is injected with a narrow needle and often the point concentration is a good approximation and presents nice mathematical behaviour. Dispersion effects are created in pulsating flows that could occur in the Cardiovascular System. Dependent on initial placement of the point concentration, the anomalous diffusion $D_{\text{eff}}^{\text{Point}}(\boldsymbol{r}_\perp, t)$ will change.
Womersley solved the velocity field for an oscillating pressure with a mathematical simple treatment, which had strong similarities with the distribution of alternating current in a conductor of finite size [14]. Pulsating flows occurs in the terminal arteries to the aorta with different velocity profiles depending on the Womersley number.

Besides the ordinary Newtonian fluid, Non-Newtonian fluids effective diffusivity will also be investigated. Since Blood is a fluid which is non Newtonian, different models are used to describe it. Two models will be presented; the Power Law fluid with shear thinning properties and the Casson model. An other model is often used the Carreau-Yasuda model, but I will refrain from using it[15], [16] and [17]. Research in Taylor dispersion with regards to the non Newtonian fluids and capillaries is an ongoing subject [15].

1.1 Lab on a chip devices application to bioscience

Lab on a chip is a fast growing field both theoretically and industrially. Lab on a chip systems are small and typically deal with samples of the size 1 μL to 1 pL, giving the possibility for an easy transport of the devices and a fast analysis on locating[18]. New lab on a chip system is developing for example a cheap and portable medical test that makes different genetic tests [19]. Also acoustophoresis is used in lab on a chip devices, to separate species via acoustic waves, this is a new field in rapid growth.
My supervisor, professor H. Bruus, his fellow Ph.D. student R. Barnkob and collaboraters in Lund have, in order to enhance the separation of cells, used ultrasonic standingwaves and microfluidics. The cell lines investigated have been living human embryonic ventral mesencephalic cells within studies of Parkinson and isolating circulating tumor cells from White blood cells within studies of cancer [20], [21]. Currently, my supervisor and his other Ph.D. Student S. Vedel are also working on the collective motile behaviour of cells [22].

Hopefully, in the future these devices will help doctors diagnose diseases in their practices for a faster diagnoses. These devices could eventually help diagnose aids or other diseases. This may sound easy and fantastic but lab on a chip systems requires a lot of skill with regards to experimental and theoretical knowledge. There is a lot of theory in making lab on a chip systems, especially with regards to flow. Fortunately, they often have low reynolds numbers, making Navies-Stokes equation easier to handle and the flow laminar, which is also the case in the cardiovascular system.

This gives the solute limited mixing abilities, yielding the effective diffusion as one mixing effect for the solute. Other mixing method are magnetophoresis, electroosmoostic pumping, electrophoresis e.t.c

1.2 Governing Equations and effective diffusion

To use the Navier-Stokes Equation, the continuum hypothesis needs to be valid. The continuum hypothesis simple states that the fluid can be seen as perfectly continuous in structure on a macroscopic scale, although it is not on a particle level[18]. But on a macroscopic level the fluctuations of the consisting of molecules can be averaged out by representative elementary volume(REV). The Navier-Stokes equation is using an Eulerian description where fixed points in space are use to represent the field variable for example, velocity or mass as value's averaged over the volume of (REV) and the Navier-Stokes equation describe how these fixed point value change over time, specially for the velocity field.
In microfluidics, the fluid water can be seen as incompressible fluids so,

$$\boldsymbol{\nabla}\cdot\mathbf{v} = 0. \tag{1.1}$$

Getting the Navier-Stokes equation for an incompressible fluid,

$$\rho\Big(\partial_t\mathbf{v} + (\mathbf{v}\cdot\boldsymbol{\nabla})\mathbf{v}\Big) = -\boldsymbol{\nabla}p + \eta\nabla^2\mathbf{v} + \rho\,\mathbf{g}. \tag{1.2}$$

The Navier-Stokes equation is used for calculating the velocity profile from the forces acting on the fluid. The forces on the fluid can be pressure or liquid friction also called viscosity this is treated in chap.5 along with other forces as electro forces.

The Navier-Stokes equation is hard to solve or, in many cases, impossible since its a non-linear differential equation. Often in text book examples, special geometries with symmetries are used to remove the convective acceleration term $(\mathbf{v}\cdot\boldsymbol{\nabla})\mathbf{v}$. This also happens in Microfluidics because of low Reynolds numbers or when long straight symmetric channels are used, as in this thesis where a long translational invariant channel is used making the Navier-Stokes equation solvable and getting the velocity field.
It is assumed that the solute does not affect the flow of the solution when inserted to the media or the density of the fluid. When the solute is transported around in fluid, the Navier-Stokes equation only gives the velocity field. The description of the concentration distribution is done by the Advection-Diffusion equation. The concentration distribution is changed in time $\partial_t c$ two ways, by diffusion $D\nabla^2 c$ a thermally induced random motion of the particles[18] and from convection $\mathbf{v}\cdot\boldsymbol{\nabla}c$ where the velocity field $\mathbf{v}$ was found in the Eq. (1.2).

$$\partial_t c + \mathbf{v}\cdot\boldsymbol{\nabla}c = D\nabla^2 c. \tag{1.3}$$

When no convection is present, we get the diffusion equation, this is solvable for different initial concentrations, also the point concentration. But when convection is added,

Eq. (1.3) has generally no solutions, leading us to Taylor dispersion and Aris method of statistical moments. Once the governing equation are in place, the Taylor dispersion can be discussed.

1.3 Taylor dispersion and combining the governing equation

Combining the two governing equations and solving them will give the time evolution of the concentration field and the dispersion but this is, unfortunately, impossible for most cases and numerical tool as Comsol and Matlab is used often. Extra smearing occurs in the Advection Diffusion equation when the solute is in the solution's velocity field, from the advection term $\mathbf{v}\cdot\boldsymbol{\nabla}c$. A Sketch of what happen in the simple Poiseuille flow Fig. 1.1, when the concentration Fig. 1.1(black) diffuses out in the transverse direction Fig. 1.1(green),the parabolic velocity profile Fig. 1.1(red) changes the shape of the concentration because of the changing velocity in the transverse direction Fig. 1.1(blue). This gives rise to an extra spread in the concentration in the longitudinal x-direction (black interval).

1.3.1 Aris moments

But with Aris statistical method of moments, the spread can be calculated in one direction with the assumption of unidirectional flow that eliminates all convective terms except in the axial one. In this way a solution is found for the Taylor dispersion see (chap. 2). A lot of research have been done in Taylor dispersion, also on the skewness of the concentration, here are some references to the work that has been done [23, 24, 25, 26, 27, 28, 12]. Even in pharmacokinetic, there is a need to take account for the Taylor dispersion [29].

1.4 Theoretical foundation and goals

In my thesis a continuation of the work done by S. Vedel and H. Bruus will be presented. Here a point concentration will be applied to the framework. To observe and compare the dynamic of the point concentration compared to the uniform cross sectional distribution. To observe anomalous diffusion effects in different time scale in the steady flow as well as single-frequency pulsating flows and many-frequency pulsating flows. To applied the frame work to non-Newtonian fluids, and see D_{eff} for fluid that have common features to blood, and see how D_{eff} changes for the parameters of the fluid.

1.5 Outline of thesis

1.5.0.1 Chapter 2: Basic Theory

A summary of the theory in Transient Taylor-Aris dispersion in time dependent flows by Vedel and Bruus [1]. First the geometry of the long straight channel are set, then the operators are defined. The Navier-Stokes equation and the advection diffusion are non dimensionalized and a bracket notation is used for easy handling the integrals. The method

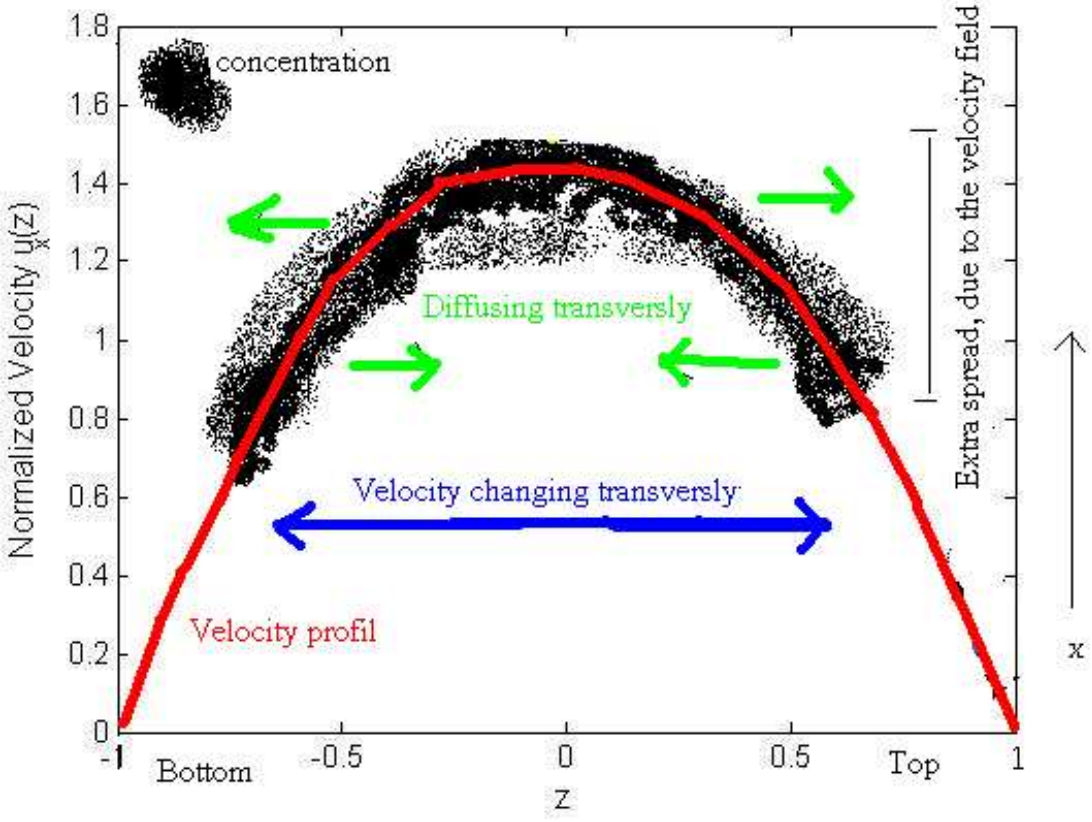

Figure 1.1: $D_{\text{eff}}(t)$. Here is a sketch of the Taylor dispersion for a point concentration placed in the center. Extra spreading, due to the velocity field can be seen.

of statistical moments are used to set up the axial moments so the effective diffusion can be solved. This is done by solving the axial moments recursively, and subsequently getting the effective diffusion.

1.5.0.2 Chapter 3: Point concentration in the infinite parallel-plate channel

Once the theoretical framework has been presented, the formula for $D_{\text{eff}}(t)$ can be used for a specific geometry. The infinite parallel plate channel is set-up, the velocity field is solved and the coefficient for $D_{\text{eff}}^{\text{Point}}(z_0, t)$ is found with respect to the location of the point concentration. Different parameters sweep are done, especially changing the location of the point concentration in the transverse direction.

1.5.0.3 Chapter 4: Point concentration in cylinder

The same is done here as in chapter 3, slight differences appear in the circular channels D_{eff} due to the geometry of the channel. Peak in the effective diffusivity D_{eff} are thoroughly

investigated in this chapter. Phase shift is examined for the differently initial placed point concentrations and period doubling is also investigated.

1.5.0.4 Chapter 5: Non-Newtonian fluids

A Power law fluid and a Casson Fluid is investigated for $D_{\text{eff}}(t)$ and for different parameters specific for these fluids and the effect on $D_{\text{eff}}(t)$. The placement of the point concentration will also be changed to observe the effect of the initial placement.

Chapter 2

Basic Theory

Here is an overview of how S. Vedel and H. Bruus expressions are derived. The derivation is done in the same way and great resemble to the article will occur since is rewritten. For greater detail see the article [1] or in appendix. B.
First, the coordinates and the channel are arranged, the non-dimensionel numbers are found and nondimensionalization of the governing equation are done. The statical moments are setup and solved and the genereal formula or framework is found for D_{eff}.

2.1 Long straight channel

The channels characteristics: long, straight, parallel to the x-axis and translational invariant along the x-axis.
The coordinates system is written $\boldsymbol{r} = (x, \boldsymbol{r}_\perp)$, where the transverse ($y$, z)-plane is denoted $\boldsymbol{r}_\perp$, so that the full coordinates are written as $\boldsymbol{r} = (x, \boldsymbol{r}_\perp)$. The gradient operator $\boldsymbol{\nabla}$ and the Laplace operator ∇^2 are using the same notation.

$$\boldsymbol{r} = (x, \boldsymbol{r}_\perp), \qquad \text{with} \quad \boldsymbol{r}_\perp = (y, z), \tag{2.1a}$$
$$\boldsymbol{\nabla} = \mathbf{e}_x \partial_x + \boldsymbol{\nabla}_\perp, \quad \text{with} \quad \boldsymbol{\nabla}_\perp = \mathbf{e}_y \partial_y + \mathbf{e}_z \partial_z, \tag{2.1b}$$
$$\nabla^2 = \partial_x^2 + \nabla_\perp^2, \qquad \text{with} \quad \nabla_\perp^2 = \partial_y^2 + \partial_z^2. \tag{2.1c}$$

The channel is described with length $\mathcal{L}$ and with the cross sectional Ω area is $\mathcal{A} = \int_\Omega \mathrm{d}\boldsymbol{r}_\perp 1$, and the volume is $\mathcal{V} = \mathcal{L}\mathcal{A}$. The concentration field is denoted $c(x, \boldsymbol{r}_\perp, t)$, and the velocity $\vec{v} = u(\boldsymbol{r}_\perp, t)\vec{e}_x$.

2.1.1 Non-dimensionalising

For an easier handling of the equations we non-dimensionalize them using the following characteristic transverse length L_o, diffusion time T_o, advection velocity U_o from a scale

U_{char} in the time-dependent flow, shear-induced pressure P_{o}, and solute concentration C_{o},

$$L_{\mathrm{o}} = a,\ T_{\mathrm{o}} \quad = \frac{L_{\mathrm{o}}^2}{D},\ U_{\mathrm{o}} = U_{\mathrm{char}},\ P_{\mathrm{o}} \quad = \frac{\eta U_{\mathrm{o}}}{L_{\mathrm{o}}},\ C_{\mathrm{o}} = \frac{1}{\mathcal{V}} \int_{-\frac{1}{2}\mathcal{L}}^{\frac{1}{2}\mathcal{L}} \mathrm{d}x \int_{\Omega} \mathrm{d}\boldsymbol{r}_{\perp}\, c(\boldsymbol{r}_{\perp}, 0).$$

the choice of U_char is not unique, normally the mean velocity is chosen, but if the velocity field consists of oscillating flow, a different characteristic velocity should be chosen to describe the magnitude of the velocity.
By non-dimensionalising the Navier–Stokes equation, we get the stokes equation and non-dimensionalising advection-diffusion equation we get the well known three dimensionless numbers: the Péclet number Pé (the ratio of convection speed to mass diffusion speed), the Schmidt number Sc (the ratio of momentum diffusion speed to mass diffusion speed), and the Womersley number Wo (the square root of the ratio of oscillation speed at frequency $\tilde{\omega}_{\mathrm{o}}$ to momentum diffusion speed),[1]

$$\mathrm{Pé} = \frac{L_{\mathrm{o}}\, U_{\mathrm{o}}}{D}, \qquad \mathrm{Sc} = \frac{\nu}{D}, \qquad \mathrm{Wo} = \sqrt{\frac{L_{\mathrm{o}}^2 \tilde{\omega}_{\mathrm{o}}}{\nu}}. \tag{2.2}$$

2.1.2 the Velocity field

The velocity field is derived from the incompressible Navier-Stokes equation Eq. (1.2), because of symmetry in the long straight channel $(\mathbf{v}\cdot\boldsymbol{\nabla})\mathbf{v} = 0$ and non-dimensionalizing with respect to the diffusion time, we get the time-dependent Stokes equation,

$$\partial_t u(\boldsymbol{r}_{\perp}, t) = \mathrm{Sc}\Big[\nabla_{\perp}^2 u(\boldsymbol{r}_{\perp}, t) + \frac{1}{\mathcal{L}} \Delta p(t)\Big], \tag{2.3}$$

now $\vec{v} = u(\boldsymbol{r}_{\perp}, t)\vec{e}_x$ is linear and the velocity field can be represented by a Fourier series representation with Fourier components u_ℓ for each higher harmonics $\ell\omega_{\mathrm{o}}$ (ℓ being an integer), where the harmonics in this problem is given a priori,

$$u(\boldsymbol{r}_{\perp}, t) = \sum_{\ell=-\infty}^{\infty} u_\ell(\boldsymbol{r}_{\perp})\, \mathrm{e}^{\mathrm{i}\ell\omega_{\mathrm{o}} t}, \tag{2.4}$$

so Eq. (2.4) is set into Eq. (2.3), and the velocity field spatial representation is found in the specific geometry and then its dimensionlized with respect to U_{char} which is chosen to be the mean velocity. Then the velocity profile is non-dimensionalized,

$$\tilde{u}(\tilde{\boldsymbol{r}_{\perp}}, \tilde{t}) = \sum_{\ell=-\infty}^{\infty} \tilde{u}_\ell(\tilde{\boldsymbol{r}_{\perp}})\, \mathrm{e}^{\mathrm{i}\ell\omega_0 \tilde{t}}, \tag{2.5}$$

By requiring $u_{-\ell}(\boldsymbol{r}_{\perp}) = u_\ell^*(\boldsymbol{r}_{\perp})$, the asterisk is the complex conjugation, then the velocity field is real. The momentum of the fluid reacts to changes in driving pressure with an the momentum diffusion time $1/\alpha_{\mathrm{fl}}$, this is equivalent to the diffusion of concentration. The momentum diffusion time is derived from the momentum equation,$\partial_t u = \mathrm{Sc}\nabla_{\perp}^2 u$,

$$\alpha_{\mathrm{fl}} \propto \mathrm{Sc} \tag{2.6}$$

and where this relation also occurs,

$$\mathrm{Wo}^2 = \frac{\omega_\mathrm{o}}{\mathrm{Sc}} \propto \frac{\omega_\mathrm{o}}{\alpha_\mathrm{fl}} \tag{2.7}$$

2.1.3 The bra-ket notation for spatial dependence

The definition and the relations for the bra-ket notation.

$$\big\langle f\big|g\big\rangle = \frac{1}{\mathcal{V}} \int_{-\frac{1}{2}\mathcal{L}}^{\frac{1}{2}\mathcal{L}} \mathrm{d}x \int_\Omega \mathrm{d}\boldsymbol{r}_\perp \, f^*(x, \boldsymbol{r}_\perp, t)\, g(x, \boldsymbol{r}_\perp, t). \tag{2.8}$$

the longitudinal direction is averaged out and a bra-ket's defined in the transverse coordinates $\boldsymbol{r}_\perp$ is also needed,

$$\big\langle f_\perp\big|g_\perp\big\rangle = \frac{1}{\mathcal{A}} \int_\Omega \mathrm{d}\boldsymbol{r}_\perp \, f_\perp^*(\boldsymbol{r}_\perp, t)\, g_\perp(\boldsymbol{r}_\perp, t), \tag{2.9}$$

as the x-integration trivially gives unity. linearity

$$\big\langle f\big|A_1 g_1 + A_2 g_2\big\rangle = A_1\big\langle f\big|g_1\big\rangle + A_2\big\langle f\big|g_2\big\rangle, \tag{2.10}$$

since the velocity field is real, the relations occurs,

$$\big\langle u_\ell\big|g\big\rangle = \big\langle g\big|u_\ell\big\rangle^* = \big\langle g^*\big|u_{-\ell}\big\rangle, \tag{2.11a}$$

$$\big\langle u_\ell \, \mathrm{e}^{\mathrm{i}\ell\omega_\mathrm{o} t}\big|g\big\rangle = \mathrm{e}^{-\mathrm{i}\ell\omega_\mathrm{o} t}\big\langle u_\ell\big|g\big\rangle. \tag{2.11b}$$

completeness and orthonormal conditions,

$$\sum_{n=0}^{\infty} \big|f_n\big\rangle\big\langle f_n\big| = 1, \quad \text{and} \quad \big\langle f_m\big|f_n\big\rangle = \delta_{m,n}, \tag{2.12}$$

Any function $\big|g\big\rangle$ can be expanded by an orthonormal basis,

$$\big|g\big\rangle = \sum_{n=0}^{\infty} a_n \big|f_n\big\rangle, \tag{2.13a}$$

$$a_m = \big\langle f_m\big|g\big\rangle, \; m = 0, 1, 2, \ldots. \tag{2.13b}$$

Note that other similar bra-ket notation will be defined when the infinite parallel plate and the circular channel D_eff are derived.

2.1.4 The advection-diffusion equation

The transport of solute is described is by the dimensionless advection-diffusion equation.

$$\begin{aligned} \partial_t c(x, \boldsymbol{r}_\perp, t) + \mathrm{P\acute{e}}\, u(\boldsymbol{r}_\perp, t)\, \partial_x c(x, \boldsymbol{r}_\perp, t) \\ = (\partial_x^2 + \nabla_\perp^2)\, c(x, \boldsymbol{r}_\perp, t). \end{aligned} \tag{2.14}$$

The boundary conditions,

$$\vec{n} \cdot \boldsymbol{\nabla}_\perp c = 0, \text{ on all walls,} \tag{2.15a}$$
$$c(x, \boldsymbol{r}_\perp, 0) = \tilde{c}(x, \boldsymbol{r}_\perp), \tag{2.15b}$$
$$x^s \partial_x^q c \to 0, \text{ for } |x| \to \frac{\mathcal{L}}{2} \text{ and } s, q = 0, 1, 2, \ldots, \tag{2.15c}$$

with no flux on the wall of the channel, where $\vec{n}$ is the surface normal of the channel and $\tilde{c}$ is the given initial concentration, the last condition (2.15c) just states that all spatial gradients in c and c itself vanish far away the center in the longitudinal direction of the channel.

2.2 Method of statistical moments

The method of statistical moments is used to rewrite the advection-diffusion equation to give additional information about the solute distribution. The statistical moments are solved recursively starting with the first c_0 then afterwards obviously c_1[3]. The lower moment have direct physical meaning as M_0 is the averaged out concentration of the whole volume and M_1 the time-dependent axial center of mass $\bar{x}$.

2.2.1 Definition of the statistical moments

the concentrations $c(x, \boldsymbol{r}_\perp, t)$ axial moment pth $c_p(\boldsymbol{r}_\perp, t)$ and the associated full moment $M_p(t)$ are defined as

$$c_p(\boldsymbol{r}_\perp, t) = \frac{1}{\mathcal{L}} \int_{-\frac{1}{2}\mathcal{L}}^{\frac{1}{2}\mathcal{L}} \mathrm{d}x \, x^p c(x, \boldsymbol{r}_\perp, t), \quad p = 0, 1, 2, \ldots, \tag{2.16a}$$

$$M_p(t) = \langle x^p | c \rangle = \frac{1}{\mathcal{A}} \int_\Omega \mathrm{d}\boldsymbol{r}_\perp \, c_p(\boldsymbol{r}_\perp, t), \; p = 0, 1, 2, \ldots. \tag{2.16b}$$

Taking Eqs. (2.16a) and (2.16b) and using the advection-diffusion equation (2.14) on the moment's, the recursive equations of motion for c_p and M_p is found,

$$\partial_t c_p(\boldsymbol{r}_\perp, t) - \nabla_\perp^2 c_p(\boldsymbol{r}_\perp, t) = p(p-1) c_{p-2}(\boldsymbol{r}_\perp, t) + \mathrm{P\acute{e}}\, u(\boldsymbol{r}_\perp, t) p \, c_{p-1}(\boldsymbol{r}_\perp, t), \tag{2.17a}$$
$$\partial_t M_p(t) = \quad p(p-1) \langle 1 | c_{p-2} \rangle + \mathrm{P\acute{e}}\, p \langle u | c_{p-1} \rangle, \quad p = 0, 1, 2, \ldots, \tag{2.17b}$$

with the boundary conditions and initial conditions

$$\vec{n} \cdot \boldsymbol{\nabla}_\perp c_p = 0, \text{ on all walls,} \tag{2.18a}$$
$$c_p(\boldsymbol{r}_\perp, t) < \infty, \tag{2.18b}$$
$$c_p(\boldsymbol{r}_\perp, 0) = \tilde{c}_p(\boldsymbol{r}_\perp), \tag{2.18c}$$
$$M_p(0) = \langle x^p | \tilde{c} \rangle. \tag{2.18d}$$

M_0 is the averaged out concentration of the whole volume, gives the unit norm of c and M_1 is the time-dependent axial center of mass $\bar{x}$ of c,

$$M_0 = \langle 1|c\rangle = 1, \tag{2.19a}$$
$$M_1 = \langle x|c\rangle = \bar{x}(t). \tag{2.19b}$$

It is also useful to define the pth moment μ_p about the center of mass,

$$\mu_p(t) = \langle (x-\bar{x})^p|c\rangle, \tag{2.20}$$

and by the linearity, Eq. (2.10), we find for $p = 0$, 1 and 2,

$$\mu_0(t) = \langle 1|c\rangle = 1, \tag{2.21a}$$
$$\mu_1(t) = \langle (x-\bar{x})|c\rangle = 0, \tag{2.21b}$$
$$\mu_2(t) = \langle (x-\bar{x})^2|c\rangle = M_2(t) - M_1(t)^2. \tag{2.21c}$$

μ_2 relates to the time-dependent spatial variance of the solute concentration and thus to the solute diffusivity D and the effective diffusivity D_{eff}. Notice that μ_2 is in an moving frame since the spatial variance should be defined from the center of mass.

2.2.2 Effective diffusivity and statistical moments

From [1] they derived $\mathrm{d}\mu_2/\mathrm{d}t = 2D$ when no advection was present $u(\boldsymbol{r}_\perp, t) = 0$. Which gives a perfect expression for the diffusivity for $u = 0$ then $\frac{1}{2}\frac{\mathrm{d}\mu_2}{\mathrm{d}t}$ is calculated a nonzero velocity velocity field which gives the effective diffusivity, which is time derivative of the solute spatial variance,

$$D_{\text{eff}}(t) = \frac{1}{2}\frac{\mathrm{d}\mu_2}{\mathrm{d}t} = \frac{1}{2}\frac{\mathrm{d}M_2}{\mathrm{d}t} - M_1\,\frac{\mathrm{d}M_1}{\mathrm{d}t}, \tag{2.22}$$

2.3 Mathematical procedure

To find the effective diffusivity, Eq. (2.22) a number of calculations are needed first to determine $c_{\text{o}}(\boldsymbol{r}_\perp, t)$. Then by recursively solving Eq. (2.17a) we get $c_1(\boldsymbol{r}_\perp, t)$. Now the full moments M_1 and M_2 is found from Eq. (2.17b) with $p = 1$ and 2, which then are fed into Eq. (2.22) to determine D_{eff}.

2.3.1 The zeroth axial moment and basis functions

We begin by analyzing the $p = 0$ axial moment equation (2.17a) for $c_{\text{o}}(\boldsymbol{r}_\perp, t)$,

$$\big(\partial_t - \nabla_\perp^2\big)\big|c_{\text{o}}(\boldsymbol{r}_\perp, t)\big\rangle = 0. \tag{2.23}$$

This moment fulfills the Neumann boundary condition

$$\vec{n}\cdot\boldsymbol{\nabla}_\perp c_{\text{o}} = 0, \text{ on all walls}, \tag{2.24}$$

and has the initial condition

$$c_{\mathrm{o}}(\boldsymbol{r}_\perp, 0) = \tilde{c}_0(\boldsymbol{r}_\perp) = \int_{-\frac{1}{2}\mathcal{L}}^{\frac{1}{2}\mathcal{L}} \mathrm{d}x\, \tilde{c}(x, \boldsymbol{r}_\perp). \tag{2.25}$$

Using separation of variables, the solution for $c_{\mathrm{o}}(\boldsymbol{r}_\perp, t)$ can be written as the expansion

$$\big|c_{\mathrm{o}}(\boldsymbol{r}_\perp, t)\big\rangle = \sum_{n=0}^{\infty} a_{0n} \mathrm{e}^{-\lambda_n t} \big|f_n(\boldsymbol{r}_\perp)\big\rangle, \tag{2.26}$$

where the time-independent eigenfunctions $f_n(\boldsymbol{r}_\perp)$ with eigenvalues λ_n are defined by

$$(\lambda_n + \nabla_\perp^2)\big|f_n(\boldsymbol{r}_\perp)\big\rangle = 0, \ n = 0, 1, 2, \ldots, \tag{2.27a}$$

$$\vec{n} \cdot \boldsymbol{\nabla}_\perp \big|f_n(\boldsymbol{r}_\perp)\big\rangle = 0, \text{ on all walls}, \tag{2.27b}$$

and form a complete orthonormal basis in the sense of Eq. (2.12). Note that the lowest eigenvalue is zero, $\lambda_0 = 0$, and the corresponding eigenfunction is unity, $f_0(\boldsymbol{r}_\perp) = 1$, while for $n > 0$ the eigenvalues are positive, $\lambda_n > 0$. This method is particularly convenient for problems involving the Laplace operator, because often the corresponding basis functions and eigenvalues are known.

As in Eq. (2.13b), the expansion coefficients a_{0m} are found by multiplying Eq. (2.26) at $t = 0$ by $\big\langle f_m\big|$,

$$a_{0m} = \big\langle f_m \big| \tilde{c}_0 \big\rangle, \quad m = 0, 1, 2, \ldots. \tag{2.28}$$

When time approaches infinity, all terms in the expansion except $n = 0$ decay exponentially, and we obtain

$$\big|c_{\mathrm{o}}(\boldsymbol{r}_\perp, \infty)\big\rangle = a_{00}\big|f_0(\boldsymbol{r}_\perp)\big\rangle = \big\langle 1\big|\tilde{c}_0\big\rangle\big|1\big\rangle = \big|1\big\rangle, \tag{2.29}$$

representing the state where by diffusion the solute concentration has spread out uniformly in space.

2.3.2 The first axial moment and basis functions

The $p = 1$ axial moment equation (2.17a) for $c_1(\boldsymbol{r}_\perp, t)$ is analyzed in a similar manner. Using that $c_{\mathrm{o}}(\boldsymbol{r}_\perp, t)$ is now a known function, we have

$$\begin{aligned} \big(\partial_t - \nabla_\perp^2\big)\big|c_1(\boldsymbol{r}_\perp, t)\big\rangle &= \mathrm{P\acute{e}}\, u(\boldsymbol{r}_\perp, t)\, \big|c_{\mathrm{o}}(\boldsymbol{r}_\perp, t)\big\rangle \\ &= \mathrm{P\acute{e}}\, u(\boldsymbol{r}_\perp, t) \sum_{n=0}^{\infty} a_{0n} \mathrm{e}^{-\lambda_n t} \big|f_n(\boldsymbol{r}_\perp)\big\rangle, \end{aligned} \tag{2.30a}$$

where c_1 fulfills the Neumann boundary condition

$$\vec{n} \cdot \boldsymbol{\nabla}_\perp c_1 = 0, \text{ on all walls}, \tag{2.30b}$$

and the initial condition

$$c_1(\boldsymbol{r}_\perp, 0) = \tilde{c}_1(\boldsymbol{r}_\perp) = \int_{-\frac{1}{2}\mathcal{L}}^{\frac{1}{2}\mathcal{L}} \mathrm{d}x\, x\, \tilde{c}(x, \boldsymbol{r}_\perp). \tag{2.30c}$$

solving the inhomogeneous partial differential equation (2.30a) for c_1 see [1], from this solution the coefficient are used to find the effective diffusivity

$$\gamma_{1n} = \big\langle f_n \big| u_0(\boldsymbol{r}_\perp) \big| f_n \big\rangle, \tag{2.31}$$

and the β-coefficients are given by

$$\beta_{kn}^{\ell} = (1 - \delta_{\ell,0}\delta_{k,n}) \, \frac{\big\langle f_k \big| u_\ell(\boldsymbol{r}_\perp) \big| f_n \big\rangle}{\lambda_k - \lambda_n + \mathrm{i}\ell\omega_\mathrm{o}}. \tag{2.32}$$

note that, $\beta_{kn}^{-\ell} = (\beta_{kn}^{\ell})^*$ ensures real values of the resulting fields. The coefficients a_{1n}

$$a_{1n} = \frac{1}{\mathrm{Pé}} \big\langle f_n \big| \tilde{c}_1(\boldsymbol{r}_\perp) \big\rangle - \sum_{k=0}^{\infty} a_{0k} \sum_{l=-\infty}^{\infty} \beta_{nk}^{\ell}. \tag{2.33}$$

Collecting all terms, we write the formal solution as

$$\begin{aligned} \big| c_1(\boldsymbol{r}_\perp, t) \big\rangle = \mathrm{Pé} \sum_{m=0}^{\infty} \sum_{n=0}^{\infty} \Bigg[& (a_{0n}\gamma_{1n} t + a_{1n}) \delta_{n,m} \\ & + a_{0n} \Big(\sum_{\ell=-\infty}^{\infty} \beta_{mn}^{\ell} \mathrm{e}^{\mathrm{i}\ell\omega_\mathrm{o} t} \Big) \Bigg] \mathrm{e}^{-\lambda_n t} \big| f_m \big\rangle. \end{aligned} \tag{2.34}$$

All results are explicitly real because of the pairwise summation of complex conjugate terms with index ℓ and $-\ell$.

2.3.3 Expressions for the effective diffusivity

Now that c_0 and c_1 are found in the form of basis functions, the effective diffusivity $D_\mathrm{eff} = \frac{1}{2}\frac{\mathrm{d}M_2}{\mathrm{d}t} - M_1 \frac{\mathrm{d}M_1}{\mathrm{d}t}$ can now be expressed in terms of a basis function expansion. The time derivative $\frac{\mathrm{d}M_1}{\mathrm{d}t} = \mathrm{Pé} \big\langle u \big| c_\mathrm{o} \big\rangle$ of the full moment M_1 in Eq. (2.17b) becomes

$$\frac{\mathrm{d}M_1}{\mathrm{d}t} = \mathrm{Pé} \sum_{n=0}^{\infty} \sum_{\ell=-\infty}^{\infty} a_{0n} \big\langle u_\ell \big| f_n \big\rangle \, \mathrm{e}^{-(\lambda_n + \mathrm{i}\ell\omega_\mathrm{o})t}, \tag{2.35a}$$

where we have used Eq. (2.11b) for the phase factor. By proper choice of the coordinate system, the initial centroid $\bar{x}(0)$ of the distribution is zero. This combined with Eq. (2.19b) determines the initial value $M_1(0) = \bar{x}(0) = 0$, and time integration of Eq. (4.42a) gives

$$M_1 = \mathrm{Pé} \sum_{n=0}^{\infty} \sum_{\ell=-\infty}^{\infty} a_{0n} \big\langle u_\ell \big| f_n \big\rangle \, \frac{1 - \mathrm{e}^{-(\lambda_n + \mathrm{i}\ell\omega_\mathrm{o})t}}{\lambda_n + \mathrm{i}\ell\omega_\mathrm{o}}. \tag{2.35b}$$

Here, the term $(n, \ell) = (0, 0)$ depends linearly on time because $\lim_{q\to 0} \big[(1 - \mathrm{e}^{-qt})/q\big] = t$. Similarly, for the time derivative $\frac{\mathrm{d}M_2}{\mathrm{d}t} = \big\langle 1 \big| c_\mathrm{o} \big\rangle + \mathrm{Pé} \big\langle u \big| c_1 \big\rangle$ of the full moment M_2,

Eq. (2.17b), we obtain

$$\frac{1}{2}\frac{\mathrm{d}M_2}{\mathrm{d}t} = 1 + \mathrm{P\acute{e}}^2 \sum_{m=0}^{\infty}\sum_{n=0}^{\infty}\sum_{k=-\infty}^{\infty} \langle u_k | f_m \rangle \, \mathrm{e}^{-(\lambda_n + \mathrm{i}k\omega_\mathrm{o})t} \times \left[(a_{0n}\gamma_{1n}t + a_{1n})\delta_{n,m} + a_{0n} \sum_{\ell=-\infty}^{\infty} \beta_{mn}^{\ell} \mathrm{e}^{i\ell\omega_\mathrm{o}t} \right], \tag{2.35c}$$

valid for any initial distribution of solute, in this thesis the initial distribution will be a point concentration in different geometries.

The time-averaged diffusivity $D_{\mathrm{eff}}^{\mathrm{avr}}(t)$ over one oscillation period $\tau_0 = 2\pi/\omega_\mathrm{o}$ is defined as,

$$D_{\mathrm{eff}}^{\mathrm{avr}}(t) = \frac{1}{\tau_0}\int_t^{t+\tau_0} D_{\mathrm{eff}}(t)\,\mathrm{d}t. \tag{2.36a}$$

2.3.4 Axial moments for the point concentration

A point concentration $C(x, \mathbf{r}_\perp, t)$ is used where $\mathcal{V}$ is the volume of the channel and N_0 is the number of particles. The point concentration is always placed in the middle of the longitudinal direction at $x = 0$, this is a convenient placement regarding the initial condition and the formalism since $\tilde{c_1}(\mathbf{r}_\perp, 0)$. Transversely it is placed $\mathbf{r}_\perp^0$

$$C(x, \mathbf{r}_\perp, t) = N_0\delta(x)\delta(\mathbf{r}_\perp - \mathbf{r}_\perp^0) \tag{2.37}$$

$\langle 1 | C_0 \rangle = \frac{N_0}{\mathcal{V}} = \frac{N_0}{\mathcal{A}\mathcal{L}}$ is the average concentration, and normalising with respect to this average concentration we get the initial non-dimensional concentration,

$$\tilde{C}(x, \mathbf{r}_\perp, t) = \mathcal{A}\mathcal{L}\delta(x)\delta(\mathbf{r}_\perp - \mathbf{r}_\perp^0) \tag{2.38}$$

The initial condition for the zero axial moments,

$$\tilde{c_0}(\mathbf{r}_\perp, 0) = \frac{1}{\mathcal{L}}\int_{-\frac{1}{2}\mathcal{L}}^{\frac{1}{2}\mathcal{L}} \mathrm{d}x\mathcal{A}\mathcal{L}\delta(x)\delta(\mathbf{r}_\perp - \mathbf{r}_\perp^0) = \mathcal{A}\delta(\mathbf{r}_\perp - \mathbf{r}_\perp^0) \tag{2.39}$$

and the first axial moments, where the first axial moment is always equal to zero since the concentration is always placed in the middle of the longitudinal direction $\delta(x)x = 0$,

$$\tilde{c_1}(\mathbf{r}_\perp, 0) = \frac{1}{\mathcal{L}}\int_{-\frac{1}{2}\mathcal{L}}^{\frac{1}{2}\mathcal{L}} \mathrm{d}x\mathcal{A}\mathcal{L}\delta(x)\delta(\mathbf{r}_\perp - \mathbf{r}_\perp^0)x = 0 \tag{2.40}$$

Chapter 3

Point concentration in the infinite parallel-plate channel

Now the infinite parallel-plate channel effective diffusivity $D_{\text{eff}}^{\text{Point}}(z_0, t)$ will be examined, in this case for a point concentration. This is a more complicated calculation than the uniform concentration since spatial dependence is present in the transverse direction. First the problem is set-up and all the equations are solved.
The velocity profile is solved from the stokes equation Eq. (2.3) in the infinite parallel plate channel. Then the basis functions are found from the zeroth axial moments in this geometry. Because of the basis functions, a convenient bra-ket notation is made for this problem. The bra-ket can be calculated and the formalism can be used, depending on the initial concentration location and its form.

The set-up is similar to the rectangular cross sections in [1], where in this case the initial concentration is a point concentration and the velocity field only has velocity gradients in the z-direction due to the parallel plate. Now the effective diffusivity can be calculated from the formalism. For shortness sometimes the initial point concentration will be referred to as the point, and the uniform distribution in the cross sectional plane as the uniform concentration.

3.1 The velocity profile

The channel has x as longitudinal direction and y, z in the transverse direction with $2a$ as the distance of the plate or height. First step is to find the well known parallel plate steady state velocity profile and then nondimensionalize it with respect to mean velocity,

$$0 = \partial_z^2 u_0(z) + \frac{\Delta p_0}{\eta \mathcal{L}}. \tag{3.1}$$

the solution, with no slip at $u_0(-a) = u_0(a) = 0$,

$$u_0(z) = \frac{\Delta p_0}{2\eta \mathcal{L}}(a^2 - z^2). \tag{3.2}$$

finding the mean velocity,

$$U_{char} = \frac{1}{2a}\int_{-a}^{a} \frac{\Delta p_0}{2\eta\mathcal{L}} \mathrm{d}z(a^2 - z^2) = \frac{\Delta p_0 a^2}{3\eta\mathcal{L}}. \tag{3.3}$$

Now nondimensionalizing with respect to the mean velocity U_{char}, and $z = a\tilde{z}$ where the characteristic length scale is determined to be $L_0 = a$, with $a \leq w$ as an aspect ratio $R = \frac{w}{a}$. In the nondimensionlized units the rectangular cross section is placed such that $-1 \leq \tilde{z} \leq 1$ where $z = a\tilde{z}$ and $\frac{y}{a} = \tilde{y}$ where $-R \leq \tilde{y} \leq R$ the width is later used for placement of a boundary condition Fig. 3.1 and where $\epsilon_l = \frac{\Delta p_l}{\Delta p_0}$ and $\frac{\Delta p_0}{\Delta p_0} = \epsilon_0 = 1$.

$$\tilde{u}_0(\tilde{z}) = \frac{3\epsilon_0}{2}(1 - \tilde{z}^2). \tag{3.4}$$

Then using the stokes equation Eq. (2.3) to find the time dependent velocity profiles where $l \neq 0$,

$$\partial_z^2 u_l(z) = \frac{\mathrm{i}l\omega_0}{\nu} u_l(z) - \frac{\Delta p_l}{\eta\mathcal{L}}. \tag{3.5}$$

the solution that satisfies the no slip boundary condition $u_l(-1) = u_l(1) = 0$ using $z = a\tilde{z}$ so $-1 \leq \tilde{z} \leq 1$ and $k_l = \sqrt{\frac{a^2 l\omega_0}{\mathrm{i}\nu}} = \sqrt{-\mathrm{i}l\mathrm{Wo}}$,

$$u_l(\tilde{z}) = \frac{\Delta p_l a^2}{k_l^2 \eta\mathcal{L}} \left(\frac{\cos(\tilde{z}k_l)}{\cos(k_l)} - 1 \right). \tag{3.6}$$

nondimensionalizing $u_l(\tilde{z})$ with respect to mean velocity U_{char},

$$\tilde{u}_l(\tilde{z}) = \frac{3\epsilon_l}{k_l^2} \left(\frac{\cos(\tilde{z}k_l)}{\cos(k_l)} - 1 \right). \tag{3.7}$$

where the whole velocity field is,

$$\tilde{u}(\tilde{z}, \tilde{t}) = \sum_{\ell=-\infty}^{\infty} \tilde{u}_\ell(\tilde{z})\, \mathrm{e}^{\mathrm{i}\ell\omega_0\tilde{t}}, \tag{3.8}$$

3.2 Basis functions

The time-independent eigenfunctions $f_{(n,m)}(y,z) = g_n(y)h_m(z)$ and eigenvalues $\lambda_{(n,m)}$ are needed for the parallel plate problem to solve the zeroth axial moment equation $p = 0$,

$$(\lambda_{(n,m)} - \nabla_\perp^2) \mid g_n(y)h_m(z)\rangle = 0. \tag{3.9}$$

Then only Neumann boundary conditions exist on the top and bottom plate. The Boundary condition on the sides is missing, but creating special no flux side walls with slip

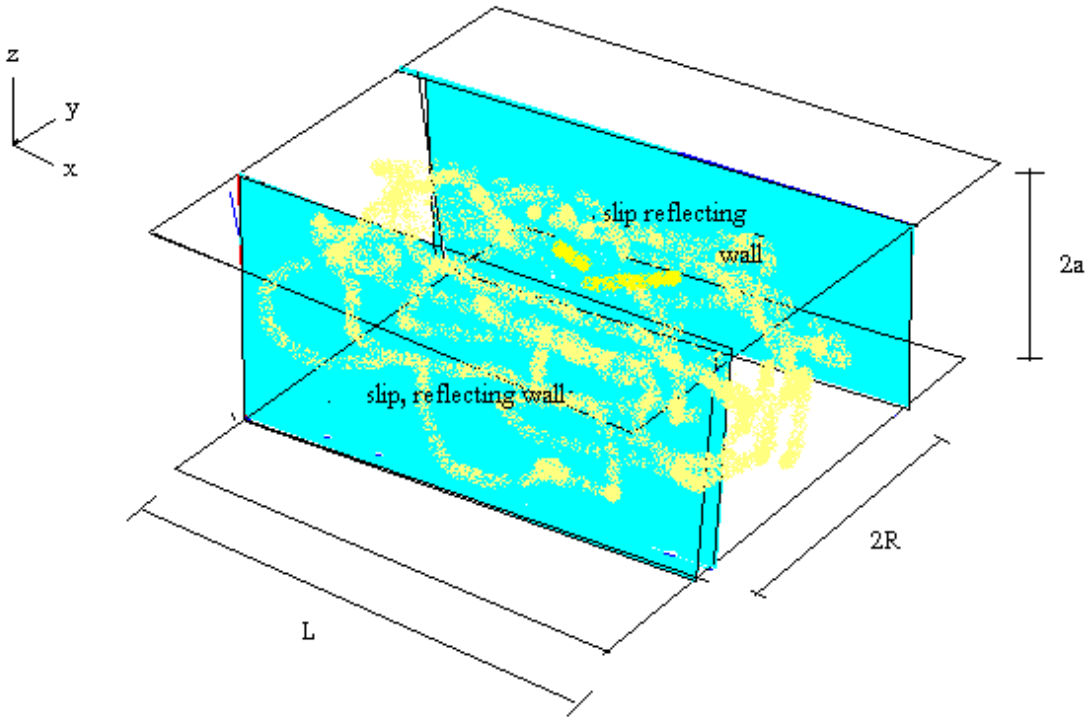

Figure 3.1: Here is the infinite parallel plate channel with length L($\mathcal{L}$) and height $2a$. The light green walls are slip boundaries with no flux. The yellow points are examples of solutes particles.

conditions takes care of this problem. This wall can be seen in the Fig. 3.1. With these assumptions the basis functions $g_n(y)h_m(z)$,

$$g_n(y) = \sqrt{\frac{2}{1+\delta_{n,0}}}\cos\left(n\pi\frac{1+\frac{y}{R}}{2}\right) \tag{3.10}$$
$$h_m(z) = \sqrt{\frac{2}{1+\delta_{m,0}}}\cos\left(m\pi\frac{1+z}{2}\right).$$

and the eigenvalues,

$$\lambda_{(n,m)} = \left(n\pi\frac{1}{2R}\right)^2 + \left(m\pi\frac{1}{2}\right)^2. \tag{3.11}$$

are the same as in Bruus and Vedel [1]. For the no slip walls the placement in y is irrelevant since the velocity profile is only changing in the z direction and only inducing shear in that direction. Later in the calculation, it will be seen that the basis functions $g_n(y)$ will drop out from the bra-kets and $D_{\text{eff}}(t)$. Thereby the fluid momentum equilibration rate

can be found as,

$$\alpha_{fl} = \left(\frac{\pi^2}{4}\right) \mathrm{Sc}. \tag{3.12}$$

Due to $n = 0$ in the expression for $D_{\mathrm{eff}}^{\mathrm{Point}}(z_0, t)$ giving only one inherent length: the z-direction. Since only one inherent length along the z-direction is present this introduces the solute equilibration rate,

$$\lambda_{(0,1)} = \left(\frac{\pi}{2}\right)^2. \tag{3.13}$$

The time when most of the anomalous diffusion is decreased is around $\frac{1}{\lambda_{(0,1)}} = \frac{4}{\pi^2} \approx 0.4 < t$. This is similar to Vedel and Bruus, "The rectangular cross section" [1].

3.2.1 Inner product

Because of the basis functions, a convenient bra-ket notation is made for this problem, where orthogonality is used in the bra-ket thereby getting rid all the y dependence, this is later used for the $D_{\mathrm{eff}}(t)$ formalism. For the Cartesian coordinates $f_\perp(\boldsymbol{r}_\perp) = g(y)h(z)$ and $\tilde{f}_\perp(\boldsymbol{r}_\perp) = \tilde{g}(y)\tilde{h}(z)$ in $2D$ we have,

$$\langle f_\perp \mid \tilde{f}_\perp \rangle = \frac{1}{\mathcal{A}} \int_\Omega \mathrm{d}\boldsymbol{r}_\perp f_\perp^*(\boldsymbol{r}_\perp)\tilde{f}_\perp(\boldsymbol{r}_\perp) = \langle g \mid \tilde{g}\rangle\langle f \mid \tilde{f}\rangle, \tag{3.14}$$

where we have introduced the new bra-ket in y, z with $2a$ as height and $2w$ as width. Defined as,

$$\langle g \mid \tilde{g}\rangle = \frac{1}{2w} \int_{-w}^{w} \mathrm{d}y g^*(y)\tilde{g}(y). \tag{3.15}$$

and z,

$$\langle h \mid \tilde{h}\rangle = \frac{1}{2} \int_{-1}^{1} \mathrm{d}z h^*(z)\tilde{h}(z). \tag{3.16}$$

Also having the relation

$$\langle u_l(z) \mid g_n(y)h_m(z)\rangle = \langle g_n(y)h_m(z) \mid u_l(z)\rangle^* \tag{3.17}$$

since we have the geometry, basis functions, eigenvalues and the velocity profiles. Now the bra-ket defined is used, starting with $\langle u_l(z) \mid f_{(n,m)}(y, z)\rangle$,

$$\langle u_l(z) \mid g_n(y)h_m(z)\rangle = \langle 1 \mid g_n(y)\rangle\langle u_l(z) \mid h_m(z)\rangle = \delta_{n,0}\langle u_l(z) \mid h_m(z)\rangle. \tag{3.18}$$

because $g_0(y) = 1$ and $\langle g_0(y) \mid g_n(y)\rangle = \delta_{n,0}$. The next bracket $\langle f_{(n,m)}(y, z) \mid u_0(z) \mid f_{(n,m)}(y, z)\rangle$,

$$\langle g_n(y)h_m(z) \mid u_0(z) \mid g_n(y)h_m(z)\rangle = \langle h_m(z) \mid u_l(z) \mid h_m(z)\rangle \tag{3.19}$$

obviously $\langle g_n(y) \mid g_n(y)\rangle = 1$, since it is a basis function. To the last and most complicated bra-ket $\langle f_{(n,m)}(y, z) \mid u_0(z) \mid f_{(p,j)}(y, z)\rangle$

$$\langle g_n(y)h_m(z) \mid u_0(z) \mid g_p(y)h_j(z)\rangle = \delta_{n,p}\langle h_m(z) \mid u_l(z) \mid h_j(z)\rangle \tag{3.20}$$

this gives significantly simplifications in further calculations and now the placement of the no-flux wall is irrelevant since no y-dependence is in the bra-kets.

3.2.2 Reproducing results existing in Literature for the infinite parallel plate channel.

Before the results of the analysis are shown, earlier results from the literature will be found for the uniform distribution in the cross- sectional plane. Thereby verifying the implementation of the work $D_{\text{eff}}(t)$ with an uniform distribution in the cross-sectional plane in matlab. It was possible to recover the coefficient χ_{rect} found by Chatwin and Sullivan for the infinite parallel plate with a uniform concentration in the cross sectional plane [27],

$$D_{\text{eff}}^{\text{steady}}(\infty) = 1 + \chi_{\text{rect}}\text{Pé}^2, \text{ for } R \to \infty, \tag{3.21a}$$

$$\chi_{\text{rect}} = \frac{2}{105} \approx 0.019, \text{ infinite parallel plates} \tag{3.21b}$$

This result can also be seen in Fig. 3.2.

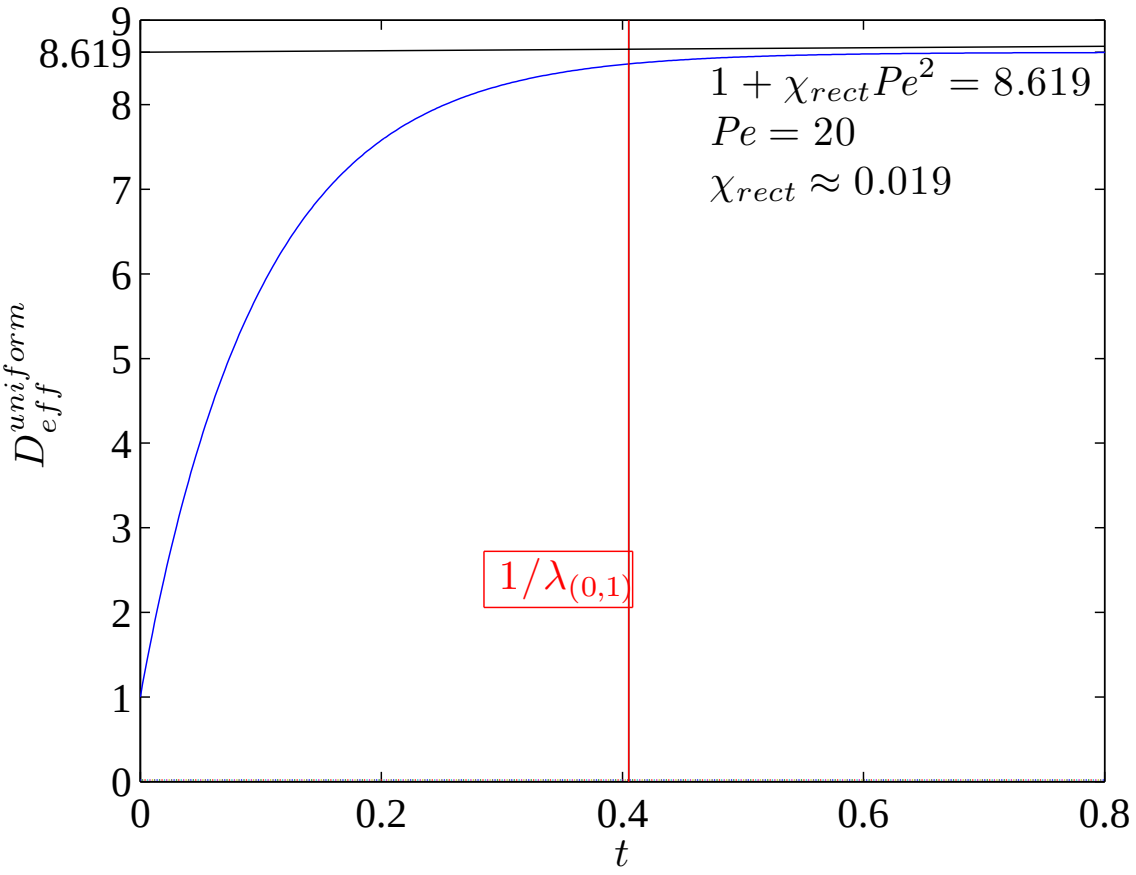

Figure 3.2: The effective diffusion $D_{\text{eff}}(t)$, for the uniform distribution in the cross sectional plane in a infinite parallel plate channel with Pé = 20. The result from Chatwin and Sullivan are obtain by getting the $\chi_{rect} = 0.019$ [27], for the infinite parallel plate channel.

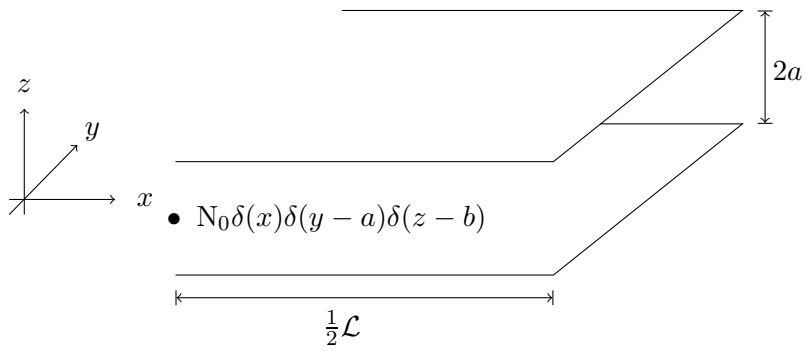

Figure 3.3: Half of the infinite parallel plate channel $\frac{1}{2}\mathcal{L}$ with $2a$ as height and $\mathcal{L}$ as length. The coordinate $\tilde{z}$ is chosen to run as $z = a\tilde{z}$ and $-R \leq \tilde{y} \leq R$, a point concentration is placed in the middle of the longitudinal direction $x = 0$ with freedom in the transverse direction $(y,\, z)$.

3.3 Framework for the applied point concentrations in the parallel plates channel

Firstly, the geometry is set-up and then the velocity field, the basis function and the braket are found. Now the point concentration can be applied in the formula for D_{eff}. From now on we denote y, z as nondimensionlized units, meaning that $\tilde{z} = z, \tilde{y} = y$. The initial placement of the point concentration will determine the effective diffusion $D_{\text{eff}}^{\text{Point}}(z_0, t)$.

3.3.1 Analysis of the point concentration with random placement

Putting the initial point concentration in the transverse placement $(y, z) = (a, b)$ which is normalized $\tilde{C}_0 = 1$. The initial normalized concentration is given by,

$$c(x, \mathbf{r}_\perp, 0) = V\delta(x)\delta(y-a)\delta(z-b). \tag{3.22}$$

finding the initial condition for the zero axial moments from Eq. (2.25),

$$\tilde{c_0}(y, z, 0) = \frac{1}{\mathcal{L}} \int_{-\frac{1}{2}\mathcal{L}}^{\frac{1}{2}\mathcal{L}} dx V\delta(x)\delta(y-a)\delta(z-b) = \mathcal{A}\delta(y-a)\delta(z-b). \tag{3.23}$$

and the initial first axial moment is zero because of the location in the center $x = 0$ of the longitudinal x-direction. Since the basis function and the velocity field are known, then the different coefficients are needed to calculate the effective diffusion coefficient starting with $a_{0,(m,n)}$ from Eq. (2.28),

$$a_{0,(m,n)} = \left\langle \frac{2\cos\left(n\pi\frac{R+y}{2R}\right)\cos\left(m\pi\frac{1+z}{2}\right)}{\sqrt{(1+\delta_{n,0})(1+\delta_{m,0})}} \mid \mathcal{A}\delta(y-a)\delta(z-b) \right\rangle \tag{3.24}$$

giving

$$a_{0,(m,n)} = \frac{2\cos\left(n\pi\frac{1+\frac{a}{R}}{2}\right)\cos\left(m\pi\frac{1+b}{2}\right)}{\sqrt{(1+\delta_{n,0})(1+\delta_{m,0})}} \tag{3.25}$$

all the $a_{0,(m,n)}$ coefficients give values unless a, b is placed in some period of the cosines or if it is placed in the center, many terms will drop out this is investigated later in this section. Then calculating the coefficient $\beta^l_{(n,m),(p,j)}$ with $n = (n, m)$ and $m = (p, j)$ because of the geometry from Eq. (3.27),

$$\beta^l_{(n,m),(p,j)} = (1 - \delta_{l,0}\delta_{n,p}\delta_{m,j})\frac{\langle g_n(y)h_m(z) \mid u_l(z) \mid g_p(y)h_j(z)\rangle}{\lambda_{(n,m)} - \lambda_{(p,j)} + \mathrm{i}l\omega_0}, \tag{3.26}$$

using Eq. (3.20),

$$\beta^l_{(n,m),(p,j)} = (1 - \delta_{l,0}\delta_{n,p}\delta_{m,j})\frac{\delta_{n,p}\langle h_m(z) \mid u_l(z) \mid h_j(z)\rangle}{\lambda_{(n,m)} - \lambda_{(n,j)} + \mathrm{i}l\omega_0}, \tag{3.27}$$

so $\beta^l_{(n,m),(p,j)}$ can be rewritten,

$$\delta_{n,p}\beta^l_{(n,m),(p,j)} = \beta^l_{(n,m),(n,j)} \tag{3.28}$$

Calculating $a_{1,(n,m)}$, since $\tilde{c_1}\rangle = 0$ and using earlier defined coefficients. Remembering orthogonality when $n \neq p$ removing the p-sum,

$$a_{1,(n,m)} = -\sum_{p=0}^{\infty}\sum_{j=0}^{\infty} a_{0,(p,j)} \sum_{l=-\infty}^{\infty} \beta^l_{(n,m),(p,j)} = -\sum_{j=0}^{\infty} a_{0,(n,j)} \sum_{l=-\infty}^{\infty} \beta^l_{(n,m),(n,j)}, \tag{3.29}$$

finding $\gamma_{1,(0,m)}$

$$\gamma_{1,(0,m)} = \langle g_n(y)h_m(z) \mid u_0(z) \mid g_n(y)h_m(z)\rangle = \langle h_m(z) \mid u_0(z) \mid h_m(z)\rangle \tag{3.30}$$

Now all the coefficients are found and we can calculate $\frac{\mathrm{d}M_1}{\mathrm{d}t}$ and since it contains $\delta_{n,0}\langle u_l(z) \mid h_m\rangle$, the n sum is removed,

$$\frac{\mathrm{d}M_1}{\mathrm{d}t} = \mathrm{Pe}\sum_{m=0}^{\infty}\sum_{l=-\infty}^{\infty} a_{0,(0,m)}\langle u_l(z) \mid h_m(z)\rangle e^{-(\lambda_{0,m}+\mathrm{i}l\omega_0)t} \tag{3.31}$$

and calculating M_1,

$$M_1 = \mathrm{Pe}\sum_{m=0}^{\infty}\sum_{l=-\infty}^{\infty} a_{0,(0,m)}\langle u_l(z) \mid h_m(z)\rangle \frac{1 - e^{-(\lambda_{(0,m)}+\mathrm{i}l\omega_0)t}}{\lambda_{(0,m)} + \mathrm{i}l\omega_0} \tag{3.32}$$

multiplying $M_1\frac{\mathrm{d}M_1}{\mathrm{d}t}$,

$$M_1\frac{\mathrm{d}M_1}{\mathrm{d}t} = \mathrm{Pe}^2\sum_{k=-\infty}^{\infty}\sum_{j=0}^{\infty}\sum_{m=0}^{\infty}\sum_{l=-\infty}^{\infty} a_{0,(0,m)}a_{0,(0,j)}\langle u_l(z) \mid h_m(z)\rangle \langle u_k(z) \mid h_j(z)\rangle \frac{1 - e^{-(\lambda_{0,m}+\mathrm{i}l\omega_0)t}}{\lambda_{0,m} + \mathrm{i}l\omega_0} e^{-(\lambda_{0,j}+\mathrm{i}k\omega_0)t} \tag{3.33}$$

finding $\frac{1}{2}\frac{\mathrm{d}M_2}{\mathrm{d}t}$ using Eq. (4.42c) but now where the sums $n = (n, m)$ and $m = (p, j)$. Because of Eq. (3.18) and Eq. (3.20), when $n \neq 0$ the sum is always zero and $\delta_{p,n}$,

$$\frac{1}{2}\frac{\mathrm{d}M_2}{\mathrm{d}t} = 1 + \mathrm{Pe}^2 \sum_{n,m=0}^{\infty} \sum_{k=-\infty}^{\infty} \sum_{p,j=0}^{\infty} \delta_{n,0} \langle u_k(z) \mid h_m(z) \rangle e^{-(\lambda_{(p,j)} + \mathrm{i}k\omega_0)t} \tag{3.34}$$
$$\times \delta_{n,p} \left[(a_{0,(p,j)}\gamma_{1,(p,j)}t + a_{1,(p,j)})\delta_{m,j}\delta_{0,p} + a_{0,(0,j)} \sum_{l=-\infty}^{\infty} \beta^{l}_{(0,m),(0,j)} e^{\mathrm{i}l\omega_0 t} \right]$$

simplifying $\frac{1}{2}\frac{\mathrm{d}M_2}{\mathrm{d}t}$ by removing the sums $n,\ p$ because $\delta_{n,0}\delta_{n,p} = \delta_{n,0}\delta_{p,0}$ and for increasing computational speed in Matlab implementation, the sums are split and also using $\delta_{m,j}$,

$$\frac{1}{2}\frac{\mathrm{d}M_2}{\mathrm{d}t} = 1 + \mathrm{Pe}^2 \sum_{m=0}^{\infty} \left(\sum_{k=-\infty}^{\infty} \langle u_k(z) \mid h_m(z) \rangle e^{-\mathrm{i}k\omega_0 t} \right) \sum_{j=0}^{\infty} e^{-(\lambda_{(0,j)})t} \tag{3.35}$$
$$\left((a_{0,(0,j)}\gamma_{1,(0,j)}t + a_{1,(0,j)})\delta_{m,j} + a_{0,(0,j)} \sum_{l=-\infty}^{\infty} \beta^{l}_{(0,m),(0,j)} e^{\mathrm{i}l\omega_0 t} \right)$$

combining to the expression $D^{\mathrm{Point}}_{\mathrm{eff}}(z_0, t) = \frac{1}{2}\frac{\mathrm{d}M_2}{\mathrm{d}t} - M_1\frac{\mathrm{d}M_1}{\mathrm{d}t}$.

3.3.2 Notes on $D^{\mathrm{Point}}_{\mathrm{eff}}(z_0, t)$ and Changing the Peclet number

As mentioned before, the y dependence vanished, this can been seen in both $\frac{1}{2}\frac{\mathrm{d}M_2}{\mathrm{d}t}$ and $M_1\frac{\mathrm{d}M_1}{\mathrm{d}t}$ where no dependence in the y-direction is present. This means that the placement of the point concentration in y has a symmetry and this is due to the velocity field independence of the y-direction. Note also that, there is a term in the sum of $\frac{\mathrm{d}M_1}{\mathrm{d}t}$ that is increasing linearly with time, when $k = j = m = l = 0$ and using $\lim_{\mathrm{q}\to\infty}[(1-e^{-qt})/q = t]$ the term is $a_{0,(0,0)}a_{0,(0,0)}\langle u_0(z) \mid 1\rangle\langle u_0(z) \mid 1\rangle t = \langle u_0(z) \mid 1\rangle\langle u_0(z) \mid 1\rangle t$ since $a_{0,(0,0)} = 1$. But also $\frac{1}{2}\frac{\mathrm{d}M_2}{\mathrm{d}t}$ has a linearly increasing terms with respect to time for $k = j = m = l = 0$, this is equal to $\langle u_k(z) \mid h_m(z)\rangle e^{-\mathrm{i}k\omega_0 t}e^{-(\lambda_{(0,0)})t}(a_{0,(0,0)}\gamma_{1,(0,0)}t$. $\frac{1}{2}\frac{\mathrm{d}M_2}{\mathrm{d}t}$ and $M_1\frac{\mathrm{d}M_1}{\mathrm{d}t}$ are removing each other with respect to the terms, which are increasing linearly with time, because of opposite signs this ensures convergence of $D_{\mathrm{eff}}(t)$.
The Peclet number Pé occurs here as square with respect to the effective diffusion $D_{\mathrm{eff}} \propto \mathrm{Pé}^2 \propto U_{\mathrm{o}}^2$ as expected. Since Pé appears as a square in both $\frac{1}{2}\frac{\mathrm{d}M_2}{\mathrm{d}t}$ and $M_1\frac{\mathrm{d}M_1}{\mathrm{d}t}$.

3.3.3 Analysis of Point concentration in the center

The initial point concentration is placed in the center in the transverse plane $(y, z) = (0, 0)$, this gives some reduction in the number of terms because of symmetry. The initial normalized concentration $\tilde{C} = 1$ is,

$$\tilde{C}(x, \mathbf{r}_\perp, 0) = \frac{N_0\delta(x)\delta(y)\delta(z)}{\frac{N_0}{\mathcal{V}}} = \mathcal{AL}\delta(x)\delta(y)\delta(z) \tag{3.36}$$

The initial condition for the zero axial moment,

$$\tilde{c}_0(\mathbf{r}_\perp, 0) = \frac{1}{\mathcal{L}} \int_{-\frac{1}{2}\mathcal{L}}^{\frac{1}{2}\mathcal{L}} \mathrm{d}x \mathcal{A}\mathcal{L}\delta(x)\delta(y)\delta(z) = \mathcal{A}\delta(y)\delta(z) \tag{3.37}$$

and the initial first axial moment is zero. then the different coefficients is needed to calculate the effective diffusion coefficient starting with $a_{0,(n,m)}$,

$$a_{0,(n,m)} = \langle g_n(y)h_m(z) \mid \mathcal{A}\delta(y)\delta(z) \rangle = g_n(0)h_m(0) \tag{3.38}$$

Since $a_{0,(n,m)}$ only takes values when n and m are even. Now if n, m are assumed even $a_{0,(n,m)}$ can be written,

$$a_{0,(m,n)} = \frac{2\cos(n\pi\frac{1}{2})\cos(m\pi\frac{1}{2})}{\sqrt{(1+\delta_{n,0})(1+\delta_{m,0})}} = \frac{2(-1)^{\frac{n+m}{2}}}{\sqrt{(1+\delta_{n,0})(1+\delta_{m,0})}},\ n, m \text{ even} \tag{3.39}$$

for the point concentration in the center, the calculations and results are nearly the same as in the random placement with the slight change that values only occurs for n and m even. Since $a_{0,(n,m)}$ is multiplied with all the terms, the following restriction in the formula $D_{\text{eff}}^{Point}(0,t)$ exists; n and m are even written as n, m even.

3.4 Simulations of effective diffusion $D_{\text{eff}}^{\text{Point}}(z_0, t)$ for the point concentration in the infinite parallel plate channel

Notice that from now on the effective diffusion $D_{\text{eff}}(t)$ for the point concentration will be denoted as $D_{\text{eff}}^{\text{Point}}(z_0, t)$, taking care of the spatial dependence of z and utilizing y-directional independence. In these simulations, the effective diffusivity denoted $D_{\text{eff}}^{\text{Point}}(z_0, t)$, is investigated with respect to especially the initial position of the point concentration denoted z_0. Because of symmetry, the interval $0 \leq z_0 \leq$ is only used for the initial positions of the point concentrations. For the steady flow $\epsilon_0 = 1$ the short time anomalous diffusive behaviour, also called transient phase, happens around the time $0 \leq t0.1$ and is different from uniform cross sectional distribution in the short time behaviour of the $D_{\text{eff}}(t)$.

Other parameters are also investigated, such as the frequency. A Steady flow $\epsilon_0 = 1$, a single frequency flow $\epsilon_1 = 1$ and a Steady plus oscillating flow is investigated ϵ_0, ϵ_1.

3.4.1 Applied point concentration in a steady flow $\epsilon_0 = 1$

A point concentration can be applied at different locations. In the analysis above the x, y location was discarded ending with the z as a parameter for investigation of $D_{\text{eff}}^{\text{Point}}(z_0, t)$. Four phases are discovered, a short time dynamic phase before $t < 0.04$(with intersections of the curves), a linear phase around $0.04 < t \lesssim 0.25$ and a phase of very small peak in $D_{\text{eff}}^{\text{Point}}(z_0, t)$ around $1.1 < t < 1.3$ and at last a convergence phase where the point concentration converges to the uniform cross sectional distribution at around $0.18 \lesssim t$.

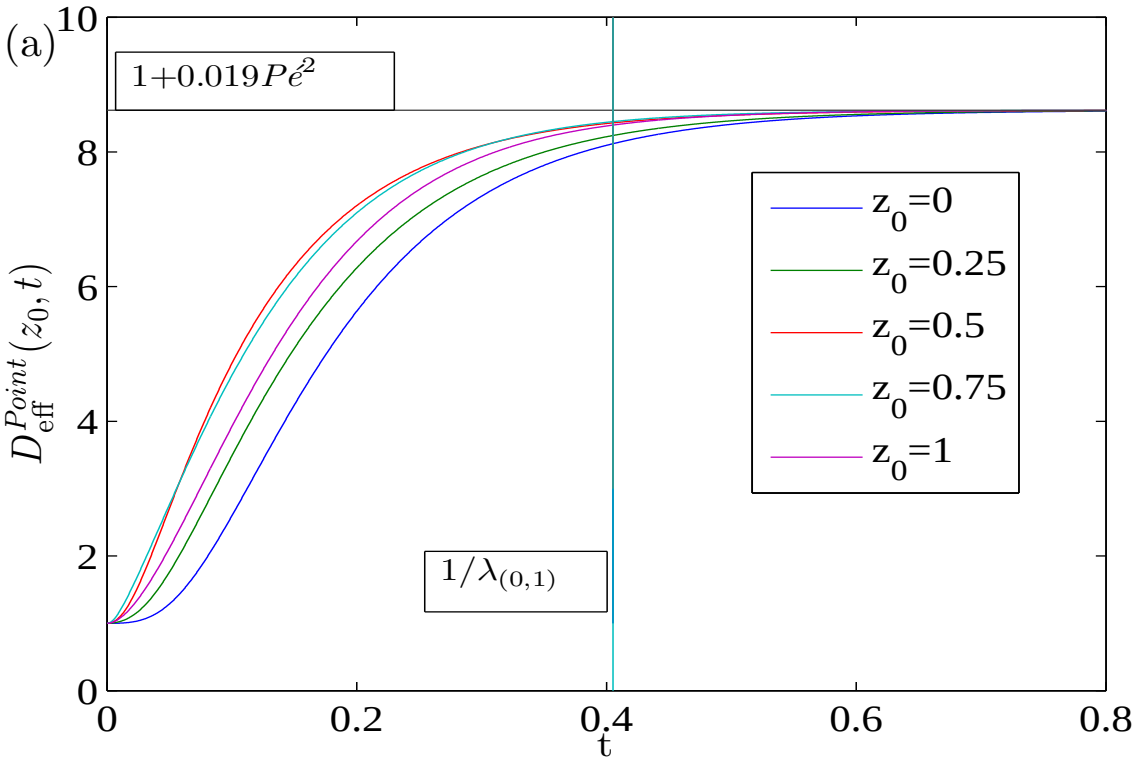

Figure 3.4: $D_{\text{eff}}^{\text{Point}}(z_0,t)$ in a infinite parallel plate channel with Pé = 20. Placing z_0 the initial point concentration at $r_0 = 0$(blue), $r_0 = 0.25$(green), $r_0 = 0.5$(red), $r_0 = 0.75$(turquoise) and $r_0 = 1$(violet). The vertical turquoise line shows the diffusion time $1/\lambda_1$ and the horizontal black line shows the steady value $D_{\text{eff}}^{\text{Point}}(z_0,t)$ that converges to the well known steady result $D_{\text{eff}}^{\text{Point}}(z_0,t) = 1 + 0.019\text{Pé}^2$ for the uniform distribution in the cross sectional plane for the infinite parallel plate[27]. The point concentrations has different transient or short time dynamic of $D_{\text{eff}}^{\text{Point}}(z_0,t)$ before the convergence depending on the placement z_0 of the point concentration. The point concentration $z_0 = 0$(blue) has a slower increase than $z_0 = 0.75$(turquoise) in the effective diffusion $D_{\text{eff}}^{\text{Point}}(z_0,t)$.

These phases can be observed in the Fig. 3.4 and will later be described.
First the short time anomalous dynamic is thoroughly analysed and afterwards the remaining phases will be described. The short time anomalous dynamic has intersections of the effective diffusion depending on the initial position of the point concentration.

3.4.1.1 Description and modelling of the short time anomalous Dynamic of the effective diffusivity $D_{\text{eff}}^{\text{Point}}(z_0,t)$

The behaviour of $D_{\text{eff}}^{\text{Point}}(z_0,t)$ depends strongly on the starting position of the point concentration. The gradient of the velocity field near the center $z \approx 0$ is very small for a parabolic velocity profile see Fig. 3.7(a). This creates small shear and thereby low effective diffusion $D_{\text{eff}}^{Point}(z \approx 0,t)$ for point concentrations in the center in the time pe-

riod $t < 0.1$. Initial position of the point farther from the center, where the gradients are larger Fig. 3.7(a)($r_0 > 0$) will lead to an earlier increase in the effective diffusivity $D_{\text{eff}}^{Point}(z_0 > 0, t)$. All this can be seen in the Fig. 3.4 where the point concentrations initially starting in the small gradients around $z_0 \approx 0$ as $z_0 = 0$(blue) and $z_0 = 0.25$(green), increases slowly in effective diffusion $D_{\text{eff}}^{Point}(z \approx 0, t)$. Whereas the point concentrations initially starting in the larger gradients around $z_0 > 0.4$ for $z_0 = 0.5$(red) and $z_0 = 0.75$(turquoise), increases faster in the effective diffusion $D_{\text{eff}}^{Point}(z > 0.4, t)$.
The short time anomalous dynamic of the initial placement of the point concentration will be modelled with different approximations of the starting concentrations. These models will be compared to the implemented framework of $D_{\text{eff}}^{\text{Point}}(z_0, t)$.

The nondimensionlized velocity is found in Eq. (2.14) to be Pé $u(z, t)$, where Pé $= 20$ was used for the simulations of $D_{\text{eff}}(t)$ like the Fig. 3.4(a). The models of $D_{\text{eff}}^{\text{Point}}(z_0, t)$ are based on the equation Eq. (2.21c) and approximations of the concentrations. Afterwards the Eq. (2.21c) is differentiated with respect to time yielding the expression for the effective diffusion $D_{\text{eff}} = \mathrm{d}\mu_2/\mathrm{d}t$. The four below mentioned different approximations of the concentration will be used.
1). A uniform normalized diffusing line in the z-direction.
2). A uniform normalized diffusing box in $3D$.
3). A Gauss distribution spreading in the z direction.
4). A Gauss distribution, spreading in the z-direction using method of images.
These models are investigating the short time anomalous dynamics $0 < t < 0.1$. and the initial placement of the point concentration. In these models the y-direction is normalized out for the uniform models and for the Gauss distributions the diffusion is ignored in this direction. The time-dependent axial center of mass $\bar{x} = u(z_0)t$, is set to move with the velocity of the fluid in the starting position of z_0.

3.4.1.2 A uniform normalized diffusing line in the z-direction

Here diffusion in the x-axes is ignored, but unity is added to the effective diffusion for molecular diffusion $D_{\text{eff}}(t) = \mathrm{d}\mu_2/\mathrm{d}t + 1$. Since no velocity gradients are in the y-direction, it is later divided out by a normalising factor for the concentration.
In order to define the approximation of the concentration, the Heaviside function S_z will be used to spread uniformly and normalised in the z-direction. The concentration will be moved with the speed $v_x(z)$ in the x-direction, at the position z. This will lead to a parabolic infinite thin uniform shaped concentration which is flowing with the speed of the velocity field. From the initial placement z_0 of the growing Heaviside function, the diffusion speed of the Heaviside function in the z direction is chosen to be $\sqrt{6t}$. Where $\sqrt{6t}$ is the speed for diffusion of a point concentration in 3D.

$$S_z(z, t) = s(z + \sqrt{6t} - z_0) - s(z - \sqrt{6t} - z_0) \tag{3.40}$$
$$c(x, y, z, t) = \mathcal{A}\delta(x - \text{Pé}\frac{3}{2}(1 - z^2)t)S_z(z, t)$$

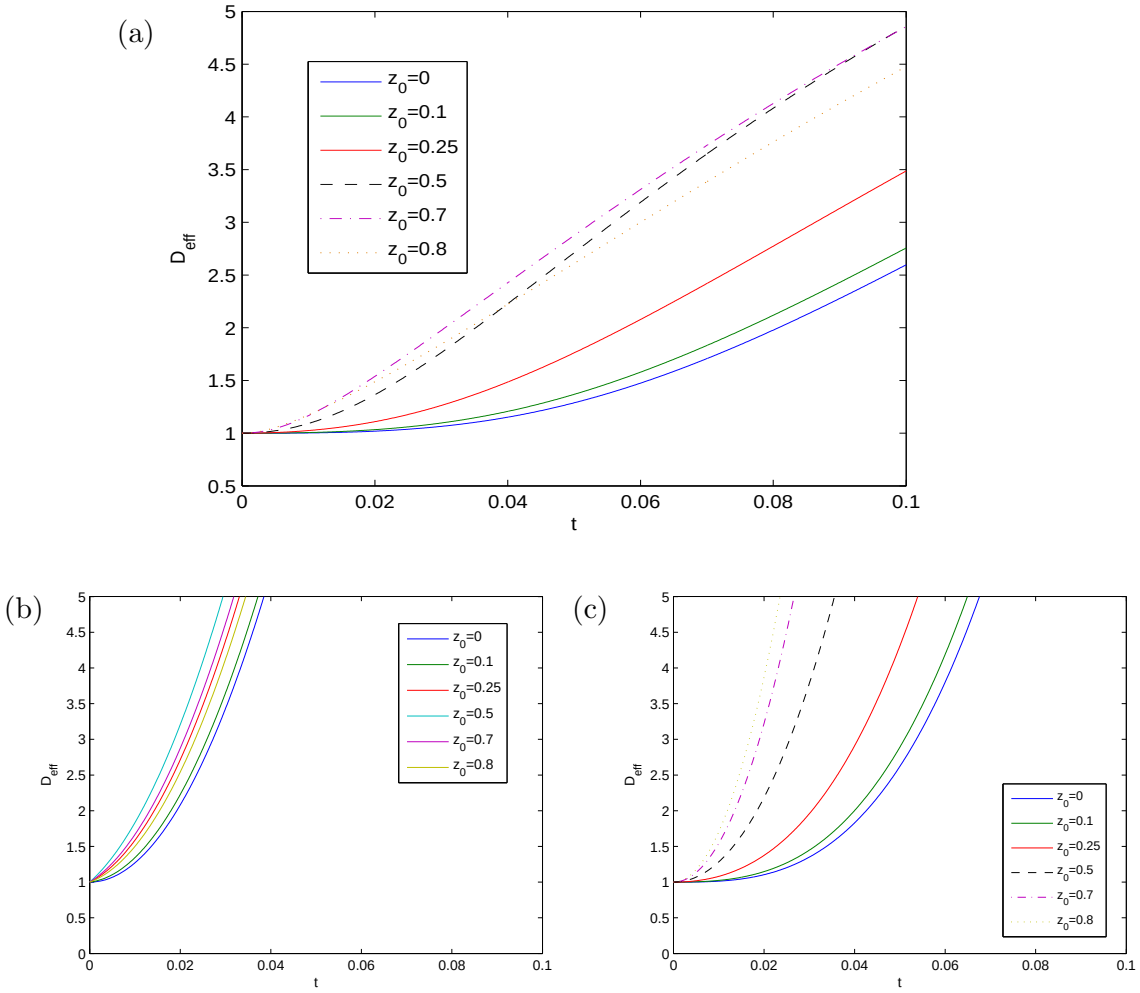

Figure 3.5: Simulation of the short time dynamics in the time period $0 \leq t \leq 1$, $\epsilon_0 = 1$ and Pé $= 20$, with the 6 different initial placed point concentrations $z_0 = 0$(blue), $z_0 = 0.1$(green), $z_0 = 0.25$(red), $z_0 = 0.5$(black), $z_0 = 0.7$(violet) and $z_0 = 0.8$(yellow). (a) The implemented framework for effective diffusivity in the time region $0 \ll t \ll 0.1$. (b) A uniform normalized diffusing line in the z direction, the $D_{\text{eff}}^{\text{Point}}(z_0, t)$ has increasing transients for increasing displacement in the center of z_0.(c)A uniform normalized diffusing box in $3D$. The effective diffusion $D_{\text{eff}}^{\text{Point}}(z_0, t)$ has increasing transients for increasing displacement in the center of z_0.

where the mass center is set to follow the starting position $\bar{x} = u(z_0)t$,

$$\mu_2(t) = \left\langle (x - u(z_0)t)^2 \middle| c \right\rangle = 2t + \frac{\int_{-\sqrt{6t}+z_0}^{\sqrt{6t}+z_0} \mathrm{d}z (\text{Pé}\frac{3}{2}(1-z^2)t - \text{Pé}\frac{3}{2}(1-z_0^2)t)^2}{\int_{-\sqrt{6t}+z_0}^{\sqrt{6t}+z_0} \mathrm{d}z 1} \tag{3.41}$$

$$\frac{1}{2}\frac{\mathrm{d}\mu_2}{\mathrm{d}t} = 1 + 900z_0^2 t - 1800z_0^3 t + 2700t^2 + 900z_0^4 t \tag{3.42}$$

Problem with the uniform normalized diffusing line in the z-direction. The concentration will be a uniform concentration profile, this is a very rough approximation compared to the Gaussian distribution. This model also has the problem since it divides with zero at the time $t = 0$, when normalizing the concentration. The model will be started in the time $t_0 = 10^{-6}$, to avoid singularity. Note that in medicine, the drug injection will happen at a finite volume, so it seems reasonable to start at for example $t_0 = 10^{-6}$ with a very small volume, this could be comparable to the injection of a needle. The model also has the problem that it neglects the spread in the x-direction, which has the effect that makes the concentration profile plug like. For big molecular diffusion coefficients, this model will have a problem as this model overestimates the effective diffusion. Also neglecting the molecular diffusion, this will be included in the next model.

3.4.1.3 A uniform normalized diffusing box in $3D$

Nearly the same model as the one presented previously, a concentration profile diffusing as a box in $3D$ but neglecting the y diffusion, because of independence of the velocity and thereby it is divided out by normalising factor. The box sides moving with the diffusion speed $\sqrt{6Dt}$ and a velocity which is depending on the z-placement. Here diffusion is included and unity molecular diffusion will not be added, calculating $\frac{1}{2}\frac{\mathrm{d}\mu_2}{\mathrm{d}t}$ the molecular diffusion apparently appears as unity.

$$\begin{aligned} S_x(x,z,t) &= s(x+\sqrt{6t}-\text{Pé}(1-z^2)t) - s(x-\sqrt{6t}-\text{Pé}(1-z^2)t) \\ S_z(z,t) &= s(z+\sqrt{6t}-z_0) - s(z-\sqrt{6t}-z_0) \\ c(x,y,z,t) &= \mathcal{A}Sx(x,z,t)Sz(z,t) \end{aligned} \tag{3.43}$$

So calculating the spread, since y is independent of the velocity and divide out by the normalising factor.

$$\begin{aligned} \mu_2(t) &= \left\langle (x-u(z_0)t)^2 \middle| c \right\rangle \\ &= \frac{\int_{-\sqrt{6t}+z_0}^{\sqrt{6t}+z_0} \mathrm{d}z \int_{-\sqrt{6t}+\text{Pé}\frac{2}{3}(1-z^2)t}^{\sqrt{6t}+\text{Pé}\frac{2}{3}(1-z^2)t} \mathrm{d}x (\text{Pé}\tfrac{2}{3}(1-z^2)t - \text{Pé}\tfrac{2}{3}(1-z_0^2)t)^2}{\int_{-\sqrt{6t}+z_0}^{\sqrt{6t}+z_0} \mathrm{d}z \int_{-\sqrt{6t}+\text{Pé}\frac{2}{3}(1-z^2)t}^{\sqrt{6t}+\text{Pé}\frac{2}{3}(1-z^2)t} \mathrm{d}x} \\ &= 2t + 7200t^3 z_0^2 + 6480t^4 \end{aligned} \tag{3.44}$$

$$\frac{1}{2}\frac{\mathrm{d}\mu_2}{\mathrm{d}t} = 1 + 10800t^2 z_0^2 + 12960t^3 \tag{3.45}$$

Problems with the uniform $3D$ box; Same problems are observed as for the uniform line, here the molecular diffusion is included in the model. This model also has the problem that it divides with zero at the starting time $t = 0$, to normalize the concentration. This model will also be started in the time $t_0 = 10^{-6}$, to avoid singularity.

3.4.1.4 Comparing the two uniform models to the implemented framework of $D_{\text{eff}}^{\text{Point}}(z_0,t)$

In the Fig. 3.5(a) the framework $D_{\text{eff}}^{\text{Point}}(z_0,t)$ is used to plot different located point concentrations. In the Fig. 3.5(b) the uniform line is increasing faster than the framework in effective diffusivity. The uniform line model achieves to represent the initial placement of z_0 versus the increase in effective diffusion $D_{\text{eff}}^{\text{Point}}(z_0,t)$ well compared the framework of $D_{\text{eff}}^{\text{Point}}(z_0,t)$. Getting the importance of the gradients versus the placement of the point z_0 right with respect to the the short time anomalous dynamic. The effect of the wall is neglected and more fine dynamics is not observed in the uniform model.
Fig. 3.5(c) The uniform $3D$ model is also increasing faster than the framework in effective diffusivity. The uniform $3D$ model also achieves to represent the initial placement of z_0 versus the increase of effective diffusion well compared the framework of $D_{\text{eff}}^{\text{Point}}(z_0,t)$. Actually this is done better by the uniform $3D$ model than the uniform line model since greater difference between the $D_{\text{eff}}^{\text{Point}}(z_0,t)$ and the placement is observed as in the framework (a). The effect of the wall is also neglected here and more fine dynamics is not observed in here either.
For a more precise description of the concentration profile in z-direction a Gauss distribution is now used.

3.4.1.5 A Gauss distribution spreading in the z-direction

The Gaussian distribution is used for a more precise description of the concentration profile in z-direction,

$$c(z,t) = (4\pi t)^{-\frac{1}{2}} e^{-\frac{(z-z_0)^2}{4t}} \delta(x - \frac{3}{2}(1-z^2)t) \tag{3.46}$$

where the mass center is set to follow the starting position $\bar{x} = u(z_0)t$,

$$\mu_2(t) = 2t + \left\langle (x - u(z_0)t)^2 \middle| c \right\rangle = \int_{-1}^{1} \mathrm{d}z (\text{Pé}\frac{3}{2}(1-z^2)t - \text{Pé}\frac{3}{2}(1-z_0^2)t)^2 c(z,t) \tag{3.47}$$

$\frac{\mathrm{d}\mu_2}{\mathrm{d}t}$ is calculated numerically in *matlab* and is shown in the Fig. 3.6(b).

Problems with the Gaussian distribution Here the concentration very fast starts diffusing out of the integral, underestimating the $D_{\text{eff}}^{\text{Point}}(z_0,t)$ of the initial point concentrations located around the wall. The next model takes care of the no flux boundary condition by using the method of mirrors.

3.4.1.6 A Gauss distribution, spreading in the z-direction using method of images.

The last and most complex model is using the method of images to simulate the concentration. A concentration, symmetrical placed around the wall, takes care of the lost concentration due to the no-flux boundary condition on the wall. This should give a more

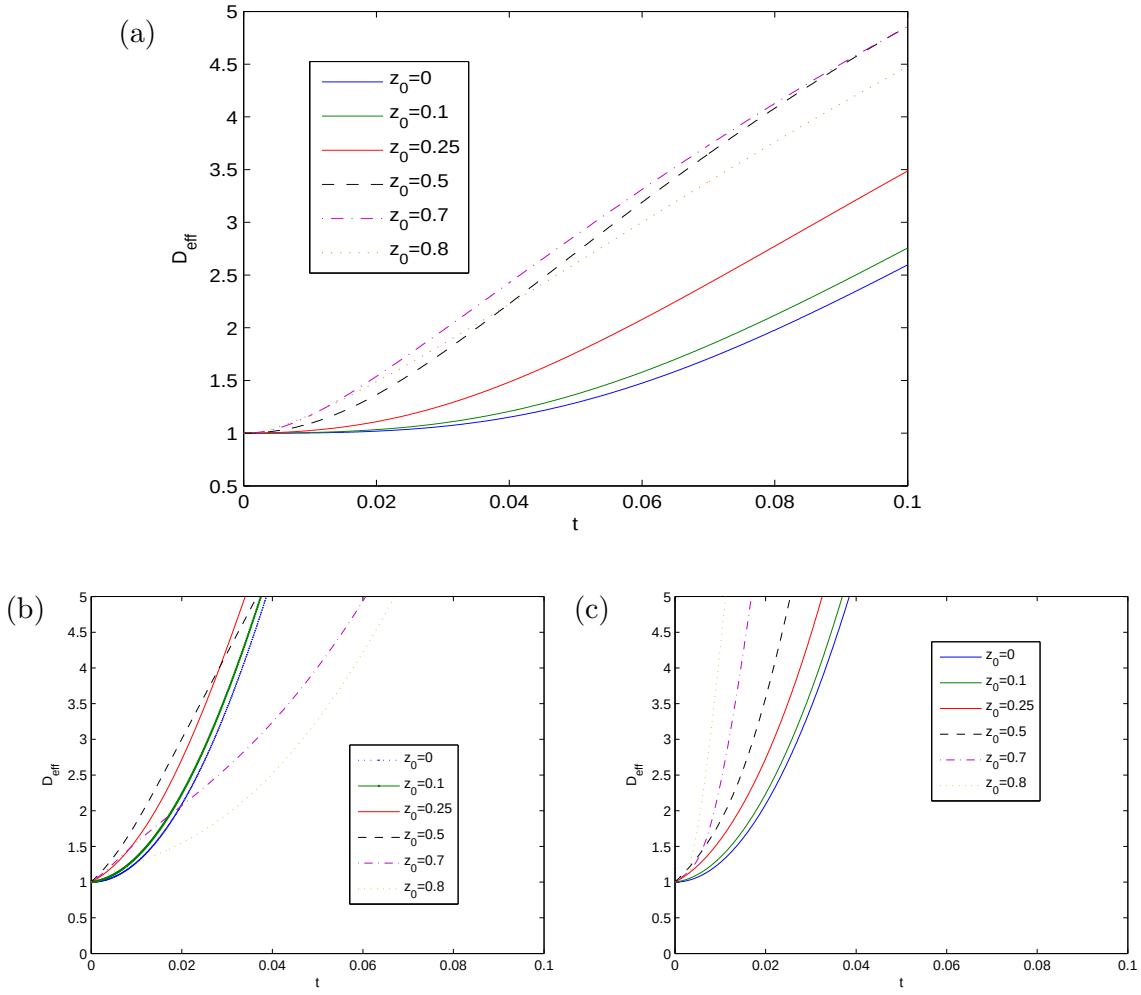

Figure 3.6: Simulation of the starting period of the steady flow in the time period $0 \leq t \leq 1$, $\epsilon_0 = 1$ and Pé $= 20$, with 6 different initial placed point concentrations $z_0 = 0$(blue), $z_0 = 0.1$(green), $z_0 = 0.25$(red), $z_0 = 0.5$(black), $z_0 = 0.7$(violet) and $z_0 = 0.8$(yellow). (a)The implemented framework for effective diffusivity in the time region $0 \ll t \ll 0.1$. (b) The Gauss model in the first time period $0 \leq t \leq 0.07$. c)The Gauss model with method of images in the time interval $0 \leq t \leq 0.1$

accurate description of the concentration profile, when the point concentration is located near the wall.

$$c(z,t) = (4\pi t)^{-1} e^{-\frac{(z-z_0)^2}{4t}} \delta(x - \text{Pé}\frac{3}{2}(1-z^2)t) + (4\pi t)^{-1} e^{-\frac{(z-(2-z_0))^2}{4t}} \delta(x - \text{Pé}\frac{3}{2}(1-z^2)t) \tag{3.48}$$

$$+ (4\pi t)^{-1} e^{-\frac{(z-(z_0-2))^2}{4t}} \delta(x - \text{Pé}\frac{3}{2}(1-z^2)t)$$

this is set into $\mu_2(t)$ and then $\mathrm{d}\mu_2/\mathrm{d}t$ is calculated numerically in Matlab. Furthermore unity is added for molecular diffusion.

3.4.1.7 Discussion of the models

Common features for the models see in Fig. 3.5(b), (c) and Fig. 3.6(b),(c) are noted, the initial placement of the point concentration gives similar dynamics with respect to the increase of $D_{\mathrm{eff}}(t)$ as the framework. The point concentrations placed in the middle is increasing slower in $D_{\mathrm{eff}}^{\mathrm{Point}}(z_0, t)$. But all the simulated curves increase faster than the formula for $D_{\mathrm{eff}}(t)$ and the intersection is not present in the models except in model 3, Fig. 3.6(b) but here the decrease of the curves yellow $z_0 = 0.8$ and violet $z_0 = 0.7$ is because the concentration flow trough the wall, or the integral only goes to the wall, losing some of $D_{\mathrm{eff}}(t)$.

A problem exists in all four models; after a short time the axial center of mass $\bar{x}$ is wrong because it changes with time. Especially the initial point concentrations located close to the wall will be estimated to have a low axial center of mass $\bar{x}$ for the models. This is the reason for the high estimated values of the effective diffusion $D_{\mathrm{eff}}^{\mathrm{Point}}(z_0, t)$ for the initial point concentrations located close to the wall. On the other hand, if the points concentrations are located around the middle, the speed of the axial center of mass $\bar{x}$ is too high also overestimating $D_{\mathrm{eff}}^{\mathrm{Point}}(z_0, t)$. Neglecting the diffusion or not handling it correctly in the x-direction and z-direction also give errors. The diffusion in the z direction due to the velocity profile is neglected and the plug like shaped of the concentration, normally known from Taylor dispersion [18], will be missing.

So all the models could show the slower short time anomalous dynamic of the diffusion for the point concentration placed in the middle, compared to the point concentrations placed in bigger gradients in the start. This is obvious since the concentration gets more stretched by the velocity gradients near the wall and the concentration gets pushed from each other by the varying velocity in the z direction.

This behaviour is caused by reflections of particles from the wall returning to the same low velocities, see in Fig. 3.8(right). This does not enhance the dispersion as much as meeting new gradients. So for $z_0 = 1$(violet) hitting the wall happens already in the start $t = 0$ for $z_0 = 0.75$(turquoise) at little later and for $z_0 = 0.5$(red) even later and this can been seen in Fig. 3.4a).

3.4.1.8 Intersections of $D_{\mathrm{eff}}^{\mathrm{Point}}(z_0, t)$ for point concentrations and the wall

For further investigation of the wall behaviour and a plot of $z_0 = 0.8$(turquoise) intersected by point concentrations located closer to the middle can be seen in the Fig. 3.7(c). In this figure the point located at $z_0 = 0.8$ has a slower anomalous diffusion $D_{\mathrm{eff}}^{Point}(z_0 < 0.8, t)$ than the points initially placed closer to the center at some time around $0.01 < t < 0.04$.

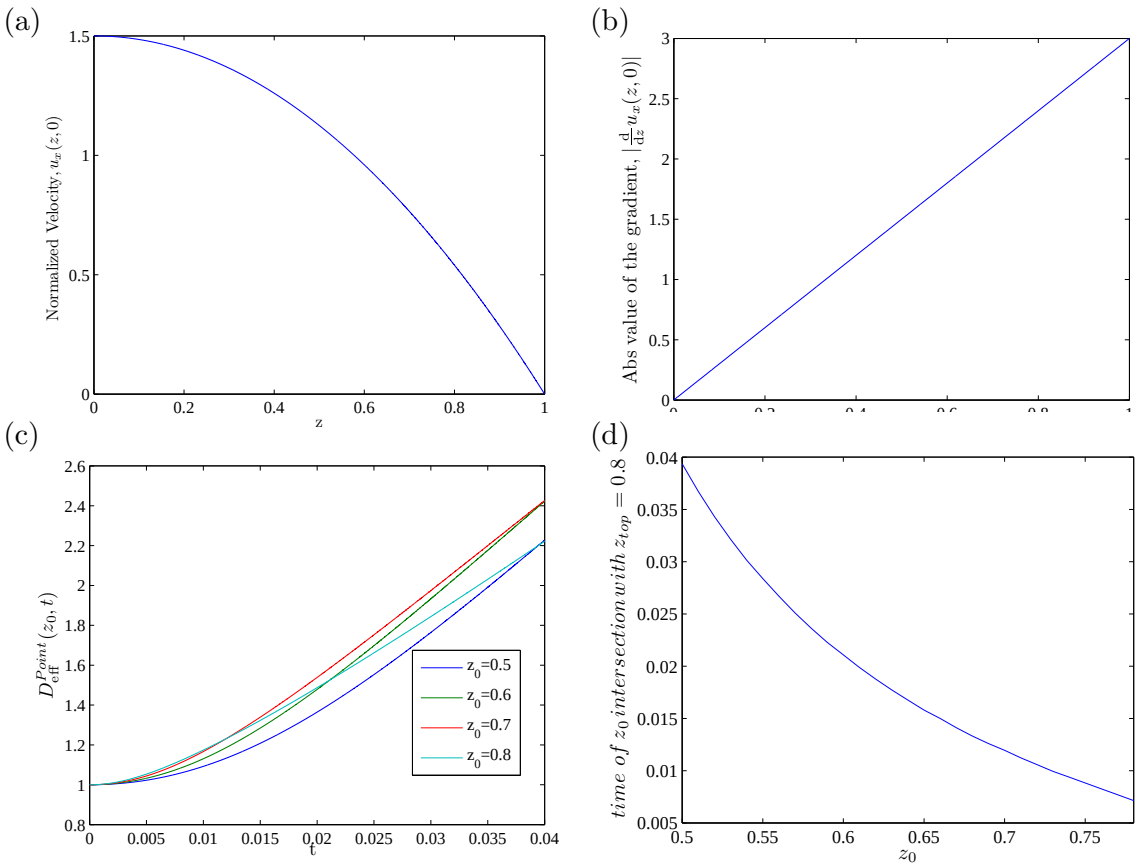

Figure 3.7: Investigating the intersections of $Deffpz$ compared to the initial placement of $z_0 = 0$ where Pé $= 20$ and Sc $= 10^3$. a)The velocity profile for the steady flow with $\epsilon_0 = 1$ (b)The absolute value of the velocity gradients $\frac{\mathrm{d}v_x(r)}{\mathrm{d}z}$. (c) the $D_{\text{eff}}(t)$ with varied starting position of the z_0 location from $0.5 \leq z \leq 0.8$ where $z_0 = 0.5$(blue), $z_0 = 0.6$(green), $z_0 = 0.7$(red) and $z_0 = 0.8$(turquoise). (d)Time $t_{intersect}$ for point concentrations located at $z_0 < 0.8$ to reach the value or intersect the value of $D_{\text{eff}}^{Point}(0.8, t_{intersect})$(turquoise). With respect to figure (c-d); the point concentration located at $z_0 = 0.8$(turquoise), the intersection of $z_0 = 0.8$(turquoise) and $z_0 = 0.7$(red) happen around $t_{intersect} \approx 0.011$. Another intersection of $z_0 = 0.8$(turquoise) and $z_0 = 0.6$(green) happen around $t_{intersect} \approx 0.02$. At last intersection of $z_0 = 0.8$(turquoise) and $z_0 = 0.5$(blue) happen around $t_{intersect} \approx 0.039$

In Fig. 3.7(b) the absolute value of the gradient is taken Eq. (3.2), $|u_0'(z)| = 3\epsilon_0 z$. In the Fig. 3.7(c) through the time $0.012 \leq t \leq 0.04$, $z_0 = 0.8$(turquoise) gets intersected in $D_{\text{eff}}^{\text{Point}}(z_0, t)$ by the point concentrations placed closer to the center $z_0 = 0.7$(red), $z_0 = 0.6$(green), $z_0 = 0.5$(blue). When a certain time has gone for the point concentration $z_0 = 0.8$, the concentration starts to reach the wall and the wall slows down the spreading of the particles. This effect is sketched in Fig. 3.8(right), when the concentration(black) starts to diffuse into the(lightblue) into the no flux wall(darkblue arrow), it is reflected

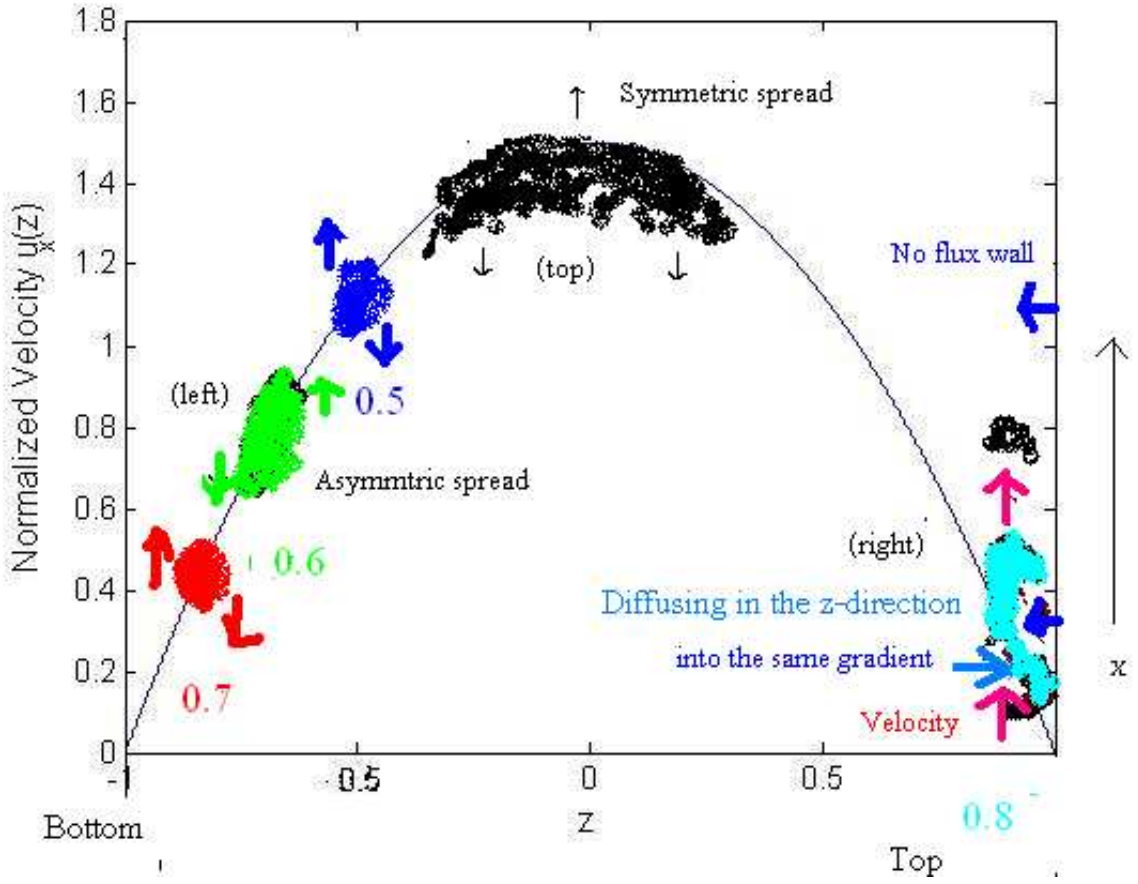

Figure 3.8: Sketch of three proposed effects for the concentration in the Steady flow. The asymmetric spread of the concentration when the point concentration is applied in the bottom to (left). The point concentration is spread symmetrical when it is applied in the middle (top). Wall effect, the concentration is reflected back by the no flux boundary to the same small velocity (right).

back into the same velocities(red arrow), thereby not enhancing the spreading much. Whereas for the point concentration farther away from the wall $z_0 = 0.7$(red), $z_0 = 0.6$(green) and $z_0 = 0.5$(blue) will continue to hit new gradient where just a very little part of the concentration has reached the wall when $t < 0.04$. In Fig. 3.8(left)the concentration will be pulled by the gradient in the x-direction creating a large $D_{\text{eff}}^{\text{Point}}(z_0, t)$ which is denoted asymmetric spread. This must be the reason for the intersection of the initial point $z_0 = 0.8$ and the initial point concentration $0.5 \leq z_0 < 0.8$. The walls slow the spread of $z_0 = 0.8$ and the asymmetric spread increases the $D_{\text{eff}}^{\text{Point}}(z_0, t)$. The Fig. 3.7(d) shows the time it takes for point concentrations placed closer to the center than $z_0 < 0.8$, to overtake or intersect $z_0 = 0.8$ the value of $D_{\text{eff}}^{\text{Point}}(z_0, t)$. It takes more time for 0.5 to intersect $z_0 = 0.8$, since it is placed in the middle and needs to reach the bigger gradients.

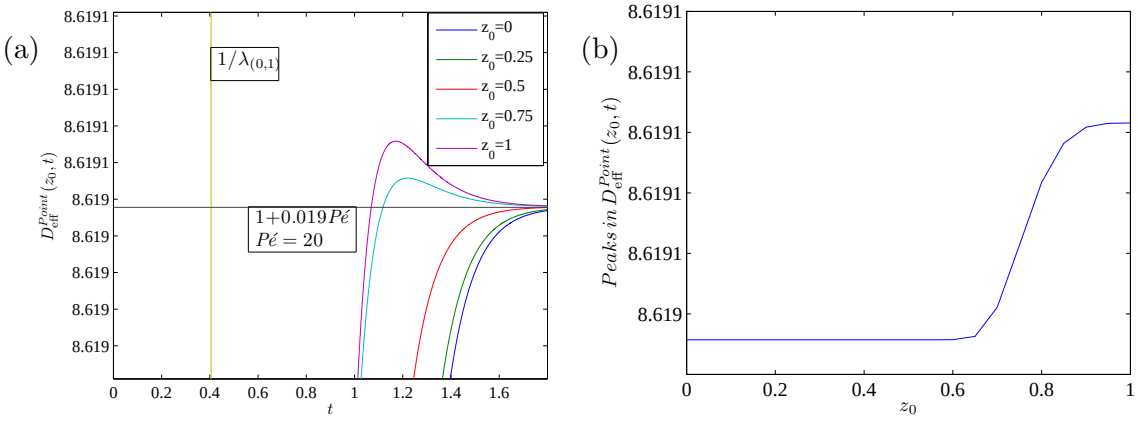

Figure 3.9: Steady flow and Pé = 20(a)$D_{\text{eff}}^{\text{Point}}(z_0, t)$ for the initial point concentration placed at $r_0 = 0$(blue), $r_0 = 0.25$(green), $r_0 = 0.5$(red), $r_0 = 0.75$(turquoise) and $r_0 = 1$(violet) $z_0 = 0$. (b) Peaks of $D_{\text{eff}}^{\text{Point}}(z_0, t)$ versus the placement z_0 of the point concentration, the largest peak occur for the initial placement of the point concentration at $z_0 = 1$.

3.4.1.9 Linear phase

Fig. 3.4(a) a linear phase for the point concentrations effective diffusion $D_{\text{eff}}^{\text{Point}}(z_0, t)$ occurs at around the time $0.03 \leq t \leq 0.3$ could be seen in Fig. 3.4, similar to the uniform concentration in the cross-sectional plane case. The linear phase for the uniform cross sectional concentration distribution can be seen in Fig. 3.2(the linear phase occurs directly$t = 0$). Because the concentration is already smeared out and utilizing the gradients. Where the point concentration needs to be diffused out in the transverse direction, before the linear phase occurs. The reason that the linear phase does not occur around $1/\lambda_1 = 0.4$ is not discovered yet, altough in the circular channel the linear phase start around $1/\lambda_1 = 0.068$. Maybe it is due to diffusion in the y-direction or the infinite parallel plates inducing less shear.

3.4.1.10 Peaks in the $D_{\text{eff}}^{\text{Point}}(z_0, t)$

Peaks in the $D_{\text{eff}}(t)$ does not happen for the steady flow of a uniform distribution in the cross-sectional plane, this can be seen in Fig. 3.2. Peaks in the $D_{\text{eff}}^{\text{Point}}(z_0, t)$ were found and from now on the peaks are defined as the maximum before an asymptotic decrease towards the steady state value of $D_{\text{eff}}(\infty)$, or just the largest value of $D_{\text{effPeak}}^{\text{Point}}(z_0, t_{peak})$. These peaks may have been found solving $\frac{1}{2}\frac{\mathrm{d}(\frac{\mathrm{d}\mu_2}{\mathrm{d}t})}{\mathrm{d}t} = 0$, but this is a very complicated expression and it may not give a lot of physical insight. These peaks are also dependent on the position z_0 of the point concentration as seen in Fig. 3.9(a). The max peak is small in relative size compared to the steady D_{eff} value $100\% \times \frac{8.6191-8.619}{8.619} = 6 \times 10^{-4}\%$ and occurs later compared to the diffusion time $1/\lambda_{(0,1)} = 0.4$ around $1.1 < t < 1.3$. The peak $D_{\text{effPeak}}^{\text{Point}}(z_0, t_{peak})$ are largest around the initial points placed towards the wall $z_0 \approx 0$.

Larger peaks will later be observed for the steady flows in the circular channel with the Newtonian fluid and the non-Newtonian Power law fluid.

Reason for the peak must be the spatial relation between concentration and the gradients in the transient period, before convergence. The wall could play an effect and how the wall is placed, since the largest peak for the circular channel is when the initial point is placed at $z_0 = 0$.

3.4.1.11 $D_{\text{eff}}^{\text{Point}}(z_0, t)$ convergence

After the time period $1.6 < t$, when the concentration has diffused to a approximately uniform concentration in the transverse direction, removing the spatial dependence of the point concentration. The same steady flow results as in the uniform distribution in the cross-sectional plane, is obtained $D_{\text{effSteady}}^{\text{Point}}(z_0, \infty) = D_{\text{eff}}^{uniform}(\infty) = 8.6191 = 1{+}20^2 0.019$ as Chatwin and Sullivan [27]. This can also be seen in Fig. 3.4(a) where all the points converges to the same value as the uniform concentration, seen in Fig. 3.2.

3.4.2 Applied point concentration with only a pulsating flow $\epsilon_0 = 0, \epsilon_1 = 1$

If only a single frequency flow is applied many effects can be studied with respect to the effective diffusivity $D_{\text{eff}}^{\text{Point}}(z_0, t)$. When making this analysis, there are overall three numbers in the equations you can change to check the different dynamics; the Schmidt number Sc, the Womersley number Wo and the Peclet number Pé. With fixed amplitude $\epsilon_0 = 0, \epsilon_1 = 1$ and Pé $= 20$ and a Schmidt NaCl $D = 10^{-9} \frac{\text{m}^2}{\text{s}}$ as the solute and water as the solution $\nu = 10^{-6} \frac{m^2}{s}$ we obtain Sc $= \frac{\nu}{D} = 10^3$. This leaves us with the Womersley number as the only variable, since the nondimensionlized frequency is determined by the Womersley number.

First changing the initial placement z_0 of the point concentration is examined with respect to the effective diffusion $D_{\text{eff}}^{\text{Point}}(z_0, t)$.
Compared to the uniform concentration [1], the point concentration will have different short time dynamics and slightly different behaviour is expected for different placement in the z-direction, especially for higher frequencies and larger Womersley number due to the spatial change of the velocity profile see Fig. 4.4(a). Changing the Womersley number gives rise to different phenomena; a change in the spatial form of the velocity profile and a decrease in momentum diffusion. This gives a decrease in $D_{\text{eff}}(t)$ and the characteristic of the $D_{\text{eff}}(t)$ curve changes due to the slightly different gradient.

3.4.2.1 Reversal of flow, oscillating value of $D_{\text{eff}}(t)$ and frequency of the flow ω_{o}

Now the parameters are fixed and only the Peclet number or the frequency ω_{o} can be changed. The frequency of the flow compared to the solute equilibration rate determines if the $D_{\text{eff}}^{\text{Point}}(z_0, t)$ experiences negative effective diffusion $D_{\text{eff}}^{\text{Point}}(z_0, t)$. Negative $D_{\text{eff}}^{\text{Point}}(z_0, t)$

is experienced when diffusion relaxing is not possible at around $\omega_o > \lambda_{0,2} = \pi^2$ This means that the larger the frequency the smaller value $D_{\mathrm{eff}}(t)$ and vice versa, this effect can be seen in the later appearing Fig. 3.15(a) where $\omega_o = 0.1$ the blue has higher value of $D_{\mathrm{eff}}(t)$ than $\omega_o = 2.5$ red.

When the flow is reversing, and if there is time for the diffusion in the transverse direction

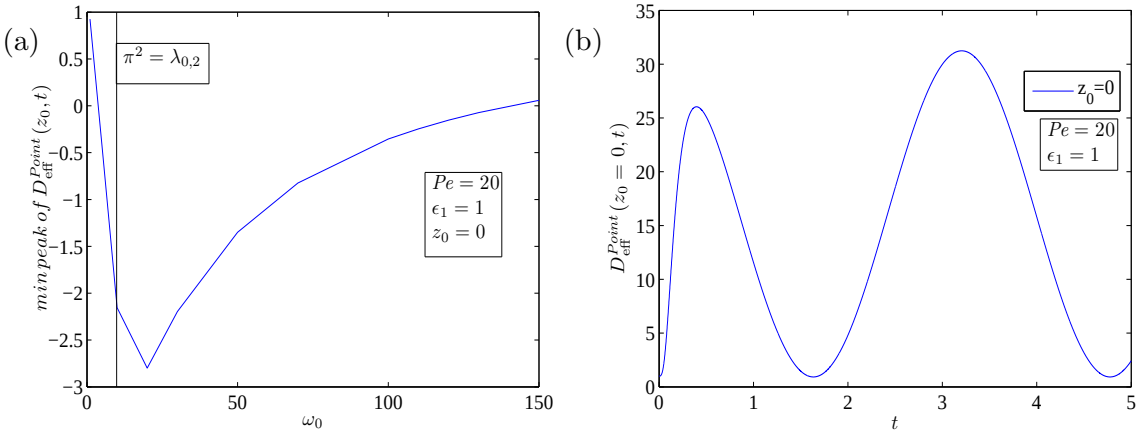

Figure 3.10: The Schmidt number Sc = 1000 and the Peclet number Pé = 20, with an amplitude $\epsilon_1 = 1$ for the single frequency flow. The point concentration was placed in the center $z_0 = 0$. (a) The minimum peak of $D_{\mathrm{eff}}^{\mathrm{Point}}(z_0, t)$ versus the frequency ω_o. (b) Example of a low frequency flow $\omega_o = 1$ where $1 \leq D_{\mathrm{eff}}(t)$ oscillates above the molecular diffusion.

to relax before the reversal of the flow begins, then $\frac{1}{2}\frac{\mathrm{d}\mu_2}{\mathrm{d}t}$ minimum is around the molecular diffusion, when the $\omega_0 > 1$ the reversal of the flow begins to be faster than the diffusion can relax and the concentration in the middle starts to get thrown forth and back with the flow before it can diffuse in transverse direction. Because the concentration of the solute around the wall moves slower relative to the solute in middle, this creates a bigger spread $\mu_2(t)$ in the time period of where the flow has peak velocity. When the flow reverses, the solute molecules in the middle travel back and get closer to the solute molecules at the wall decreasing the spread $\mu_2(t)$ and making $\frac{1}{2}\frac{\mathrm{d}\mu_2}{\mathrm{d}t}$ negative. In the Fig. 3.10(b) the frequency $\omega_o = 1$, here the diffusion has time to relax and effective diffusion is only increased by the oscillating flow. In Fig. 3.10(a) the negative values of the effective diffusion is investigated with respect to the frequency omega ω_o. In the Fig. 3.10a) The negative effective diffusion starts appearing around $\omega_0 = 1$, this is due to the relaxation time of diffusion is exceeded. The minimum $D_{\mathrm{eff}}(t)$ is reached around $\omega_o \approx 22$, later the curves start getting more positive, this is due to limited momentum diffusion. Altough the momentum diffusion time $1/\alpha fl$ is larger, still a decrease will occur. In Fig. 3.10a) the effective diffusion oscillates above the molecular diffusion, meaning that at each half period diffusion has time to diffuse out before the flow reverses. Later the flow will reverse to a settled uniform concentration profile. So if a good mixing of the solute is wanted with a single frequency

flow, then a smaller frequency will give better mixing. Also because ω_0 is a damping factor in $D_{\text{eff}}^{\text{Point}}(z_0, t)$, this can be seen the equation for Eq. (2.22).

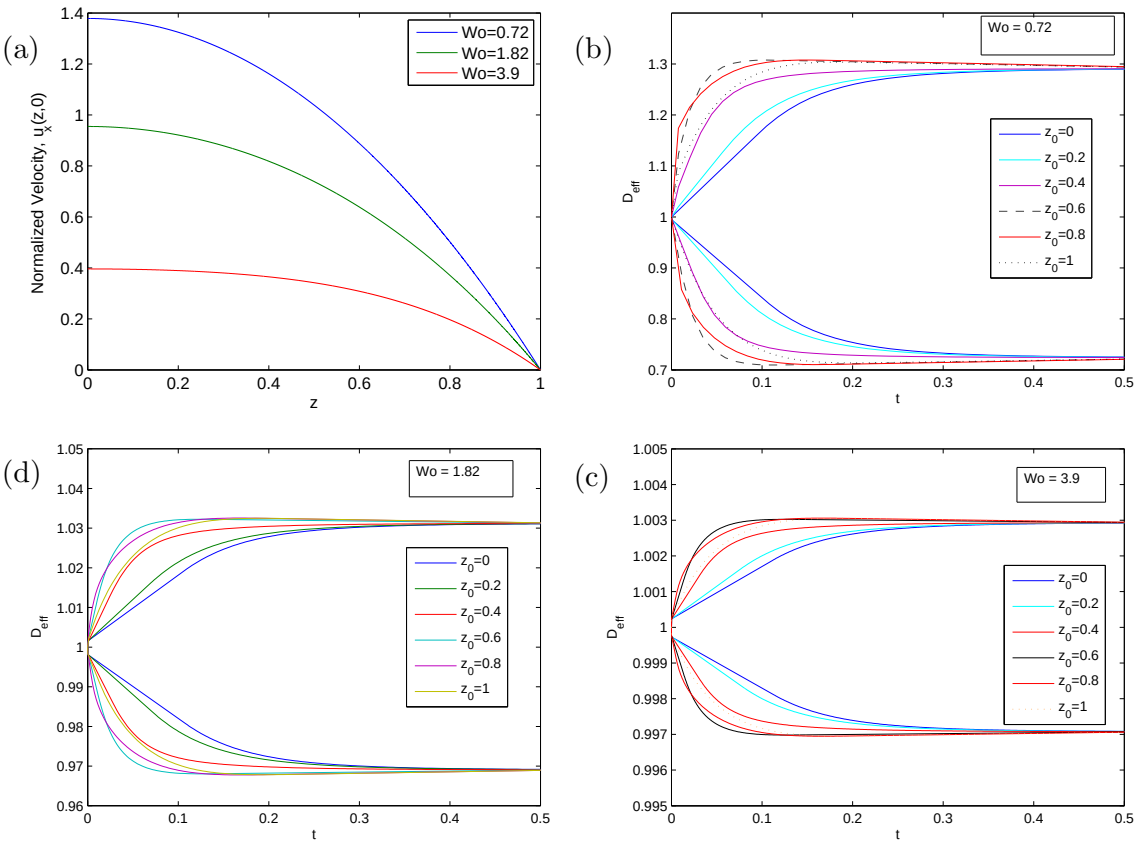

Figure 3.11: A harmonically oscillating flow, Sc = 1000, with amplitude $\epsilon_1 = 1, \epsilon_0 = 0$, Pé = 20 and varied Wo $= 0.72, \text{Wo} = 1.82, \text{Wo} = 3.9$. (a-c) Normalized velocity profiles at time $t = 0$ for Wo $= 0.72, \text{Wo} = 1.82, \text{Wo} = 3.9$. (d-f) different starting position for the point concentration $z_{\text{loc}} = 0, 0.2, 0.4, 0.6, 0.8, 1$, also with the respecting $Wo = 0.72, \text{Wo} = 1.82\text{Wo} = 3.9$. $D_{\text{eff}}(t)$ amplitudes decrease significantly with each of the new increased Womersley numbers by a factor of around 10.

3.4.2.2 The velocity profile versus Wo and the $D_{\text{eff}}^{\text{Point}}(z_0, t)$

In Fig. 4.4from a) to c) the amplitude of the velocity field gets weaker and thereby the velocity gradients too, which induces less shear and thereby the gradient decreases, see d) to f)Fig. 4.4. A slight difference in the shape of the velocity profile can be seen in Fig. 4.4from a) to c). Since it is an infinite parallel plate channel, less shear is induced because no side walls with no-slip conditions are present in the y-directions compared to a cylinder. The amplitude of the velocity profile gets smaller since momentum diffusion cannot follow the oscillation of the pressure, this also makes the $D_{\text{eff}}(t)$ smaller Fig. 4.4(d) to (f).

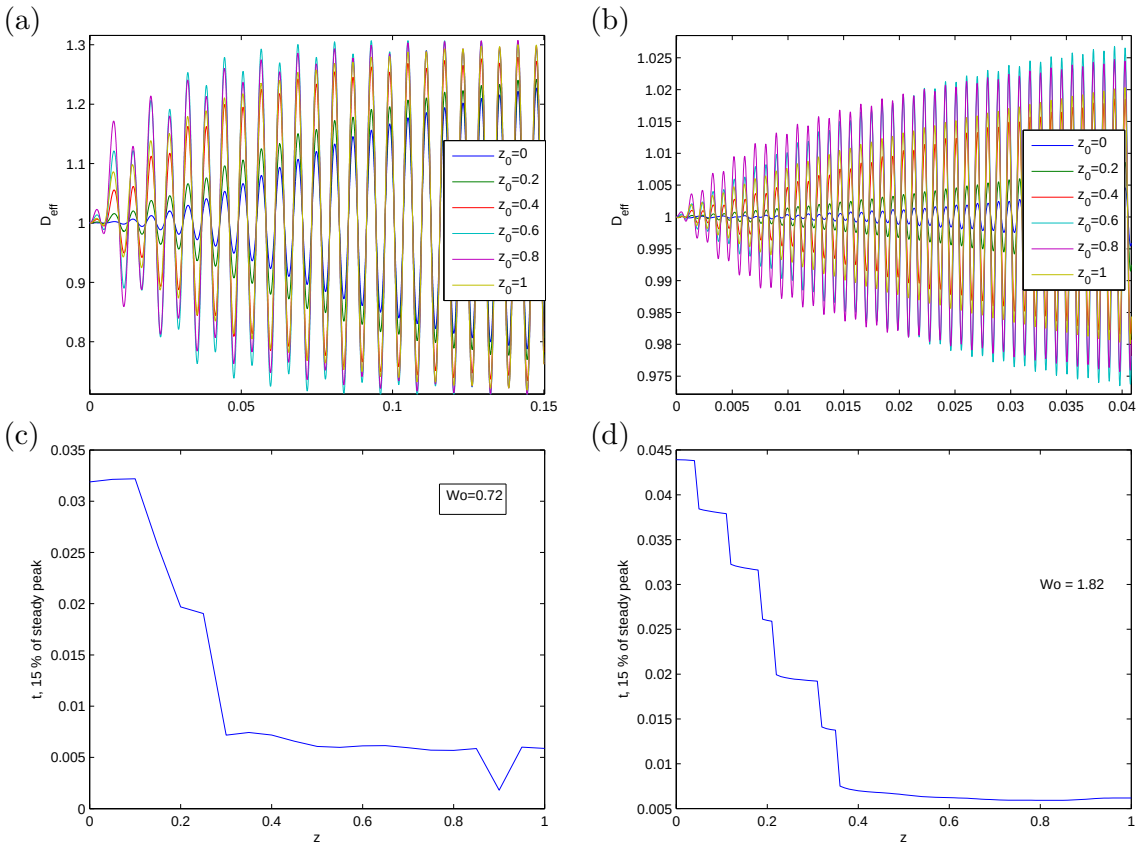

Figure 3.12: Transient behaviour, of a harmonically oscillating flow, $\epsilon_1 = 1$ and Sc $= 1000$, point concentration located at $z_0 = 0$, 0.2, 0.4, 0.6, 0.8, 1 and Pé $= 20$. (a-b) Varied point concentrations locations with Wo $= 0.72$ and Wo $= 1.82$. (c-d)Time for the transient to develop 15% of the steady peak for $0 \leq z_0 \leq 1$ for the Womersley numbers Wo $= 0.72$ and Wo $= 1.82$.

3.4.2.3 Transient of $D_{\text{eff}}(t)$ versus placement of point concentration

The transient behaviour is also investigated in the single frequency flow. The placement of the point concentration has similar behaviour as in the steady flow case. The transient behaviour depends on the placement of point concentration compared to the gradients. If the point concentration is placed around the middle, a slower transient increase of $D_{\text{eff}}(t)$ will happen this can be seen in the Fig. 4.5(a)$z_0 = 0$(blue).

Increasing the Womersley number will change the velocity profile shape and thereby also the transient behaviour for the D_{eff}. For very large Womersley number Wo > 10, the region in the middle will be larger since the momentum diffusion cannot reach the middle from the plates.
the Fig. 4.5c) and d) the transient build up to 15% of the steady max peak of $D_{\text{eff}}^{\text{Point}}(z_0, \infty)$, which is investigated with different placement z_0 of the point concentration. It is seen that the point concentrations which start in the high velocity gradient $0.4 \leq z_0 \leq 1$ are faster in reaching the 15% of the positive steady peak of effective diffusion for Wo $= 0.72$ and Wo $= 1.82$. In the Fig. 4.5(c) and (d), the locations of the point concentrations z_0 had a big significance for the transient build up.

3.4.2.4 Peaks in the effective diffusion $\epsilon_0 = 0\,\epsilon_1 = 1$, where the Schimdt number is $\text{Sc} = 10^3$

So earlier the minimum was found for $D_{\text{eff}}^{\text{Point}}(z_0, t)$, now the peak are investigated, that also occur in the single frequency flow $\epsilon_0 = 0\,\epsilon_1 = 1$ as it did in the steady case $\epsilon_0 = 1$. First looking at $D_{\text{eff}}^{\text{Point}}(z_0, t)$ for different initial placed point concentrations and varying the Womersley numbers Wo $= 0.72$ and Wo $= 3.9$.
For the Fig. 3.13(a) and (b) a plot of the effective diffusion $D_{\text{eff}}^{\text{Point}}(z_0, t)$ where peaks in $D_{\text{eff}}^{\text{Point}}(z_0, t)$ are present for placements around $z_0 \approx 0.75$ for the point concentration when Wo $= 0.72$. For Wo $= 3.9$ the peak are nearly neglectable in size, but a shift happens of the peaks $D_{\text{eff}}^{\text{Point}}(z_0, t)$ in the initial placement $z_0 \approx 1$. Probably due to the change of the velocity profile when the Womersley number is changed to Wo $= 3.9$ and the momentum diffusion from the wall will not reaching the middle. For the Fig. 3.13(c) and (d) the maximum peak of $D_{\text{eff}}^{\text{Point}}(z_0, t)$ versus the initial placements z_0 of the point concentrations. In Fig. 3.13(c)Wo $= 0.72$ the peak occur for the point concentrations with initial placements around $z_0 \approx 0.75$ where the gradients are presented, probably because of the parabolic velocity profile. In Fig. 3.13(d)Wo $= 3.9$ the peaks are shifted towards the wall due to the change of gradient of the velocity.

Concluding why the peak occur, the peaks occur due to the gradients and is expected to move towards the wall for higher Womerley numbers Wo. Since the momentum diffusion can reach the middle, giving a flat velocity profile in the middle. Probably also because the larger concentration can be used in the high gradients around the wall(high Wo), before the solute diffusion time $t_{peak} < 0.4 = 1/\lambda_1$. Since it diffuses to lower gradients with a low concentration.

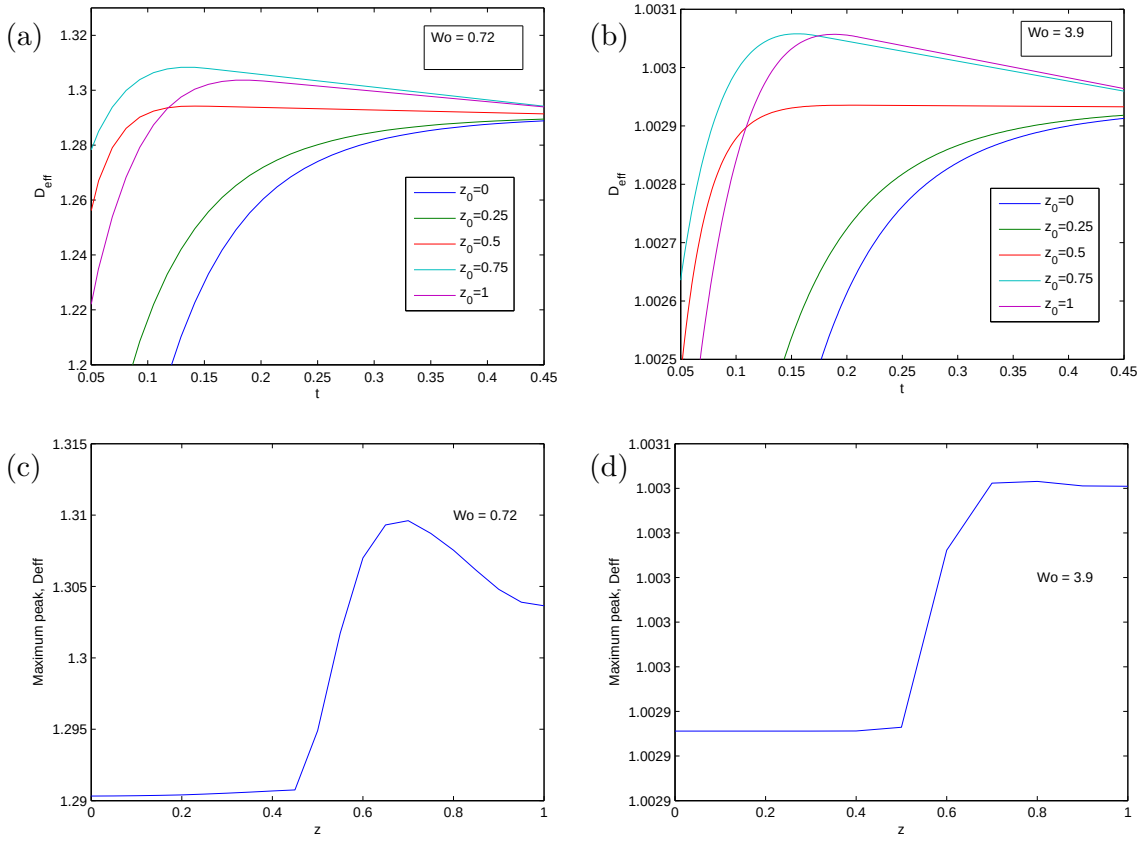

Figure 3.13: A harmonically oscillating flow, Sc = 1000, with amplitude $\epsilon_1 = 1$, Pé = 20 and varied Wo = 0.72 and Wo = 3.9. (a-b) investigated peaks for the initial placement $z_0 = 0$(blue), $z_0 = 0.25$(turquoise), $z_0 = 0.5$(black), $z_0 = 0.75$(red) and $z_0 = 1$(yellow) for Wo = 0.72 and Wo = 3.9. (c-d)Maximum peak of $D_{\mathrm{eff}}^{\mathrm{Point}}(z_0, t)$ for the z interval with the respecting Wo = 0.72 and Wo = 3.9. (c-d)time before maximum peak versus the initial placement z_0, with the respecting Wo = 0.72 and Wo = 3.9.

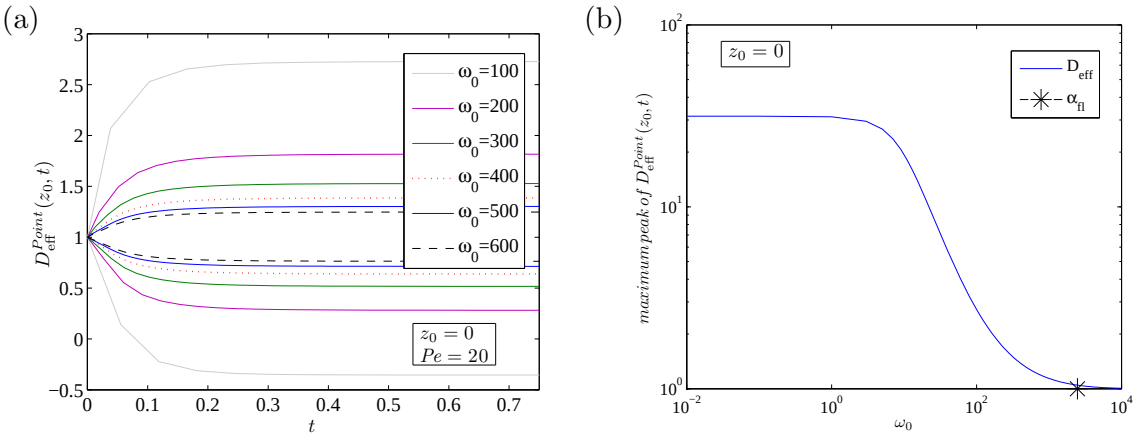

Figure 3.14: A harmonically oscillating flow, $\epsilon_1 = 0, \epsilon_0 = 1$, $z_{\text{loc}} = 0$ and Pé $= 20$. (a)Varying the frequencies $\omega_0 = 100, 200, 300, 400, 500, 600$ in the time interval $0 \ll t \ll 0.8$(b)A plot of the peak steady effective diffusivity $D_{\text{eff}}^{\text{Point}}(z_0, t)$ versus the frequency ω_{o}.

3.4.2.5 Frequency ω_{o} versus the size of $D_{\text{eff}}(t)$

I have chosen the steady state peak, to measure the size of the effective diffusivity $D_{\text{eff}}(t)$ for the different frequencies ω_{o}. For high frequencies the pressure oscillation is so fast that solvent-momentum diffusion is limited and the momentum diffusion does not have time to react to the fast changing frequency of the pressure. This will happen when the frequency of the flow exceeds the fluid momentum diffusion rate $\omega_{\text{o}} > \alpha_{fl} = \left(\frac{\pi^2}{4}\right)$ Sc. This can be seen in Fig. 3.14(b).

3.5 Decreasing the Schmidt number to Sc $= 10^{-1}$, for larger effect of the number Womersley Wo

Due to the earlier small values of the $D_{\text{eff}}^{\text{Point}}(z_0, t)$ and large frequencies ω_{o}, for moderate Womersley numbers, the Schmidt is decreased. This will give a more clear idea of the effect of the momentum diffusion from the no slip wall.
The relationship between the Womersley number and the Schmidt number is given by $\omega_0 = \text{Wo}^2\text{Sc}$, for a fixed ω_0 and varying Wo and Sc will give rise to different effects. Because of the small momentum diffusion when Sc $= 10^3$ gives high frequencies $\omega_{\text{o}} > 25000$ for the moderate Womersley numbers Wo > 5. To get the Womersley number to affect the velocity profile more for smaller frequencies ω_{o}. The Schmidt number is now decreased to the value of gas Sc $= 0.1$ and the incompressibility assumption is still used. Then the velocity profiles where the momentum diffusion from the wall is smaller λ_d, is found by using the dimensionless numbers Wo, ω_0 and Sc. Where the momentum diffusion length $\tilde{\lambda_d} = \sqrt{\frac{\nu}{\tilde{\omega}_{\text{o}}}}$ from [30], then the dimensionless momentum diffusion length is found by using

the dimensionless numbers Wo, ω_0 and Sc.

$$\lambda_d = \sqrt{\frac{\mathrm{Sc}}{\omega_0}} = \frac{1}{\mathrm{Wo}} \tag{3.49}$$

3.5.1 Womersley numbers and phase shift in $D_{\mathrm{eff}}^{\mathrm{Point}}(z_0, t)$, for $\mathrm{Sc} = 10^{-1}$

Phase shift in $D_{\mathrm{eff}}^{\mathrm{Point}}(z_0, t)$ is discovered between initial point concentrations located at large gradient compared to the region with small gradients. When the diffusion time to reach the large gradient was longer than the frequency of the flow, then phase shift will be discovered between the point concentrations.
In the Fig. 3.15(a) to (c) the point concentrations in the center z_0 hit the gradients later, but still nearly in phase with the other point concentration, in Fig. 3.15(c) a slight phase shift can be seen. First in Fig. 3.15(d) a phase shift occurs for the initial point concentration in the center $z_0 = 0$(blue) versus the point concentrations located at $z_0 > 0.5$. This is because the diffusion in the transverse direction first hits the velocity gradients when the flow reverses. in Fig. 3.15(d) the point concentration placed in the middle $z_0 = 0$(blue) and another point concentration placed a bit from the center $z_0 > 0.5$($z_0 = 0.5$green, $z_0 = 0.7$red and $z_0 = 0.9$violet). These two point concentrations will meet the velocity gradient at different times due to the diffusion time to the gradients. If the frequency is fast enough then the two points can be out of phase, because the concentration in the middle first has reached the gradient at the reversal of the flow. This can been seen in Fig. 3.15 for the point $z_0 = 0$(blue) compared to the other points($r_0 > 0.5$).

In order of magnitude, phase shift will happen between the two point concentrations $z_0 = 0$ and $z_{0+\lambda_d} = 1-\lambda_d$, when the diffusion cannot reach the momentum region $1-\lambda_d > \sqrt{6t_{D_{\mathrm{eff}}}}$, before the reversal of the flow $\frac{\pi}{\omega_0} \ll t_{D_{\mathrm{eff}}}$. This order of magnitude, has the problem that $\sqrt{6t_{D_{\mathrm{eff}}}}$ is too large a part of the concentration, so small part of the concentration will meet the gradients already raising the $D_{\mathrm{eff}}^{\mathrm{Point}}(z_0, t)$.

The initial point in the middle $z_0 = 0$(blue) from Fig. 3.15(d) is used as an example of calculating the order of magnitude. The first peak of the flow is missed since the distance to where the momentum reaches $1 - \lambda_d = \frac{1}{\mathrm{Wo}} = 0.96$ is too far compared with the diffusion length $0.96 = \sqrt{6t_{D_{\mathrm{eff}}}}$ and the time the peak is lasting(half period) $\frac{0.5\pi}{62.5} = 0.0251 << (0.96)^2/6 = 0.1536$. Simply the time was too short before the reversal of flow compared to the diffusion in the transverse direction to reach momentum diffusion or the velocity gradients. First when the flow reversed at the time $t = 0.05$, $\cos(0.05 \times 62.5) = -0.99$ the diffusion's first standard deviation has reached $\sqrt{0.05 \times 6} = 0.54$, but now a sufficiently part of the concentration has reached the annular region of gradient to get a increase in $D_{\mathrm{eff}}^{\mathrm{Point}}(z_0, t)$.

3.5.1.1 Peaks in the effective diffusion $\epsilon_0 = 0\,\epsilon_1 = 1$, for $\mathrm{Sc} = 10^{-1}$

Peaks in $D_{\mathrm{eff}}^{\mathrm{Point}}(z_0, t)$ are also observed here and the peak probably arises due to the high level of concentration gradient, that is able to use the velocity gradient to spread the

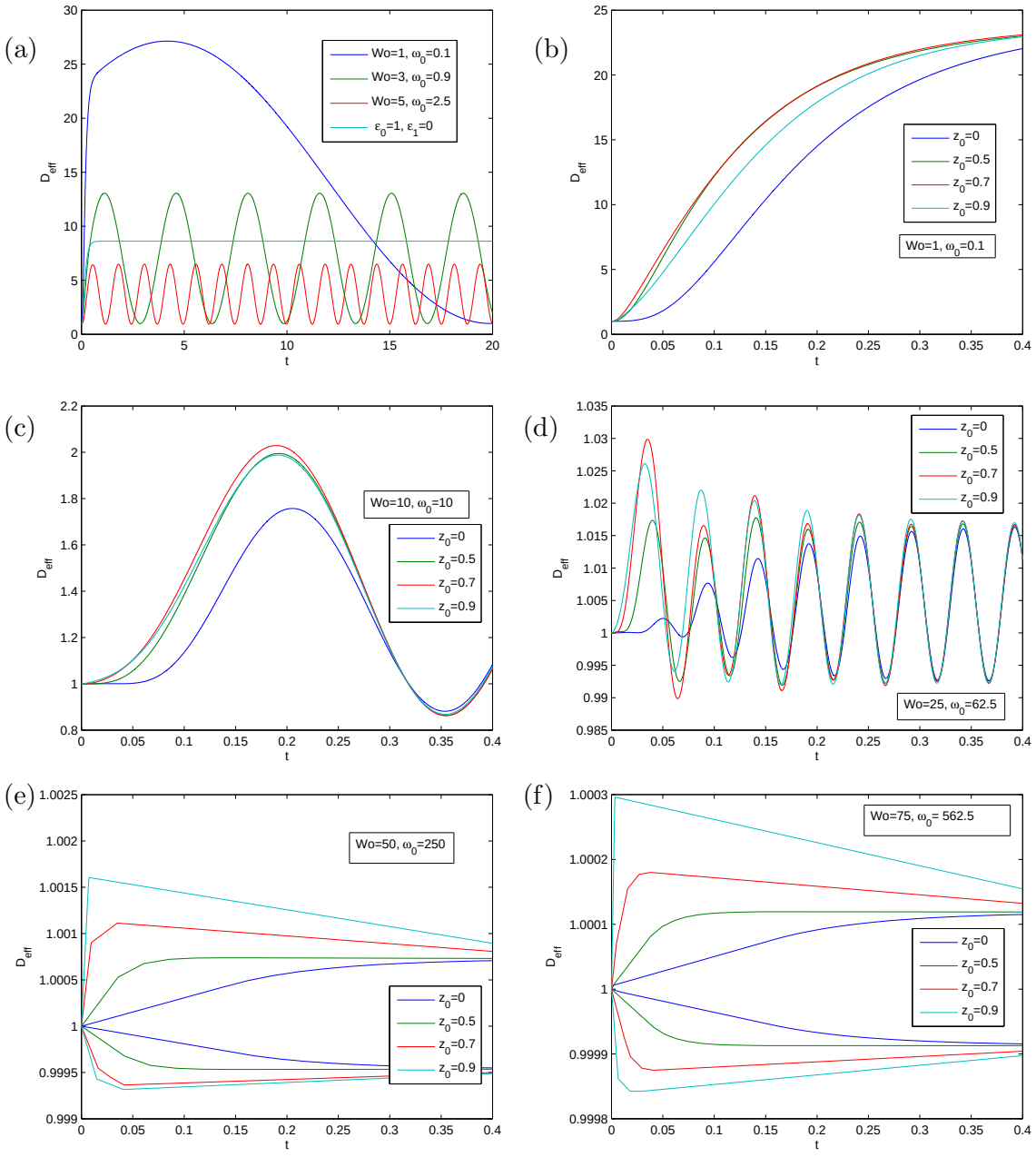

Figure 3.15: $D_{\text{eff}}^{\text{Point}}(z_0, t)$ with Pé $= 20$ and Sc $= 0.1$ for different parameters. (a)The $D_{\text{eff}}^{\text{Point}}(z_0 = 0, t)$ for Wo $= 1$(blue), Wo $= 3$(green), Wo $= 5$(red) and the steady flow $D_{\text{eff}}^{\text{Point}}(z_0 = 0, \infty)$ for $\epsilon_0 = 1$, in the time $0 \leq t \leq 20$. (b)For Wo $= 1$ with the positions of the point concentration $z_0 = 0$(blue), $z_0 = 0.5$(green), $z_0 = 0.7$(red) and $z_0 = 0.9$(turquoise) $0 \leq t \leq 0.4$.(c)For Wo $= 3$. (c)For Wo $= 10$. (d)For Wo $= 25$. (e)the envelope function is used to represent $D_{\text{eff}}^{\text{Point}}(z_0, t)$ for Wo $= 50$. (f)the envelope function is used to represent $D_{\text{eff}}^{\text{Point}}(z_0, t)$ for Wo $= 75$. In (c) a phase shift occur between the point located in the center and the point located $z_0 > 0.5$. Peaks are observed for Wo $= 25$, Wo $= 50$ and Wo $= 75$.

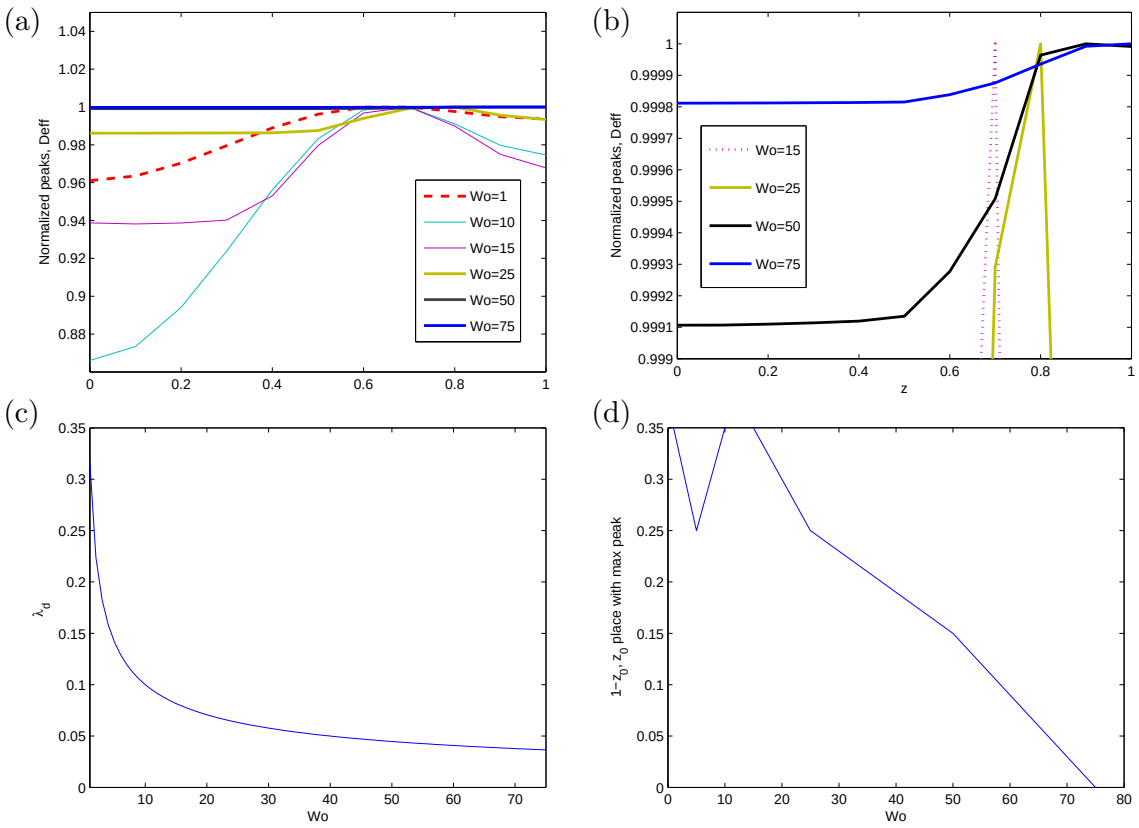

Figure 3.16: Observing maximum peak in $D_{\text{eff}}^{\text{Point}}(z_0, t)$ versus the initial point placement, for Pé = 20 and Sc = 0.1 and for different Womersley numbers Wo. (a)initial position z_0 of the point (horizontal axes), versus the normalised maximum peaks $D_{\text{eff}}^{\text{Point}}(z_0, t)/D_{\text{eff}}^{\text{PointPeak}}(z_0, t_{peak})$(vertical axes) for the Womerley numbers Wo = 1(red), Wo = 10(turquoise), Wo = 15(violet), Wo = 25(yellow), Wo = 50(black), Wo = 75(blue) numbers the peaks of the different point concentration are plotted.(b)Same plots as (a), just a zoom in on the highest peak of $D_{\text{eff}}^{\text{Point}}(z_0, t)/D_{\text{eff}}^{\text{PointPeak}}(z_0, t_{peak})$ with respect to the initial placement z_0 of the point, only regarding the highest Womersley numbers, Wo = 15(violet), Wo = 25(yellow), Wo = 50(black), Wo = 75(blue). (c) a plot of the diffusion length of momentum versus the Wo number. (d) A plot of the initial point concentration with the maximum peak $D_{\text{eff}}^{\text{Point}}(z_0, t)$ placement in $1 - z_0$(horizontal axes) versus the Wo number(vertical axes). Its seen that the the initial point concentrations with the maximum peak, distance to the wall $1 - z_0^{peak}$ follows the momentum diffusion length from the wall nicely.

concentration, later the concentrations is lower in the high velocity gradients giving a lower spread. This becomes a more present effect for higher frequencies where the relative peaks get bigger compared to the steady peak, this can be seen in Fig. 3.15(e-f) and the point concentration placed in the middle $z_0 = 0$(blue) has a long diffusion path in the transverse direction before meeting the region where the momentum diffusion is present. Further investigation is done in order to find the peaks of $D_{\text{eff}}^{\text{Point}}(z_0, t)$ for the initial location of the point concentrations versus the momentum diffusion length for higher Wo numbers. So for higher Wo it is expected that the initial point concentration with the maximum peak in $D_{\text{eff}}^{\text{Point}}(z_0, t)$ is moved with the momentum diffusion towards the wall where the velocity gradients are present. This effect can be seen in Fig. 3.16(a-b) when Wo increases the maximum peak of the point(z_0) in the $D_{\text{eff}}^{\text{Point}}(z_0, t)$ gets moved towards the wall with respect to the initial point concentration where the momentum diffusion can reach. In Fig. 3.16(c) the calculated momentum diffusion length $\lambda_d = \frac{1}{\text{Wo}}$ is plotted versus the Wo number. In Fig. 3.16(d)the initial point concentration z_0 with the maximum peak in $D_{\text{eff}}^{\text{Point}}(z_0, t)$ is plotted versus the Wo number, note that is plotted as the distance to the wall $1 - z_0$ and not z_0, for comparison of Fig. 3.16(c). The highest peak for the point concentration gets moved towards the right for higher Wo number. it was shown that, the initial point concentration with maximum peak gets shifted towards the region with velocity gradients and where the momentum diffusion reaches in the z-direction.

3.5.2 Remarks about the single frequency flow, $\epsilon_0 = 0, \epsilon_1 = 1$

Here phase shift was shown and further investigation will be done in the cylinder geometry since the cylinder encapsulates the whole fluid, thereby induced more shear and more reaction from the wall giving more curvature to the velocity profile for smaller Wo and ω_{o} while Sc = 1000 numbers. Because of the complexity of the implemented model in Matlab and running time, high frequencies requires a high number of data points, for a good resolution off the frequency and the behaviour of $D_{\text{eff}}(t)$.

3.5.3 Applied point with steady and a plus one frequency flow $\epsilon_0 = 1$, ϵ_1, with the Schmidt number 10^{-1}

Now the Schmidt number is reset to $\text{Sc} = 10^3$. Period doubling will occur for the point concentration as in the uniform distribution [1] and the same behaviour was observed. In Fig. 3.17(a) different located point concentrations with a steady flow and a one frequency flow $\epsilon_0 = 1, \epsilon_1 = 0.05$ here the steady flow dominating the $D_{\text{eff}}(t)$. What happen if the amplitude of the oscillating flow is turned up to $\epsilon_1 = 50, \epsilon_0 = 1$ this is shown in Fig. 3.17(b) it looks like a period doubling occurred. This is because when the oscillating flow is decreasing the steady flow will take over making an additional smaller peak in the $D_{\text{eff}}(t)$. This can be seen in Fig. 3.17(d) where $D_{\text{eff}}(t)$ is normalized as $D_{\text{eff}}(t)/D_{\text{eff}}^{\text{avr}}(\infty)$, by dividing with the time-averaged diffusivity $D_{\text{eff}}^{\text{avr}}(t)$ over one oscillation period $\tau_0 = 2\pi/\omega_{\text{o}}$, where

$$D_{\text{eff}}^{\text{avr}}(t) = \frac{1}{\tau_0} \int_t^{t+\tau_0} D_{\text{eff}}(t)\, \mathrm{d}t \tag{3.50a}$$

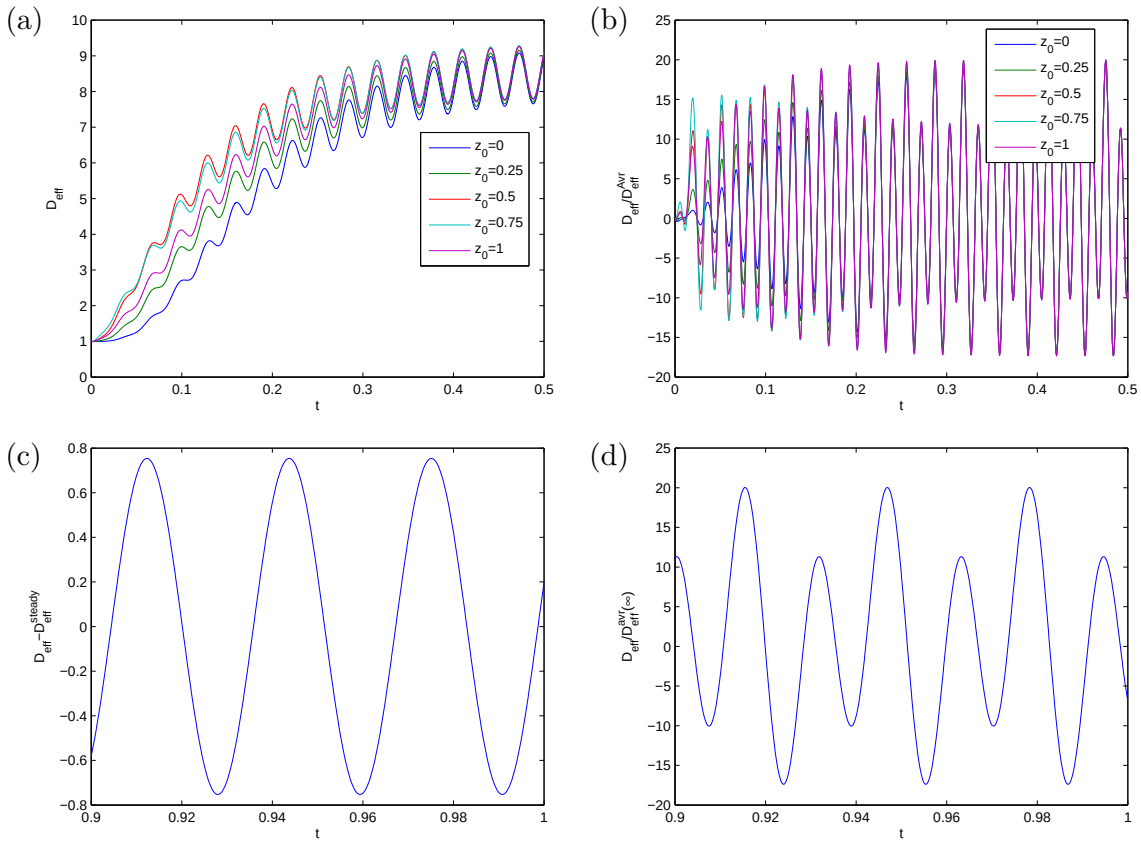

Figure 3.17: A harmonically oscillating flow superimposed on a steady flow, with the frequency $\omega_0 = 200$, Wo $= 0.447$ and Pé $= 20$. (a) Point concentrations with the starting positions $z_{\text{loc}} = 0, 0.25, 0.5, 0.75, 1$ and $\epsilon_1 = 0.05, \epsilon_0 = 1$ (c) $D_{\text{eff}}(t) - D_{\text{eff}}^{\text{steady}}(t)$ for the steady regime $0.9 < t < 1$ with $z_{\text{loc}} = 0.5$, showing the same behaviour as [1] and [10](d) Normalized effective diffusivity $D_{\text{eff}}(t)/D_{\text{eff}}^{\text{avr}}(\infty)$, period doubling occurs with increased amplitude of oscillating flow $\epsilon_1 = 50$ this shows again the same dynamic behaviour as [1].

this is calculated in Matlab. This can be compared with the Fig. 3.17(c) for $\epsilon_1 = 0.05$ where no period doubling occurs, here $D_{\text{eff}}(t)$ is subtracted from the steady effective diffusion to get the effect just from the oscillatory flow. Other investigations can be made as S. Vedel and H. Bruus where ϵ_1 is increased and a cross-over from the linear regime occurs, where $D_{\text{eff}}^{\text{avr}}(\infty)/D_{\text{eff}}^{\text{steady}}(\infty) \approx 1$, to a non-linear regime, where $D_{\text{eff}}^{\text{avr}}(\infty)/D_{\text{eff}}^{\text{steady}}(\infty) \propto \epsilon_1^2$, happens at the frequency-dependent critical value ϵ_1^c which is Wo $\lesssim \xi_{0,1} \approx 2.40$ [1].

3.5.3.1 Concluding Remarks

It was possible to show for the points concentration convergence towards the uniform distribution in the cross-sectional plane in the effective diffusion. This is a good result and indicates the correctness of the framework theoretically and the implementation in Matlab for the point concentration. The linear phase also shows some common features between

the point concentration and the plane uniform distribution.

Depending on the initial starting placement $z_0 = 0$ of the point concentration, different short time dynamic $0 < t < 0.0 < 0.08$ will be obtain dependent on the gradients in the z-direction. In the case of a steady flow the point concentration initially placed around the center $z_0 \approx 0$, will have slower increase for the $D_{\text{eff}}^{\text{Point}}(z_0, t)$. The point concentration starts near the wall will have greater gradients and thereby a bigger increase in $D_{\text{eff}}(t)$ in the short time dynamic. It was possible to partially model this short time dynamic with the four models with the exception of the effect from the wall.
For a single frequency flow, the frequency ω_{o} determines if $D_{\text{eff}}(t)$ gets to minus, due to diffusion time in the transverse direction compared to the dimensional frequency. If the diffusion has time to reach the wall before the reversal of the flow $D_{\text{eff}}(t)$ will oscillate above molecular diffusion if not, the concentration in the middle will shifted forth and back making $D_{\text{eff}}(t)$ oscillate around the molecular diffusion. This effects start to happen around $\omega_0 = 1$, when the frequency gets over around $\omega_0 > 20$ the momentum diffusion cannot reach the middle and also the amplitude of the velocity profile gets smaller. This gives a smaller $D_{\text{eff}}^{\text{Point}}(z_0, t)$ and a different shape of the velocity profile. Phase shifts will also occur dependent on the position of the initial point concentration and if high enough frequency is applied. Period doubling also occurs, if a steady flow is superimposed on a harmonically oscillating flow, and the oscillating flow has a big enough amplitude ϵ_1.

My conclusion is that the behaviour of $D_{\text{eff}}^{\text{Point}}(z_0, t)$ can mainly be explained by just looking at the gradient of the velocity field. The exact physical explanation for the peak of $D_{\text{eff}}^{\text{Point}}(z_0, t)$ is hard to explain since many physical phenomena occur simultaneously.

Chapter 4

Applied point concentration in a circular channel

Now a circular channel's effective diffusivity $D_{\text{eff}}^{\text{Point}}(r_0, t)$ will be investigated. First the formula for the point concentration in the circular channel will be made from the velocity profile, basis functions, $\frac{1}{2}\frac{\mathrm{d}M_2}{\mathrm{d}t}$ and $M_1\,\frac{\mathrm{d}M_1}{\mathrm{d}t}$ are calculated to find $D_{\text{eff}}^{\text{Point}}(r_0, t)$. Similar effects for the circular channel as in the parallel plate channel can be expected. Just with a slight difference, which is that the wall encapsulates all the fluids now inducing more shear stress. Some investigations from the parallel plate channel will be left out like the four models of short time dynamic, since the same behaviour is expected.

First the steady case will be investigated, then the single frequency flow and finally the single frequency superimposed on the steady flow.

4.1 The velocity profile

The circular channel velocity profile depends on the time-dependent pressure drop with the components $\epsilon_\ell \Delta p\, \mathrm{e}^{\mathrm{i}\ell\omega_\mathrm{o}t}$ (ϵ_ℓ is the dimensionless amplitude) in the longitudinal direction of a circular tube of unit radius. Using cylindrical coordinates and the generalized wavenumber k_ℓ, then the velocity component u_ℓ fulfilling the boundary conditions $u|_{r=1} = 0$ and $\partial_r u|_{r=0} = 0$[1, 18, 14] is,

$$k_\ell = k_\ell(\mathrm{Wo}) = \sqrt{-\mathrm{i}\ell\mathrm{Wo}^2} = \sqrt{-\mathrm{i}\ell\omega_\mathrm{o}/\mathrm{Sc}}, \tag{4.1a}$$

$$\left|u_\ell\right\rangle = \epsilon_\ell \frac{8}{k_\ell^2}\left[\frac{J_0(k_\ell r)}{J_0(k_\ell)} - 1\right]. \tag{4.1b}$$

where the steady-state Poiseuille solution in the limit of ℓ goes to zero is $u_0(r) = \lim_{\ell\to 0} u_\ell(r) = \epsilon_0 2(1 - r^2)$. The Characteristic velocity is taken to be the average steady state velocity $U_\mathrm{o} = \Delta p\, a^2/(8\eta\mathcal{L})$ for $\epsilon_0 = 1$.

4.2 Basis functions

From the diffusion equation,

$$(\lambda_m+\nabla_\perp^2)\big|f_m(r,\varphi\rangle = 0,\ m = 0,1,2,\dots, \tag{4.2}$$

having the Laplacian in cylinder coordinates,

$$\frac{1}{r}\partial_r(r\partial_r f_m) + \frac{1}{r^2}\partial_\varphi^2 f_m = -\lambda_m f_m. \tag{4.3}$$

using seperation of variables, $f_m(r,\varphi) = R(r)_m\Phi(\varphi)$,

$$-\partial_\varphi^2\Phi = C\Phi \tag{4.4}$$

since $e^{in\varphi}$ is the solution, then the constant is $C = n^2$, then getting $n = -\infty, -1, 0, 1, .., \infty$ equations for each m,

$$(r^2\partial_r^2 + r\partial_r + n^2 + r^2\lambda_{n,m})f_{n,m} = 0 \tag{4.5}$$

with the eigenvalues $\lambda_{n,m}$, coming from the boundary conditions where m is the root and n is the order of the Bessel function $R_{m,n}(r)$ and n oscillation counter for $\Phi_n(\varphi)$.

$$\vec{n}\cdot\boldsymbol{\nabla}_\perp\big|f_{n,m}(r,\varphi)\big\rangle = 0, \text{ on the wall,} \tag{4.6a}$$

$$\vec{n} = \vec{e}_r, \text{ so } \vec{n}\cdot\boldsymbol{\nabla}_\perp = \partial_r \tag{4.6b}$$

and $\xi_{n,m}$ is the solution to,

$$\frac{1}{2}(J_{n-1}(\xi_{n,m}) - J_{n+1}(\xi_{n,m})) = 0, \tag{4.7}$$

finding the eigenvalues and eigenvectors

$$\lambda_n = (1-\delta_{n,0}\delta_{m,0})\xi_{m,n}^2 \tag{4.8}$$

getting the solution and remembering normalizing constants,

$$f_{(n,m)}(r,\varphi) = \frac{J_n(\xi_{n,m}r)}{\sqrt{(1-n^2/\xi_{n,m}^2)}J_n(\xi_{n,m})}e^{in\varphi}, \tag{4.9}$$

$$R_{n,m}(r) = \frac{J_n(\xi_{n,m}r)}{\sqrt{(1-n^2/\xi_{n,m}^2)}J_n(\xi_{n,m})},\quad \Phi_n(\varphi) = \frac{1}{\sqrt{1+\delta_{(n,0)}}}e^{in\varphi} \tag{4.10}$$

with the condition,

$$f_{(-n,m)}(r,\varphi) = f^*_{(n,m)}(r,\varphi) \tag{4.11}$$

later φ independence will be shown, then it is possible to find the solute equilibration rate and the fluid momentum equilibration rate. Thereby the fluid momentum equilibration rate can be found as,

$$\alpha_{fl} = \mathrm{Sc}\xi_{0,1}^2 \tag{4.12}$$

and the solute equilibration rate,

$$\lambda_{(0,1)} = \xi_{0,1}^2 \tag{4.13}$$

The time when most of the anomalous diffusion is decreased is around $\frac{1}{\lambda_{(0,1)}} = \frac{1}{\xi_{0,1}^2} \approx 0.068 < t$ from [1].

4.2.1 Inner product

The bra-kets for the cylindrical coordinates are defined as

$$\left\langle R_{n,m}\middle|\tilde{R}_{p,j}\right\rangle = 2\int_0^1 \mathrm{d}r\, rR^*_{n,m}(r)\,\tilde{R}_{n,m}(r), \tag{4.14}$$

$$\left\langle \Phi\middle|\tilde{\Phi}\right\rangle = \frac{1}{2\pi}\int_0^{2\pi} \mathrm{d}\varphi\, \Phi^*\tilde{\Phi} \tag{4.15}$$

where we have,

$$\langle 1 \mid \Phi_n(\varphi)\rangle = \langle \Phi_0(\phi) \mid \Phi_n(\varphi)\rangle = \delta_{n,0} \tag{4.16}$$

and

$$\langle \Phi_n(\varphi) \mid \Phi_p(\varphi)\rangle = \delta_{n,p},\ n \neq 0 \tag{4.17}$$

so for the $f_{n,m}(r,\varphi) = R_{n,m}(r)\Phi_n(\varphi)$ and $\tilde{f}_{p,j}(r,\varphi) = \tilde{R}_{p,j}(r)\tilde{\Phi}_p(\varphi)$ we have

$$\langle f_{n,m} \mid \tilde{f}_{p,j}\rangle = \frac{1}{\mathcal{A}}\int_\Omega \mathrm{d}\boldsymbol{r}_\perp f^*_{n,m}\tilde{f}_{p,j} = \langle R_{n,m} \mid \tilde{R}_{p,j}\rangle\langle \Phi_n \mid \tilde{\Phi}_p\rangle = \tag{4.18}$$

$$\langle R_{n,m} \mid \tilde{R}_{p,j}\rangle\delta_{n,p} = \delta_{n,p}\delta_{m,j}(1-n^2/\xi^2_{n,m})J_n(\xi_{n,m})^2$$

Now orthogonality is used again as in the rectangular channel, with a similar notion,

$$\langle u_l(r) \mid \Phi_n(\varphi)R_{n,m}(r)\rangle = \langle 1 \mid \Phi_n(\varphi)\rangle\langle u_l(r) \mid R_{n,m}(r)\rangle = \delta_{n,0}\langle u_l(r) \mid R_{n,m}(r)\rangle \tag{4.19}$$

The next bracket $\langle f_{(n,m)}(r,\varphi) \mid u_0(r) \mid f_{(n,m)}(r,\varphi)\rangle$,

$$\langle \Phi_n(\varphi)R_{n,m}(r) \mid u_0(r) \mid \Phi_n(\varphi)R_{n,m}(r)\rangle = \langle R_{n,m}(r) \mid u_l(r) \mid R_{n,m}(r)\rangle \tag{4.20}$$

To the last $\langle f_{(n,m)}(r,\varphi) \mid u_l(r) \mid f_{(p,j)}(r,\varphi)\rangle$

$$\langle \Phi_n(\varphi)R_{n,m}(r) \mid u_l(r) \mid \Phi_p(\varphi)R_{p,j}(r)\rangle = \delta_{n,p}\langle R_{n,m}(r) \mid u_l(r) \mid R_{p,j}(r)\rangle \tag{4.21}$$

now that all the bra-kets are defined the analysis can start.

4.2.2 Reproducing results existing in Literature for the circular channel.

Before the formula derived earlier for the $D^{\mathrm{Point}}_{\mathrm{eff}}(r_0,t)$ is implemented in Matlab, earlier results in the literature is reproduced to check the bra-kets and verify the code. For the cylindrical coordinates $\left\langle f\middle|g\right\rangle = \int_0^1 \mathrm{d}r\, 2rf^*(r)\,g(r)$, the bra-ket was calculated numerically in Matlab and compared to the value,

$$\left\langle f_n\middle|u_\ell\right\rangle = -\epsilon_\ell\frac{16}{(\xi^2_{1,n}-k^2_\ell)k_\ell}\,\frac{J_1(k_\ell)}{J_0(k_\ell)},\ \text{for } n>0, \tag{4.22}$$

and $\left\langle f_n\middle|u_0\right\rangle = \lim_{\ell\to 0}\left\langle f_n\middle|u_\ell\right\rangle = -8/\xi^2_{1,n}$ for the steady term [1]. These bra-kets were possible to get with numerical implementation in Matlab. Then Barton's steady-flow result [4] was implemented, $D^{\mathrm{steady}}_{\mathrm{eff}}(t) = 1 + \mathrm{P\acute{e}}^2\big[\frac{1}{48} - \sum_{n=1}^{\infty}(64/\xi^6_{1,n})\exp(-\xi^2_{1,n}t)\big]$ This can be seen in Fig. 4.1(a). A harmonically oscillating flow of frequency ω_{o} superimposed on the steady flow shows period doubling for $\epsilon_0 = 1$, $\epsilon_1 = 50$ in Fig. 4.1(d) compared to $\epsilon_0 = 1, \epsilon_1 = 0.05$ in Fig. 4.1(c) as in S. Vedel and Bruus [1].

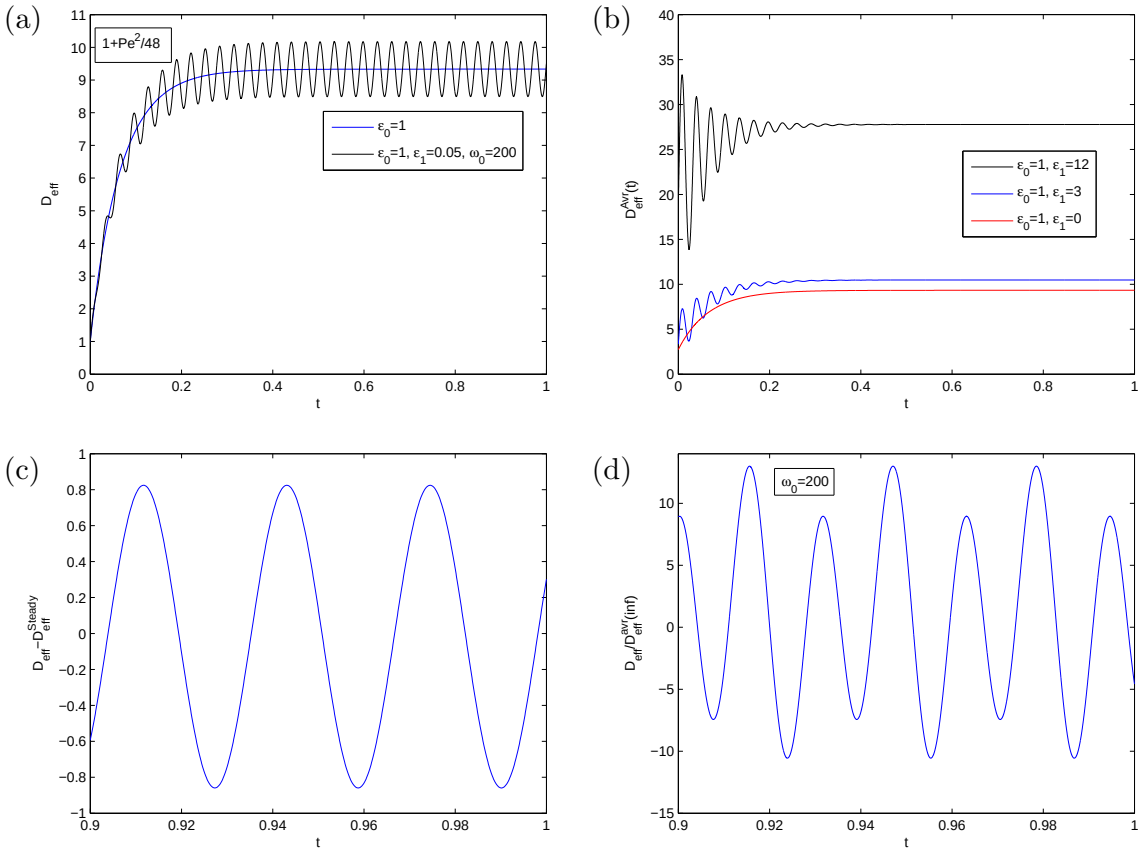

Figure 4.1: $D_{\text{eff}}(t)$ for the uniform distribution in the cross sectional plane in cylinder channel with the value Pé $= 20$. (a) $D_{\text{eff}}(t)$ for $\omega_0 = 200$, Wo $= 0.447$ and velocity amplitudes $\epsilon_1 = 0.05\,, \epsilon_0 = 1$ (black line) oscillating around $D_{\text{eff}}^{\text{steady}}(t)$(blue line). (b)$D_{\text{eff}}^{\text{avr}}(t)$ for velocity amplitudes $\epsilon_1 = 0$, $\epsilon_0 = 1$ (red line), $\epsilon_1 = 3$, $\epsilon_0 = 1$ (blue line) and $\epsilon_1 = 12$, $\epsilon_0 = 1$ (black line),(c) the steady regime $0.9 < t < 1$ for $\epsilon_1 = 0.05 \ll \epsilon_0 = 1$ is in agreement with Mukherjee and Mazumder [10] and [1](d) for Normalized effective diffusivity $D_{\text{eff}}(t)/D_{\text{eff}}^{\text{avr}}(\infty)$ showing period doubling when $\epsilon_1 = 50$, $\epsilon_0 = 1$. All this is in agreement with S.Vedel and H.Bruus [1].

4.3 Random placement of point concentration

The calculation is quite similar to the rectangular channel since the velocity profile in this case is independent of the angle φ because of rotational symmetry. This later makes a simplification in the bra-kets, that is also why the notion with the indices m, n are used. The point concentration is defined so

$$\tilde{C}(x, \mathbf{r}_\perp, 0) = \frac{\mathcal{V}}{N_0} N_0 \delta(x)\delta(r)\delta(\varphi) = \mathcal{L}\mathcal{A}\delta(x)\delta(r - r_0)\delta(\varphi - \varphi_0) \tag{4.23}$$

The initial condition for the zero axial moments,

$$\tilde{c}_0(\mathbf{r}_\perp, 0) = \frac{1}{\mathcal{L}} \int_{-\frac{1}{2}\mathcal{L}}^{\frac{1}{2}\mathcal{L}} \mathcal{L}\mathcal{A}\delta(x)\delta(r)\delta(\varphi) = \mathcal{A}\delta(r - r_0)\delta(\varphi - \varphi_0) \tag{4.24}$$

finding $a_{0,(n,m)}$

$$a_{0,(n,m)} = \langle \frac{J_n(\xi_{n,m} r)}{\sqrt{(1 - n^2/\xi_{n,m}^2)} J_n(\xi_{n,m})} e^{\mathrm{i}n\varphi} \mid \mathcal{A}\delta(r - r_0)\delta(\varphi - \varphi_0) \rangle = \frac{J_n(\xi_{n,m} r_0)}{\sqrt{(1 - n^2/\xi_{n,m}^2)} J_n(\xi_{n,m})} e^{\mathrm{i}n\varphi_0} \tag{4.25}$$

calculating $\frac{\mathrm{d}M_1}{\mathrm{d}t}$ and since it contains the expression as in Eq. (4.16), $\delta_{n,0}\langle u_l(r) \mid R_{n,m}(r) \rangle$, the n sum is removed due to independence of the angle φ. Then having only Bessel zero functions, where m is the root of the Bessel zero functions,

$$\frac{\mathrm{d}M_1}{\mathrm{d}t} = \mathrm{Pe} \sum_{m=0}^{\infty} \sum_{l=-\infty}^{\infty} a_{0,(0,m)} \langle u_l(r) \mid R_{0,m}(r) \rangle e^{-(\lambda_{0,m} + \mathrm{i}l\omega_0)t} \tag{4.26}$$

and calculating M_1,

$$M_1 = \mathrm{Pe} \sum_{m=0}^{\infty} \sum_{l=-\infty}^{\infty} a_{0,(0,m)} \langle u_l(r) \mid R_{0,m}(r) \rangle \frac{1 - e^{-(\lambda_{(0,m)} + \mathrm{i}l\omega_0)t}}{\lambda_{(0,m)} + \mathrm{i}l\omega_0} \tag{4.27}$$

then the $\beta^l_{(n,m),(p,j)}$ is defined,

$$\beta^l_{(n,m),(p,j)} = (1 - \delta_{l,0}\delta_{n,p}\delta_{m,j}) \frac{\langle \Phi_n(\varphi) R_{n,m}(r) \mid u_l(r) \mid \Phi_p(\varphi) R_{p,j}(r) \rangle}{\lambda_{(n,m)} - \lambda_{(p,j)} + \mathrm{i}l\omega_0}, \tag{4.28}$$

because of orthogonality Eq. (4.17) and the independence of the velocity in the angular direction φ,

$$\beta^l_{(n,m),(n,j)} = (1 - \delta_{l,0}\delta_{m,j}) \frac{\langle R_{n,m}(r) \mid u_l(r) \mid R_{n,j} \rangle}{\lambda_{(n,m)} - \lambda_{(n,j)} + \mathrm{i}l\omega_0}, \tag{4.29}$$

in this case $\lambda_{(n,m)} - \lambda_{(n,j)} \neq \lambda_{(0,m)} - \lambda_{(0,j)}$ since n describes the order of the Bessel function and $m,\ j$ describes the Bessel roots. Then calculating $a_{1,(n,m)}$, since $\tilde{c_1}\rangle = 0$ and using earlier defined coefficients. Remembering orthogonality when $n \neq p$ removing the p-sum,

$$a_{1,(n,m)} = -\sum_{p=0}^{\infty} \sum_{j=0}^{\infty} a_{0,(p,j)} \sum_{l=-\infty}^{\infty} \beta^l_{(n,m),(p,j)} = -\sum_{j=0}^{\infty} a_{0,(n,j)} \sum_{l=-\infty}^{\infty} \beta^l_{(n,m),(n,j)}, \tag{4.30}$$

the $\gamma_{1,(n,m)}$,

$$\gamma_{1,(n,m)} = \langle \Phi_n(\varphi) R_{n,m}(r) \mid u_0(r) \mid \Phi_n(\varphi) R_{n,m}(r) \rangle \tag{4.31}$$

a last finding $\frac{1}{2}\frac{\mathrm{d}M_2}{\mathrm{d}t}$, again because of orthogonality Eq. (4.17), p runs to $\sum_{p=-\infty}^{\infty}$ since it is the angles,

$$\frac{1}{2}\frac{\mathrm{d}M_2}{\mathrm{d}t} = 1 + \mathrm{Pe}^2 \sum_{k=-\infty}^{\infty} \sum_{j=0}^{\infty} \sum_{m=0}^{\infty} \langle u_k(r) \mid R_{0,m}(r) \rangle e^{-(\lambda_{(0,j)} + \mathrm{i}k\omega_0)t} \tag{4.32}$$

$$\times \left[(a_{0,(0,j)}\gamma_{1,(0,j)}t + a_{1,(0,j)})\delta_{m,j} + a_{0,(0,m)} \sum_{l=-\infty}^{\infty} \beta^l_{(0,m),(0,j)} e^{\mathrm{i}l\omega_0 t} \right]$$

at last combining the calculated coefficients to Eq. (2.22) $D_{\text{eff}}(t) = \frac{1}{2}\frac{\mathrm{d}\mu_2}{\mathrm{d}t} = \frac{1}{2}\frac{\mathrm{d}M_2}{\mathrm{d}t} - M_1\frac{\mathrm{d}M_1}{\mathrm{d}t}$,.

4.4 Placement of point concentration in the center $r_0 = 0$

When the point concentration is placed in the center, further simplifications occurs. The initial concentration is first placed in the center $r = 0$, and in the middle of the longitudinal direction. The initial normalized concentration $\tilde{C} = 1$ is,

$$\tilde{C}(x, \mathbf{r}_\perp, 0) = \frac{\mathcal{V}}{N_0} N_0 \delta(x)\delta(r)\delta(\varphi) = \mathcal{L}\mathcal{A}\delta(x)\delta(r)\delta(\varphi). \tag{4.33}$$

The initial condition for the zero axial moments,

$$\tilde{c}_0(\mathbf{r}_\perp, 0) = \frac{1}{\mathcal{L}} \int_{-\frac{1}{2}\mathcal{L}}^{\frac{1}{2}\mathcal{L}} \mathcal{L}\mathcal{A}\delta(x)\delta(r)\delta(\varphi) = \mathcal{A}\delta(r)\delta(\varphi) \tag{4.34}$$

and the initial first axial moments is zero $\tilde{c}_1 = 0$ Eq. (2.40). All the angular dependence φ is gone and the problem is similar to one-length-scale cross section in [1]. So the general solution with the corresponding eigenfunctions and eigenvalues is [1],

$$\big|f_n\big\rangle = \delta_{n,0} + (1 - \delta_{n,0})\frac{J_0(\xi_{1,n}\, r)}{J_0(\xi_{1,n})}, \tag{4.35a}$$

$$\lambda_n = (1 - \delta_{n,0})\xi_{1,n}^2, \tag{4.35b}$$

$J_s(x)$ is the Bessel function of the first kind J of order s, and $\xi_{s,n}$ is the nth root of the Bessel function $J_s(x)$[1]. Now the basis functions and the velocity profile is found, the inner products can be calculated. Some of the inner products are already calculated Eq. (4.22). Also needing the bra-ket

$$\big\langle f_n\big|u_0\big|f_n\big\rangle \tag{4.36}$$

and

$$\big\langle f_n\big|u_l\big|f_m\big\rangle \tag{4.37}$$

these bra-kets are calculated numerically in Matlab for the later simulations. Now the formalism can be used starting with finding the coefficients $a_{0,m}$,

$$a_{0,m} = \langle f_m \mid \tilde{c}_0\rangle = \delta_{m,0} + (1 - \delta_{m,0})\frac{1}{J_0(\xi_{1,m})} \tag{4.38}$$

$$\gamma_{1n} = \big\langle f_n\big|u_0\big|f_n\big\rangle, \tag{4.39}$$

where the β-coefficients is,

$$\beta_{kn}^{\ell} = (1 - \delta_{\ell,0}\delta_{k,n})\,\frac{\big\langle f_k\big|u_\ell\big|f_n\big\rangle}{\lambda_k - \lambda_n + \mathrm{i}\ell\omega_{\mathrm{o}}}. \tag{4.40}$$

finding a_{1n} where $\frac{1}{\mathrm{Pé}}\left\langle f_n \middle| \tilde{c}_1 \right\rangle = 0$ since $\tilde{c}_1 = 0$

$$a_{1n} = -\sum_{k=0}^{\infty} a_{0k} \sum_{l=-\infty}^{\infty} \beta_{nk}^{\ell}. \tag{4.41}$$

finding $\frac{\mathrm{d}M_1}{\mathrm{d}t}$

$$\frac{\mathrm{d}M_1}{\mathrm{d}t} = \mathrm{Pé} \sum_{n=0}^{\infty} \sum_{\ell=-\infty}^{\infty} a_{0n} \left\langle u_\ell \middle| f_n \right\rangle \mathrm{e}^{-(\lambda_n + \mathrm{i}\ell\omega_\mathrm{o})t}, \tag{4.42a}$$

then M_1

$$M_1 = \mathrm{Pé} \sum_{n=0}^{\infty} \sum_{\ell=-\infty}^{\infty} a_{0n} \left\langle u_\ell \middle| f_n \right\rangle \frac{1 - \mathrm{e}^{-(\lambda_n + \mathrm{i}\ell\omega_\mathrm{o})t}}{\lambda_n + \mathrm{i}\ell\omega_\mathrm{o}}. \tag{4.42b}$$

and $\frac{1}{2}\frac{\mathrm{d}M_2}{\mathrm{d}t}$

$$\begin{aligned} \frac{1}{2}\frac{\mathrm{d}M_2}{\mathrm{d}t} = 1 + \mathrm{Pé}^2 \sum_{m=0}^{\infty} \sum_{n=0}^{\infty} \sum_{k=-\infty}^{\infty} \left\langle u_k \middle| f_m \right\rangle \mathrm{e}^{-(\lambda_n + \mathrm{i}k\omega_\mathrm{o})t} \\ \times \left[(a_{0n}\gamma_{1n}t + a_{1n})\delta_{n,m} + a_{0n} \sum_{\ell=-\infty}^{\infty} \beta_{mn}^{\ell} \mathrm{e}^{i\ell\omega_\mathrm{o}t} \right], \end{aligned} \tag{4.42c}$$

combining these into,

$$D_{\mathrm{eff}}^{\mathrm{Point}}(r_0, t) = \frac{1}{2}\frac{\mathrm{d}M_2}{\mathrm{d}t} - M_1 \frac{\mathrm{d}M_1}{\mathrm{d}t} \tag{4.43}$$

4.5 Simulations of $D_{\mathrm{eff}}^{\mathrm{Point}}(r_0, t)$ for the point concentration in the circular channel

Notice that from now on the effective diffusion $D_{\mathrm{eff}}(t)$ for the point concentration will be denoted as $D_{\mathrm{eff}}^{\mathrm{Point}}(r_0, t)$, taking care of the spatial dependence of r and utilizing φ-directional independence. Once the $D_{\mathrm{eff}}^{\mathrm{Point}}(r_0, t)$ is implemented in Matlab by the above calculations of the framework, simulations be made of the point concentration. Similar investigation, as in the case for infinite parallel plate channels, is made and comparison is made. Different studies will be made with respect to the placement of the point concentration in the r-direction and the behaviour of $D_{\mathrm{eff}}^{\mathrm{Point}}(r_0, t)$.
In the single frequency flow, more emphasis will be made on changing the Wo with the Schmidt number $\mathrm{Sc} = 1000$. More shear stress is generated by the wall, because it encapsulates the whole fluid. Then at lower Womersley number greater changes occurs in the velocity profile and more dynamics can be seen.

A plus one frequency flow superimposed on the steady flow, is also investigated with respect to period doubling for $D_{\mathrm{eff}}^{\mathrm{Point}}(r_0, t)$.

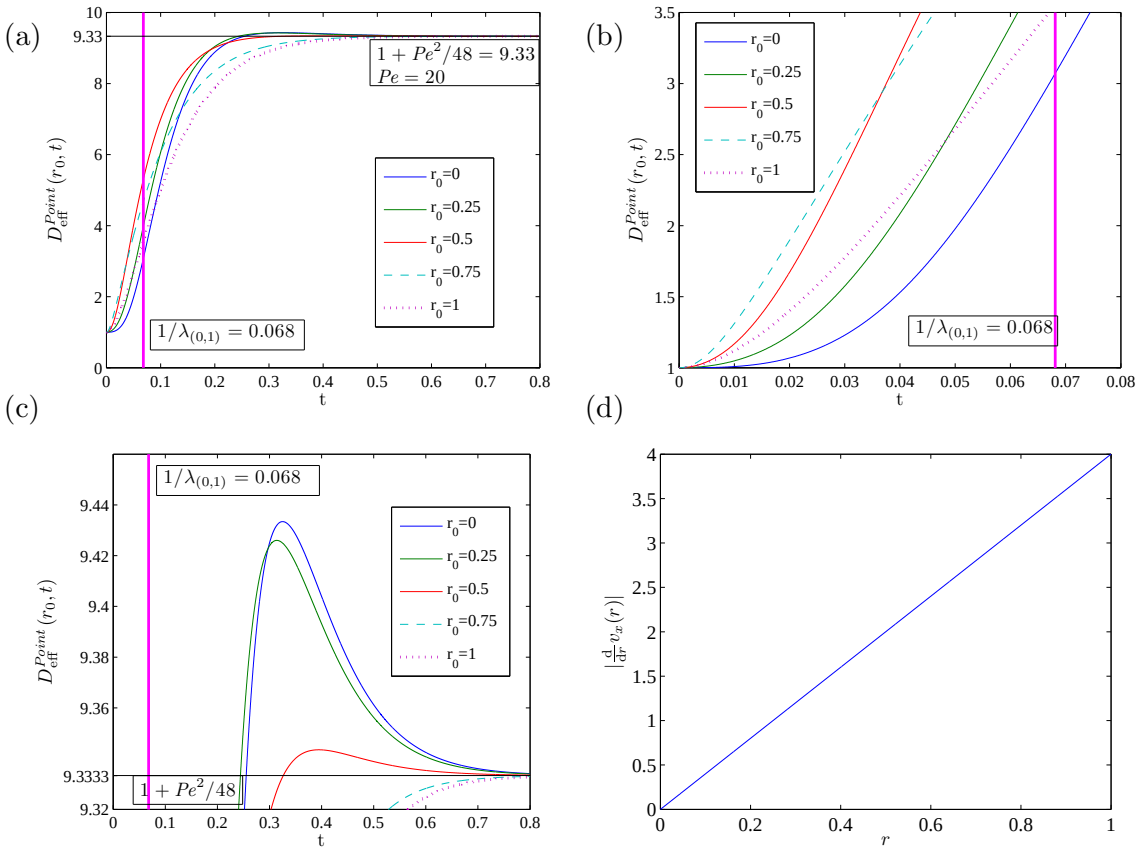

Figure 4.2: $D_{\text{eff}}^{\text{Point}}(r_0, t)$ in a cylinder with unit radius and Pé = 20, varying the starting position of the z-location from $0 \leq z \leq 1$ with 5 equally spaced points and where $\epsilon_0 = 1$. (a)$D_{\text{eff}}^{\text{Point}}(r_0, t)$ in the time period $0 \leq t \leq 1$ for the five differently placed point concentrations $r_0 = 0$(blue), $r_0 = 0.25$(green), $r_0 = 0.5$(red),$r_0 = 0.75$(dotted turquoise) and $r_0 = 1$(violet). (b)$D_{\text{eff}}(t)$ in the time period around $0 \leq t < 0.08$where the diffusion time is $0.0681 = 1/\lambda_1$. The short time anomalous dynamic can be seen here for the five point concentrations and their intersections. (c) $D_{\text{eff}}(t)$ in the time period $0 \ll t \ll 1$ peaks occur in the $D_{\text{eff}}(t)$ for $r_0 = 0$(blue), $r_0 = 0.25$(green), $r_0 = 0.5$(red). Notice that y-axes is zoomed in $9.32 < D_{\text{eff}} < 9.46$. d) the absolute value of the gradient of the velocity profile.

4.6 Applied point concentration with a Steady flow $\epsilon_0 = 1$

In the steady flow the initial placement of point concentration will be investigated and comparison of the point concentration in the infinite parallel plate channel will be made. $D_{\text{eff}}^{\text{Point}}(r_0, t)$ is affected by the initial placement of the point concentration. This can be seen in the Fig. 4.2(a) where the point concentrations are located differently. Four phases can be seen, a short time dynamic phase before $t < \frac{1}{\lambda_1}$. Where the transverse diffusion time $1/\lambda_1 = 0.068$ is plotted as the vertical pink line in Fig. 4.2(a). A linear phase around the time $0.068 < t \lesssim 0.15$, peaks occur around the time $0.15 \lesssim t \lesssim 0.7$ depending on the initial placements of the point concentrations, at last the time phase $0.7 \lesssim t$ of convergence towards the same value as the uniform distribution in the cross sectional plane $1 + \text{Pé}^2/48$. Where in this case Pé $= 20$, making $1 + \text{Pé}^2/48 = 9.3333$ the black vertical line in Fig. 4.2(a).

4.6.0.1 Time dynamic $t < 0.1$

In the Fig. 4.2(b), the short time behaviour for the placement of the point is similar to what was observed in the infinite parallel plate case. The point concentration located in the center $r_0 = 0$(blue) has a slow increase in $D_{\text{eff}}^{\text{Point}}(r_0, t)$ due to the gradient which is zero in the center. The absolute gradient can be seen in the Fig. 4.2(e). The increase gets bigger in $D_{\text{eff}}^{\text{Point}}(r_0, t)$, when the point concentration gets placed more towards the gradient $r_0 = 0.25$(green), $r_0 = 0.5$(red) and $r_0 = 0.75$(turquoise). Then a slight change occur when the point concentration gets closer to the wall around the point concentration $z_0 = 0.75$(turquoise) is intersected by $r_0 = 0.5$(red). The $z_0 = 1$(violet) has a slower increase in $D_{\text{eff}}^{\text{Point}}(r_0, t)$ due to the wall as described in chap. 3. The intersection was thoroughly investigated in the infinite parallel plate and the intersections in the circular channels looks similar so other dynamics will be studied.

4.6.0.2 The linear phase

Fig. 3.4(a) a linear phase for the $D_{\text{eff}}^{\text{Point}}(r_0, t)$ occurs at the time $0.068 \leq t \lesssim 0.2$ similar to the uniform concentration in the Fig. 4.1(a) the blue line with $\epsilon_0 = 1$. This suits perfectly with the diffusion time $1/\lambda_{(0,1)}$, since the concentrations just has diffused in the transverse direction yielding a possible similar concentrations profile as the uniform cross sectional concentration distribution. In the uniform cross sectional concentration distribution the linear phase occurs directly, because the concentration is already smeared out and can utilize the gradients. The ending of the linear phase occurs around the same time $t \approx 0.2$ for the uniform and the point concentration.

4.6.0.3 $D_{\text{eff}}^{\text{Point}}(r_0, t)$ convergence

The initially point concentrations $D_{\text{eff}}^{\text{Point}}(r_0, t)$ converged towards the uniform distribution in the cross sectional plane $D_{\text{effSteady}}^{\text{Point}}(r_0, \infty) = D_{\text{eff}}^{uniform}(\infty) = 1 + \text{Pé}^2/48 = 9.33$, Pé $= 20$, Barton's steady-flow result citeBarton1983, this is shown in Fig. 4.2(a)(black line).

4.6.0.4 Analyses of peak in the effective diffusivity of the steady flow $\epsilon_0 = 1$

The peaks are also investigated in the circular channel with the same definition as in the infinite parallel plate channel. The peaks in the circular channel is arranged differently compared to the infinite parallel plate channel.
In the circular channel the peaks are biggest for the point concentration in the middle see Fig. 4.2c) $r_0 = 0$(blue) and $r_0 = 0.25$(green) the peaks decreases for the point concentrations towards the wall $r_0 = 1$(dotted violet) this can be seen in Fig. 4.3a). In Fig. 4.3b) The time where the peak occurs versus the initial placement of the point concentration. The peaks occur earlier for the initial point concentration around the center, also due to the fact that the initial points around $r_0 < 0.5$ just converged towards their steady value. The relative size of the peak compared to the steady value is $100\%\,(\frac{9.43-9.33}{9.33}) = 1\%$ this is a bigger effect in the circular channel probably due to the wall encapsulating the fluid. This effect is not seen in the uniform concentration in the cross section and must be an effect due to spatial evolution of the concentration in the velocity field.
The point concentration located $r_0 > 0.5$ did really not experience any peak and also shown by the time which suits the time where the steady region is.

Proposing reasons for the peak in $D_{\text{eff}}^{\text{Point}}(r_0, t)$; more gradients are present in the circular geometry compared to the infinite parallel plates. The point in the middle Fig. 4.2c)$r_0 = 0$(blue) is diffusing out to new gradients and when the concentration has spread sufficiently in the r-direction. So before the concentration is uniform around the wall a peak will occur, due to the relative velocity of the center concentration and the concentration closer two the wall. When the concentration is uniform in the r-direction , the wall will

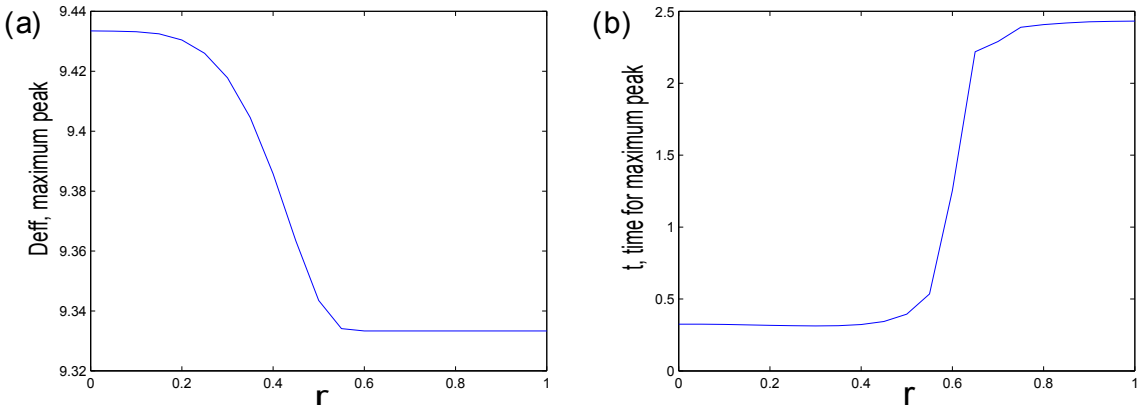

Figure 4.3: Steady flow with Pé = 20. (a) Maximum of $D_{\text{eff}}^{\text{Point}}(r_0, t)$ dependent on the initial placement of the point concentration in r_0. The maximum is biggest for the initial position of the concentration in the center and decreases towards the wall. Probably it is due to the initial point in the center reached the wall later with the concentration, not getting slow down with respect to the relative velocities. b)time t, to reach the maximum peak of $D_{\text{eff}}^{\text{Point}}(r_0, t)$ depending on the placement of the point concentration in r, note that the initial points located $r_0 > 0.6$ never experience a real peak in $D_{\text{eff}}^{\text{Point}}(r_0, t)$.

slow the spreading and make a small decrease in $D_{\text{eff}}^{\text{Point}}(r_0,t)$ as also discussed in chap. 3. This is my guess for the peak phenomena in the circular channel. The velocity field and the geometry of the gradients in the circular channel is probably more comparable to the rectangular geometry from the "Two-length-scale-cross sections" example in S. Vedel and H. Bruus [1]. Where the infinite parallel plate channel only has gradients in the z-direction. The effect of the wall and the gradients on $D_{\text{eff}}^{\text{Point}}(r_0,t)$ is very complex and a proposals has been made for the behaviour of the peaks.

4.7 Applied point concentration with only a single frequency flow $\epsilon_0 = 0$, $\epsilon_1 = 1$

There are overall three number in the equations you can change to get different dynamics, the Peclet number Pé, Womersley number Wo and Schmidt number Sc which is from the start fixed as $\text{Sc} = 10^3$. Now time-dependence occurs with respect to the oscillating flow and further complexity occurs when spatial dependence of placing the initial point concentration.

As long as the Womersley number is low, a parabolic shaped velocity field will occur for larger Womersley numbers a change of the shape will happen for the velocity profile and give rise to different velocity gradients and thereby different behaviour of $D_{\text{eff}}^{\text{Point}}(r_0,t)$. This can be seen in Fig. 4.4(a)-(c). In Fig. 4.4(a)$\text{Wo} = 0.72$(blue) the velocity profile is close to parabolic velocity profile. When the Wo is larger the profile changes shape, the maximum velocity moves out to the side and getting and a concave velocity shape in the center see $\text{Wo} = 3.9$(red). The oscillating effective diffusion $D_{\text{eff}}(t)$ will be represented in most of the figures as as envelope functions showing the maximum amplitudes in plus and minus of $D_{\text{eff}}(t)$.

When the solute-diffusion limit occurs at $\xi_{1,1}^2 = 14.6819 \ll \omega_{\text{o}}$ and for the Womersley number $0.1212 < \text{Wo}$. The time before the steady oscillating of $D_{\text{eff}}^{\text{Point}}(r_0,t)$ occurs earlier around $t \approx 0.068$ than for the steady flow around $1.6 < t$. Since diffusion has not got enough relaxation time in the oscillating period and the molecules are just pushed forth and back in the middle, as discussed in Reversal of flow in chap. 3. Since momentum diffusion has time to relax while $\omega_{\text{o}} < \alpha_{fl} = \text{Sc}\xi_{0,1}^2$, since the Schmidt number is $\text{Sc} = 10^3$ getting the values $\omega_{\text{o}} < 5.7831 \times 10^3$ and for the Womersley number $\text{Wo} < 2.4048$. This can be seen in Fig. 4.4(d) the reason for the increase in the amplitude of $D_{\text{eff}}^{\text{Point}}(r_0,t)$ is that the point concentration needs to be diffused out transversely Fig. 4.4(blue vertical line), before the concentration can be pushed forth and back. This can also be seen in the Fig. 4.4(d) because the steady period occurs around $t > 0.068$. This makes sense since the uniform distribution in the cross-sectional plane for high frequencies flow $\epsilon_0 = 1, \epsilon_1 = 1$ has no transient period for solute diffusion of $D_{\text{eff}}^{uniform}(t)$Fig. 4.4(c), but has a transient period for the momentum diffusion when $t < 1/\alpha_{fl}$. The uniform plane distribution and the point concentration converges towards the same values this can be seen in Fig. 4.4(c) versus (d) for $\text{Wo} = 0.72$ and Fig. 4.4(e) versus (f) for $\text{Wo} = 1.82$.

Changing the initial position r_0 of the point concentration gives similar result to the steady flow $\epsilon_0 = 1$ if the oscillating $D_{\text{eff}}^{\text{Point}}(r_0,t)$ is represented as an envelope function. As in the

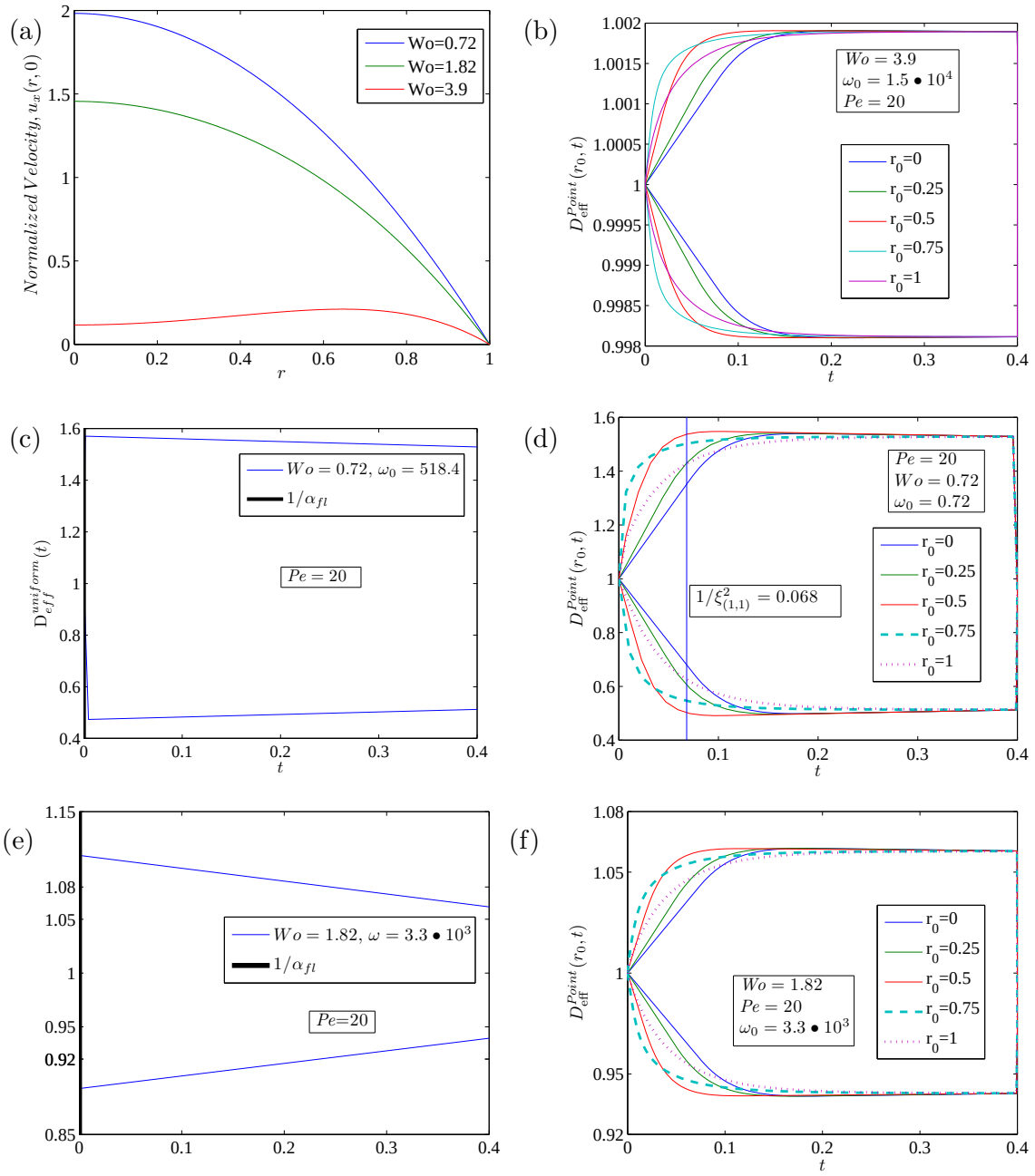

Figure 4.4: A harmonically oscillating flow, Sc = 1000, with amplitude $\epsilon_1 = 1, \epsilon_0 = 0$, Pé = 20 and varying the Womersley numbers Wo = 0.72, Wo = 1.82 and Wo = 3.9. Different initially placed point concentrations $r_0 = 0$(blue), $r_0 = 0.25$(green), $r_0 = 0.5$(red), $r_0 = 0.75$(turquoise) and $r_0 = 1$(violet). These are compared to the uniform concentrations in the plane with Womersley number Wo = 0.72 and Wo = 1.82. All the $D_{\text{eff}}(t)$ are represented with envelope functions and in the time region $0 \leq t \leq 0.4$.(a) Normalized velocity profiles at time $t = 0$ for Wo = 0.72(blue), Wo = 1.82(green) and Wo = 3.9(red). (b) A plot of $D_{\text{eff}}^{\text{Point}}(r_0, t)$ for $Wo = 3.9$, represented by an envelope function showing the maximum amplitude of the curves plotted in the time region $0 \leq t \leq 0.4$. (c) A plot of $D_{\text{eff}}^{uniform}(t)$ for $Wo = 0.72$. (d) A plot of $D_{\text{eff}}^{\text{Point}}(r_0, t)$ for $Wo = 0.72$.(e) A plot of the uniform distribution in the plane $D_{\text{eff}}^{uniform}(t)$ for $Wo = 1.82$.(f)A plot of $D_{\text{eff}}^{\text{Point}}(r_0, t)$ for $Wo = 1.82$.

steady flow the different behaviours for $\epsilon_0 = 0$, $\epsilon_1 = 1$ will be examined for the different time scales, The short time dynamic and peaks in $D_{\text{eff}}^{\text{Point}}(r_0, t)$.

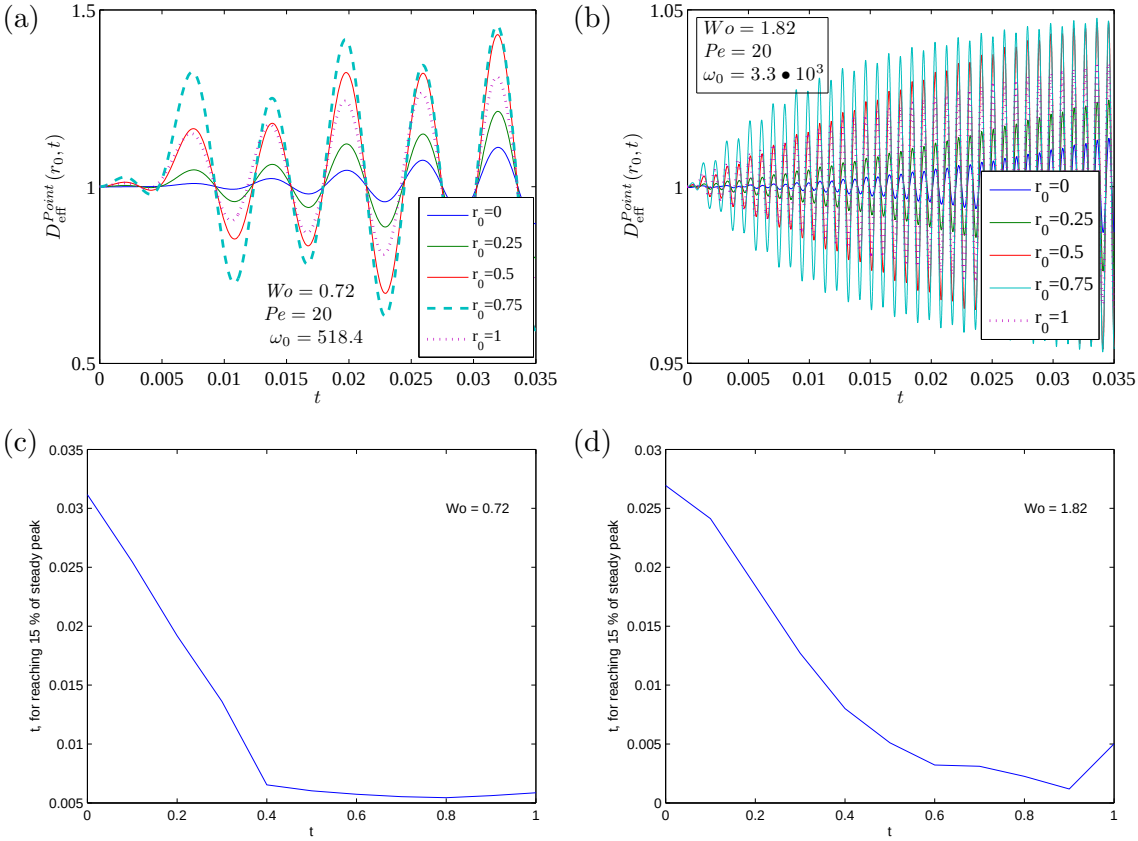

Figure 4.5: A harmonically oscillating flow, $\epsilon_1 = 0, \epsilon_0 = 1$, Pé = 20 and Sc = 1000. Different initial placements of the point concentration for $r_0 = 0$(blue), $r_0 = 0.25$(green), $r_0 = 0.5$(red), $r_0 = 0.75$(turquoise) and $r_0 = 1$(violet).(a)$D_{\text{eff}}^{\text{Point}}(r_0, t)$ for the five point concentrations with Wo = 0.72, The oscillation of the $D_{\text{eff}}^{\text{Point}}(r_0, t)$ can be seen, where $r_0 = 0$(blue) has the smallest amplitude. (b)$D_{\text{eff}}^{\text{Point}}(r_0, t)$ for the five point concentrations with Wo = 1.82.(c-d) Time for the transient to develop 15%$D_{\text{eff}}^{\text{Point}}(r_0, t)$, defined as $(D_{\text{eff}}^{peak}(\infty) - 1)0.15$ for $0 \ll r_0 \ll 1$, for the Womersley numbers Wo = 0.72 and Wo = 1.82, the time to reach 15% is longest for the initial point in the middle $r_0 = 0$, due to the low gradients in the velocity field. A slight change occur when Wo = 1.82, time larger to reach 15% and this is due to the change of the velocity profile.

4.7.1 Time, t for 15% increase in $D_{\text{eff}}^{\text{Point}}(r_0, t)$

The time to reach 15% of the effective diffusion without the molecular diffusions contribution is defined as $(D_{\text{eff}}^{peak}(\infty) - 1)0.15$. Looking at the short time dynamic in $0 \leq t \leq 0.03$ of the increase in $D_{\text{eff}}^{\text{Point}}(r_0, t)$, is dependent on the initial placement r_0 of the point concen-

tration. The Fig. 4.5(a)$z_0 = 0$(blue) has a very slow increase in $D_{\text{eff}}^{\text{Point}}(r_0, t)$ compared to Fig. 4.5(a)$z_0 = 0.75$(dotted turquoise)located closer to the wall and the velocity gradients. In the Fig. 4.5(c)-(d) the time for reaching 15% compared to the initial placement of the point concentrations r_0. The farther away from the center r_0 the faster the increase $D_{\text{eff}}^{\text{Point}}(r_0, t)$. This is because the point concentrations in the center start in smaller absolute gradients Fig. 4.4a) giving rise to a slow transient of effective diffusivity in the center. The center of mass is just pushed forth and back in the longitudinal direction until the concentration has diffused out to the gradient in the transverse direction. The point concentrations located close to the wall $0.4 \ll r_0$, reached 15% earlier, these point concentrations experience more shear in the short time $t < 0.07$. In the Fig. 4.4 (b-d) a peak can be seen around the time period $0.04 \leq t \leq 0.6$, these peaks are only present in the point concentrations located around certain initial placement from the center around $0.4 \leq r_0$.

4.8 Increasing the Womersley number

Increasing the Womersley number or frequency will decrease the width of the momentum diffusion from the wall $\lambda_d = \sqrt{\frac{\nu}{\omega}}$. giving rise to a wider region around the center where the gradients are low and an even slower increase of $D_{\text{eff}}^{\text{Point}}(r_0, t)$ would be expected for higher frequency and subsequently also the Womersley number.

4.8.1 Analyses of peak in the effective diffusivity of the single frequency flow $\epsilon_0 = 0$, $\epsilon_1 = 1$

Peaks are also present in the single frequency flow, they apparently, are located differently with respect to the initial placement of the point concentration than in the steady flow of the circular channel, peaks also occur for uniform distribution in the cross-sectional plane see Fig. 4.4(b). The peak is dependent on the Womersley number and the frequency since the velocity profile changes with increasing Wo. The proposal is, when the point concentration has diffused a certain amount and it lies in the high gradient but still has a high concentration it will give rise to peak in the effective diffusivity.

The peak appears for the point concentrations located around $0 \leq r_0 \leq 0.6$ see Fig. 4.6(d)-(f). The peak also moves with respect to the initial placement $r_0 = 0.53$ for $\text{Wo} = 0.72$ to increasing $r_0 = 0$ for $\text{Wo} = 3.9$, the moving of the peak seems reasonable since the velocity profile changes drastically shape see Fig. 4.4(a)(blue) compared to (red). How is not discovered yet.

4.8.2 Frequency contra Momentum diffusion

As seen in some of the earlier plots, the $D_{\text{eff}}^{\text{Point}}(r_0, t)$ decreases for higher frequencies this is because momentum diffusion from the wall cannot reach the fluid $\lambda_d = \frac{1}{\text{Wo}}$, thereby smaller velocity gradients are created and subsequently a smaller $D_{\text{eff}}^{\text{Point}}(r_0, t)$. I have chosen the

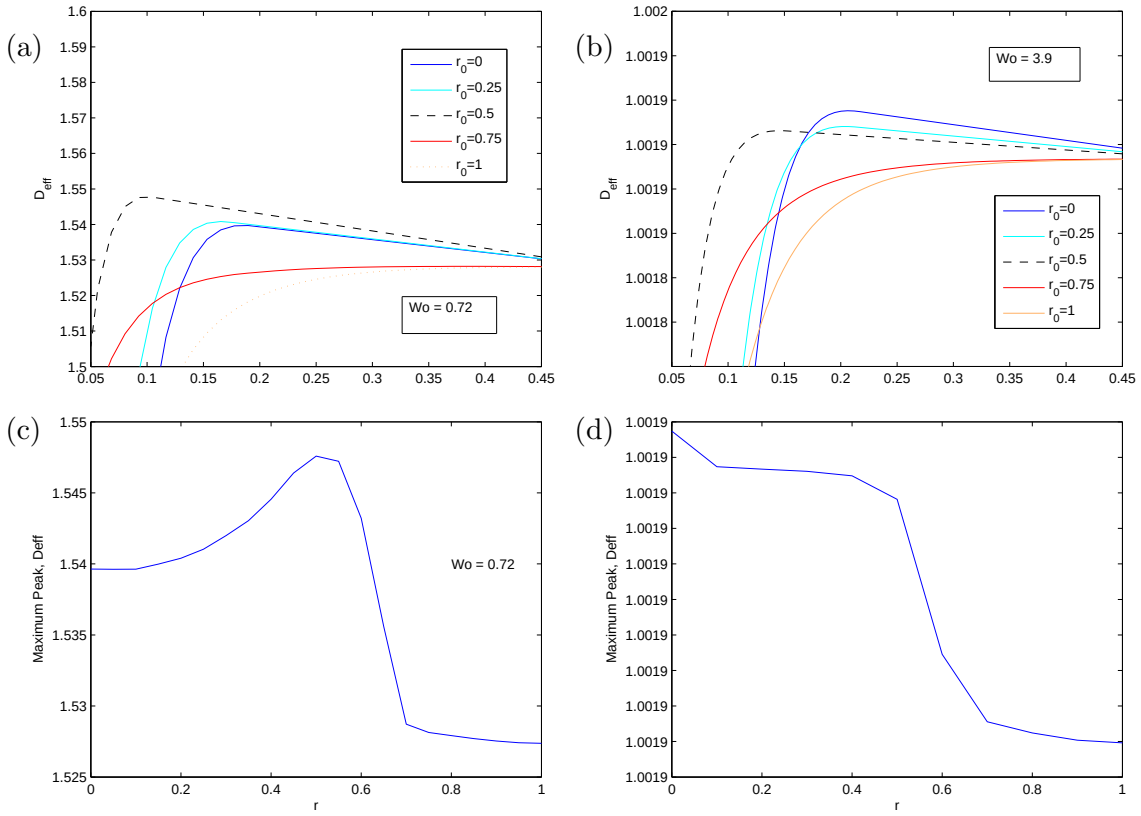

Figure 4.6: A harmonically oscillating flow, $\epsilon_1 = 1, \epsilon_0 = 0$ Sc $= 1000$, point concentration placed at $r_0 = 0$(blue), $r_0 = 0.25$(turquoise), $r_0 = 0.5$(black), $r_0 = 0.75$(red) and $r_0 = 1$(yellow) where Pé $= 20$. (a) Zoom in on the values of $D_{\text{eff}}^{\text{Point}}(r_0, t)$ where peaks occur versus the initial placements of the point concentrations, The initial point located at $r_0 = 0.5$ has the largest peak. (b)Plot of the peaks in $D_{\text{eff}}^{\text{Point}}(r_0, t)$ for the different initially located point concentrations with Womersley numbers Wo $= 0.72$(a) and Wo $= 3.9$(b), in the time region $0 \leq t \leq 0.45$. (c-d)The size of the peak in $D_{\text{eff}}^{\text{Point}}(r_0, t)$ versus the initial placement of the point concentration in r_0, for the Womersley numbers Wo $= 0.72$(c), Wo $= 3.9$(d). Note that the largest peak for Wo $= 3.9$ occur in the middle $r_0 = 0$, this is because they happen later than $t > 0.45$ and that why they do not appearing on the (b) plot.

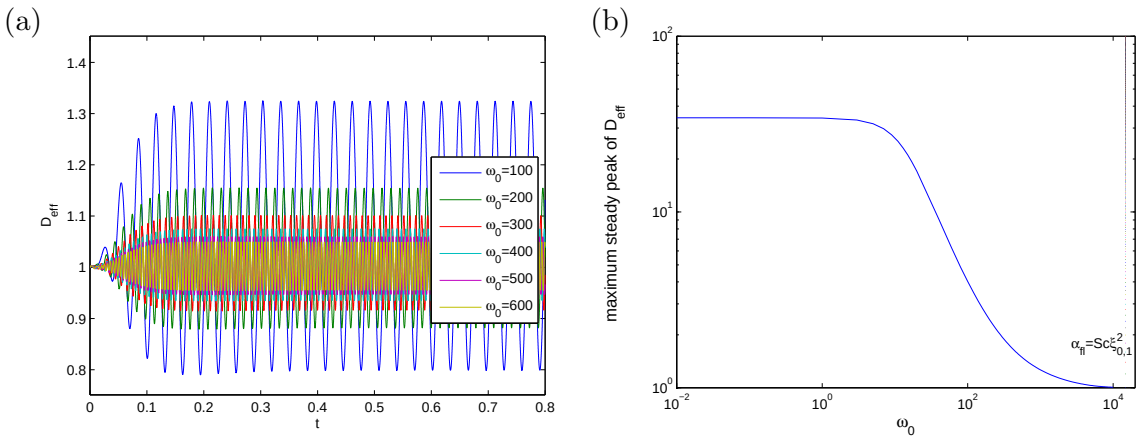

Figure 4.7: A harmonically oscillating flow, $\epsilon_1 = 0, \epsilon_0 = 1$, $z_{\text{loc}} = 0$ and Pé $= 20$. (a)Varying the frequencies $\omega_0 = 100$(blue) $\omega_0 = 200$(green) $\omega_0 = 300$(red) $\omega_0 = 400$(turquoise) $\omega_0 = 500$(violet) and $\omega_0 = 600$(yellow) in the time interval $0 \ll t \ll 0.8$, the amplitude of $D_{\text{eff}}^{\text{Point}}(r_0, t)$ is decreasing for increasing frequencyω_{o}. (b)A plot of the peak steady effective diffusivity versus the frequencies, where the dotted vertical blue line is the momentum diffusion α_{fl}.

steady state peak to measure the effective diffusivity $D_{\text{eff}}^{\text{Point}}(r_0, t)$ for the frequencies ω_{o}. For high frequencies, the pressure oscillation is so fast that the momentum diffusion does not have time to react, this happens at $\omega_{\text{o}} > \alpha_{fl}$ where $\alpha_{fl} = \text{Sc}\xi_{0,1}^2$[1].

4.8.3 Phase shift of $D_{\text{eff}}(t)$ for higher Womerley numbers

Phase shift was presented in the parallel plate and is also present in the cylinder case. In Fig. 4.9(d) phase shift in $D_{\text{eff}}^{\text{Point}}(r_0, t)$ occurs between the point concentrations initially located differently with respect to the velocity gradients. Phase shifts in $D_{\text{eff}}^{\text{Point}}(r_0, t)$ happens when the oscillation time gets shorter than the diffusion time for a point concentration to reach substantial velocity gradient. The phase shift can be seen in Fig. 4.9(d) for Wo $= 5$ where $r_0 = 0$(blue) is shifted compared to a point concentration located at the highest velocity gradient $r_0 = 0.9$(turquoise). In order of magnitude, phase shift will happen between the two point concentrations for example the point concentration in the middle $r_0 = 0$ and the point concentration located at the gradient $r_{\lambda_d} = 1 - \lambda_d$, when the diffusion has reached the velocity gradient $1 - \lambda_d = \sqrt{6t_{D_{\text{eff}}}}$ where $\lambda_d = \frac{1}{\text{Wo}}$ is the momentum diffusion length from the wall. The phase shift then happens when the diffusion time exceeds the first oscillation peak of the pressure $\frac{\pi}{\omega_0} < t_{D_{\text{eff}}}$.
This calculation has the following problem; it assumes that $1 - \lambda$ is a flat region and this only starts happens around Wo > 3 for Wo $= 5$ the phase shifts can be seen Fig. 4.9(d). When the point concentrations is located at $z_0 = 0.9$ in the highest gradient at the start $t = 0$ gives rise to the biggest increase in $D_{\text{eff}}^{\text{Point}}(r_0, t)$. Where $r_0 = 0$t(blue) curve in Fig. 4.9(d) is starting in the middle where the velocity gradients are small. Now phase shift was shown for the circular channel as also seen in the parallel plates. Since the

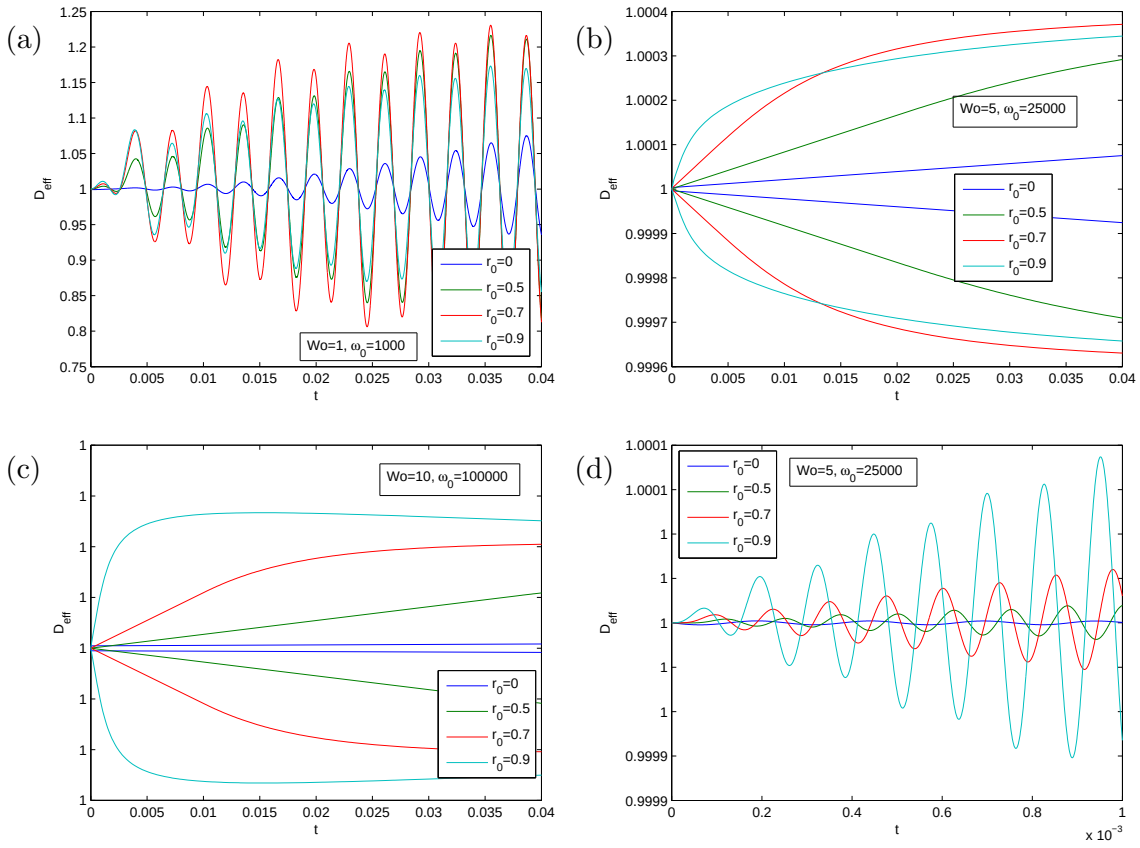

Figure 4.8: A harmonically oscillating flow with the frequency, Wo = 1, Wo = 5, Wo = 10 and Pé = 20 with 5 different points concentrations located at $r_0 = 0, 0.5, 0.7, 0.9$. (a)The 5 point concentrations with a Womersley number Wo = 1. (b)The 5 point concentrations with a Womersley number Wo = 5.(c)The 5 point concentrations with a Womersley number Wo = 10.(d)The 5 point concentrations with a Womersley number Wo = 5 zoomed in to the start $0 \leq t \leq 10^{-3}$ to see phase shift.

cylinder encapsulates the whole fluid, thereby inducing more shear and more reaction from the wall and giving more curvature to the velocity profile for smaller Wo numbers. Thereby phase shift also occur at lower Wo, since it depends on a long flat region in the middle. in Fig. 4.9 the same behaviour as in the infinite parallel plate channel is observed, though, the early peak starts to occur at lower Wo numbers for the point concentration initially located at the region of momentum diffusion. Since $\omega_0 = \mathrm{ScWo}^2$ because $\mathrm{Sc} = 10^3$ makes the frequencies higher and thereby the momentum diffusion limited at smaller Wo numbers.

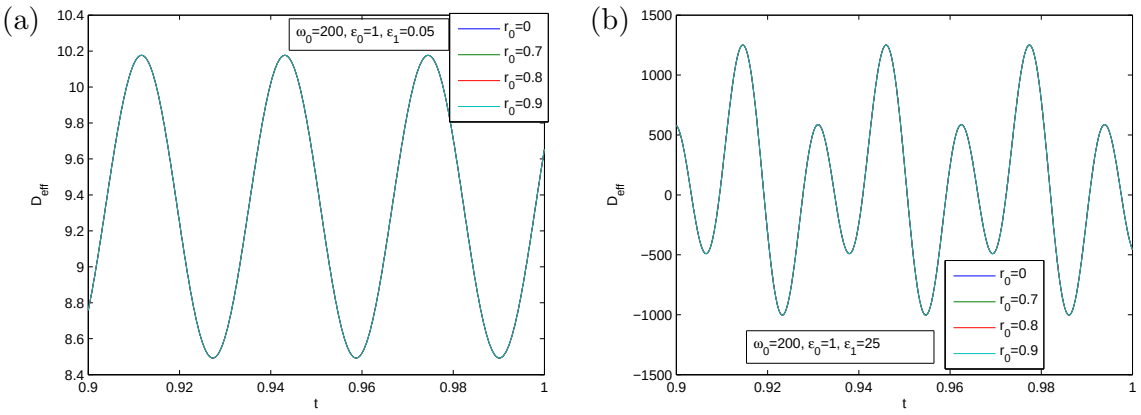

Figure 4.9: A harmonically oscillating flow superimposed on a steady flow with the frequency, $\omega_o = 200$ and Pé $= 20$. The initial four point has already converged. (a)oscillating flow superimposed on a steady flow $\epsilon_0 = 1$, $\epsilon_1 = 0.05$,The steady flow is dominating, so the oscillating part of $D_{\mathrm{eff}}^{\mathrm{Point}}(r_0, t)$ is only due to the oscillating flow.(c) Oscillating flow superimposed on a steady flow $\epsilon_0 = 1$, $\epsilon_1 = 25$, the period doubling occurs due to both contributions of the flow.

4.9 A harmonically oscillating flow superimposed on a steady flow and period doubling $\epsilon_0 = 1, \epsilon_1$.

Period doubling also occurs in the circular channel, here the oscillating flow amplitude was turned up compared to the steady $\epsilon_0 = 1$ from $\epsilon_1 = 0.05$ to $\epsilon_1 = 25$ to see the period doubling. This period doubling was observed in Fig. 4.9(a) to Fig. 4.9(b). The reason for period doubling is that the steady flow will take over and make an extra peak in $D_{\mathrm{eff}}^{\mathrm{Point}}(r_0, t)$, when the dominating oscillating flow is decreased to a low level of flow.

Complicated phase shifts could be imagined in many frequency flows due to different time-dependent gradient appears also with spacial change in the amplitude of the velocity profile. Funny peaks or double peaks could happen with the right combination of ϵ_1 and ϵ_0.

4.10 Concluding Remarks

Earlier results were reproduced to verify the implementation in Matlab. For the steady flow convergence towards the uniform concentration D_{eff} was obtained. A steady flow was first examined and the point concentration was located differently, the short time dynamic was similar to the infinite channel. The peak behaved differently than the infinite parallel plate channel both with regard to the initial point concentration and also where present at later time scales with respect to the diffusion rate.

For the oscillating flows the short time dynamic was similar to the steady flow of the circular channel, the peak in the single frequency flow behaved differently than the steady case.
The peak in the steady flow could be explained by, the initial point concentration in the center experiences most gradients before at last reaching the wall. This peak that occur later than the diffusion time also observed next in the non-Newtonian fluids with steady velocity field.

The peak in the oscillating flow could be explained by, the high concentration that are able to use the fasting changing gradients, before the diffusion time $t < \lambda_1$.

Chapter 5

Rheology and non-Newtonian fluids in a Cylinder

Rheology is the study of Non-Newtonian fluid where the fluid viscosity varies non linearly with the shear rate.
The Newtonian fluids have a linear relationship between shear stress and shear rate where the coefficient of proportionality is called the viscosity μ,

$$\tau_{rx} = \mu\dot{\gamma}_x = \mu\frac{\mathrm{d}v_x}{\mathrm{d}r}. \tag{5.1}$$

When the viscosity changes with the shear rate, the fluid is Non-Newtonian, this can been seen in ketchup or quick sand, which have shear thinning and shear thickening properties. Here the apparent viscosity η for the Non-Newtonian fluid is presented as the ratio of the shear stress to the shear, rate [31]

$$\eta(T, p, \dot{\gamma}) = \frac{\tau_{rx}}{\dot{\gamma}_x}. \tag{5.2}$$

Where the apparent viscosity η is dependent of temperature, pressure and shear rate. Normally when looking at complex fluids, the viscosity at certain shear rate is measured by viscometers. Viscometers in micro fluidics are also available and consist of magnetic beads that rotate within the fluid to measure the viscosity. Blood is a Non-Newtonian fluid which has shear thinning properties. Furthermore, blood exhibits yield stress depending on the hematocrit value, which is the volume fraction of blood. Yield stress is the minimum shear stress required to get the fluid moving. Above the yield stress and below the shear rate $100s^{-1}$ blood behaves as a Power law fluid, above the shear rate $100s^{-1}$ as a Newtonian fluid. This complex behaviour of blood is because the fluid consists of different components as white blood cells, red blood cells, proteins e.t.c. Blood is a two phase fluid consisting of an aqueous phase, that contains proteins, salt, sugar and is called the plasma. The second phase, is the cellular phase, which contains white blood cells, red blood cells and platelets[31]. The Casson model was derived to simulate a two-phase medium and adequately represents the rheology of blood. Blood exhibits yield stress depending on the

hematocrit value which is the volume fraction of blood. An approximation of the yield stress is [31],

$$\tau_0 \approx (Hct - Hct_c)^3 \tag{5.3}$$

where HCt varies dependent on your gender and the leverage you live in, typically men have 45% and women 40%. $Hct_c = 0.04$ is the critical level for the experience of yield stress of hematocrit. At low flow rates the velocity profile is flat, but at higher flow rates the velocity profile approaches the parabolic shape of the Newtonian fluid, this phenomena describes the Casson model. The constitutive equation for a Casson fluid is,

$$\sqrt{\tau} = \sqrt{\eta_N \dot{\gamma}} + \sqrt{\tau_0} \tag{5.4}$$

where η_N is the viscosity at high shear rates, where blood behaves as an Newtonian fluid.

5.1 The velocity profile for a Casson flow in cylinder

The velocitiy profile for a Casson flow is solved from Eq. (5.4), and these derivations comes from M. K. Sharp "Shear-Augmented Dispersion in Non-Newtonian Fluids".

$$u_0(r) = -\frac{1}{4\eta}\Delta p_0 \left(a^2 - r^2 - \frac{8}{3}r_c^{1/2}(a^{3/2} - r^{3/2}) + 2r_c(a-r)\right) \; r_c \le r \le a \tag{5.5a}$$

$$u_{0c}(r) = -\frac{1}{4\eta}\Delta p_0 \left(a^2 - \frac{8}{3}r_c^{1/2}a^{3/2} + 2r_c a - \frac{1}{3}r_c^2\right), \; 0 \le r \le r_c$$

Where the r_c region is determined by the yield stress from,

$$r_c = \frac{2\tau_y}{-\mathrm{d}p/\mathrm{d}x} \tag{5.6}$$

if the pressure is increased the r_c region is decreased and the velocity profile goes toward the parabolic Newtonian velocity profile. finding the mean velocity of the Casson fluid,

$$U_{char} = -\frac{1}{4\eta}\Delta p_0 \frac{1}{a^2}\int_{r_c}^{a} \mathrm{d}r 2r \left(a^2 - r^2 - \frac{8}{3}r_c^{1/2}(a^{3/2} - r^{3/2}) + 2r_c(a-r)\right) \tag{5.7}$$

$$- \frac{1}{4\eta}\Delta p_0 \frac{1}{a^2}\int_0^{r_c} \left(a^2 - \frac{8}{3}r_c^{1/2}a^{3/2} + 2r_c a - \frac{1}{3}r_c^2\right) \tag{5.8}$$

$$= \frac{1}{a^2 168\eta}\Delta p_0(-27r_c^4 + 48\sqrt{r_c}a^{7/2} - 21a^4 - 28r_c a^3)$$

and normalizing the velocity by dividing with the characteristic velocity U_{char} to find the nondimensionalized velocity profile and setting the tube radius to $a = 1$.

$$u(r) = -\frac{1}{U_{char}}\frac{1}{4\eta}\Delta p_0 \left(1^2 - r^2 - \frac{8}{3}r_c^{1/2}(1^{3/2} - r^{3/2}) + 2r_c(1-r)\right) \; r_c \le r \le 1 \tag{5.9}$$

$$u_c(r) = -\frac{1}{U_{char}}\frac{1}{4\eta}\Delta p_0 \left(1^2 - \frac{8}{3}r_c^{1/2}1^{3/2} + 2r_c 1 - \frac{1}{3}r_c^2\right), \; 0 \le r \le r_c$$

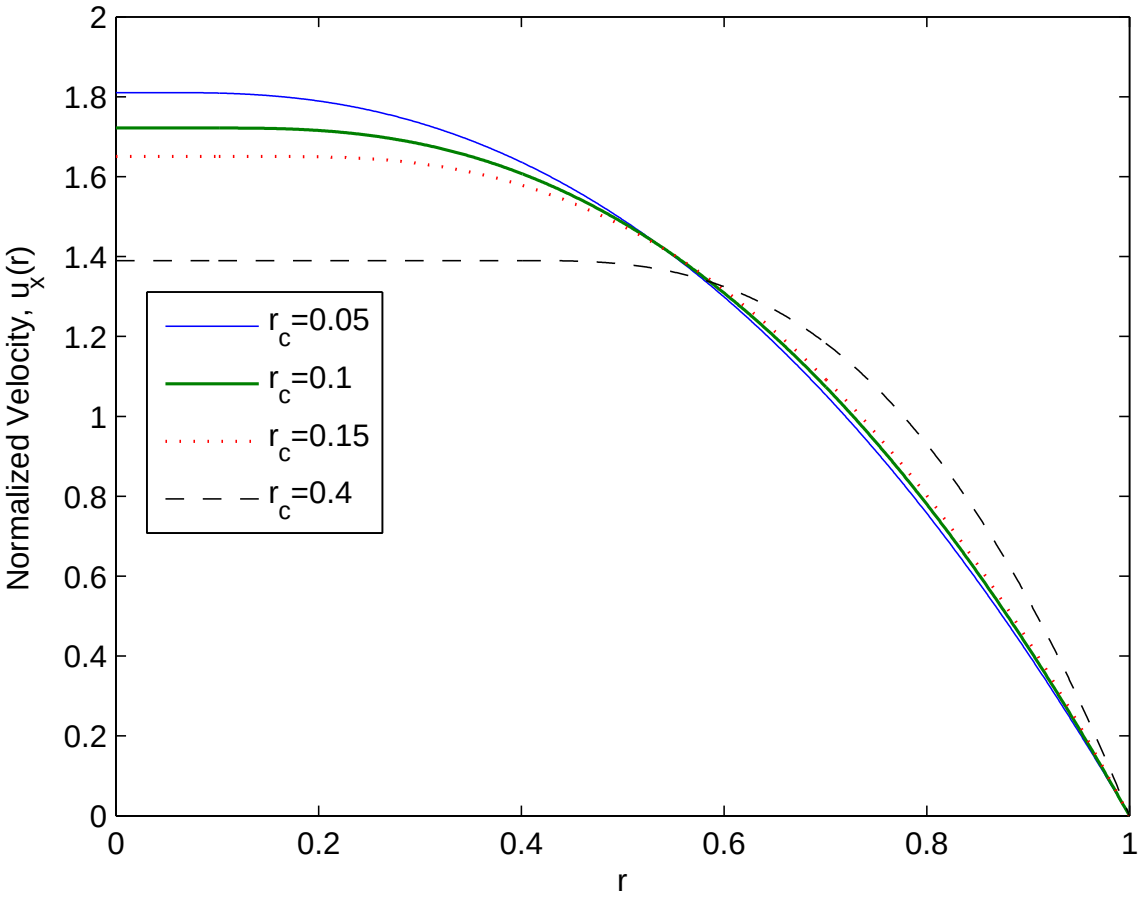

Figure 5.1: Cross sectional plot of the normalized velocity profile for the Casson fluid. (a)Velocity profile for the Casson fluid with $r_c = 0.05$, the profile looks similar to the parabolic velocity profile. (b)Velocity profile for the Casson fluid with $r_c = 0.1$. (c)Velocity profile for the Casson fluid with $r_c = 0.15$. (d)Velocity profile for the Casson fluid with $r_c = 0.4$. Notice that for larger rc the center becomes flat and the the region close to the wall gets big velocity gradients.

In the Fig. 5.1, different normalised velocity profiles are seen for the Casson fluid where the parameter r_c was varied. The Casson velocity profile changes shape dependent on r_c the larger r_c the longer the flat region see the blue curve $r_c = 0.4$. At low flow rates the velocity profile is more flat in the center having a larger r_c region. When the flow rates get higher, the profile reaches the parabolic shape of the Newtonian flow, see the black dotted line $r_c = 0.05$.

5.1.1 $D_{\text{eff}}^{\text{Point}}(r_0, t)$ for the Casson fluid

Applying the normalized the Casson fluid's velocity into the framework and getting the effective diffusion $D_{\text{eff}}^{\text{Point}}(r_0, t)$, this is straight forward since the normalized velocity profile just occurs in the bra-kets and setting the Peclet number to previous simulations Pé = 20. In Fig. 5.2 the $D_{\text{eff}}^{\text{Point}}(r_0, t)$ is shown for the four velocity profiles, where the point concentration is located at $z_0 = 0$(blue), $z_0 = 0.25$(turquoise), $z_0 = 0.5$(black dotted), $z_0 = 0.75$(red) and $z_0 = 1$(yellow dotted). Since the shape of the velocity changes for r_c so does the velocity gradients and thereby the $D_{\text{eff}}^{\text{Point}}(r_0, t)$. The smaller r_c the larger the gradients and thereby larger $D_{\text{eff}}^{\text{Point}}(r_0, t)$. For $r_c = 0.4$ has a significantly smaller $D_{\text{eff}}^{\text{Point}}(r_0, t)$ than $D_{\text{eff}}^{\text{Point}}(r_0, t)$ for $r_c = 0.05$. This is because the flat region does not induce shear and no velocity gradients are present in the r_c region, this do not increase the $D_{\text{eff}}^{\text{Point}}(r_0, t)$.

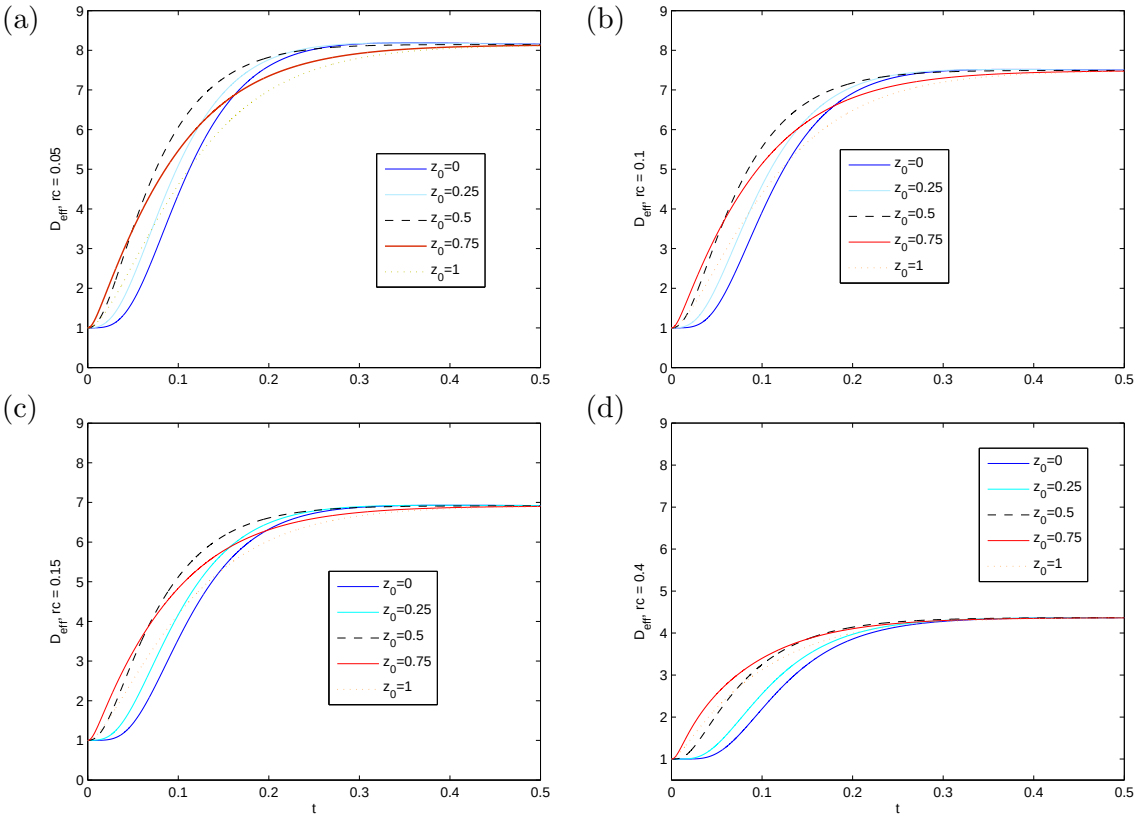

Figure 5.2: Changing the initial placement of the point concentration from 0 to 1, with 5 equally spaced points and where $z_0 = 0$(blue), $z_0 = 0.25$(turquoise), $z_0 = 0.5$(black dotted), $z_0 = 0.75$(red) and $z_0 = 1$(yellow dotted), where Pé = 20 and Sc = 10^3. (a) $D_{\text{eff}}^{\text{Point}}(r_0, t)$ for $r_c = 0.05$, here it converges very close to $1 + \text{Pé}^2/48$. (b)$D_{\text{eff}}^{\text{Point}}(r_0, t)$ for $r_c = 0.1$. (c)$D_{\text{eff}}^{\text{Point}}(r_0, t)$ for $r_c = 0.15$. (a)$D_{\text{eff}}^{\text{Point}}(r_0, t)$ for $r_c = 0.4$. Notice that the parabolic(small $r_c \approx 0$) gets larger $D_{\text{eff}}^{\text{Point}}(r_0, t)$ than the more flat profiles(higher r_c).

5.1.2 Comparing the r_c with respect to $D_{\text{eff}}^{\text{Point}}(r_0, t)$

Comparing the $D_{\text{eff}}^{\text{Point}}(r_0, t)$ for four different r_c values for a initial point concentration located at $z_0 = 0$ seeing that the smaller r_c gets bigger $D_{\text{eff}}^{\text{Point}}(r_0, t)$, this can be seen in Fig. 5.3(a) and (b). These behaviours are investigated in this Fig. 5.3(a). In Fig. 5.3(a) The curves have different transient behaviour dependent on the r_c value and the smaller the value of r_c, the faster the increase in the effective diffusion $D_{\text{eff}}^{\text{Point}}(r_0, t)$ happens and the larger steady value of $D_{\text{eff}}^{\text{Point}}(r_0, t)$. In Fig. 5.3(b) a zoom in on the curves in the transient period, here the blue curve $r_c = 0$ has a shorter flat region for $D_{\text{eff}}^{\text{Point}}(r_0, t)$ and the larger r_c the longer the flat region of $D_{\text{eff}}^{\text{Point}}(r_0, t)$. In Fig. 5.3(d) the time before $1 + 0.15(D_{\text{eff}}(t)^{steady}(\infty) - 1)$ is reached for the point concentration located $z_0 = 0$, here the larger r_c the longer the transient period and this is obvious since the time before the

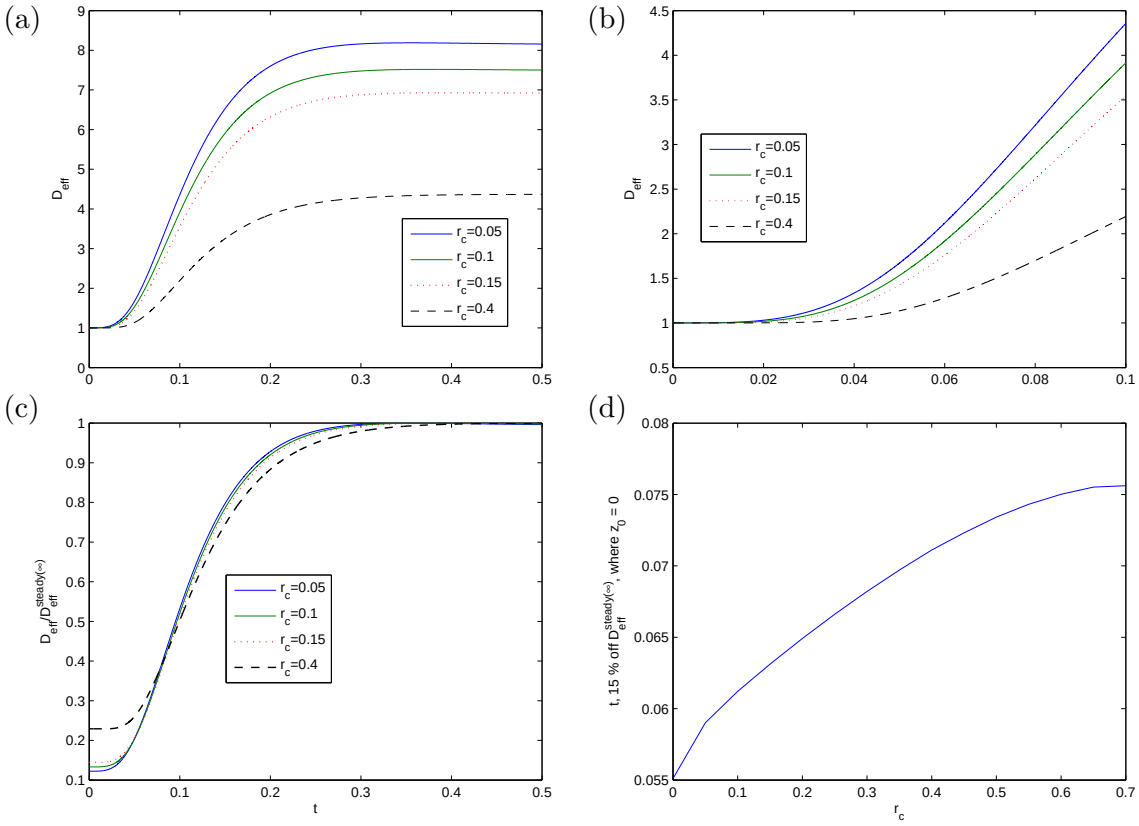

Figure 5.3: for a point concentration located in $z_0 = 0$, r_c is varied to see the effect on the $D_{\text{eff}}^{\text{Point}}(r_0, t)$ with Pé $= 20$ and Sc $= 10^3$. (a)The $D_{\text{eff}}^{\text{Point}}(r_0, t)$ for $r_c = 0.05$(blue), $r_c = 0.1$(green), $r_c = 0.15$(blue) and $r_c = 0.4$(black). (b) A zoom on the starting period $0 \ll t \ll 0.1$ for $r_c = 0.05$(blue), $r_c = 0.1$(green), $r_c = 0.15$(blue) and $r_c = 0.4$(black). (c) The $D_{\text{eff}}^{\text{Point}}(r_0, t)$ normalizes with the steady $D_{\text{eff}}^{\text{Point}}(r_0, t)/D_{\text{effSteady}}^{\text{Point}}(r_0, \infty)$ for the same value of r_c. (d) Changing the r_c value and finding the time to develop to 15% of the steady value $D_{\text{effSteady}}^{\text{Point}}(r_0, \infty)$.

concentration has diffused to the velocity gradient is longer.

5.1.2.1 Discussing of the Casson fluid

In this simulation the velocity profile is normalized, so when r_c gets smaller, the amplitude of the velocity profile is nearly the same as seen in Fig. 5.1. So the $D_{\text{eff}}^{\text{Point}}(r_0,t)$ will not get increased enough compared to simulating blood, since the amplitude of the velocity profile will increase when the pressure is increased, due to the Eq. (5.6), this would give rise to additional $D_{\text{eff}}^{\text{Point}}(r_0,t)$ for low r_c values.
In this example it is only the shape of the velocity profile that is investigated, and the smaller r_c the larger $D_{\text{eff}}^{\text{Point}}(r_0,t)$.
Converging towards $1+\text{Pé}^2/48 = 8.61$ when $r_c \to 0$ is assumed since $rc_0 = 0$ steady effective diffusion $D_{\text{effSteady}}^{\text{Point}}(r_0,\infty)$, is converging towards $1+\text{Pé}^2/48 = 8.61$ when $r_c \to 0$.

5.2 Power Law fluid

The velocity profile for the Power law fluid is from [31].

$$u_x(r) = \left(\frac{\Delta p}{2ml}\right)^{1/n}\left(\frac{a^{1+1/n}}{1+1/n}\right)\left[1-\left(\frac{r}{a}\right)^{1+1/n}\right] \tag{5.10}$$

the average velocity is the characteristic velocity U_{char} and where the characteristic length is chosen as $a = 1$.

$$U_{char} = \left(\frac{\Delta p}{2ml}\right)^{1/n}\left(\frac{1}{1+1/n}\right)\left(1-\frac{2}{1/n+3}\right) \tag{5.11}$$

and normalizing with U_{char},

$$u_x(r) = \epsilon_0 \frac{1}{\left(1-\frac{2}{1/n+3}\right)}\left[1-(r)^{1+1/n}\right] \tag{5.12}$$

shear thinning occur when $n < 1$ and this is the case for blood. Since the velocity profile is normalized with the average velocity, it is the shape of the velocity profile that determines the $D_{\text{eff}}^{\text{Point}}(r_0,t)$, The velocity profile for different ns Fig. 5.4(a), the larger the n the more linear velocity profile.

5.2.1 $D_{\text{eff}}^{\text{Point}}(r_0,t)$ for the Power law fluid

In Fig. 5.4(b-d) the $D_{\text{eff}}^{\text{Point}}(r_0,t)$ for different ns. The larger the n the larger the $D_{\text{eff}}^{\text{Point}}(r_0,t)$ will be for the point concentration placed at $z_0 = 0$. This can also be seen in Fig. 5.4(f) where the n are compared with respect to $D_{\text{eff}}^{\text{Point}}(r_0,t)$ for $r_0 = 0$.
In Fig. 5.4(d), for $n = 100$ a large peaks occur in $D_{\text{effPeak}}^{\text{Point}}(r_0,t_{peak})$, as in the the Newtonian fluid for point concentrations in the circular channel. They behave similarly, where

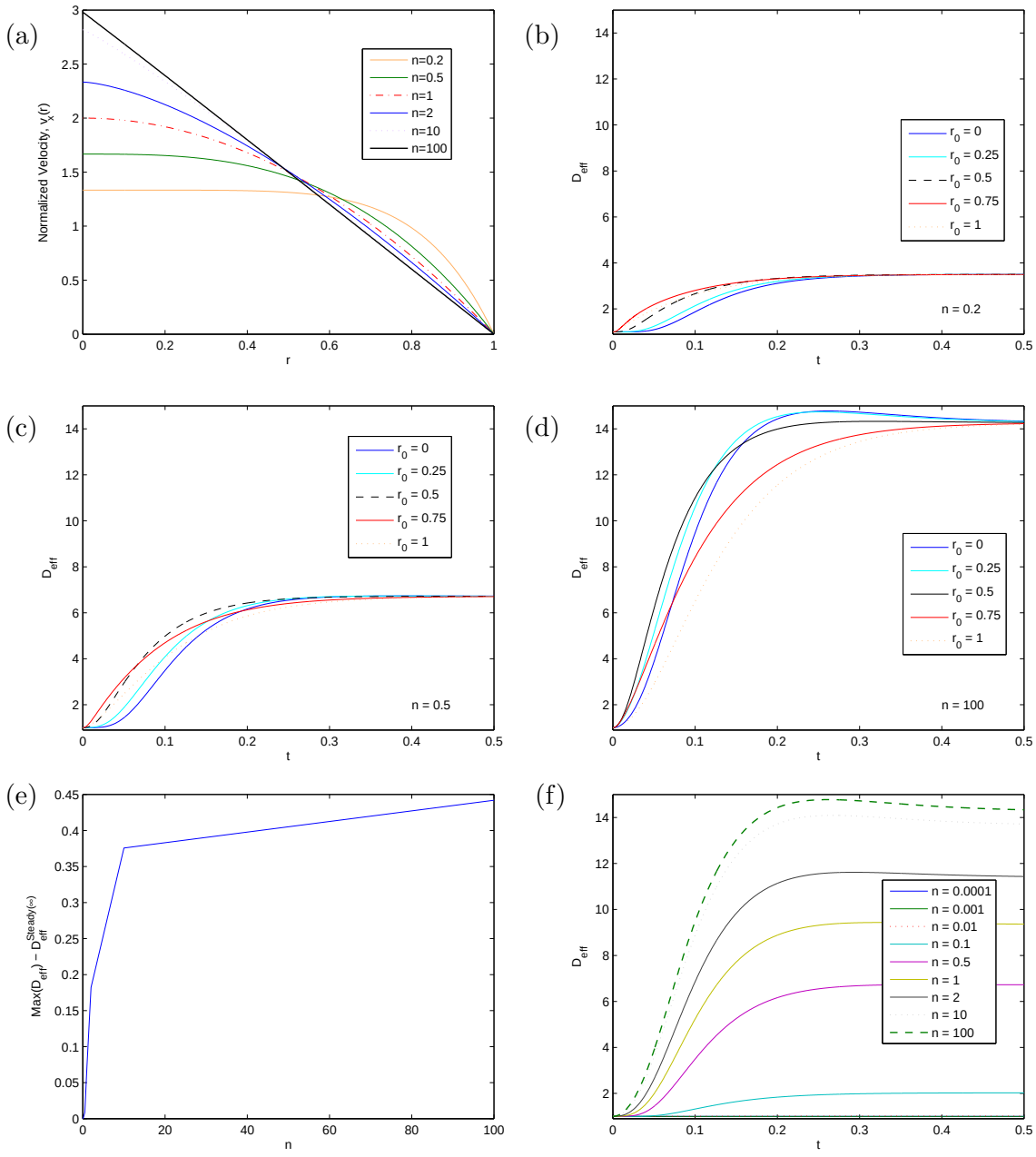

Figure 5.4: The Power law fluid where examined for different power of n where Pé $= 20$ and Sc $= 10^3$. (a)The velocity profile for different Power of n, the higher power n the more linear gradient. (b) The $D_{\text{eff}}^{\text{Point}}(r_0, t)$ for $n = 0.2$. (c)The $D_{\text{eff}}^{\text{Point}}(r_0, t)$ for $n = 0.5$. (d) The $D_{\text{eff}}^{\text{Point}}(r_0, t)$ for $n = 100$. (e) the maximum peak minus the steady effective diffusion $D_{\text{eff}}^{Peak} - D_{\text{effPeak}}^{\text{Point}}(r_0, t_{peak})$ versus the value of the power n of the fluid, the peak increases towards around 0.44 for $n \to \infty$. (f) The point concentration is located in $r_0 = 0$ where the $D_{\text{eff}}^{\text{Point}}(r_0, t)$ is plotted for different values of n for the time $0 \leq t \leq 0.5$, the larger power n the larger peak in $D_{\text{effPeak}}^{\text{Point}}(r_0, t_{peak})$ also relative to the $D_{\text{effSteady}}^{\text{Point}}(r_0, \infty)$.

the largest peak occur in the middle for the initial placement of the point, at least for power $1 \leq n$. In Fig. 5.4(e) the peaks for different powers can be seen and they increase with the power n. This is due to the gradients are present in more of the r direction when n is bigger. The biggest $D_{\text{eff}}^{\text{Point}}(r_0, t)$ will be for the highest n for the point concentration in the middle $z_0 = 0$. A table of the relative peak calculated, calculated as $(D_{\text{effPeak}}^{\text{Point}}(r_0, t_{peak}) - D_{\text{effSteady}}^{\text{Point}}(r_0, \infty))/D_{\text{effSteady}}^{\text{Point}}(r_0, \infty)$,

n	relative peak
0.0001	0
0.001	0
0.01	0
0.1	0
0.5	0.13%
1	0.77%
2	1.59%
10	2.74%
100	3.08%

The effect becomes significant around when $10 \lesssim n$ is large.

5.2.1.1 Discussing of the Power law fluid

when n is high the concentration will hit new gradients all the time, giving rise to a bigger $D_{\text{eff}}^{\text{Point}}(r_0, t)$. Because gradient will appear in a larger region of the r-direction. The point concentrations located in the middle have access to the new gradients for a long while the wall is hit and that is probably why the peaks occur later.

Intersection are also seen and behave similarly to the Newtonian fluid in the both the channel for the point concentration.

5.3 Concluding remarks

convergence towards $1 + \text{Pé}/48 = 8.61$ was expected and tested for both fluid and was obtained. In Fig. 5.4(e)$n = 1$(yellow) and In Fig. 5.2(a)$r_c = 0.05$ very close to $1+\text{Pé}/48 = 8.61$ as expected. Peak was observed and intersection between the point concentrations. Different constitutive equations have been giving for the description of blood; the Power Law fluid, the Casson fluid, Quemada model and the Carreau-Yasuda model. The Carreau-Yasuda model has shown to be the most promising model altough it needs numerical solvers as COMSOL. For different shear stresses there will be a different behaviour of $D_{\text{eff}}^{\text{Point}}(r_0, t)$ due to the shape of the velocity profile. An increase in $D_{\text{eff}}^{\text{Point}}(r_0, t)$ will also happen for higher shear stresses due to the increase in amplitude of the velocity profile. It was shown that the shape of the velocity profile would increase the $D_{\text{eff}}^{\text{Point}}(r_0, t)$ for the power of n increasing and decreasing $r_c \to 0$. But since we normalized, the behaviour of the amplitude of the velocity profile was not included in this model.

Where blood experiences shear thinning at lower flow rates, this will affect the effective diffusion, since at higher flow rates the velocity gradients and magnitude of the velocity will be greater. Where shear thinning decreases the effective diffusion due to lower velocity gradients in the center see 5.2.

Chapter 6

Conclusion

For the steady flow comparing to the uniform distribution in the cross-sectional plane in [1], the point concentration behaves differently in $D_{\text{eff}}^{\text{Point}}(z_0, t)$ and $D_{\text{eff}}^{\text{Point}}(r_0, t)$ due to the spatial dependence of the initial starting point of point concentration and the spatial arrangement of the gradients. The initial placement of the point concentration, determines the first phase of the behaviour of D_{eff} in the time period before the steady region. A more flat increase in effective diffusion D_{eff} for the point was present in the short time scales compared to the uniform cross section distribution. A linear phase in the point concentration was observed as in the uniform concentration for both the infinite parallel plate channel and circular channel. For the point concentration in the circular channel, the linear phase occur later around $t > 0.068$ when the solute had diffused transversely chap. 4. So when the point concentration was diffused out resembling the uniform concentration in the transverse direction the effective diffusion D_{eff} was similar. At last the steady region occur for the point concentrations where both the circular and the infinite parallel plate channel converged to $1 + \text{Pé}^2/48$ and $1 + 0.019\text{Pé}^2$ for all placements of the point concentrations the initial position.

For both the circular and infinite parallel plate the initial position of the point concentration gave rise to the same short time dynamic, which showed that the larger gradients the point concentration initially is placed, the larger increase in D_{eff}, unless a wall is present. The wall will reflect the molecules back to the same velocity and concentration field, thereby decreasing the effective diffusion $D_{\text{eff}}(t)$. The intersections of the initial point concentrations effective diffusion $D_{\text{eff}}^{\text{Point}}(z_0, t)$ was examined and the wall effect on this behaviour, for the infinite parallel plate channel.
Four models was made in the infinite parallel plate channel for $D_{\text{eff}}^{\text{Point}}(z_0, t)$ and these models showed some common features to the framework, as the relation of the initial starting position with respect to the gradient and the increase in $D_{\text{eff}}^{\text{Point}}(z_0, t)$.

Peaks in $D_{\text{eff}}^{\text{Point}}(r_0, t)$ occurred in the infinite parallel channel and the circular channels and also in the non-Newtonian steady flows in the circular channel. Peak was also present in the oscillating flows for these channels.

The peaks in the steady flows behaved differently for the circular and the infinite parallel plate channel, probably due to the geometry of the wall and the shear it produces.
The peak in the circular channel was shown to be biggest when the initial placement of the point was in the center. This was also the case for the non-Newtonian, where the peak was very large for the Power fluid with $n = 100$ around 10% of the steady value. The peak occurred late compared to the transverse diffusion time around $t_m athrmpeak = 0.28 \gg 0.068$.
Peaks in $D_{\text{eff}}^{\text{Point}}(z_0, t)$ was present for the steady flow in the infinite channel with a applied point concentration. These peak was a small effect around 0.1% of the steady effect and they also occurred later the than the transverse diffusion time around $t_m athrmpeak = 1.1 \gg 0.4$.

Peaks in the single frequency flow for the circular channel was present and moved towards the wall for higher Womersley numbers, due to the gradients moving that way too.
Peak in the single frequency flow for the steady flow in the infinite channel, was presented and a thorough analysis was done where it was shown that the maximum peak in $D_{\text{eff}}^{\text{Point}}(z_0, t)$ for initial point concentration follows the momentum diffusion length towards the wall, when the Womersley number is increased.

Phase shift was discovered between initial point concentrations located at large gradient compared to the region with small gradients. When the diffusion time to reach the large gradient was longer than the frequency of the flow, then phase shift will be discovered between the point concentrations, These effect was discovered in both channels.
So generally some new features was discovered and the short dynamic was clearified with respect to the initial placement of the point concentration. Peak in $D_{\text{eff}}(t)$ was observed and discussed, the linear phase and the convergence was common features to the uniform concentration in the cross-sectional plane. Negative values of $D_{\text{eff}}^{\text{Point}}(z_0, t)$ was discussed with respect to diffusion and momentum time and when it occurs. Phase shift and period doubling also occurred.

6.1 outlook and discussion of the project

Many effects were discovered and good suggestions were made to these effects. A more theoretical or mathematical treatment of these effect might have been appropriate, but due to the complexity of the phenomena and the frame work is was not possible in the time frame of this project. A more thorough investigation could have been made of the peak in D_{eff} where the rectangular channel was included and the gradient was studied with respect to geometry. The phase shift could have been investigated with respect to a combination of many oscillating flows and so could the peak.
Physiological Modelling of blood vessel and non-Newtonian fluid could have been made and predictions of the D_{eff} effects on the physiology. Comsol models of the Carreau-Yasuda rheological model could have been made and the D_{eff} could have been compared to the Powerlaw fluids and the Casson fluid.

Bibliography

[1] S. Vedel and H. Bruus, "Transient taylor-aris dispersion in time-dependent flows," *under review in J. Fluid Mech.*, 2011.

[2] G. I. Taylor, "Dispersion of soluble matter in solvent flowing slowly through a tube," *P Roy Soc Lond A Mat*, vol. 219, no. 1137, p. 186, 1953.

[3] R. Aris, "On the dispersion of a solute in a fluid flowing through a tube," *P Roy Soc Lond A Mat*, vol. 235, no. 1200, pp. 67–77, 1956.

[4] N. G. Barton, "On the method of moments for solute dispersion," *J Fluid Mech*, vol. 126, pp. 205–218, 1983.

[5] H. G. Harris and S. L. Goren, "Axial diffusion in a cylinder with pulsed flow," *Chem Eng Sci*, vol. 22, pp. 1571–1576, 1967.

[6] P. C. Chatwin, "On the longitudinal dispersion of passive contaminant in oscillatory flows in tubes," *J Fluid Mech*, vol. 71, pp. 513–527, 1975.

[7] E. J. Watson, "Diffusion in oscillatory pipe flow," *J Fluid Mech*, vol. 133, pp. 233–244, 1983.

[8] A. M. Thomas and R. Narayanan, "Physics of oscillatory flow and its effect on the mass transfer and separation of species," *Phys Fluids*, vol. 13, no. 4, pp. 859–866, 2001.

[9] K. M. Jansons, "On Taylor dispersion in oscillatory channel flows," *P Roy Soc Lond A Mat*, vol. 462, pp. 3501–3509, 2006.

[10] A. Mukherjee and B. S. Mazumder, "Dispersion of contaminant in oscillatory flows," *Acta Mech*, vol. 74, p. 107, 1988.

[11] S. Bandyopadhyay and B. S. Mazumder, "Unsteady convective diffusion in a pulsatile flow through a channel," *Acta Mech*, vol. 134, pp. 1–16, 1999.

[12] M. Latini and A. Bernoff, "Transient anomalous diffusion in Poiseuille flow," *J Fluid Mech*, vol. 441, pp. 399–411, 2001.

[13] R. Camassa, Z. Lin, and R. McLaughlin, "The exact evolution of scalar variance in pipe and channel flow," *Commun Math Sci*, vol. 8, no. 2, pp. 601–626, 2010.

[14] J. R. Womersley, "Method for the calculation of velocity, rate of flow and viscous drag in arteries when the pressure gradient is known," *J Physiol*, vol. 127, pp. 553–563, 1955.

[15] A. Vikhansky and W.Wang, "Taylor dispersion in finite-length capillaries. (2011) 642?649," *Chemical Engineering Science*, vol. 66, pp. 642–649, 2011.

[16] G. T. K. Rohlf K, "The role of the womersley number in pulsatile blood flow a theoretical study of the casson model," *J Biomech*, vol. Jan. 34, pp. 141–8, 2001.

[17] J. Boyd and J. M. Buick, "Comparison of newtonian and non-newtonian flows in a two-dimensional carotid artery model using the lattice boltzmann method vol. 52(20), pp. 6215–6228, 2007.

[18] H. Bruus, *Theoretical Microfluidics*. Oxford: Oxford University Press, 2008.

[19] A. S. J. L. D. M. L. M. P. G. V. Kaigala, V. N. Hoang and C. J. Backhouse, "An inexpensive and portable microchip-based platform for integrated rtpcr and capillary electrophoresis," *Analyst*, vol. 133, pp. 331–338, 2008.

[20] P. Augustsson, R. Barnkob, C.Grenvall, T. Deierborg, P. Brundin, H. Bruus, and T. Laurell, "Measuring the acoustophoretic contrast factor of living cells in microchannels.," *Proc. 14th MicroTAS*, vol. 14th, 2010.

[21] R. Barnkob, P. Augustsson, C. Magnusson, H. Lilja, T. Laurell, and H. Bruus, "Measuring density and compressibility of white blood cells and prostate cancer cells by microchannel acoustophoresis.," *submitted to Proc. 15th MicroTAS*, 2011.

[22] D. J. H. B. Søren Vedel, Savas Tay, S. R. Q.
to be presented at the workshop Signals, and D. A. . Space: Spatio-temporal patterns in simple bio system, Niels Bohr Institute, "Motile behavior of cells in social context," August 2011.

[23] M. E. Erdogan and P. C. Chatwin, "Effects of curvature and buoyancy on laminar dispersion of solute in a horizontal tube," *J Fluid Mech*, vol. 29, no. Part 3, pp. 465–484, 1967.

[24] P. C. Chatwin, "Initial development of longitudinal dispersion in straight tubes," *J Fluid Mech*, vol. 80, pp. 33–48, 1977.

[25] R. Sankarasubramanian and W. N. Gill, "Unsteady convective diffusion with interphase mass-transfer," *P Roy Soc Lond A Mat*, vol. 333, no. 1592, pp. 115–132, 1973.

[26] M. R. Doshi, P. M. Daiya, and W. N. Gill, "Three dimensional laminar dispersion in open and closed rectangular conduits," *Chem Eng Sci*, vol. 33, pp. 795–804, 1978.

[27] P. C. Chatwin and P. J. Sullivan, "The effects of aspect ratio on longitudinal diffusivity in rectangular channels," *J Fluid Mech*, vol. 120, pp. 347–358, 1982.

[28] C. van den Broeck, "A stochastic description of longitudinal dispersion in uniaxial flows," *Physica A*, vol. 112, pp. 343–352, 1982.

[29] M. S. Fallon, B. A. Howell, and A. Chauhan, "Importance of taylor dispersion in pharmacokinetic and multiple indicator dilution modelling," *Math Med Biol*, vol. 26, pp. 263–296, 2009.

[30] S. Vedel, L. H. Olesen, and H. Bruus, "Pulsatile microfluidics as an analytical tool for determining the dynamic characteristics of microfluidic systems," *J Micromech Microeng*, vol. 20, p. 035026, 2010.

[31] D. F. K. G. Truskey, F. Yuan, *Transport Phenomena in biological systems*. Pearson Prentice Hall, 2004.

Chapter 7

Matlab implementation of a point concentration for the $D_{\text{eff}}(t)$

The script for $D_{\text{eff}}^{\text{Point}}(z_0, t)$ in the infinite parallel plate channel

```
%clear all
%close all
%clc
%point source location
%zloc=0.62;funny curve
%zloc=0.9;
figure
hold off
%figure
yloc=0;
% Constants (Remember to adjust beta to the new constants)
pih=pi/2;
Sc=1e3;
%nu=10^(-6);
I=sqrt(-1);
epsvec=[1];%husk periode dobbling for zloc=0.5
Pe=20;
PeSqr=Pe^2;
mMax=20;
%Wo=1.82
Wo=0.72%sqrt(5/10^3);
omega0=Wo^2*Sc;%200;
%Wo=sqrt(omega0/Sc);%1/sqrt(5);
R=10;
%tmax=floor(omega0*50/pi);
%avr
%tvec= linspace(tmax-,tmax,1000);Davr=trapz(tvec,Deff)/tau=131.8146
tvec= linspace(0,2,5000)%floor(omega0*30))%ceil(omega0*1/(2*pi)));

%tvec=logspace(-3,0,1000);
```

```
SaveData2File=0;

% END OF USER INPUT!!
count=0;
%Derived constants
NumHarm=length(epsvec)-1;
Iomg0=omega0*I;

anullar=sqrt(Sc/omega0)
Position=0:0.25:1;
sizePosition=size(Position);
Deff=zeros(sizePosition,length(tvec));
for zloc=Position
%Variables used for summing in loop's
count=1+count;
%for M1
M1=0;
%linear time term in M1
M1t=0;
%Steady term for M1 still decaying
M1Steady=0;

%for dM1/dt
ddM1dt=0;

%steady decaying term for dM1/dt when m different from zero
%(m~=0 && l==0)
ddM1dtSteady=0;

%multiply them... M1*dM1/dt


%1/2*dM2/dt
hM2=0;
hM2t=0;

%--------------------------
%Vector's

%to compare the M's
M1vector=zeros(1,length(tvec));
M1dddM1dtvector=zeros(1,length(tvec));
M2vector=zeros(1,length(tvec));
%see linear time terms and compare for ..M2. and ..M1.
M1t=zeros(1,length(tvec));
M2t=zeros(1,length(tvec));
%IMPORTANT vectors


```

```
80
81  %Braket vectors
82  ulh0m=zeros(mMax,NumHarm*2+1);
83  gamma1=zeros(1,mMax);
84  %betanmj
85  betalmj=zeros(NumHarm,mMax,mMax);
86
87  %Vectors for constant's
88  a0=zeros(mMax,mMax);
89  a1=zeros(1,mMax);
90
91  %----------z dismonsionless coordinet -1<=z<=1
92  %z is numerical points used for the integration of brackets
93  dz=1/(mMax*100);
94  z = -1:dz:1;
95  sizez=size(z);
96  %--------------velocity field
97
98
99  u=zeros(NumHarm,sizez(1,2));
100 for l=0:NumHarm
101     if(l==0)
102         %u0(z)
103         u(1,:)=3/2*epsvec(1)*(1-z.^2);
104     else
105         %ul(z)
106         k=sqrt(-I*l*Wo);
107         u(l+1,:)=3*epsvec(1+abs(l))/(k^2)*(cos(z*k)/cos(k)-1);%just
                conj=>-l..
108     end
109
110 end
111
112 % figure
113 %  plot(z,real(u(1,:)))
114
115
116 %-------------Basis Function
117 %finding all h(m+1,:) for the interval of z
118 h=zeros(mMax,sizez(1,2));
119 for m=0:mMax
120     %husk forskydning af m
121     h(m+1,:)=cos(pih*m.*(1+z))*sqrt(2/(1+KroneckerDelta(0,m)));
122 end
123
124 %---------------Eigenvalues
125 %Sorting the lambdaa's for size
126
127 %lambdaaSort=zeros((mMax*2)^2,3);
```

```
%first column, value lambdaa, second column n value, third column m value
%creating eigenvalues
% counter=1;
% for n=0:(mMax*2-1)
%     lambdaan=(n*pih/R)^2;
%     for m=0:(mMax*2-1)
%
%         lambda(1,m+1)=(m*pih)^2;
%
%         lambdaaSort(counter,2)=n;
%         lambdaaSort(counter,3)=m;
%         lambdaaSort(counter,1)=lambda(1,m+1)+lambdaan;
%         counter=1+counter;
%     end
% end
% lambdaaSort=sortrows(lambdaaSort);
%-------------------------------------------------------


%---------lambdaa/eigenvalues
%finding eigenvalues, only needed in z-direction
lambda=zeros(1,mMax);
for m=0:mMax-1
    %husk forskydning af m
    lambda(1,m+1)=(m*pih)^2;
end
%---------------------------------------

%------------Calculating a0
for n=0:mMax-1
    for m=0:mMax-1
        %multi with 2?????????,see hm also!!!
        a0(n+1,m+1)= (cos(n*pih*(1+yloc/R))*cos(m*pih*(1+zloc)))*2/sqrt((1+KroneckerDelta(n,0))*(1+KroneckerDelta(0,m)));
    end
end

%-----------------------------------------------------------------

%-------------------Beta and a1
%Calculating everything that contains beta. Now a1(n,m)=a1(0,m) and beta used in M2
%change a1 and beta...
Suma1=0;

%n=0 since 1/2dM2/dt ..<u_k | gn hm> => gn=0..See later
for m=0:mMax-1
    Suma1=0;
```

```
    for j=0:mMax-1

        for l=0:NumHarm
            if(KroneckerDelta(m,j)*KroneckerDelta(l,0)==1)
                beta=0;
            else
                betafrac=(1)/(lambda(1,m+1)-lambda(1,j+1)+Iomg0*l);
                beta = betafrac*trapz(z,h(j+1,:).*u(l+1,:).*h(m
                   +1,:))/2;
            end
            betalmj(l+1,m+1,j+1)=beta;
            if(l>0)
                Suma1=Suma1 - a0(1,j+1)*2*real(beta);   %beta(l,n,m
                   ,k,omega0,epsvec);
                %betalmj, k is harmonics, m and j is basis indexs.
            else
                Suma1=Suma1 - a0(1,j+1)*beta;
            end
        end % l-loop ends

    end %j-loop ends
    %a1 have a value for each m,where n=0
    a1(1,m+1)=Suma1;
end %m-loop ends


%finding  gamma1 =<fnm|u_0|fnm> and the  bra-ket <ul|f0m>
for m=0:mMax-1
   %gamma1 = <fnm | u_0 | fnm>=
    %<hm | u_0 | hm>
    %normalising
    gamma1(m+1)=trapz(z,h(m+1,:).^2.*u(1,:))/2;
    for l=0:NumHarm
            ulh0m(m+1,l+1) = trapz(z,conj(u(l+1,:)).*h(m+1,:))/2;
    end %l-loop ends
end %m-loop ends
%-----------------------------------
%Ending  gamma1 =<fnm|u_0|fnm> and <ul|f0m> bracket


%
    ------------------------------------------------------------------------


%
    %%%%%%%%%%%%%%%%%%%%%%%%%%%%%%%%%%%%%%%%%%%%%%%%%%%%%%%%%%%%%%%%%%%%%%%


%starting calculating Deff for different times
%
```

```
    %-------------------------------------------------------------------------

%
    %%%%%%%%%%%%%%%%%%%%%%%%%%%%%%%%%%%%%%%%%%%%%%%%%%%%%%%%%%%%%%%%%%%%%%%%

%starting calculating Deff for different times
for tt=1:length(tvec)
    t=tvec(tt);
    Iomg0t=Iomg0*t;

    if(tt>2)
        disp(['Time ' num2str(t) ' Step #' num2str(tt-1) ' of '
           num2str(length(tvec)-1) ' sum ' num2str(Deff(1,tt-1))])
    end

    %
        %---------------------------------------------------------------------

    %first calculating M1 and M1/dt
    %using dM1/dt and M1 summing variables

    %M1 summing
    M1=0;
   %dM1/dt summing variables
    dM1dt=0;
    %using (1-e^(-q)t)/..=t
    %m=0, l=0
    M1=a0(1,1)*ulh0m(1,1)*t;
    for m=0:mMax-1
        lambdat=(lambda(1,m+1))*t;
        %l=0
        %dM1/dt
        dM1dt=dM1dt+a0(1,m+1)*ulh0m(m+1,1)*exp(-lambdat);  %+Iomg0*
           l)*t);
        %steady state term, still decaying
        if(m>0)
            M1=M1+a0(1,m+1)*ulh0m(m+1,1)*(1-exp(-lambdat))/(lambda
               (1,m+1));%(1-exp(-(lambda(1,m+1)+Iomg0*l)*t))/(
               lambda(1,m+1)+Iomg0*l);
        end
        %l>0
        for l=1:NumHarm
            lambml=lambda(1,m+1)+Iomg0*l;
            expmlt=exp(-lambml*t);
            a0ulhm=a0(1,m+1)*ulh0m(m+1,1+l);
            %dM1/dt oscillations
            %oscillations
            dM1dt=dM1dt+2*real(a0ulhm*expmlt);
```

```
256             %M1
257             %oscillations,
258             M1=M1+2*real(a0ulhm*(1-expmlt)/lambml);
259         end %l-loop ends
260
261     end %m-loop ends
262 %
263 %       %saving value for M1*dM1/dt
264     M1ddM1dtvector(1,tt)=(M1)*(dM1dt);
265 %       M1vector(1,tt)=M1;
266 %       dM1dtvector(1,tt)=dM1dt;
267 %
268 %
269
270     %-------------------------------------------------------------
271     %starting calculating dM2/dt
272   summ=0;
273   for m=0:mMax-1%k-loop for beta and NOT FOR M1-dM/dt
274
275       %k sum
276       sumk=ulh0m(m+1,1);%k=0
277       for k=1:NumHarm
278           sumk=sumk+2*real(ulh0m(m+1,k+1)*exp(-Iomg0t*k));
279       end % end k-loop
280
281       %j-sum
282       sumj=0;
283       for j=0:mMax-1
284
285           %l-sum
286           suml=betalmj(1,m+1,j+1);%l=0
287           for l=1:NumHarm
288               suml = suml + 2*real(betalmj(l+1,m+1,j+1)*exp(Iomg0t*
                      l));
289           end %end l-loop
290           suml=a0(1,j+1)*suml;
291
292           if(j==m)
293               sumj=sumj+(suml+(a0(1,m+1)*gamma1(m+1)*t+a1(1,m+1)))*
                      exp(-lambda(1,j+1)*t);
294           else
295               sumj=sumj+suml*exp(-lambda(1,j+1)*t);
296           end
297           %hM2=hM2+exp(-lambda(1,j+1)*t)*ulhmexp*(Sum2+Sumbeta);
298       end % end j-loop
299
300       summ=summ+sumk*sumj;
301   end %end m-loop
302
```

```
303     hM2=summ;
304
305
306
307     M2vector(1,tt)=hM2;
308     %------------------------------ending M2
309
310
311     Deff(count,tt)=1 + PeSqr*(hM2-M1*dM1dt);
312
313
314     %resetting the sums for the new time calculation
315
316
317
318 end %t-loop ends ------------------
319
320
321 %
        ------------------------------------------------------------------------
322 %
        %%%%%%%%%%%%%%%%%%%%%%%%%%%%%%%%%%%%%%%%%%%%%%%%%%%%%%%%%%%%%%%%%%%%%%
323 %loglog(tvec,Deff)
324 %semilogx(tvec,Deff)
325 % x = tvec; y = Deff(count,:);
326 %
327 % k = convhull(x,y);
328 % plot(x(k),y(k))
329
330 plot(tvec,Deff(count,:))%/Deff(length(Deff)))
331 xlabel('t')
332 ylabel('D_{eff}')
333 hold all
334 deffpoint{count}=['z_0=' num2str(zloc)];
335 % hold on
336 % plot(R^2/10^(-9),linspace(min(Deff),max(Deff),50),'--')
337
338 end% end zloc loop
339 legend(deffpoint,0)
340 %plot(1/(1*pi/2)^2,linspace(min(Deff),max(Deff),50),'--')
341 %plot([0 tvec(length(tvec))],[1 1],'--')
342 %
343 % if NumHarm>1
344 %     title([num2str(NumHarm) ' harmonics, Sc = ' num2str(Sc) ', Wo
        = ' num2str(Wo) ', R = ' num2str(R)])
345 % else
346 %     title([ 'Sc= ' num2str(Sc) ', Pe=' num2str(Pe)])
```

```
% end

%
% tvec= linspace(0,0.0005,ceil(omega0*1/(2*pi)));
% figure
% plot(tvec,real(exp(I*omega0*tvec)))
% hold on
% tvec= linspace(0,0.0005,ceil(omega0*10/(2*pi)));
% plot(tvec,real(exp(I*omega0*tvec)))

figure
plot(tvec,0+ PeSqr*(M2vector),'--rs')
hold on
plot(tvec,0+ PeSqr*(-M1ddM1dtvector),'--bs')

plot(tvec,Deff)
```

The script for $D_{\text{eff}}^{\text{Point}}(r_0, t)$ in the circular channel

```
clear all
 close all
% clc
%cylinder
%placement
% Constants (Remember to adjust beta to the new constants)
    pih=pi/2;
    Sc=1e3;
    nu=10^(-6);
    I=sqrt(-1);
    epsvec=[1 50];
    Pe=20;
    PeSqr=Pe^2;
    mMax=40;
    Wo=1/(10^(3/2));%0.72%1/sqrt(5);
    R=5;

    %tvec= linspace(0,1,1000);
    SaveData2File=0;

    % END OF USER INPUT!!

    %Derived constants
    NumHarm=length(epsvec)-1;
    omega0=Wo^2*Sc;
    Iomg0=I*omega0;

    %Variables used for summing in loop's

    %for M1
    M1=0;
```

```
33
34      %for dM1/dt
35      dM1dt=0;
36      %1/2*dM2/dt
37      hM2=0;
38
39      %IMPORTANT vectors
40      %Deff=zeros(1,length(tvec));
41
42
43      %the first have more than pi 3.14 in distance, easier just to
            input value
44      %lambd(1,1)=3.83170597020751;
45      %lambd(1,2)=7.01558666981561;
46      %lambd(1,3)=10.1734681350627;
47      xi=zeros(1,mMax);
48      bessj1 = inline('besselj(1,x)');
49      xi(1,1)=0;
50      for m = 1:mMax-1
51          xi(1,m+1) = fzero(bessj1,[m-1 m]*pi+[0.8 0.8]);
52      end
53
54      %---------------------------------------
55
56      %---------------------------------------
57      %z is numerical points used for the integration of brackets
58      %dependent on mMax
59      r = 0:1/(mMax*100):1;
60      %finding all R(m+1,:) for the interval of z
61      sizer=size(r);
62      R=zeros(mMax,sizer(1,2));
63      %f index is push one to the right
64      R(1,:)=ones(1,sizer(1,2));
65      for m=1:mMax-1
66          %husk forskydning af m
67          R(m+1,:)=besselj(0,r.*xi(1,m+1))/besselj(0,xi(1,m+1));
68      end
69      %trapz(r,r.*R(5,:).*R(5,:))*2=1
70      %check bessel roots
71      %close all
72      %plot(r,R(4,:))
73      %---------------------------------------
74      lambda=zeros(1,mMax);
75      lambda(1,1)=0;
76      for m=1:mMax-1
77          lambda(1,m+1)=xi(1,m+1)^2;
78      end
79
80
```

```
81
82
83      %----------- the velocity fields
84      u=zeros(NumHarm,sizer(1,2));
85      k=zeros(1,NumHarm);
86      %steady Veloctiy
87      u(1,:)=2*epsvec(1)*(1-r.^2);
88      %oscillating Velocity
89      for l=1:NumHarm
90          k(l)=sqrt(-I*l*Wo^2);
91          u(l+1,:)=8*epsvec(1+l)/(k(l)^2)*(besselj(0,r*k(l))/besselj
                (0,k(l))-1);
92      end
93      %plot(r,real(u(2,:)));
94      %----------gamma1=<fnm|u_0|fnm>
95
96      %finding  gamma1 =<fnm|u_0|fnm> and <ul|f0m> bracket
97      for m=0:mMax-1
98          %gamma1 = <fnm | u_0 | fnm>=
99          %<hm | u_0 | hm>
100         gamma1(m+1)=2*trapz(r,r.*u(1,:).*R(m+1,:).^2);%.*R(m+1,:));
101         %Bra-ket <u_l|Pih_n=0 Rm>
102         %first <u_0| Rm>
103         %ulRm(m+1,1) = 2*trapz(r,r.*R(m+1,:).*u(1,:));
104         %Test for l=0 and m not 0
105         %           if(m~=0)
106         %               ulRm(m+1,1);
107         %               -8/(xi1(1,m+1)^2);
108         %           end
109
110         %Next <u_l| Rm>
111         for l=0:NumHarm
112             %<ul|Rm>
113             ulRm(m+1,l+1) = 2*trapz(r,r.*conj(u(l+1,:)).*R(m+1,:));
114             %Test
115             %               if(m>0)
116             %                   ulRm(m+1,l+1);
117             %                   -epsvec(l+1)*16/((xi1(1,m+1)^2-k(l)
                    ^2)*k(l))*besselj(1,k(l))/besselj(0,k(l));
118             %               end
119         end %l-loop ends
120     end %m-loop ends
121
122     %-------------------------------------
123     %Ending  gamma1 =<fnm|u_0|fnm> and <ul|f0m> bracket
124 %tperiod=5*pi/omega0;
125 tvec= linspace(0,1,5000)%omega0*50/pi)%linspace(0,tperiod,200)%
        omega0*40/pi)%floor(omega0*40/pi));
126 count=0;%used in plot
```

```
127 Position=[0 0.5]%:0.25:1;%0:0.2:1
128 sizePosition=size(Position);
129 Deff=zeros(sizePosition,length(tvec));
130 for rloc=Position
131     count=1+count;
132     %-----------------------------------------------------------------
133     %Calculating a0(n=0,m)
134     a0=zeros(1,mMax);
135     for n=0:mMax-1
136 
137         a0(1,n+1)= besselj(0,rloc*xi(1,n+1))/besselj(0,xi(1,n+1));
138 
139     end
140 
141 %-----------------------------------------------------------------
142     %beta
143     %Calculating everything that contains beta. Now a1(n,m)=a1(0,m)
        and beta used in M2
144     %change a1 and beta...
145     Suma1=0;
146     for m=0:mMax-1
147         Suma1=0;
148         for j=0:mMax-1
149             for l=0:NumHarm
150 
151                 %(1-KroneckerDelta(m,j)*KroneckerDelta(l,0))<fnm|ul
                    |fpj>/(xi1
152                 %(1,m+1)-xi1(1,j+1)+I*l*omega0)
153                 %betafrac=(1-KroneckerDelta(m,j)*KroneckerDelta(l
                    ,0))/(xi1(1,m+1)-xi1(1,j+1)+I*l*omega0)
154 
155                 if(KroneckerDelta(m,j)*KroneckerDelta(l,0)==1)
156                     betafrac=0;
157                 else
158                     %lambda
159                     betafrac=1/(lambda(1,m+1)-lambda(1,j+1)+I*l*
                        omega0);
160                 end
161                 %integral <f0j|u_l|f0m>=
162                 %<hj|u_l|hm>
163                 beta = betafrac*2*trapz(r,r.*R(j+1,:).*u(l+1,:).*R(
                    m+1,:));
164 
165                 %
                        ----------------------------------------------------------
166                 %Finish calculating beta for the step
167 
168                 if(l~=0)
```

```
                    Suma1=Suma1 - a0(1,j+1)*2*real(beta);   %beta(l,n,m,k,omega0,epsvec);
                    %betalmj, k is harmonics, m and j is basis indexs.
                else
                    Suma1=Suma1 - a0(1,j+1)*beta;
                end
                betalmj(l+1,m+1,j+1)=beta;
            end % l-loop ends

        end %j-loop ends

        %a1 have a value for each m.
        a1(1,m+1)=Suma1;
    end %m-loop ends



    % --------------------------------------------------------------------------
    % %%%%%%%%%%%%%%%%%%%%%%%%%%%%%%%%%%%%%%%%%%%%%%%%%%%%%%%%%%%%%%%%%%%%%%%%%%

    %starting calculating Deff for different times
    % --------------------------------------------------------------------------
    % %%%%%%%%%%%%%%%%%%%%%%%%%%%%%%%%%%%%%%%%%%%%%%%%%%%%%%%%%%%%%%%%%%%%%%%%%%

    %starting calculating Deff for different times
    for tt=1:length(tvec)
        t=tvec(tt);
        Iomg0t=Iomg0*t;

        if(tt>2)
            disp(['Time ' num2str(t) ' Step #' num2str(tt-1) ' of ' num2str(length(tvec)-1) ' sum ' num2str(Deff(1,tt-1))])
        end

        % --------------------------------------------------------------------
        %first calculating M1 and M1/dt
        %using dM1/dt and M1 summing variables
```

```
204
205         %M1 summing
206         M1=0;
207         %dM1/dt summing variables
208         dM1dt=0;
209         %using (1-e^(-q)t)/..=t
210         %m=0, l=0
211         M1=a0(1,1)*ulRm(1,1)*t;
212         for m=0:mMax-1
213             lambdat=(lambda(1,m+1))*t;
214             %l=0
215             %dM1/dt
216             dM1dt=dM1dt+a0(1,m+1)*ulRm(m+1,1)*exp(-lambdat);  %+
                    Iomg0*l)*t);
217             %steady state term, still decaying
218             if(m>0)
219                 M1=M1+a0(1,m+1)*ulRm(m+1,1)*(1-exp(-lambdat))/(
                        lambda(1,m+1));%(1-exp(-(lambda(1,m+1)+Iomg0*l)*
                        t))/(lambda(1,m+1)+Iomg0*l);
220             end
221             %l>0
222             for l=1:NumHarm
223                 lambml=lambda(1,m+1)+Iomg0*l;
224                 expmlt=exp(-lambml*t);
225                 a0ulhm=a0(1,m+1)*ulRm(m+1,1+l);
226                 %dM1/dt oscillations
227                 %oscillations
228                 dM1dt=dM1dt+2*real(a0ulhm*expmlt);
229                 %M1
230                 %oscillations,
231                 M1=M1+2*real(a0ulhm*(1-expmlt)/lambml);
232             end %l-loop ends
233
234         end %m-loop ends
235         %
236         %     %saving value for M1*dM1/dt
237         %     M1ddM1dtvector(1,tt)=(M1)*(dM1dt);
238         %     M1vector(1,tt)=M1;
239         %     dM1dtvector(1,tt)=dM1dt;
240         %
241         %
242
243         %-------------------------------------------------------------
244         %starting calculating dM2/dt
245         summ=0;
246         for m=0:mMax-1%k-loop for beta and NOT FOR M1-dM/dt
247
248             %k sum
249             sumk=ulRm(m+1,1);%k=0
```

```
250             for k=1:NumHarm
251                 sumk=sumk+2*real(ulRm(m+1,k+1)*exp(-Iomg0t*k));
252             end % end k-loop
253 
254             %j-sum
255             sumj=0;
256             for j=0:mMax-1
257 
258                 %l-sum
259                 suml=betalmj(1,m+1,j+1);%l=0
260                 for l=1:NumHarm
261                     suml = suml + 2*real(betalmj(l+1,m+1,j+1)*exp(
                            Iomg0t*l));
262                 end %end l-loop
263                 suml=a0(1,j+1)*suml;
264 
265                 if(j==m)
266                     sumj=sumj+(suml+(a0(1,m+1)*gamma1(m+1)*t+a1(1,m
                            +1)))*exp(-lambda(1,j+1)*t);
267                 else
268                     sumj=sumj+suml*exp(-lambda(1,j+1)*t);
269                 end
270                 %hM2=hM2+exp(-lambda(1,j+1)*t)*ulhmexp*(Sum2+
                        Sumbeta);
271             end % end j-loop
272 
273             summ=summ+sumk*sumj;
274         end %end m-loop
275 
276         hM2=summ;
277 
278 
279 
280         %M2vector(1,tt)=hM2;
281         %------------------------------ending M2
282 
283 
284         Deff(count,tt)=1 + PeSqr*(hM2-M1*dM1dt);
285 
286     end %t-loop ends ------------------
287 plot(tvec,Deff(count,:))%/Deff(length(Deff)))
288 
289 %x = tvec; y = Deff(count,:);
290 %
291 % k = convhull(x,y);
292 % plot(x(k),y(k))
293 
294 xlabel('t')
295 ylabel('D_{eff}')
```

```
hold all
deffpoint{count}=['r_0=' num2str(rloc)];

end %zloc loop ends -------
  legend(deffpoint,0)

%plot(tvec,Deff)
xlabel('t')
ylabel('D_{eff}')

figure
plot(r,real(u(2,:)))
xlabel('r')
ylabel('Normalized Velocity, u_x(r,0)')

figure
plot(tvec,epsvec(2)*real(exp(I*omega0*tvec)))
xlabel('t')
ylabel('Pressure amplitude \epsilon_0=50')

% figure
% plot()
```

Transient Taylor–Aris dispersion for time-dependent flows in straight channels

Søren Vedel AND Henrik Bruus

Department of Micro- and Nanotechnology, Technical University of Denmark,
DTU Nanotech Building 345 B, DK-2800 Kongens Lyngby, Denmark

(Received 1 July 2011, resubmission)

Taylor–Aris dispersion, the shear-induced enhancement of solute diffusion in the flow direction of the solvent, has been studied intensely the past half century for the case of steady flow and single-frequency pulsating flows. Here, combining Aris's method of moments with Dirac's bra-ket formalism, we derive an expression for the effective solute diffusivity valid for transient Taylor–Aris dispersion in any given time-dependent, multi-frequency solvent flow through straight channels. Our theory shows that the solute dispersion may be greatly enhanced by the time-dependent parts of the flow, and it explicitly reveals how the dispersion coefficient depends on the external driving frequencies of the velocity field and the internal relaxation rates for mass and momentum diffusion. Although applicable to any type of fluid, we restrict the examples of our theory to Newtonian fluids, for which we both recover the known results for steady and single-frequency pulsating flows, and find new, richer structure of the dispersion as function of system parameters in multi-frequency systems. We show that the effective diffusivity is enhanced significantly by those parts of the time-dependent velocity field that have frequencies smaller than the fluid momentum diffusion rate and the solute diffusion rate.

Key Words: Taylor–Aris dispersion, time-dependent dispersion, advection, diffusion

1. Introduction

In his seminal work G.I. Taylor (1953) clarified the basic physical principles for the dispersion of the concentration profiles of solutes in a steady Poiseuille flow: the shear from the solvent flow acts to increase the dispersion, or effective diffusivity, of the solute in the direction of the flow. For a channel with a circular cross section of radius a, he derived the now classical expression for the effective diffusivity $D_{\text{eff}} = (1 + \text{Pé}^2/48)D$, where $\text{Pé} = aU_{\text{o}}/D$ is the Péclet number for the system, U_{o} being the average solvent flow speed and D the solute molecular diffusivity. This work was extended to a wider range of Péclet numbers and geometries by Aris (1956) using the elegant method of statistical moments. Many other aspects of shear-enhanced solute dispersion in steady flows have since been studied in the literature, including buoyancy and channel curvature (Erdogan & Chatwin 1967), interphase mass transfer (Sankarasubramanian & Gill 1973), transient phenomena (Chatwin 1977), effects of walls in 3D dispersion (Doshi *et al.* 1978), a stochastic description (van den Broeck 1982), influence of channel aspect ratio (Chatwin & Sullivan 1982), and generalized dispersion of mass, energy, and momentum in unbounded systems (Goddard 1993; Brenner & Edwards 1993). Taylor dispersion is now textbook material (Brenner & Edwards 1993; Probstein 1994; Bird *et al.* 2006).

Even today shear-flow-enhanced dispersion is studied actively as illustrated by the recent analyses of D_{eff} in transient anomalous diffusion of point discharges (Latini & Bernoff 2001), in electro-osmotic flow with random zeta potentials (Gleeson 2002), in

steady flows in a wide class of channel cross-sections (Dutta *et al.* 2006; Ajdari *et al.* 2006; Bontoux *et al.* 2006), in harmonically oscillating Couette–Poiseuille flows (Paul & Mazumder 2008), in steady Poiseuille flows using a Brownian-motion approach (Camassa *et al.* 2010), and in steady, non-Newtonian fluid flow (Vikhansky & Wang 2011).

In many practical applications (Skafte-Pedersen *et al.* 2009; Vedel *et al.* 2010) flows are unsteady and therefore typically generate more shear than their steady counterparts. The chemical engineering community long have recognized that increased mass transfer can be achieved by pulsating the flow, see e.g. Taylor & Leonard (1965) and Molloy & Leighton (1998), but many physical interpretations and quantitative aspects of this additional shear remains to be investigated theoretically. This is surprising given that the first investigation of Taylor dispersion in time-dependent flows dates back to Aris (1960) and its generalization by Brenner & Edwards (1993), and also given the large volume of studies dedicated to steady flows. Time-dependent phenomena that have been studied are non-transient, single-frequency pulsating flows (Harris & Goren 1967; Chatwin 1975; Watson 1983; Thomas & Narayanan 2001; Jansons 2006), the first examples of transient-flow analysis of single-frequency flows by Mazumder and coworkers (Mukherjee & Mazumder 1988; Bandyopadhyay & Mazumder 1999), and dispersion in a time-dependent flow in an unbounded system (Leighton 1989).

Here, we go beyond the previous results on dispersion in single-frequency flows and study any given time-dependent laminar flow in a straight channel of any constant cross-sectional shape, in particular relevant for microfluidic systems. Based on Aris's scheme we derive a general and compact expression for the transient, effective Taylor–Aris diffusivity $D_{\rm eff}(t)$ with explicit dependence on the externally applied flow frequencies $\ell\omega_{\rm o}$ and the internal relaxation rates λ_1 and $\alpha_{\rm fl}$ for solute mass diffusion and solvent momentum diffusion, respectively. We show that $D_{\rm eff}$ is enhanced significantly by those frequency-components of the time-dependent velocity field which have an oscillation frequency smaller than any relaxation rate of the system, and thus provide enough time for the solute to equilibrate. We further show how this enhancement is diminished each time a frequency is increased and becomes larger than a given relaxation rate. Moreover, for the start-up of a Poiseuille flow, which includes any flow frequency, we find that the transient time of $D_{\rm eff}$ is determined by the slowest of the relaxation processes, i.e. the maximum of $1/\lambda_1$ and $1/\alpha_{\rm fl}$. Finally, we demonstrate the practical usefulness of our theory as a design tool by characterizing the dispersion generated by a microfluidic, peristaltic pump.

2. The physical model and Aris's method of moments

In the following we establish our physical model together with our notation and present the well-known method of moments for calculating the dispersion coefficient $D_{\rm eff}$. We consider a long, straight channel parallel to the x-axis, and assume that it is translational invariant along this axis with an arbitrary, but constant, cross section Ω. The coordinates in the transverse yz-plane are denoted $\boldsymbol{r}_\perp = (y,z)$, so that the full coordinates are written as $\boldsymbol{r} = (x, \boldsymbol{r}_\perp)$, and likewise for the gradient operator $\boldsymbol{\nabla}$ and the Laplace operator ∇^2,

$$\boldsymbol{r} = (x, \boldsymbol{r}_\perp), \qquad \text{with} \quad \boldsymbol{r}_\perp = (y,z), \tag{2.1a}$$

$$\boldsymbol{\nabla} = \mathbf{e}_x\partial_x + \boldsymbol{\nabla}_\perp, \quad \text{with} \quad \boldsymbol{\nabla}_\perp = \mathbf{e}_y\partial_y + \mathbf{e}_z\partial_z, \tag{2.1b}$$

$$\nabla^2 = \partial_x^2 + \nabla_\perp^2, \qquad \text{with} \quad \nabla_\perp^2 = \partial_y^2 + \partial_z^2. \tag{2.1c}$$

The channel has length $\mathcal{L}$, cross-sectional area $\mathcal{A} = \int_\Omega \mathrm{d}\boldsymbol{r}_\perp 1$, and volume $\mathcal{V} = \mathcal{L}\mathcal{A}$. Our analysis involves expansion of the spatial dependence of functions into linear combinations of suitably chosen basis functions. For notational convenience we shall therefore rely

on a Hilbert-space representation using the compact Dirac bra-ket notation, employed more often in quantum mechanics (Dirac 1981) than in fluid mechanics (Bruus 2008; Mortensen *et al.* 2006; Mortensen & Bruus 2006). For any pair of functions $f(x,\boldsymbol{r}_\perp,t)$ and $g(x,\boldsymbol{r}_\perp,t)$ represented by the bra $\langle f|$ and the ket $|g\rangle$, the inner product $\langle f|g\rangle$, is defined by the integral, where the asterisk indicates complex conjugation,

$$\langle f|g\rangle = \frac{1}{\mathcal{V}}\int_{-\frac{1}{2}\mathcal{L}}^{\frac{1}{2}\mathcal{L}}\mathrm{d}x\int_\Omega \mathrm{d}\boldsymbol{r}_\perp\, f^*(x,\boldsymbol{r}_\perp,t)\, g(x,\boldsymbol{r}_\perp,t), \tag{2.2}$$

This definition also includes the case, where the involved functions only depend on the transverse coordinates $\boldsymbol{r}_\perp$. For $f_\perp(\boldsymbol{r}_\perp,t)$ and $g_\perp(\boldsymbol{r}_\perp,t)$ we obtain

$$\langle f_\perp|g_\perp\rangle = \frac{1}{\mathcal{A}}\int_\Omega \mathrm{d}\boldsymbol{r}_\perp\, f_\perp^*(\boldsymbol{r}_\perp,t)\, g_\perp(\boldsymbol{r}_\perp,t), \tag{2.3}$$

as the x-integration trivially gives unity. Details and useful properties of the bra-ket notation are given in the Appendix.

From now on we use dimensionless quantities defined in terms of the characteristic transverse length L_o, often the shortest distance a from the center line of the channel to the wall, the diffusion time T_o from the molecular diffusivity D of the solute, the advection velocity U_o from a scale U_char in the time-dependent flow, and the average solute concentration C_o of the solute concentration field $c(x,\boldsymbol{r}_\perp,t)$,

$$L_\mathrm{o}=a,\quad T_\mathrm{o}=\frac{L_\mathrm{o}^2}{D},\quad U_\mathrm{o}=U_\mathrm{char},\quad C_\mathrm{o}=\langle 1|c(x,\boldsymbol{r}_\perp,0)\rangle. \tag{2.4}$$

The specific choice of U_char in Eq. (2.4) is not unique: for a steady flow it could be taken as the mean velocity; for a single-frequency oscillating flow as the rms-velocity. See Appendix for a list of symbols.

Denoting the base angular frequency of the solvent flow $\tilde{\omega}_\mathrm{o}$ (rad/s), the system is characterized by three dimensionless numbers: the Péclet number Pé (the ratio of advection speed to mass diffusion speed), the Schmidt number Sc (the ratio of momentum diffusion speed to mass diffusion speed), and the Womersley number Wo (the square root of the ratio of oscillation speed at frequency $\tilde{\omega}_\mathrm{o}$ to momentum diffusion speed for a Newtonian fluid of kinematic viscosity ν),

$$\mathrm{Pé}=\frac{L_\mathrm{o}U_\mathrm{o}}{D},\qquad \mathrm{Sc}=\frac{\nu}{D},\qquad \mathrm{Wo}=\sqrt{\frac{L_\mathrm{o}^2\tilde{\omega}_\mathrm{o}}{\nu}}. \tag{2.5}$$

For non-Newtonian fluids with an internal molecular stress relaxation time τ_mol, the Deborah number $\mathrm{De}=\tau_\mathrm{mol}\,\omega_\mathrm{o}$ would appear, but this is not treated in this work.

2.1. *The time-dependent velocity field*

We take the velocity field to be any axis-parallel channel flow $\boldsymbol{v}=u(\boldsymbol{r}_\perp,t)\boldsymbol{e}_x$, and represent $u(\boldsymbol{r}_\perp,t)$ by a standard Fourier series with components u_ℓ for each higher harmonic $\ell\omega_\mathrm{o}$ (ℓ being an integer) in the dimensionless base frequency $\omega_\mathrm{o}=\tilde{\omega}_\mathrm{o}T_\mathrm{o}=\mathrm{Wo}^2\mathrm{Sc}$,

$$u(\boldsymbol{r}_\perp,t)=\sum_{\ell=-\infty}^{\infty}u_\ell(\boldsymbol{r}_\perp)\,\mathrm{e}^{\mathrm{i}\ell\omega_\mathrm{o}t}, \tag{2.6}$$

where complex notation is introduced for the time with $\mathrm{i}=\sqrt{-1}$. By demanding that $u_{-\ell}(\boldsymbol{r}_\perp)=u_\ell^*(\boldsymbol{r}_\perp)$, we ensure that the velocity field is real (Brenner & Edwards 1993).

The fluid responds to changes in external conditions on a time scale which depends on its internal stress relaxation time, and whether fluid inertia dominates may be estimated

by the product of the driving frequency $\tilde{\omega}_\mathrm{o}$ and this internal time scale. For Newtonian fluids the stress relaxation time scale is given by the momentum diffusion time $1/\alpha_\mathrm{fl}$, related to the momentum diffusion rate α_fl, which is derived from the momentum diffusion equation $\partial_t u = \mathrm{Sc}\nabla_\perp^2 u$ and given by

$$\alpha_\mathrm{fl} \propto \mathrm{Sc} \tag{2.7}$$

with a geometry-dependent proportionality factor. Note that since $\alpha_\mathrm{fl} \propto \mathrm{Sc}$, the square of the Womersley number is proportional to the ratio of the dimensionless driving frequency ω_o and the momentum diffusion equilibration rate,

$$\mathrm{Wo}^2 = \frac{\omega_\mathrm{o}}{\mathrm{Sc}} \propto \frac{\omega_\mathrm{o}}{\alpha_\mathrm{fl}}. \tag{2.8}$$

2.2. *Dispersion and the advection-diffusion equation*

The transport of the diffusive solute concentration c in the above-mentioned velocity field is given by the dimensionless advection-diffusion equation,

$$\partial_t c(x,\boldsymbol{r}_\perp,t) + \mathrm{Pé}\, u(\boldsymbol{r}_\perp,t)\,\partial_x c(x,\boldsymbol{r}_\perp,t) = (\partial_x^2 + \nabla_\perp^2)\, c(x,\boldsymbol{r}_\perp,t). \tag{2.9}$$

The corresponding boundary conditions are

$$\boldsymbol{n}\cdot\boldsymbol{\nabla}_\perp c = 0, \text{ on all walls,} \tag{2.10a}$$

$$c(x,\boldsymbol{r}_\perp,0) = \tilde{c}(x,\boldsymbol{r}_\perp), \tag{2.10b}$$

$$x^s\partial_x^q c \to 0, \text{ for } |x| \to \frac{\mathcal{L}}{2} \text{ and } s,q = 0,1,2,\ldots, \tag{2.10c}$$

where $\boldsymbol{n}$ is the surface normal and $\tilde{c}$ is a given initial concentration field, and condition (2.10c) states that all spatial gradients in c as well as c itself vanish far away along the axis of the channel.

Using Aris's method of moments the effective diffusivity $D_\mathrm{eff}(t)$ is defined by the time-derivative of the axial variance $\mu_2(t) = \langle (x-\bar{x})^2 | c\rangle$ of the solute distribution, $\bar{x}(t) = M_1(t)$ being the center of mass, Eq. (A 5b), and may be computed as (Aris 1956, 1960; Chatwin 1975; Barton 1983; Mukherjee & Mazumder 1988; Brenner & Edwards 1993)

$$D_\mathrm{eff}(t) = \frac{1}{2}\frac{\mathrm{d}\mu_2(t)}{\mathrm{d}t} = \frac{1}{2}\frac{\mathrm{d}M_2}{\mathrm{d}t} - M_1\frac{\mathrm{d}M_1}{\mathrm{d}t}, \tag{2.11}$$

where the pth full moment $M_p(t)$ of the solute concentration field $c(x,\boldsymbol{r}_\perp,t)$ and the associated axial moment $c_p(\boldsymbol{r}_\perp,t)$ are defined by

$$M_p(t) = \langle x^p | c\rangle = \frac{1}{\mathcal{A}}\int_\Omega \mathrm{d}\boldsymbol{r}_\perp\, c_p(\boldsymbol{r}_\perp,t), \quad p = 0,1,2,\ldots, \tag{2.12a}$$

$$c_p(\boldsymbol{r}_\perp,t) = \frac{1}{\mathcal{L}}\int_{-\frac{1}{2}\mathcal{L}}^{\frac{1}{2}\mathcal{L}} \mathrm{d}x\, x^p c(x,\boldsymbol{r}_\perp,t), \qquad p = 0,1,2,\ldots. \tag{2.12b}$$

The derivation of Eq. (2.11) is sketched in the Appendix, where we also show that the moments $c_p(\boldsymbol{r}_\perp,t)$ and $M_p(t)$ evolve according to the recursive equations of motion,

$$\partial_t c_p(\boldsymbol{r}_\perp,t) - \nabla_\perp^2 c_p(\boldsymbol{r}_\perp,t) = p(p-1)c_{p-2}(\boldsymbol{r}_\perp,t) + \mathrm{Pé}\, u(\boldsymbol{r}_\perp,t)p\, c_{p-1}(\boldsymbol{r}_\perp,t), \quad p = 0,1,2,\ldots, \tag{2.13a}$$

$$\frac{\mathrm{d}M_p(t)}{\mathrm{d}t} = p(p-1)\langle 1 | c_{p-2}\rangle + \mathrm{Pé}\, p\langle u | c_{p-1}\rangle, \quad p = 0,1,2,\ldots, \tag{2.13b}$$

with the boundary and initial conditions

$$\boldsymbol{n}\cdot\boldsymbol{\nabla}_\perp c_p = 0, \text{ on all walls,} \tag{2.14a}$$
$$c_p(\boldsymbol{r}_\perp, t) < \infty, \tag{2.14b}$$
$$c_p(\boldsymbol{r}_\perp, 0) = \tilde{c}_p(\boldsymbol{r}_\perp), \tag{2.14c}$$
$$M_p(0) = \langle x^p | \tilde{c} \rangle. \tag{2.14d}$$

The main goal of this paper is to solve Eq. (2.11) for general time-dependent flows in straight channels of arbitrary, constant cross-section, and to study how D_{eff} depends on the physical frequencies and relaxation rates of the systems.

3. Dispersion for multiple-frequency flow

The solution solution procedure of the problem was introduced by Barton (1983) for steady flows and later extended to also include single-frequency harmonic pulsatile flows by Mukherjee & Mazumder (1988). The expressions presented in this section generalize their results to any given time-dependent flow. We derive them using the more compact bra-ket formalism as follows: from Eq. (2.13*a*) with $p = 0$ and 1 we determine the axial moment $c_{\text{o}}(\boldsymbol{r}_\perp, t)$ and subsequently $c_1(\boldsymbol{r}_\perp, t)$. With these at hand, the full moment M_1 as well as the time derivatives $\frac{\mathrm{d}M_1}{\mathrm{d}t}$ and $\frac{\mathrm{d}M_2}{\mathrm{d}t}$ can be obtained from Eq. (2.13*b*) with $p = 1$ and 2, which then are fed into Eq. (2.11) to determine D_{eff}.

3.1. *The zeroth axial moment and basis functions*

We begin by analyzing the $p = 0$ axial moment equation (2.13*a*) for $c_{\text{o}}(\boldsymbol{r}_\perp, t)$,

$$\big(\partial_t - \nabla_\perp^2\big)\big|c_{\text{o}}(\boldsymbol{r}_\perp, t)\big\rangle = 0. \tag{3.1}$$

This moment fulfills the Neumann boundary condition

$$\boldsymbol{n}\cdot\boldsymbol{\nabla}_\perp c_{\text{o}} = 0, \text{ on all walls,} \tag{3.2}$$

and has the initial condition

$$c_{\text{o}}(\boldsymbol{r}_\perp, 0) = \tilde{c}_0(\boldsymbol{r}_\perp) = \int_{-\frac{1}{2}\mathcal{L}}^{\frac{1}{2}\mathcal{L}} \mathrm{d}x\, \tilde{c}(x, \boldsymbol{r}_\perp). \tag{3.3}$$

Using separation of variables, the solution for $c_{\text{o}}(\boldsymbol{r}_\perp, t)$ can be written as the expansion

$$\big|c_{\text{o}}(\boldsymbol{r}_\perp, t)\big\rangle = \sum_{n=0}^{\infty} a_{0n} \mathrm{e}^{-\lambda_n t} \big|f_n(\boldsymbol{r}_\perp)\big\rangle, \tag{3.4}$$

where the time-independent eigenfunctions $f_n(\boldsymbol{r}_\perp)$ with eigenvalues λ_n are defined by

$$(\lambda_n + \nabla_\perp^2)\big|f_n(\boldsymbol{r}_\perp)\big\rangle = 0, \ n = 0, 1, 2, \ldots, \tag{3.5a}$$
$$\boldsymbol{n}\cdot\boldsymbol{\nabla}_\perp\big|f_n(\boldsymbol{r}_\perp)\big\rangle = 0, \text{ on all walls,} \tag{3.5b}$$

and form a complete orthonormal basis in the sense of Eq. (A 3). Note that the lowest $n = 0$ eigenvalue is zero, $\lambda_0 = 0$, with eigenfunction unity, $f_0(\boldsymbol{r}_\perp) = 1$, while for $n > 0$ the eigenvalues are positive, $\lambda_n > 0$. We remark that although the general advection-diffusion problem Eq. (2.9) is non-Hermitian, the reduced, transverse problem Eq. (3.5) is Hermitian, and we can take full advantage of the Dirac Hilbert-space formulation.

The expansion coefficients a_{0m} are found by multiplying Eq. (3.4) at $t = 0$ by $\langle f_m|$,

$$a_{0m} = \langle f_m | \tilde{c}_0 \rangle, \quad m = 0, 1, 2, \ldots. \tag{3.6}$$

For infinite time, all terms in Eq. (3.4) except $n = 0$ decay exponentially, and we obtain

$$\big|c_{\mathrm{o}}(\boldsymbol{r}_\perp,\infty)\big\rangle = a_{00}\big|f_0(\boldsymbol{r}_\perp)\big\rangle = \big\langle 1\big|\tilde{c}_0\big\rangle\big|1\big\rangle = \big|1\big\rangle, \tag{3.7}$$

representing the state where, by diffusion, the solute concentration has spread out uniformly in space.

3.2. *The first axial moment and basis functions*

The $p = 1$ axial moment equation (2.13a) for $c_1(\boldsymbol{r}_\perp, t)$ is analyzed in a similar manner. Using that $c_{\mathrm{o}}(\boldsymbol{r}_\perp, t)$ is now a known function, we have

$$\big(\partial_t - \nabla_\perp^2\big)\big|c_1(\boldsymbol{r}_\perp,t)\big\rangle = \mathrm{P\acute{e}}\, u(\boldsymbol{r}_\perp,t)\,\big|c_{\mathrm{o}}(\boldsymbol{r}_\perp,t)\big\rangle = \mathrm{P\acute{e}}\, u(\boldsymbol{r}_\perp,t)\sum_{n=0}^{\infty} a_{0n}\mathrm{e}^{-\lambda_n t}\big|f_n(\boldsymbol{r}_\perp)\big\rangle, \tag{3.8a}$$

where c_1 fulfills the Neumann boundary condition

$$\boldsymbol{n}\cdot\boldsymbol{\nabla}_\perp c_1 = 0, \text{ on all walls,} \tag{3.8b}$$

and the initial condition

$$c_1(\boldsymbol{r}_\perp,0) = \tilde{c}_1(\boldsymbol{r}_\perp) = \int_{-\frac{1}{2}\mathcal{L}}^{\frac{1}{2}\mathcal{L}} \mathrm{d}x\; x\,\tilde{c}(x,\boldsymbol{r}_\perp). \tag{3.8c}$$

As pointed out by Barton (1983), solving the inhomogeneous partial differential equation (3.8a) for c_1 requires some care regarding the null-space of the differential operator $(\partial_t - \nabla_\perp^2)$. Using the time Fourier expansion Eq. (2.6) of the velocity field $u(\boldsymbol{r}_\perp, t)$, we see that, due to the time-independent $\ell = 0$ component of u, the right-hand side of Eq. (3.8a) contains terms of the form $\mathrm{P\acute{e}}\, a_{0n}u_0(\boldsymbol{r}_\perp)e^{-\lambda_n t}\big|f_n\big\rangle$, which have nonzero overlap with kets of the form $e^{-\lambda_n t}\big|f_n\big\rangle$. Noting that

$$(\partial_t - \nabla_\perp^2)\big[e^{-\lambda_n t}\big|f_n\big\rangle\big] = 0, \tag{3.9a}$$

$$(\partial_t - \nabla_\perp^2)\big[t\,e^{-\lambda_n t}\big|f_n\big\rangle\big] = e^{-\lambda_n t}\big|f_n\big\rangle, \tag{3.9b}$$

we thus expand $c_1(\boldsymbol{r}_\perp, t)$ in terms of both $e^{-\lambda_n t}\big|f_n\big\rangle$ and $t\,e^{-\lambda_n t}\big|f_n\big\rangle$, and seek solutions of $\big|c_1(\boldsymbol{r}_\perp,t)\big\rangle$ of the form

$$\big|c_1\big\rangle = \mathrm{P\acute{e}}\sum_{n=0}^{\infty}\Big[(\gamma_{1n}a_{0n}t + a_{1n})\big|f_n\big\rangle + a_{0n}\big|\phi_n\big\rangle\Big]\mathrm{e}^{-\lambda_n t}, \tag{3.10}$$

where the unknown coefficients, γ_{1n} and a_{1n}, as well as the unknown time-dependent ket $\big|\phi_n(\boldsymbol{r}_\perp,t)\big\rangle$ are determined in the following. Inserting this trial expansion of $\big|c_1(\boldsymbol{r}_\perp,t)\big\rangle$ into the equation of motion (3.8a) leads to

$$(\partial_t - \nabla_\perp^2 - \lambda_n)\big|\phi_n(\boldsymbol{r}_\perp,t)\big\rangle = \big[u(\boldsymbol{r}_\perp,t) - \gamma_{1n}\big]\big|f_n(\boldsymbol{r}_\perp)\big\rangle. \tag{3.11}$$

The unknown ket $\big|\phi_n(\boldsymbol{r}_\perp,t)\big\rangle$ is now expanded in a Fourier series in time and a $\big|f_m(\boldsymbol{r}_\perp)\big\rangle$ series in space,

$$\big|\phi_n(\boldsymbol{r}_\perp,t)\big\rangle = \sum_{\ell=-\infty}^{\infty}\sum_{m=0}^{\infty}\beta_{mn}^{\ell}\mathrm{e}^{\mathrm{i}\ell\omega_{\mathrm{o}}t}\big|f_m(\boldsymbol{r}_\perp)\big\rangle, \tag{3.12}$$

which upon insertion into Eq. (3.11) followed by multiplication by $\big\langle f_k\big|$ results in the following matrix equation for the coefficients β_{kn}^{ℓ},

$$(\lambda_k - \lambda_n + \mathrm{i}\ell\omega_{\mathrm{o}})\beta_{kn}^{\ell} = \big\langle f_k\big|u_\ell\big|f_n\big\rangle - \gamma_{1n}\,\delta_{\ell,0}\,\delta_{k,n}. \tag{3.13}$$

Here, we see that the special case of the time-independent term $\ell = 0$, together with the diagonal term $k = n$, only allows a solution if we choose

$$\gamma_{1n} = \langle f_n | u_0(\boldsymbol{r}_\perp) | f_n \rangle, \tag{3.14}$$

while the β-coefficients are given by

$$\beta_{kn}^{\ell} = (1 - \delta_{\ell,0}\delta_{k,n}) \, \frac{\langle f_k | u_\ell(\boldsymbol{r}_\perp) | f_n \rangle}{\lambda_k - \lambda_n + \mathrm{i}\ell\omega_\mathrm{o}}. \tag{3.15}$$

Note that any value of β_{nn}^{0} is allowed, so for convenience we set it to zero. Moreover, $\beta_{kn}^{-\ell} = (\beta_{kn}^{\ell})^*$ ensures real values of the resulting fields.

Lastly, the coefficients a_{1n} are found using the initial condition (3.8c) in Eq. (3.10) at $t = 0$, multiplying by $\langle f_k|$, and finally exchanging the indices n and k,

$$a_{1n} = \frac{1}{\mathrm{Pé}} \, \langle f_n | \tilde{c}_1(\boldsymbol{r}_\perp) \rangle - \sum_{k=0}^{\infty} a_{0k} \sum_{l=-\infty}^{\infty} \beta_{nk}^{\ell}. \tag{3.16}$$

Collecting all terms, we write the formal solution as

$$|c_1(\boldsymbol{r}_\perp, t)\rangle = \mathrm{Pé} \sum_{m=0}^{\infty} \sum_{n=0}^{\infty} \left[(a_{0n}\gamma_{1n}t + a_{1n})\delta_{n,m} + a_{0n} \Big(\sum_{\ell=-\infty}^{\infty} \beta_{mn}^{\ell} \mathrm{e}^{\mathrm{i}\ell\omega_\mathrm{o}t} \Big) \right] \mathrm{e}^{-\lambda_n t} |f_m\rangle. \tag{3.17}$$

3.3. *Expressions for the effective diffusivity*

The effective diffusivity $D_\mathrm{eff} = \frac{1}{2}\frac{\mathrm{d}M_2}{\mathrm{d}t} - M_1 \frac{\mathrm{d}M_1}{\mathrm{d}t}$ can now be expressed in terms of a basis function expansion. The time derivative $\frac{\mathrm{d}M_1}{\mathrm{d}t} = \mathrm{Pé} \, \langle u | c_\mathrm{o} \rangle$ of the full moment M_1 in Eq. (2.13b) becomes

$$\frac{\mathrm{d}M_1}{\mathrm{d}t} = \mathrm{Pé} \sum_{n=0}^{\infty} \sum_{\ell=-\infty}^{\infty} a_{0n} \langle u_\ell | f_n \rangle \, \mathrm{e}^{-(\lambda_n + \mathrm{i}\ell\omega_\mathrm{o})t}, \tag{3.18a}$$

where we have used Eq. (A 2b) for the phase factor. By proper choice of the coordinate system, the initial centroid $\bar{x}(0)$ of the distribution is zero. This, combined with Eq. (A 5b), determines the initial value $M_1(0) = \bar{x}(0) = 0$, and time integration of Eq. (3.18a) gives

$$M_1 = \mathrm{Pé} \sum_{n=0}^{\infty} \sum_{\ell=-\infty}^{\infty} a_{0n} \langle u_\ell | f_n \rangle \, \frac{1 - \mathrm{e}^{-(\lambda_n + \mathrm{i}\ell\omega_\mathrm{o})t}}{\lambda_n + \mathrm{i}\ell\omega_\mathrm{o}}. \tag{3.18b}$$

Here, the term $(n, \ell) = (0, 0)$ depends linearly on time because $\lim_{q\to 0} \left[(1 - \mathrm{e}^{-qt})/q\right] = t$. Similarly, for the time derivative $\frac{1}{2}\frac{\mathrm{d}M_2}{\mathrm{d}t} = \langle 1 | c_\mathrm{o} \rangle + \mathrm{Pé} \, \langle u | c_1 \rangle$ of the full moment M_2, Eq. (2.13b), we obtain

$$\begin{aligned} \frac{1}{2}\frac{\mathrm{d}M_2}{\mathrm{d}t} = 1 + \mathrm{Pé}^2 \sum_{m=0}^{\infty} \sum_{n=0}^{\infty} \sum_{k=-\infty}^{\infty} \langle u_k | f_m \rangle \, \mathrm{e}^{-(\lambda_n + \mathrm{i}k\omega_\mathrm{o})t} \\ \times \left[(a_{0n}\gamma_{1n}t + a_{1n})\delta_{n,m} + a_{0n} \sum_{\ell=-\infty}^{\infty} \beta_{mn}^{\ell} \mathrm{e}^{i\ell\omega_\mathrm{o}t} \right]. \end{aligned} \tag{3.18c}$$

All expressions derived so far are explicitly real because of the pairwise summation of complex conjugate terms with index ℓ and $-\ell$. Furthermore, they apply to any initial solute distributions, such as the non-uniform distributions recently studied by Camassa *et al.* (2010), as well as any given velocity field, which can be represented by Eq. (2.6).

We now study the special case of an initial solute distribution $\tilde{c}$ being uniform in the

cross-sectional plane. This introduces significant simplifications in D_{eff}, which otherwise depends on the channel cross-section, the flow profile u, and the initial solute distribution $\tilde{c}$ through the coefficients u_ℓ, a_{0n}, a_{1n}, γ_{1n}, and β_{kn}^{ℓ}. Transverse uniformity leads to

$$\big|\tilde{c}_0\big\rangle = \big|1\big\rangle, \quad \text{and} \quad \big|\tilde{c}_1\big\rangle = 0, \tag{3.19}$$

and a_{0n}, β_{j0}^{ℓ} and a_{1n} therefore reduce to

$$a_{0n} = \delta_{n,0} \tag{3.20a}$$

$$\beta_{j0}^{\ell} = (1-\delta_{\ell,0}\delta_{j,0})\,\frac{\big\langle f_j\big|u_\ell\big\rangle}{\lambda_j + \mathrm{i}\ell\omega_{\mathrm{o}}}, \tag{3.20b}$$

$$a_{1n} = -\sum_{\ell=-\infty}^{\infty}(1-\delta_{\ell,0}\delta_{n,0})\,\frac{\big\langle f_n\big|u_\ell\big\rangle}{\lambda_n + \mathrm{i}\ell\omega_{\mathrm{o}}}, \tag{3.20c}$$

where $\big\langle f_j\big|u_\ell\big|f_0\big\rangle = \big\langle f_j\big|u_\ell\big|1\big\rangle = \big\langle f_j\big|u_\ell\big\rangle$ has been used. Hence Eq. (3.18) becomes

$$\frac{\mathrm{d}M_1}{\mathrm{d}t} = \mathrm{P\acute{e}}\sum_{k=-\infty}^{\infty}\big\langle u_k\big|1\big\rangle\,\mathrm{e}^{-\mathrm{i}k\omega_{\mathrm{o}}t}, \tag{3.21a}$$

$$M_1 = \mathrm{P\acute{e}}\sum_{\ell=-\infty}^{\infty}\big\langle u_\ell\big|1\big\rangle\frac{1-\mathrm{e}^{-\mathrm{i}\ell\omega_{\mathrm{o}}t}}{\mathrm{i}\ell\omega_{\mathrm{o}}} = \mathrm{P\acute{e}}\left\{\big\langle u_0\big|1\big\rangle\,t + \sum_{\ell=-\infty}^{\infty}(1-\delta_{\ell,0})\big\langle 1\big|u_\ell\big\rangle\frac{\mathrm{e}^{\mathrm{i}\ell\omega_{\mathrm{o}}t}-1}{\mathrm{i}\ell\omega_{\mathrm{o}}}\right\}, \tag{3.21b}$$

$$\frac{1}{2}\frac{\mathrm{d}M_2}{\mathrm{d}t} = 1 + \mathrm{P\acute{e}}^2\left\{\sum_{\ell=-\infty}^{\infty}\big\langle u_\ell\big|1\big\rangle\big\langle u_0\big|1\big\rangle\,t\,\mathrm{e}^{-\mathrm{i}\ell\omega_{\mathrm{o}}t} + \sum_{m=0}^{\infty}\sum_{\ell=-\infty}^{\infty}\sum_{k=-\infty}^{\infty}\frac{\big\langle u_k\big|f_m\big\rangle\big\langle f_m\big|u_\ell\big\rangle}{\lambda_m + \mathrm{i}\ell\omega_{\mathrm{o}}}\right.$$
$$\left.\times\,(1-\delta_{m,0}\delta_{\ell,0})\Big[\mathrm{e}^{\mathrm{i}\ell\omega_{\mathrm{o}}t} - \mathrm{e}^{-\lambda_m t}\Big]\mathrm{e}^{-\mathrm{i}k\omega_{\mathrm{o}}t}\right\}, \tag{3.21c}$$

and after a final index change of m to n we arrive at

$$D_{\mathrm{eff}}(t) = 1 + \mathrm{P\acute{e}}^2\sum_{n=1}^{\infty}\sum_{\ell=-\infty}^{\infty}\sum_{k=-\infty}^{\infty}\frac{\big\langle u_k\big|f_n\big\rangle\big\langle f_n\big|u_\ell\big\rangle}{\lambda_n + \mathrm{i}\ell\omega_{\mathrm{o}}}\Big[\mathrm{e}^{\mathrm{i}(\ell-k)\omega_{\mathrm{o}}t} - \mathrm{e}^{-(\lambda_n+\mathrm{i}k\omega_{\mathrm{o}})t}\Big]. \tag{3.22}$$

This is the main theoretical result of our work: a closed expression for the transient Taylor–Aris dispersion $D_{\mathrm{eff}}(t)$ for any given time-dependent, axial flow field $u(\boldsymbol{r}_\perp, t)$ in the case of complete transverse diffusion. The flow frequencies $\ell\omega_{\mathrm{o}}$ and solute diffusion relaxation rates λ_n appears explicitly, while the momentum relaxation rates α_{fl} are implicit in $\big\langle f_n\big|u_\ell\big\rangle$. The result (3.22), which generalizes previous steady and single-frequency results, is particularly relevant in the field of microfluidics characterized by laminar flow in channels of small cross-sectional dimensions compared to the channel lengths.

The time-averaged diffusivity $D_{\mathrm{eff}}^{\mathrm{avr}}(t)$ over one oscillation period $\tau_0 = 2\pi/\omega_{\mathrm{o}}$ is

$$D_{\mathrm{eff}}^{\mathrm{avr}}(t) = \frac{1}{\tau_0}\int_t^{t+\tau_0} D_{\mathrm{eff}}(t)\,\mathrm{d}t \tag{3.23a}$$

$$= 1 + \mathrm{P\acute{e}}^2\sum_{n=1}^{\infty}\sum_{\ell=-\infty}^{\infty}\sum_{k=-\infty}^{\infty}\frac{\big\langle u_k\big|f_n\big\rangle\big\langle f_n\big|u_\ell\big\rangle}{\lambda_n + \mathrm{i}\ell\omega_{\mathrm{o}}}\Big[\delta_{\ell,k} - \frac{1-\mathrm{e}^{-\lambda_n\tau_0}}{(\lambda_n + \mathrm{i}k\omega_{\mathrm{o}})\tau_0}\,\mathrm{e}^{-(\lambda_n+\mathrm{i}k\omega_{\mathrm{o}})t}\Big], \tag{3.23b}$$

which in the long-time limit $t \gg 1/\lambda_1$ reduces to

$$D_{\text{eff}}^{\text{avr}}(\infty) = 1 + \text{Pé}^2 \sum_{n=1}^{\infty} \left[\frac{|\langle u_0 | f_n \rangle|^2}{\lambda_n} + \sum_{\ell=1}^{\infty} \frac{2\lambda_n |\langle u_\ell | f_n \rangle|^2}{\lambda_n^2 + \ell^2 \omega_{\text{o}}^2} \right]. \tag{3.24}$$

Note that the ℓ-sum only runs over positive integers and not as previously over all integers.

Finally, in the case of a steady flow given by

$$|u_\ell\rangle = \delta_{\ell,0} \, |u_0\rangle, \tag{3.25}$$

expression (3.22) for the effective diffusivity reduces to

$$D_{\text{eff}}^{\text{steady}}(t) = 1 + \text{Pé}^2 \sum_{n=1}^{\infty} \frac{|\langle u_0 | f_n \rangle|^2}{\lambda_n} \left(1 - \text{e}^{-\lambda_n t}\right), \tag{3.26}$$

and hence we recover the steady-flow, transient-solute result of Barton (1983).

4. General aspects of dispersion and relaxation rates

Our main result Eq. (3.22) implies directly that for all time-dependent flows the effective diffusivity depends on the velocity squared, $D_{\text{eff}} \propto \text{Pé}^2 \propto U_{\text{o}}^2$. However the specific form of D_{eff} depends on the magnitude of the amplitude $||u_\ell||$, of a given velocity component with frequency $\ell\omega_{\text{o}}$, relative to the amplitude $||u_0||$ of the steady component.

For small oscillation amplitudes $||u_\ell|| \ll ||u_0||$, the velocity field remains unidirectional, but its magnitude, and hence the shear gradients in the velocity, oscillates with frequency $\ell\omega_{\text{o}}$ around the steady value. Consequently, $D_{\text{eff}}(t)$ oscillates with frequency $\ell\omega_{\text{o}}$ around its time-averaged value $D_{\text{eff}}^{\text{avr}}(\infty)$. For sufficiently large amplitudes $||u_\ell|| \gg ||u_0||$ (the exact limit depends on the channel cross section geometry), the direction of the velocity field changes sign with frequency $2\ell\omega_{\text{o}}$. As a result, due to the terms with $k = -\ell$ in Eq. (3.23*b*), $D_{\text{eff}}(t)$ also oscillates with the double period $2\ell\omega_{\text{o}}$. Moreover, because this period-doubling ensures a non-zero, time-averaged effective diffusivity $D_{\text{eff}}^{\text{avr}} \propto ||u_\ell||^2 \text{Pé}^2$, $D_{\text{eff}}^{\text{avr}}$ increases above $D_{\text{eff}}^{\text{steady}}$. This reflects that now $||u_\ell|| U_{\text{o}}$ and not U_{o} should be chosen as U_{char} in Eq. (2.4), thus quantifying the observations made in the chemical engineering community that pulsating flows lead to increased mass transfer (Taylor & Leonard 1965).

By definition, the variance of the solute distribution $\mu_2(t)$ is positive at all times, but this does not imply that the differential variance $D_{\text{eff}}(t) = \frac{1}{2}\frac{\text{d}\mu_2}{\text{d}t}$ also remains positive; in fact, negative values of $D_{\text{eff}}(t)$ are often encountered. In general, for short times $t \ll 1/\lambda_1, 1/(2\ell_{\max}\omega_{\text{o}})$, we find $D_{\text{eff}}(t) = 1 + t\,\text{Pé}^2 \sum_{n=1}^{\infty} \left|\langle f_n | u(0) \rangle\right|^2 > 0$, see Appendix, while for steady flow oscillations of large amplitudes $||u_\ell|| \gg ||u_0||$ the transient contraction of the solute concentration field associated with each reversal of the solvent flow direction leads to negative values of $D_{\text{eff}}(t)$. The cross-over point to negative values of $D_{\text{eff}}(t)$ depends on the relative amplitudes of all components of the velocity field, and is therefore not easily estimated in the general case. However, for the simple case of a single-frequency flow the cross-over point can be identified from Eq. (3.24). The time-averaged (positive) level is set by the diagonal terms $\ell = k$ for -1, 0, and 1 in the n-sum given by $|\langle u_0 | f_n \rangle|^2/\lambda_n + |\langle u_1 | f_n \rangle|^2 2\lambda_n/(\lambda_n^2 + \omega_{\text{o}}^2)$, while the cross-terms $\ell = -k$ for -1 and 1 gives the oscillating terms $2\text{Re}\left[\left(\langle u_1 | f_n \rangle \text{e}^{\text{i}\omega_{\text{o}} t}\right)^2/(\lambda_1 + \text{i}\omega_{\text{o}})\right]$. For the dominant $n = 1$ term at the intermediate frequency $\lambda_1 \ll \omega_{\text{o}} \lesssim \text{Sc}$, we can neglect λ_1 in the denominators, and since $\text{Wo} = \sqrt{\omega_{\text{o}}/\text{Sc}} \lesssim 1$ we have $\langle u_1 | f_n \rangle \approx \langle u_0 | f_n \rangle ||u_1||/||u_0||$, which results in $D_{\text{eff}} \propto 1 + 2\frac{||u_1||^2}{||u_0||^2}\frac{\lambda_1}{\omega_{\text{o}}}\left[\frac{\lambda_1}{\omega_{\text{o}}} + \sin(2\omega_{\text{o}} t + 2\phi_0)\right]$, where the phase ϕ_0 is

given by $\langle u_1 | f_n \rangle = |\langle u_1 | f_n \rangle| \, \mathrm{e}^{\mathrm{i}\phi_0}$. Negative values of $D_{\mathrm{eff}}(t)$ are therefore expected for $||u_1|| > ||u_0|| \sqrt{\omega_{\mathrm{o}}/(2\lambda_1)}$.

In the absence of a steady component in the velocity field, $u_0 = 0$, the period doubling is always present. Thus, for purely oscillating flows one finds a shear-enhanced dispersion above molecular diffusion, even though there is no net flow.

General conclusions for the shape dependence of D_{eff} may be obtained by applying random matrix theory (Mehta 2004) to the geometry-dependent inner product/eigenvalue expressions (3.22), (3.24), and (3.26) following the analysis of the shape-dependent quantum transport through quantum dots (Bruus & Stone 1994). For a non-integrable system the values of the inner products in Eq. (3.26) can be regarded as a random distribution with an average of the order unity. We therefore expect the sum to be dominated by the lowest eigenvalues, for which $\lambda_n \propto 1/R^2$, where R is the aspect ratio of the characteristic length scales of the two cross section directions ($R \geq 1$), which for a rectangle is the wide "width" divided by the short "height". Consequently $(D_{\mathrm{eff}}^{\mathrm{steady}} - 1) \propto \mathrm{Pé}^2 R^2$, indicating that the dominating length scale no longer is the short "height" but the wide "width". This is in agreement with the analysis of the shallow, slowly varying cross-sections studied by Ajdari *et al.* (2006) and Dutta *et al.* (2006).

The solute dispersion can be calculated from Eq. (3.22), if the Fourier series of the flow velocity is known, e.g. the single-frequency flow in a Newtonian fluids (Womersley 1955) or steady non-Newtonian fluid flow (Fan & Wang 1966). However, in the rest of the paper we restrict the application of our theory to the case of incompressible Newtonian fluids of kinematic viscosity (or momentum diffusivity) ν in the laminar regime which are governed by the time-dependent Stokes equation,

$$\partial_t u(\boldsymbol{r}_\perp, t) = \mathrm{Sc}\Big[\nabla_\perp^2 u(\boldsymbol{r}_\perp, t) + \frac{1}{\mathcal{L}} \Delta p(t)\Big]. \tag{4.1}$$

Here, $\Delta p(t)$ is the time-dependent pressure drop along the channel of length $\mathcal{L}$, resolved by the components $\varepsilon_\ell \Delta p \, \mathrm{e}^{\mathrm{i}\ell\omega_{\mathrm{o}} t}$ (ε_ℓ is a dimensionless amplitude) with the dimensionless base frequency $\omega_{\mathrm{o}} = \mathrm{Wo}^2\mathrm{Sc}$, and the dimensionfull pressure has been normalized by the shear-induced pressure $P_{\mathrm{o}} = \frac{\eta U_{\mathrm{o}}}{L_{\mathrm{o}}}$. The Schmidt number Sc appears since the time scale has been chosen to be the transverse mass diffusion time, and not the momentum diffusion time. The linearity of this equation allows us to solve the flow problem analytically and thereby obtain the Fourier coefficients u_ℓ and the momentum diffusion rate α_{fl}. The dispersion $D_{\mathrm{eff}}(t)$ depends on α_{fl}, and thus on Wo by Eq. (2.8), implicitly through the velocity components u_ℓ.

The effective diffusivity varies greatly depending on the system parameters. Below, we provide explicit estimates of the relaxation rates of the solute and fluid momentum, by analyzing specific time-dependent systems of increasing complexity through the addition of more time scales to both motion of the solvent and diffusion of the solute. We interpret the results for D_{eff} in terms of the relaxation rates and the flow frequencies in agreement with the general considerations just outlined.

5. Multiple-frequency flow in one-length-scale cross sections

We begin by analyzing channel cross sections with only one inherent length scale, such as the circular tube or the infinite parallel-plate slit, and the associated time scale for transverse solute diffusion. All results presented in this section are computed for the circular cross section, but qualitatively they apply to other single-length cross sections. We consider a circular tube of unit radius (the radius being $a = L_{\mathrm{o}}$ in dimensionfull coordinates) and calculate the velocity field from the Stokes equation, Eq. (4.1). Using

cylindrical coordinates and a generalized wavenumber k_ℓ, the velocity component u_ℓ fulfilling the boundary conditions $u|_{r=1} = 0$ and $\partial_r u|_{r=0} = 0$ is (Womersley 1955)

$$k_\ell = k_\ell(\mathrm{Wo}) = \sqrt{-\mathrm{i}\ell\mathrm{Wo}^2} = \sqrt{-\mathrm{i}\ell\omega_\mathrm{o}/\mathrm{Sc}}, \tag{5.1a}$$

$$\big|u_\ell\big\rangle = \varepsilon_\ell \frac{8}{k_\ell^2}\left[\frac{J_0(k_\ell r)}{J_0(k_\ell)} - 1\right], \tag{5.1b}$$

where the steady-state Poiseuille solution is $u_0(r) = \lim_{\ell\to 0} u_\ell(r) = \varepsilon_0 2(1-r^2)$. The velocity scale is taken to be the average steady state velocity $U_\mathrm{o} = \Delta p\, a^2/(8\eta\mathcal{L})$ for $\varepsilon_0 = 1$. The eigenfunctions and eigenvalues corresponding to Eq. (3.4) are

$$\big|f_n\big\rangle = \delta_{n,0} + (1-\delta_{n,0})\frac{J_0(\xi_{1,n}\, r)}{J_0(\xi_{1,n})}, \tag{5.2a}$$

$$\lambda_n = (1-\delta_{n,0})\xi_{1,n}^2, \tag{5.2b}$$

where $J_s(x)$ is the Bessel function of the first kind of order s, and $\xi_{s,n}$ is the nth root of $J_s(x)$. For cylindrical coordinates (axisymmetric case) $\big\langle f\big|g\big\rangle = \int_0^1 \mathrm{d}r\, 2r f^*(r)\, g(r)$, so

$$\big\langle f_n\big|u_\ell\big\rangle = -\varepsilon_\ell \frac{16}{(\xi_{1,n}^2 - k_\ell^2)k_\ell}\,\frac{J_1(k_\ell)}{J_0(k_\ell)},\ \text{for } n>0, \tag{5.3}$$

and $\big\langle f_n\big|u_0\big\rangle = \lim_{\ell\to 0}\big\langle f_n\big|u_\ell\big\rangle = -8/\xi_{1,n}^2$ for the steady term. Using these $\big\langle f_n\big|u_\ell\big\rangle$ in Eq. (3.22) allows us to calculate $D_\mathrm{eff}(t)$ for an unsteady flow, and by inserting them in Eq. (3.26) we recover $D_\mathrm{eff}^\mathrm{steady}(t) = 1 + \mathrm{P\acute{e}}^2\big[\frac{1}{48} - \sum_{n=1}^\infty (64/\xi_{1,n}^6)\exp(-\xi_{1,n}^2 t)\big]$, the classic result for a transient solute concentration in a steady-flow obtained by Barton (1983).

The fluid momentum equilibration rate for the circular cross section is $\alpha_\mathrm{fl} = \mathrm{Sc}\,\xi_{0,1}^2$, so the generalized wavenumber $k_\ell = \sqrt{-\mathrm{i}\ell\mathrm{Wo}^2} = \xi_{0,1}\sqrt{-\mathrm{i}\ell\omega_\mathrm{o}/\alpha_\mathrm{fl}}$ and the overlap integrals Eq. (5.3) depend explicitly on the fluid inertia through the ratio of the driving frequency ω_o to the fluid momentum equilibration rate α_fl.

5.1. *A steady-plus-one-frequency flow*

We consider now the simple case of a steady flow of fixed amplitude $\varepsilon_0 = 1$ with the addition of one oscillating component of variable amplitude ε_1. The dispersion in this particular flow has previously been studied to various levels of detail (Aris 1960; Chatwin 1975; Mukherjee & Mazumder 1988). Our theory both recovers, quantifies, and provides insight to the underlying physical mechanisms encountered in these previous studies.

$D_\mathrm{eff}(t)$ transiently builds towards a steady-oscillation level on the time scale $1/\lambda_1 = 1/\xi_{1,1}^2 = 0.068$, as seen in the example Fig. 1(a) (black line) for $\varepsilon_1 = 0.05$, $\mathrm{P\acute{e}} = 20$, $\mathrm{Sc} = 1000$, $\omega_\mathrm{o} = 200$, and $\mathrm{Wo} = \sqrt{\omega_\mathrm{o}/\mathrm{Sc}} = 0.447$. As expected from the general observations in Sec. 4, $D_\mathrm{eff}(t)$ oscillates around $D_\mathrm{eff}^\mathrm{avr}(t) \approx D_\mathrm{eff}^\mathrm{steady}(t)$ for $\varepsilon_1^2 \ll \varepsilon_0^2 = 1$ (gray line). The inset shows increasing $D_\mathrm{eff}^\mathrm{avr}(t)$ for growing oscillation amplitude, $\varepsilon_1 = 0$, 3, and 12, where $D_\mathrm{eff}^\mathrm{avr}$ changes from following D_eff fairly closely at $\varepsilon_1 = 3$ to being substantially enhanced for $\varepsilon_1 = 12$. In Fig. 1(b) we zoom in on the two gray zones of panel (a) to show the excellent agreement between our theory for $D_\mathrm{eff}(t) - D_\mathrm{eff}^\mathrm{steady}(t)$ (full line), numerics (circles, see Appendix for details), and the single-frequency theory of Mukherjee & Mazumder (1988) (stars).

Extending the physical analysis provided by Mukherjee & Mazumder (1988), we have augmented ε_1 by a factor 1000 to the value 50 in Fig. 1(c), and the normalized plot $D_\mathrm{eff}(t)/D_\mathrm{eff}^\mathrm{avr}(\infty)$ illustrates that the oscillation-induced enhancement of $D_\mathrm{eff}^\mathrm{avr}(t)$ shown in the inset of panel (a) is accompanied by both a period doubling in, and negative values of,

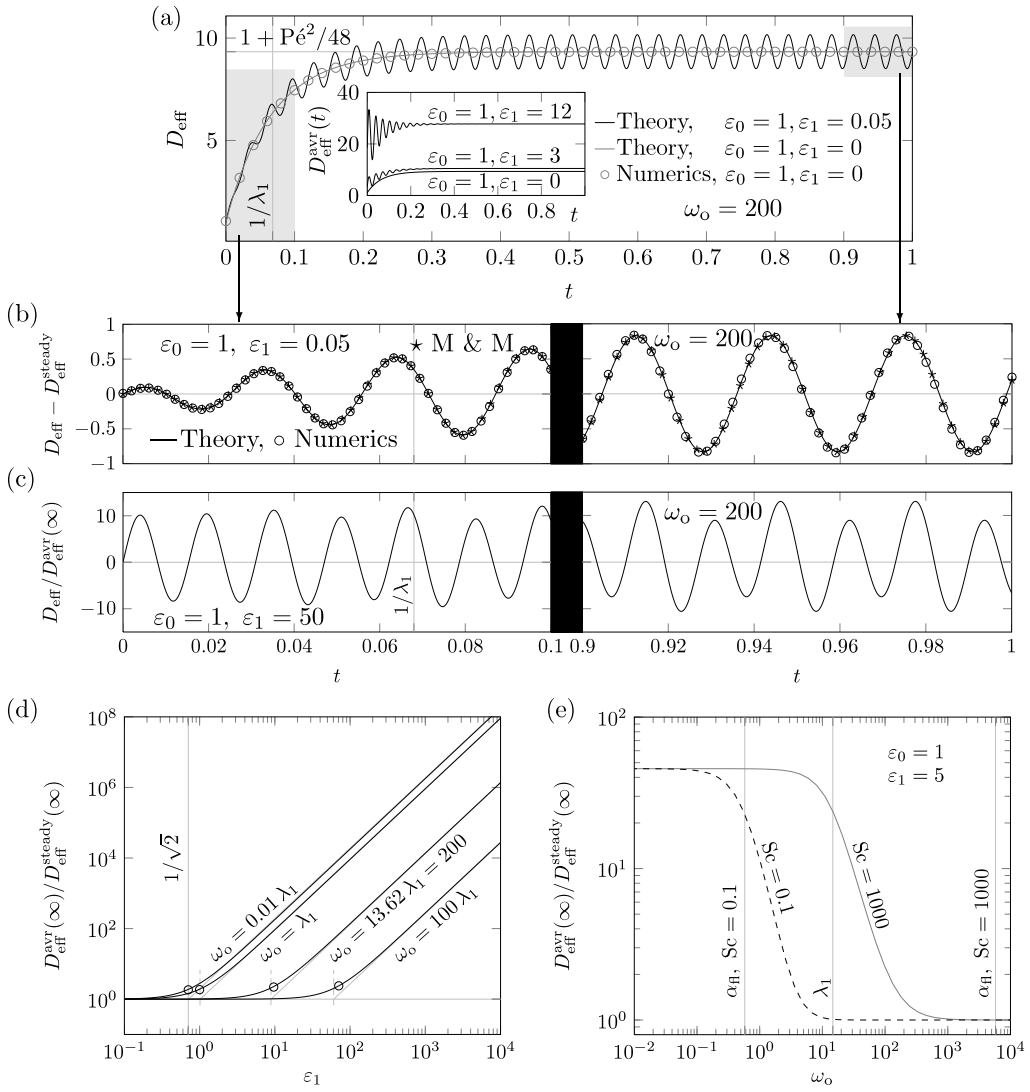

FIGURE 1. $D_{\mathrm{eff}}(t)$ calculated by Eq. (3.22) in a tube of circular cross section for a harmonically oscillating flow of frequency ω_{o} superimposed on a steady flow, Pé = 20. (a) $D_{\mathrm{eff}}(t)$ for $\omega_0 = 200$, Wo = 0.447 and velocity amplitudes $\varepsilon_1 = 0.05 \ll \varepsilon_0 = 1$ (black line) oscillating around $D_{\mathrm{eff}}^{\mathrm{steady}}(t)$ determined by theory Eq. (3.26) (gray line), and by direct numerical simulation (gray circles). The inset shows $D_{\mathrm{eff}}^{\mathrm{avr}}(t)$ for $\varepsilon_1 = 0$, 3, and 12, Eq. (3.23*b*). (b) Zoom-in on $D_{\mathrm{eff}}(t)$ for the initial transient period $0 < t < 0.1$ (left) and the steady regime $0.9 < t < 1$ (right) showing agreement between our theory (black line), our numerics (circles), and the theory of Mukherjee & Mazumder (1988) (M & M). (c) Normalized effective diffusivity $D_{\mathrm{eff}}(t)/D_{\mathrm{eff}}^{\mathrm{avr}}(\infty)$ showing period doubling; parameters as in panel (b) except now $\varepsilon_1 = 50$. (d) $D_{\mathrm{eff}}^{\mathrm{avr}}(\infty)/D_{\mathrm{eff}}^{\mathrm{steady}}(\infty)$, Eq. (5.5), versus ε_1 for four different frequencies ω_{o}. The cross-over point ε_1^c (open circles) from the linear regime ($D_{\mathrm{eff}}^{\mathrm{avr}}/D_{\mathrm{eff}}^{\mathrm{steady}} \approx 1$) to the non-linear one ($D_{\mathrm{eff}}^{\mathrm{avr}}/D_{\mathrm{eff}}^{\mathrm{steady}} \propto \varepsilon_1^2$) increases for increasing ω_{o}, as described by Eq. (5.6). (e) $D_{\mathrm{eff}}^{\mathrm{avr}}(\infty)/D_{\mathrm{eff}}^{\mathrm{steady}}(\infty)$ versus ω_{o} for two fluids. For Sc = 0.1 (gas-like, dashed line) it decreases to 1 once $\omega_{\mathrm{o}} > \alpha_{\mathrm{fl}}$ (solvent-momentum-diffusion limited), while for Sc = 1000 (water-like, gray line), it decreases to 1 when $\omega_{\mathrm{o}} > \lambda_1$ (solute-diffusion limited).

$D_{\text{eff}}(t)$ as discussed in Sec. 4. The onset of this non-linearity in the dispersion is further investigated in Fig. 1(d), where $D_{\text{eff}}^{\text{avr}}(\infty)/D_{\text{eff}}^{\text{steady}}(\infty)$ is plotted versus the oscillation amplitude ε_1: A cross-over from the linear regime, where $D_{\text{eff}}^{\text{avr}}(\infty)/D_{\text{eff}}^{\text{steady}}(\infty) \approx 1$, to the non-linear regime, where $D_{\text{eff}}^{\text{avr}}(\infty)/D_{\text{eff}}^{\text{steady}}(\infty) \propto \varepsilon_1^2$, happens at a frequency-dependent critical value ε_1^c. We estimate ε_1^c in the low-frequency limit $\text{Wo} \lesssim \xi_{0,1} \approx 2.40$ from Eq. (3.24) using that in this case $\langle u_1 | f_n \rangle \approx \langle u_0 | f_n \rangle$, and since

$$\varepsilon_\ell = \delta_{\ell,0} + \varepsilon_1 \big(\delta_{\ell,-1} + \delta_{\ell,1} \big), \tag{5.4}$$

it follows that

$$D_{\text{eff}}^{\text{avr}}(\infty) \approx 1 + \text{Pé}^2 \sum_{n=1}^{\infty} \left[1 + \frac{2\varepsilon_1^2}{1 + (\omega_{\text{o}}/\lambda_n)^2} \right] \frac{|\langle u_0 | f_n \rangle|^2}{\lambda_n}. \tag{5.5}$$

Thus, the cross-over to period-doubled behavior (dominance of the ε_1^2 term) happens when ε_1 equals

$$\varepsilon_1^c = \frac{1}{\sqrt{2}} \sqrt{1 + \frac{\omega_{\text{o}}^2}{\lambda_1^2}} = \begin{cases} \dfrac{1}{\sqrt{2}}, & \text{for } \omega_{\text{o}} \ll \lambda_1, \\ \dfrac{\omega_{\text{o}}}{\sqrt{2}\,\lambda_1}, & \text{for } \omega_{\text{o}} \gg \lambda_1. \end{cases} \tag{5.6}$$

When $\omega_{\text{o}} \ll \lambda_1$, the solute fully equilibrates by diffusion (λ_1 is the solute diffusion equilibration rate) and thereby exploits all velocity gradients, so the cross-over to period-doubled behavior happens as soon as the amplitude of the sinosoidal part of the velocity field exceeds that of the steady component, i.e. at the rms value $\varepsilon_1^c = 1/\sqrt{2}$ for $\varepsilon_0 = 1$. In contrast, for $\omega_{\text{o}} \gg \lambda_1$ the solute diffusion cannot fully follow the solvent oscillations, and only by increasing the amplitude significantly will the oscillation component contribute to D_{eff}, and as a consequence the cross-over amplitude scales as $\varepsilon_1^c \propto \omega_{\text{o}}/\lambda_1$. In Fig. 1(d) is shown that the estimates of Eq. (5.6) are correct. This result further agrees with, and quantifies, the observations of Chatwin (1975) and Watson (1983), but disagrees with Aris (1960), who based on cases with $\varepsilon_1 \leq 1$ predicted that the pulsatile contribution to $D_{\text{eff}}^{\text{avr}}(\infty)$ is less than one percent, which is clearly incorrect for large values of ε_1. For $\varepsilon_1 > \varepsilon_1^c$ we have $(D_{\text{eff}}^{\text{avr}} - 1) \propto \varepsilon_1^2 \text{Pé}^2$ signalling the change of characteristic velocity scale discussed in Sec. 4.

In addition to these limitations set by the equilibration of the solute, the dispersion may also be limited by fluid inertia, which similarly to the solute diffusion equilibration rate is characterized by a solvent-momentum equilibration rate α_{fl}. All time scales can be resolved by the solute when the driving frequency is much lower than the two equilibration rates, allowing time enough to establish the time-dependent velocity gradients and for the solute to diffuse in them, see Fig. 1(e). However, D_{eff} decreases if ω_{o} exceeds either of these equilibration rates.

The behavior of D_{eff} seems quantitatively similar whether the limiting factor is solute diffusion or solvent momentum diffusion, but the underlying physical mechanisms are different. For solute/solvent combinations which are limited by solute diffusion, $\lambda_1 \ll \alpha_{\text{fl}}$ (full gray line in Fig. 1(e)), the solute is constantly oscillating back and forth in addition to the steady motion as caused by the velocity field. This is still the case when $\omega_{\text{o}} > \lambda_1$, but here the solute only has time to diffuse by the gradients created by the steady velocity; new solute gradients are created by the oscillating part faster than the old gradients are smoothed out by diffusion. This corresponds to the case where the fluid is water.

In the other limit of solute/solvent configuration, $\alpha_{\text{fl}} \ll \lambda_1$, the limiting factor is the diffusion of fluid momentum (inertia): The fluid momentum does not have time to react

to the pressure oscillations at the driving frequency, so the fluid will only be moved by the steady part of the pressure. Thus, only the steady velocity field will shear the solute distribution resulting in the dispersion of only the steady flow. This effect is seen in the dashed black line in Fig. 1(e), which corresponds to the case where channel radius is the same as for the water case above (thus keeping λ_1 fixed) but the fluid is air (Lide 1995).

5.2. *A steady-plus-two-frequencies flow*

Through the driving pressure, we now add a second time scale to the flow so it consists of a steady component, and the two frequencies ω_o and $\tilde{\ell}\omega_o$, $\tilde{\ell}$ being an integer. The effects in D_{eff} of the previous subsection extend to the second frequency, and we continue to find good agreement between theory and numerics, see Fig. 2. We first take $\tilde{\ell} = 2$. As expected from the general observations in Sec. 4, $D_{\text{eff}}(t)$ oscillates around $D_{\text{eff}}^{\text{steady}}$ with the frequencies of the velocity field when the oscillation amplitudes ε_1 and ε_2 are sufficiently small (limits given below), see Fig. 2(a), while period-doubling and negative values appear when ε_1 and ε_2 become large, see Fig. 2(b). As for the single-frequency case, there is substantial increase of $D_{\text{eff}}^{\text{avr}}(\infty)/D_{\text{eff}}^{\text{steady}}(\infty)$ for large values of ε_1 and ε_2 and the cross-over to non-linearity for $\tilde{\ell} = 2$ may be predicted from simple estimates for $\text{Wo} \lesssim \xi_{0,1}$ as follows. Since

$$\varepsilon_\ell = \delta_{\ell,0} + \varepsilon_1\big(\delta_{\ell,-1} + \delta_{\ell,1}\big) + \varepsilon_2\big(\delta_{\ell,-2} + \delta_{\ell,2}\big), \tag{5.7}$$

we distinguish between the three regimes $\varepsilon_2 \ll 1$, $\varepsilon_1 \ll 1$ and $\varepsilon_1 = \varepsilon_2$. In the first case we trivially retrieve the result Eq. (5.6), while the second case similarly yields

$$\varepsilon_2^c = \frac{1}{\sqrt{2}}\sqrt{1 + \frac{4\omega_o^2}{\lambda_1^2}} = \begin{cases} \dfrac{1}{\sqrt{2}}, & \text{for } \omega_o \ll \lambda_1, \\[2ex] \dfrac{\sqrt{2}\,\omega_o}{\lambda_1}, & \text{for } \omega_o \gg \lambda_1. \end{cases} \tag{5.8}$$

Hence, the period doubling for each of the velocity field frequencies is independent, since a significant non-linear effect is found when either $\varepsilon_1 > \varepsilon_1^c$ or $\varepsilon_2 > \varepsilon_2^c$. In the third case of $\varepsilon_1 = \varepsilon_2 = \varepsilon$, we find

$$\varepsilon^c = \frac{1}{\sqrt{2}}\sqrt{\frac{1 + \frac{5\omega_o^2}{\lambda_1^2} + \frac{4\omega_0^4}{\lambda_1^4}}{1 + \frac{5\omega_o^2}{\lambda_1^2}}} = \begin{cases} \dfrac{1}{\sqrt{2}}, & \text{for } \omega_o \ll \lambda_1, \\[2ex] \sqrt{\dfrac{2}{5}}\dfrac{\omega_o}{\lambda_1}, & \text{for } \omega_o \gg \lambda_1, \end{cases} \tag{5.9}$$

where both thresholds are slightly lower than those of the single-frequency Eq. (5.6).

Our understanding of the behavior of $D_{\text{eff}}^{\text{avr}}$ from the involved diffusion processes of fluid momentum and solute, presented in the previous section on single-frequency flow, applies to each of the frequencies of the flow. The addition of a second velocity frequency introduces more shear and hence more gradients to the concentration field and $D_{\text{eff}}^{\text{avr}}$ therefore increases even further when all velocity frequencies can be resolved, see dashed line in Fig. 2 (c), where solute diffusion is the limiting process ($\lambda_1 \ll \alpha_{\text{fl}}$) and where for clarity the second frequency is $30\omega_o$ instead of the $2\omega_o$. Two distinct decreases are found in this curve: the first is when the solute equilibration rate λ_1 surpasses $30\omega_o$, and the second when λ_1 increases past the base frequency. The decreases arise because the gradients created by $30\omega_o$ and ω_o, respectively, can no longer be exploited by the solute. When both frequencies can be resolved $D_{\text{eff}}^{\text{avr}}$ is almost a factor two greater than the single-frequency case of Fig. 1(e), here reproduced as the gray line, so the second

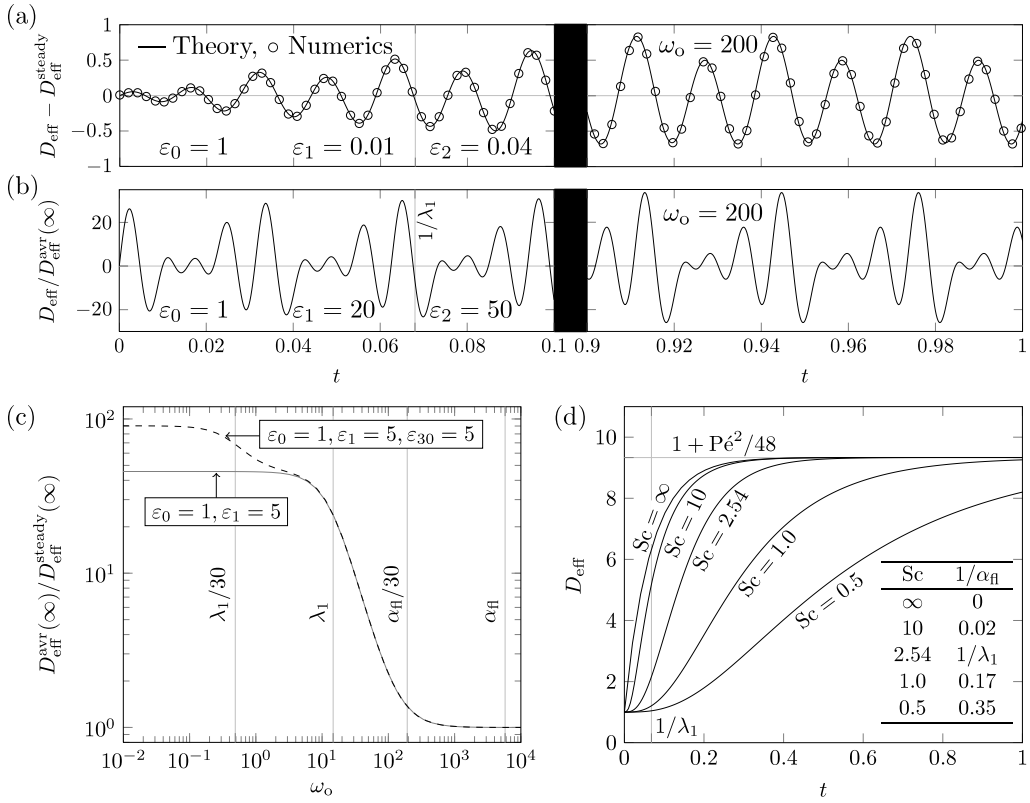

FIGURE 2. Calculated $D_{\text{eff}}(t)$ for a circular cross section as in Fig. 1, but with a second oscillating velocity component added. (a) $D_{\text{eff}}(t) - D_{\text{eff}}^{\text{steady}}(t)$ from Eq. (3.22) (black line) and numerics (circles) the transient period (left) and the steady regime (right) for small amplitudes, $\varepsilon_1 = 0.01$ and $\varepsilon_2 = 0.04$. (b) As in panel (a), but for large amplitudes, $\varepsilon_1 = 20$ and $\varepsilon_2 = 50$, showing period doubling for both ω_o and $2\omega_o$. (c) $D_{\text{eff}}^{\text{avr}}(\infty)/D_{\text{eff}}^{\text{steady}}(\infty)$ versus ω_o for $\text{Sc} = 10^3$ and $\varepsilon_0 = 1$, $\varepsilon_1 = \varepsilon_{30} = 5$ (dashed curve). For clarity $\tilde{\ell} = 30$ is used instead of $\tilde{\ell} = 2$ to better illustrate the effects of each frequency. $D_{\text{eff}}^{\text{avr}}(\infty)$ decreases in two steps as ω_o crosses $\lambda_1/30$ and λ_1. The one-frequency case Fig. 1(e), $\text{Sc} = 10^3$ (gray curve), is shown for comparison. (d) Startup of tube flow from rest: Calculated $D_{\text{eff}}(t)$ versus time for $\text{Pé} = 20$. For $\text{Sc} \lesssim 1$ the dispersion saturates on the solvent acceleration time scale $1/\alpha_{\text{fl}} \approx 1/\text{Sc}$, while for $\text{Sc} \gg 1$ it saturates on the solute diffusion time $1/\lambda_1 = 1/\xi_{1,1}^2 \approx 0.07$. The Fourier series has $T = 5$ and contains 1000 terms.

velocity frequency leads to a large enhancement of D_{eff}. Had we chosen $\alpha_{\text{fl}} \ll \lambda_1$ in the figure, the same decreases would have been observed around $30\omega_o \approx \alpha_{\text{fl}}$ and $\omega_o \approx \alpha_{\text{fl}}$.

5.3. *Unsteady, unidirectional flow: startup of Poiseuille flow*

In the previous sections we found that fluid inertia limits the solute dispersion because the flow does not equilibrate to a steady state. To further investigate the inertial effects we consider solute in a circular channel where the solvent, after initially being at rest, suddenly at $t = 0$ begins to move due to an instantly applied pressure drop along the channel. The analytical solution of this startup of a Poiseuille flow is found in terms of a Fourier–Bessel expansion in the radial coordinate, where each term is multiplied by an

exponential time decay of rate α_m (Batchelor 1967),

$$u(r,t) = 2\big(r^2-1\big) - \sum_{m=1}^{\infty} \frac{16}{\xi_{0,m}^3} \frac{J_0(\xi_{0,m} r)}{J_1(\xi_{0,m})}\, \mathrm{e}^{-\alpha_m t}, \tag{5.10a}$$

$$\alpha_m = \mathrm{Sc}\, \xi_{0,m}^2, \text{ for } m = 1,2,3,\ldots. \tag{5.10b}$$

The smallest of these inertial decay rates, $\alpha_1 = \xi_{0,1}^2 \mathrm{Sc} \approx 5.78\,\mathrm{Sc} = \alpha_{\mathrm{fl}}$, sets the characteristic time of the acceleration $1/\alpha_{\mathrm{fl}}$ as in Eq. (2.7) and in Sec. 5.1. To align this solution with the developed theory, the temporal functions are written as Fourier series with a base-period T much larger than the acceleration time, $T \gg 1/\alpha_{\mathrm{fl}}$. Hence, the flow will reach a steady state significantly faster than the base-period T, and the approximation will be the correct solution for $0 < t < T$. We obtain

$$u(r,t) = 2\big(1-r^2\big) - \sum_{m=1}^{\infty} \sum_{\ell=-\infty}^{\infty} \frac{16 J_0(\xi_{0,m} r)}{\xi_{0,m}^3 J_1(\xi_{0,m})} A_{\ell m} \mathrm{e}^{\mathrm{i}\ell\omega_{\mathrm{o}} t}, \tag{5.11a}$$

$$A_{\ell m} = \frac{1-\mathrm{e}^{-\alpha_m T}}{\alpha_m T + \mathrm{i}\ell 2\pi}, \tag{5.11b}$$

where $\omega_{\mathrm{o}} = 2\pi/T$ so that $\mathrm{Wo} = \sqrt{2\pi/(\mathrm{Sc}T)} = \xi_{0,1}\sqrt{2\pi/(\alpha_{\mathrm{fl}}T)}$. The velocity scale is the same as for a steady flow in a circular tube, so the ℓth velocity component $u_\ell(r)$ is

$$u_\ell(r) = 2\left(1-r^2\right)\delta_{\ell,0} - \sum_{m=1}^{\infty} \frac{16\, A_{\ell m} J_0(\xi_{0,m} r)}{\xi_{0,m}^3\, J_1(\xi_{0,m})}. \tag{5.12}$$

Combining this with the eigenvalue solution of Eq. (5.2), we find for $n > 0$

$$\big\langle f_n \big| u_\ell \big\rangle = -\frac{8\delta_{\ell,0}}{\xi_{1,n}^2} - \sum_{m=1}^{\infty} \frac{32\left(1-\mathrm{e}^{-\alpha_m T}\right)}{\xi_{0,m}^2\big(\xi_{0,m}^2 - \xi_{1,n}^2\big)\big(\alpha_m T + \mathrm{i}\ell 2\pi\big)}. \tag{5.13}$$

The two physical processes of fluid acceleration and solute dispersion happens on the two time scales $1/\alpha_{\mathrm{fl}}$ and $1/\lambda_1$, respectively, but since fluid motion is required to generate the shear needed for the Taylor–Aris dispersion effect, the dispersion is limited by either the solute diffusion, or solvent inertia. In the first case ($\alpha_{\mathrm{fl}} \gg \lambda_1$), the fluid reaches steady state much faster than the solute, and the dispersion therefore behaves as in the case of a steady flow. Since $\alpha_{\mathrm{fl}} \propto \mathrm{Sc}$ this can be thought of as having $\mathrm{Sc} = \infty$, so the only transient behavior observed is that of the solute diffusion; this is the case of water. For the second case ($\alpha_{\mathrm{fl}} \propto \mathrm{Sc} \ll \lambda_1$) with slower momentum equilibration rates $0.1 < \mathrm{Sc} < 10$ found in gases (Lide 1995), the solute dispersion evolves in the slow increase of the velocity shear gradients, which now dominates the transient behavior, and $D_{\mathrm{eff}}(t)$ is thus smaller than $D_{\mathrm{eff}}^{\mathrm{steady}}(t)$. These inertial effects are illustrated in Fig. 2(d), where dispersion co-evolves with the transient start-up of a Poiseuille flow in a straight tube at $\mathrm{Pé} = 20$, and where the equilibration rates for solute mass diffusion and solvent momentum diffusion are equal for $\mathrm{Sc} = \xi_{1,1}^2/\xi_{0,1}^2 = 2.54$. We take $T = 5$, and to diminish unphysical effects of the Gibbs phenomenon close to $t = 0$, we include 1000 terms in the Fourier series.

In conclusion, fluid inertia limits fluid shear and hence the solute dispersion. However, given the characteristic time scale $1/\alpha_{\mathrm{fl}} \propto 1/\mathrm{Sc} \ll 1/\lambda_1$, inertial effects only become important for Taylor–Aris dispersion in gasses.

6. Multiple-frequency flow in two-length-scale cross sections

We move on to consider the effects of adding a second length scale to the cross sectional geometry. We illustrate this case by use of the rectangle, but the presented findings hold quantitatively for other cross section with two length scales, e.g. the ellipse.

6.1. *The rectangular cross section*

We denote the height of the channel $2a$ and the width $2w$, with $w \geq a$ so that the aspect ratio $R = w/a$ satisfies $R \geq 1$. We take the characteristic length scale to be $L_\mathrm{o} = a$, so Pé $= U_\mathrm{o} a/D$ and Wo $= \sqrt{a^2\tilde{\omega}_\mathrm{o}/\nu}$, and in non-dimensional units we place the rectangular cross section such that $-R \leq y \leq R$ and $-1 \leq z \leq 1$. The analytical velocity field for the steady Poiseuille flow is well-known, see e.g. Bruus (2008), and in analogy with Eq. (5.1*b*) by introducing a generalized wavenumber $q_{j\ell}$, the pulsatile velocity field is found by a trivial extension thereof,

$$q_{j\ell} = q_{j\ell}(\mathrm{Wo}) = \sqrt{\mathrm{i}4\mathrm{Wo}^2\ell + j^2\pi^2}, \tag{6.1a}$$

$$\big|u_\ell\big\rangle = \varepsilon_\ell(1+\delta_{\ell,0})\frac{24}{\Gamma}\sum_{j,\mathrm{odd}}^{\infty}\frac{1}{j\pi q_{j\ell}^2}\left[1-\frac{\cosh\left(q_{j\ell}\frac{y}{2}\right)}{\cosh\left(q_{j\ell}\frac{R}{2}\right)}\right]\sin\left(j\pi\frac{z+1}{2}\right), \tag{6.1b}$$

where the pre-factor Γ and the velocity scale U_o (chosen as the is the cross-sectional average of the steady flow with $\varepsilon_0 = 1$) are given by

$$\Gamma = \Gamma(R) = 1 - \sum_{j,\mathrm{odd}}^{\infty}\frac{1}{j^5}\frac{192}{\pi^5}\frac{1}{R}\tanh\left(j\pi\frac{R}{2}\right), \tag{6.2a}$$

$$U_\mathrm{o} = \frac{\Delta p\, a^2\,\Gamma}{3\eta\mathcal{L}}. \tag{6.2b}$$

The steady flow profile is retrieved from Eq. (6.1*b*) by the limit $u_0(y,z) = \lim_{\ell\to 0} u_\ell(y,z)$ using $q_{j0} = j\pi$. Similar to the circular cross section, the generalized wavenumber $q_{j\ell}$ depends explicitly on the fluid momentum equilibration rate $\alpha_\mathrm{fl} = (1+1/R^2)\frac{\pi^2}{4}\mathrm{Sc}$ since $q_{j\ell} = \pi\sqrt{\mathrm{i}\ell(1+\frac{1}{R^2})\frac{\omega_\mathrm{o}}{\alpha_\mathrm{fl}} + j^2}$. The corresponding basis functions and eigenvalues are

$$\big|f_{nm}\big\rangle = \frac{2\cos\left(n\pi\frac{y+R}{2R}\right)\cos\left(m\pi\frac{z+1}{2}\right)}{\sqrt{(1+\delta_{n,0})\,(1+\delta_{m,0})}}, \tag{6.3a}$$

$$\lambda_{nm} = \left(\frac{n\pi}{2R}\right)^2 + \left(\frac{m\pi}{2}\right)^2, \quad n,m = 0,1,2,\ldots \tag{6.3b}$$

which satisfy the requirement $\big|f_{00}\big\rangle = 1$ with $\lambda_{00} = 0$. The single index n of Eq. (5.2) is here changed to the double index (n,m), and $n = 0$ to $(n,m) = (0,0)$. The inner products $\big\langle f_n\big|u_\ell\big\rangle$ of Eq. (3.22) become $\big\langle f_{nm}\big|u_\ell\big\rangle$ given by,

$$\big\langle f_{nm}\big|u_\ell\big\rangle = \begin{cases} \dfrac{\epsilon_\ell(1+\delta_{l,0})}{\sqrt{(1+\delta_{n,0})\,(1+\delta_{m,0})}}\dfrac{96R}{\Gamma\pi^2}\displaystyle\sum_{j,\mathrm{odd}}^{\infty}\frac{q_{jl}R\delta_{n,0} - 2\tanh\left(\frac{q_{jl}R}{2}\right)}{q_{jl}(j^2-m^2)(n^2\pi^2+q_{jl}^2R^2)}, & n,m \text{ even}, \\ 0, & \text{otherwise}, \end{cases} \tag{6.4}$$

and sums $\sum_{n=1}^{\infty} = \sum_{n\neq 0}^{\infty}$ become $\sum_{\{n,m\}\neq\{0,0\}}^{\infty}$.

The two inherent length scales of this cross section introduce two diffusion times, one

along each coordinate direction, and hence two solute equilibration rates,

$$\lambda_{20}(R) = \frac{\pi^2}{R^2} \text{ (width)} \quad \text{and} \quad \lambda_{02} = \pi^2 \text{ (height)}. \tag{6.5}$$

We have previously described how the behavior of D_{eff} can be understood in terms of the involved diffusion processes of fluid momentum and solute, and it follows directly that while this obviously extends to the present case, the presence of the additional time scales from the second geometric dimension introduces more structure: for each frequency in the fluid velocity field, the solute dispersion will increase if it has time to equilibrate along either of its transverse directions (i.e. if $\omega_{\text{o}} \lesssim \lambda_{20}$ or $\omega_{\text{o}} \lesssim \lambda_{02}$), with more dispersivity when the frequency allows equilibration along both directions. Thus, for a velocity field with two frequency scales there will be four critical frequencies: the two solute equilibration rates for each of the two fluid time scales. This is illustrated in Fig. 3(a) for the case of $\varepsilon_0 = \varepsilon_1 = \varepsilon_{30} = 1$ with Pé $= 20$ and $R = 100$, and for a solvent/solute composition such that the equilibration rate of the solvent momentum $\alpha_{\text{fl}} = (1 + 1/R^2)\frac{\pi^2}{4}\text{Sc}$ is much greater than those of the solute diffusion, λ_{20} and λ_{02}. As function of driving frequency ω_{o}, $D_{\text{eff}}^{\text{avr}}$ decreases in four steps: The first two and most significant drops happen near $\lambda_{20}/30$ and λ_{20}, where the diffusion across the width no longer can exploit the gradients of first the $30\omega_{\text{o}}$-harmonic and then the ω_{o}-harmonic. The last two (minor) drops happen near $\lambda_{02}/30$ and finally λ_{02}, where the height-diffusion ceases to be able to follow the $30\omega_{\text{o}}$-harmonic and lastly the ω_{o}-harmonic. The substantial increases in time-averaged dispersion found for the two-frequency-flow of the previous section is again found in this case: for low frequencies ω_{o} which allow complete solute equilibration, $D_{\text{eff}}^{\text{avr}}$ is almost a factor of two greater than when only the steady velocity contributes to the solute dispersion ($D_{\text{eff}}^{\text{avr}}(\infty) = 120.41$ at $\omega_{\text{o}} = 10^{-8}$ compared to $D_{\text{eff}}^{\text{avr}}(\infty) = 60.70$ at $\omega_{\text{o}} = 10^4$). For comparison we have also included the special case of $R = 1$, a one-length-scale cross section, where the two solute diffusion equilibration rates λ_{20} and λ_{02} are identical, and where we consequently find only two decreasing steps. We have also validated our theory against numerics for the case $R = 1$ (details given in the Appendix), and find excellent agreement.

Since the solute equilibration rate λ_{20} depends on the aspect ratio R, Eq. (6.5), the same frequency ω_{o} and velocity component amplitudes ε_ℓ will give rise to different behaviors of D_{eff} in channels of different R. This is plotted in Fig. 3(b) for $\omega_{\text{o}} = 10^4$ and $\omega_{\text{o}} = 10^{-7}$ with the flow chosen as in (a) to be a two-frequency flow with amplitudes $\varepsilon_0 = \varepsilon_1 = \varepsilon_{30} = 1$. For reference we have also plotted the dependence of $D_{\text{eff}}^{\text{steady}}$ in the limit $R \to \infty$ where we retrieve the well-known result (Doshi *et al.* 1978; Chatwin & Sullivan 1982) $D_{\text{eff}}^{\text{steady}}(\infty) = 1 + \chi_{\text{rect}}\text{Pé}^2$ with $\chi_{\text{rect}} = \frac{2}{105} + \frac{11532\,\zeta(5)^2}{\pi^{10}}$ where $\zeta(x) = \sum_{j=1}^{\infty} j^{-x}$ is the Riemann zeta function. For sufficiently fast oscillation, here $\omega_{\text{o}} = 10^4$ (lower black line), we have $\omega_{\text{o}} \gg \lambda_{02}$, and as in Fig. 2(b) this is too fast for the solute diffusion to follow, and we recover the steady-flow case (triangles) and $D_{\text{eff}}^{\text{avr}}(\infty) = D_{\text{eff}}^{\text{steady}}(\infty)$. Had we chosen larger oscillation amplitudes ε_ℓ the non-linear effect discussed in Sec. 4 would had set in and increased $D_{\text{eff}}^{\text{avr}}$. For the fixed slow oscillation frequency $\omega_{\text{o}} = 10^{-7}$ (top black line), $D_{\text{eff}}^{\text{avr}}$ initially increases with R, as the solute diffusion now is able to follow the fluid movement. However, due to the R-dependence of λ_{20} in Eq. (6.5), a point is reached beyond which $\lambda_{20}(R)/30 < \omega_{\text{o}}$, and $D_{\text{eff}}^{\text{avr}}$ decreases to a lower value. Later, when $\lambda_{20}(R)$ falls below ω_{o}, a second decrease occurs, after which $D_{\text{eff}}^{\text{avr}}$ settles at $D_{\text{eff}}^{\text{steady}}(\infty) = 1 + \chi_{\text{rect}}\text{Pé}^2$, since none of the added shear of the time-dependent velocity components contribute to $D_{\text{eff}}^{\text{avr}}$.

The highest value of $D_{\text{eff}}^{\text{avr}}$ achievable for a fixed velocity field with fixed frequency ω_{o}

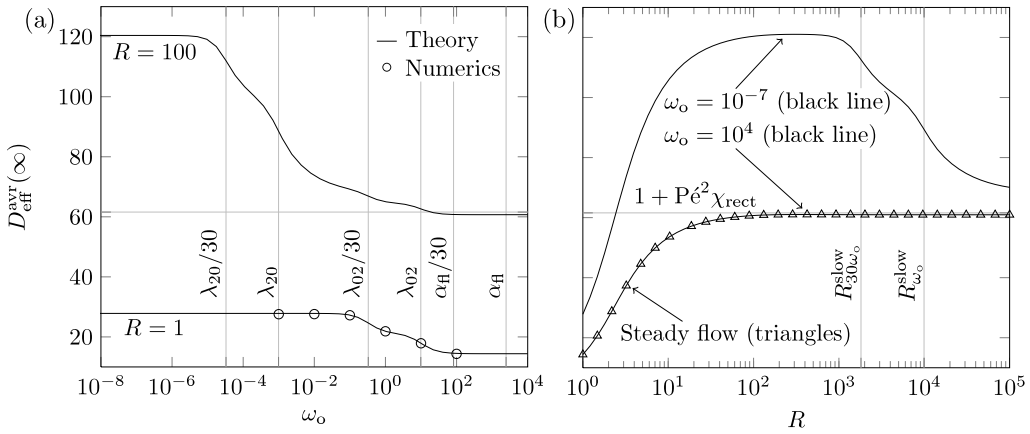

FIGURE 3. $D_{\text{eff}}^{\text{avr}}(\infty)$ for a two-frequency flow $\varepsilon_0 = \varepsilon_1 = \varepsilon_{30} = 1$ in rectangular channels of aspect ratio R. (a) $D_{\text{eff}}^{\text{avr}}(\infty)$ versus base frequency ω_{o} for $R = 1$ and $R = 100$ at Pé $= 20$, and with the agreement with numerics (circles) illustrated at $R = 1$ (details given in the Appendix). As ω_{o} increases $D_{\text{eff}}^{\text{avr}}$ decreases in four steps, namely when ω_{o} crosses $\lambda_{20}/30$, λ_{20}, $\lambda_{02}/30$, and λ_{02} (for $R = 100$). For $R = 1$ there are only two steps, namely when ω_{o} crosses $\lambda_{02}/30$ and λ_{02} this rate being the same for $R = 1$ and $R = 100$. (b) $D_{\text{eff}}^{\text{avr}}(\infty)$ versus R for fast oscillation ($\omega_{\text{o}} = 10^4$) and steady flow, both recovering the behavior of Fig. 1(a), and for slow oscillation ($\omega_{\text{o}} = 10^{-7}$), for which $D_{\text{eff}}(\infty)$ reaches a maximum before decreasing in two steps at $\lambda_{20}(R) = 30 \times 10^{-7}$ and $\lambda_{20}(R) = 10^{-7}$, marked by the aspect ratios $R_{30\omega_{\text{o}}}^{\text{slow}}$ and $R_{\omega_{\text{o}}}^{\text{slow}}$, respectively.

is found in a region with the upper limit set by $3\,\ell_{\max}\omega_{\text{o}} \approx \lambda_{20} = \pi^2/R^2$, where $\ell_{\max}$ is the maximum frequency component in the velocity field, and the lower limit is set by the value of R which ensures that the steady part of the velocity field reaches the maximum dispersion of $D_{\text{eff}}^{\text{steady}}(\infty) = 1 + \text{Pé}^2\chi_{\text{rect}}$, $R \lesssim 100$.

Finally, a brief discussion is in order regarding the behavior of $D_{\text{eff}}^{\text{steady}}(\infty)$ in the limit $R \to \infty$. It is well-known that $\chi_{\text{rect}} = \frac{2}{105} + \frac{11532\,\zeta(5)^2}{\pi^{10}} \approx 7.95\chi_{\text{plate}}$ where $\chi_{\text{plate}} = 2/105$ is the coefficient for infinite parallel plates (no side walls), which might seem to contradict the general scaling of $(D_{\text{eff}} - 1) \propto \text{Pé}^2/R^2$ described in Sec. 4. However, the rectangular cross section is integrable, and the inner products $\langle f_{n0} | u_0 \rangle \propto 1/R$, because as function of the width coordinate y, u_0 is constant except for the ends covering a fraction $1/R$ of the width, while f_{n0} oscillates, see Eqs. (6.1*b*) and (6.3*a*). As a result, the factor R^2 from $1/\lambda_{nm}$ is canceled by the factor $1/R^2$ from the inner product, and $(D_{\text{eff}}^{\text{steady}} - 1) \propto \text{Pé}^2$, making the small height the dominant length scale. This explains why in $\chi_{\text{rect}} \approx \chi_{\text{plate}}$ instead of $\chi_{\text{rect}} \approx \chi_{\text{plate}} R^2$. Physically, the steady flow in high-aspect ratio rectangular channels is independent of the channel width except for boundary layers of width unity near the side walls, while it remains parabolic in the height. Compared to the infinite parallel plate channel, the side walls therefore increase both the mean velocity and the created gradients in the concentration field along the height, causing an increase of $D_{\text{eff}}(\infty)$, which none the less remains on the order of $D_{\text{eff}}(\infty)$ from the parallel plates. For channel cross sections which vary continuously along both cross section directions (e.g. elliptic), the characteristic length scale of velocity variations is of order R, resulting in shear along all of R and the scaling $(D_{\text{eff}}^{\text{steady}} - 1) \propto \text{Pé}^2 R^2$ as described in Sec. 4

6.2. *Analysis of a peristaltic micropump*

To illustrate the pratical usefulness of the developed theory, we here shortly describe dispersion-limiting of a micropump. The pressure delivered by the novel 12-channel, eight-roller, peristaltic pump for microfluidics of Skafte-Pedersen *et al.* (2009)is pulsating

R	2.67	ε_0	1.000	α_{fl}	2810
Pé	6.92	ε_1	$0.352\exp(-2.19\mathrm{i})$	ω_{o}	2.94
Wo	0.05	ε_2	$0.203\exp(-2.24\mathrm{i})$	λ_{20}	1.39
Sc	1000	ε_3	$0.059\exp(+1.54\mathrm{i})$	λ_{02}	9.87

TABLE 1. Dimensionless parameters of the flow generated by the peristaltic pump of Skafte-Pedersen *et al.* (2009), see Sec. 6.2.

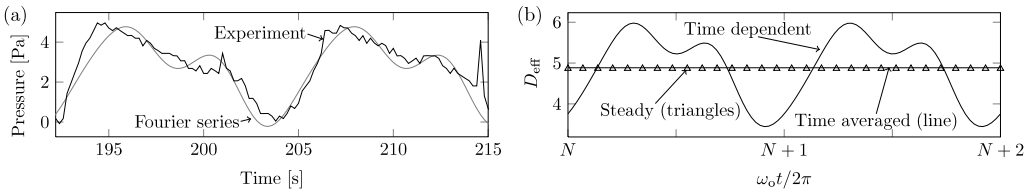

FIGURE 4. (a) Two periods of the measured time-dependent pressure delivered by the peristaltic pump (black) by Skafte-Pedersen *et al.* (2009) and of the approximate Fourier series ($|\ell| \leq 3$) used in the analysis (gray). (b) Calculated $D_{\mathrm{eff}}(t)$ for the two cycles of the peristaltic pump following period $N = 10^4$ after the decay of all transients: the Fourier series (black), only the steady component (dashed), and the time-averaged Fourier series (gray).

with the operating base frequency $\tilde{\omega}_{\mathrm{o}} = 0.52$ rad/s, as measured in a rectangular channel of $R = 2.67$ ($a = 75$ μm, $w = 200$ μm), and shown by the black line in Fig. 4(a). To analyze the influence of this time-dependent flow on the dispersion of a solute with typical molecular diffusivity $D = 10^{-9}$ m^2/s, we approximate the pressure by a Fourier series with $|\ell| \leq 3$ (gray line). The discrepancy between the approximation and the actual signal fluctuates faster than the highest harmonic and is not resolved by the solute. The velocity scale U_{o} is taken as the (dominating) steady component, and the dimensionless parameters of the system are listed in Table 1.

The pump is designed to have minimal dispersion, which follows from our theory: It is normally operated at $\omega_{\mathrm{o}} = 2.94$, which is faster than the solute equilibration rate $\lambda_{20} = 1.39$ of the width, so only the diffusion in the height-direction with $\lambda_{02} = 9.87$ is resolved. Furthermore, because the square of all oscillation amplitudes are small, $|\varepsilon_\ell| < 0.12$, their contribution to D_{eff} is minute, and $D_{\mathrm{eff}}^{\mathrm{avr}}(\infty) = 1.004 D_{\mathrm{eff}}^{\mathrm{steady}}(\infty)$, see Fig. 4(b). The dispersion may be increased by running the pump at lower frequency, e.g. $D_{\mathrm{eff}}^{\mathrm{avr}}(\infty) = 1.17 D_{\mathrm{eff}}^{\mathrm{steady}}(\infty)$ changing ω_{o} to $0.1\omega_{\mathrm{o}}$, or with higher oscillation amplitudes, $D_{\mathrm{eff}}^{\mathrm{avr}}(\infty) = 1.39 D_{\mathrm{eff}}^{\mathrm{steady}}(\infty)$ changing ε_ℓ to $10\varepsilon_\ell$ for $\ell \neq 0$. If these changes are made simultaneously, we find $D_{\mathrm{eff}}^{\mathrm{avr}}(\infty) = 2.76 D_{\mathrm{eff}}^{\mathrm{steady}}(\infty)$.

7. Concluding remarks

By combining Aris's method of moments and Dirac's bra-ket formalism, we have derived the compact, closed form (3.22) for the transient Taylor–Aris dispersion or effective diffusivity $D_{\mathrm{eff}}(t)$ valid for any time-dependent flow in a long, straight channel of arbitrary but constant cross section. For a general time-dependent flow, and as a function of system parameters, $D_{\mathrm{eff}}(t)$ exhibits a rich and non-trivial structure due to the interplay between internal equilibration rates and external driving frequencies. Our analysis based on Eq. (3.22) has led to the following conclusions:

(i) In general, the effective diffusivity is enhanced significantly by those parts of the time-dependent velocity field that have frequencies $\ell\omega_{\mathrm{o}}$ lower than the fluid momentum

diffusion rate $\alpha_{\rm fl}$ and the solute diffusion rate λ_1, in which case the dispersive effect has sufficient time to fully evolve.

(*ii*) We have explained why sufficiently large oscillation amplitudes $||u_\ell||$ lead to negative values of the instantaneous effective diffusivity $D_{\rm eff}(t)$. In Sec. 4 an amplitude threshold value for this transition has been derived for a steady-plus-one-frequency flow. This threshold depends on the ratio $\sqrt{\omega_{\rm o}/(2\lambda_1)}$.

(*iii*) As function of the normalized amplitudes ε_ℓ of the oscillatory flow components, scaling laws have been derived for the cross-over ε^c of the time-averaged effective diffusivity $D_{\rm eff}^{\rm avr}(t)$ from the linear regime of small oscillatory flow components superimposed on a large steady flow component of normalized amplitude ε_0, to the nonlinear, period-doubled regime of large oscillation amplitudes. Specific examples are shown in Secs. 5.1 and 5.2 for steady-plus-one- and steady-plus-two-frequency flows.

(*iv*) Our formulation of $D_{\rm eff}$ in terms of inner products (overlap integrals) and eigenvalues facilitates general analyses in terms of random matrix theory. As an example of such an analysis we have sketched an explanation for the well-known fact that the relevant Péclet number for the Taylor–Aris dispersion in a channel of rectangular cross section involves the short height and not as expected on general grounds, the wide width.

(*v*) For Newtonian solvents we have validated our theory by comparing it with the special cases of dispersion in steady flow and single-frequency pulsating flow treated in the literature, and by direct numerical simulations of single- and multiple-frequency flows in circular, Fig. 1(b) and Fig. 2(a), and rectangular cross sections, Fig. 3(a).

(*vi*) For Newtonian solvents in the cases of one-length-scale and steady-plus-one-frequency flow, Fig. 1(e), one-length-scale and steady-plus-two-frequency flow, Fig. 2(c), and two-length-scale and steady-plus-two-frequency flows, Fig. 3(a), we have characterized the explicit suppression of the oscillatory enhancement of $D_{\rm eff}^{\rm avr}(\omega_{\rm o})$ each time a driving frequency $\ell\omega_{\rm o}$ becomes larger than the internal diffusion relaxation rate λ_1 or the momentum relaxation rate $\alpha_{\rm fl}$. In particular in Fig. 1(e) and Fig. 2(d), we found that this suppression is controlled by the solute mass diffusion in liquids and by the solvent momentum diffusion (or inertia) in gasses.

(*vii*) In Sec. 6.2 we have illustrated the practical usefulness of the developed theory as a design tool for dispersion-control in microfluidic systems.

Our work has resulted in a compact, transparent, and efficient theoretical method for analyzing transient Taylor-Aris dispersion in straight channels. Using it, we have gained physical insight in, and made explicit predictions of, the effects of general time-dependent flows on dispersion. The theory opens up for further generalizations such as including the effects of non-Newtonian solvents and non-trivial channel topologies.

We thank Peder Skafte–Pedersen for supplying the experimental pump data of Sec. 6.2, Rune Barnkob for assisting with the 64 bit computer used for the numerical part of this work, and Howard A. Stone, Roberto Camassa, and Richard M. McLaughlin for stimulating discussions on the background literature. This research was supported by grant no. 2106-08-0018 "ProCell", under the Programme Commission on Strategic Growth Technologies, the Danish Agency for Science, Technology and Innovation.

Quantity	Symbol
Cross-sectional part of the $\boldsymbol{\nabla}$ operator	$\boldsymbol{\nabla}_\perp = \mathbf{e}_y\partial_y + \mathbf{e}_z\partial_z$
Bra of $\bullet$, and ket of $\bullet$	$\langle \bullet \vert$, and $\vert \bullet \rangle$
Complex conjugation	$*$
Cross-sectional area	$\mathcal{A}$
Channel radius/half-height	a
Concentration field of solute	c
pth axial moment of concentration	c_p
Initial value for $c(x, \boldsymbol{r}_\perp, t)$	$\tilde{c}(x, \boldsymbol{r}_\perp)$
Characteristic concentration	C_o
Molecular diffusivity	D
Effective diffusivity	D_eff
Effective diffusivity, time-averaged	$D_\mathrm{eff}^\mathrm{avr}$
Effective diffusivity, steady flow	$D_\mathrm{eff}^\mathrm{steady}$
Cartesian basis vectors	$\mathbf{e}_x$, $\mathbf{e}_y$, $\mathbf{e}_z$
nth basis function	f_n
Bessel function, first kind of order s	J_s
Generalized wavenumber, Eq. (5.1a)	k_ℓ
Channel length	$\mathcal{L}$
Characteristic length	L_o
pth full moment of concentration	M_p
Surface normal vector	$\boldsymbol{n}$
Pressure	p
Characteristic pressure	P_o
Péclet number	$\mathrm{Pé} = U_\mathrm{o}L_\mathrm{o}/D$
Generalized wavenumber, Eq. (6.1a)	$q_{j\ell}$
Channel aspect ratio	$R = w/a$
Position vector	$\boldsymbol{r}$
Cross-sectional position vector	$\boldsymbol{r}_\perp = (y, z)$
Schmidt number	$\mathrm{Sc} = \nu/D$
Characteristic time	T_o
Time	t
Characteristic velocity	U_o
Axial velocity component of solvent	u
Volume	$\mathcal{V}$
Velocity field of solvent	$\boldsymbol{v}$
Channel half-width	w
Womersley number	$\mathrm{Wo} = \sqrt{L_\mathrm{o}^2\tilde{\omega}_\mathrm{o}/\nu}$
Solute center of mass	$\overline{x}$
Cylindrical coordinates	x, r, φ
Cartesian coordinates	x, y, z
Fluid momentum equilibration rate	α_m, α_fl
Pre-factor Eq. (6.2a)	Γ
Kronecker delta	$\delta_{n,m}$
ℓth velocity component amplitude	ε_ℓ
Dynamic viscosity	η
nth root of Bessel function J_s	$\xi_{s,n}$
nth diffusion rate eigenvalue	λ_n
pth moment of conc. about the mean	μ_p
Kinematic viscosity of solvent	ν
Density of solvent	ρ
Diffusivity enhancement	χ_plate, χ_rect
Cross section	Ω
Base frequency, non-dimensionalized	$\omega_\mathrm{o} = \mathrm{Wo}^2\mathrm{Sc}$
Base frequency, dimensionfull	$\tilde{\omega}_\mathrm{o}$
Oscillation period	$\tau_0 = 2\pi/\omega_\mathrm{o}$

TABLE 2. List of quantities used in this work alphabetized by symbol (latin before greek).

Appendix A. Mathematical and numerical details; list of symbols

A.1. *The Dirac bra-ket notation for spatial dependence*

The basic concept of the bra-ket notation is the inner product of functions, defined by Eq. (2.2). It is linear

$$\langle f|A_1 g_1 + A_2 g_2\rangle = A_1\langle f|g_1\rangle + A_2\langle f|g_2\rangle, \tag{A 1}$$

and given the complex representation Eq. (2.6) of the velocity field, we often use that

$$\langle u_\ell|g\rangle = \langle g|u_\ell\rangle^* = \langle g^*|u_{-\ell}\rangle, \tag{A 2a}$$

$$\langle u_\ell\, \mathrm{e}^{\mathrm{i}\ell\omega_\circ t}|g\rangle = \mathrm{e}^{-\mathrm{i}\ell\omega_\circ t}\langle u_\ell|g\rangle. \tag{A 2b}$$

The bra-ket notation is particularly compact when working with basis function expansions. A set of functions $|f_n\rangle$, $n = 0, 1, 2, \ldots$, is said to form an orthonormal basis when it fulfills the so-called completeness and orthonormal conditions given by

$$\sum_{n=0}^{\infty} |f_n\rangle\langle f_n| = 1, \quad \text{and} \quad \langle f_m|f_n\rangle = \delta_{m,n}, \tag{A 3}$$

respectively, where by definition $\delta_{m,n} = 1$ for $m = n$, and 0 for $m \neq n$. Any function $|g\rangle$ can formally be expressed by an expansion in this basis as

$$|g\rangle = \sum_{n=0}^{\infty} a_n|f_n\rangle, \tag{A 4a}$$

$$a_m = \langle f_m|g\rangle,\ m = 0, 1, 2, \ldots. \tag{A 4b}$$

Here Eq. (A 4*b*) follows from multiplication of Eq. (A 4*a*) from the left by $\langle f_m|$ and using Eq. (A 3). Since the functions f and g in general depend on time, the inner product may also depend on time. We find that the bra-ket notion allows for better overview during formal manipulations and lets the underlying structure of the theory stand out more clearly without the clutter of voluminous expressions of integrals. The formalism is particularly convenient for problems involving the Laplace operator, like the present, because often the corresponding basis functions and eigenvalues are known.

A.2. *Method of statistical moments*

The great insight of Aris was to realize that the advection-diffusion problem can be rewritten as a series of equations for statistical moments of the solute distribution, which then can be solved sequentially (Aris 1956). Each additional moment adds new information about the distribution, and some of the lower moments have direct physical interpretations. We here give Aris's definitions and resulting equations of motion for the statistical moments reformulated in the bra-ket notation.

The pth axial moment $c_p(\boldsymbol{r}_\perp, t)$ of the solute concentration field $c(x, \boldsymbol{r}_\perp, t)$ and the associated full moment $M_p(t)$ are defined by Eqs. (2.12*b*) and (2.12*a*) in the main text. Taking the time derivative of these equations and using the advection-diffusion equation (2.9), we obtain the recursive equations of motion Eqs. (2.13*a*) and (2.13*b*) for c_p and M_p as well as their boundary conditions, Eq. (2.14). M_0 corresponds to the unit norm of c, while M_1 is the time-dependent, axial center of mass $\bar{x}$ of c,

$$M_0 = \langle 1|c\rangle = 1, \tag{A 5a}$$

$$M_1 = \langle x|c\rangle = \bar{x}(t). \tag{A 5b}$$

The pth moment μ_p about the center of mass is defined by,

$$\mu_p(t) = \big\langle (x-\bar{x})^p \big| c \big\rangle, \tag{A 6}$$

and by the linearity of the inner product, Eq. (A 1), we find for $p = 0$, 1 and 2,

$$\mu_0(t) = \big\langle 1 \big| c \big\rangle \qquad = 1, \tag{A 7a}$$

$$\mu_1(t) = \big\langle (x-\bar{x}) \big| c \big\rangle \;= 0, \tag{A 7b}$$

$$\mu_2(t) = \big\langle (x-\bar{x})^2 \big| c \big\rangle = M_2(t) - M_1(t)^2. \tag{A 7c}$$

In particular the time-dependent spatial variance μ_2 of the solute concentration is of key interest as it relates the to the solute molecular diffusivity and the effective diffusivity D_{eff}. For a vanishing velocity field, $u = 0$, μ_2 relates to the diffusivity D of the solute by $\mathrm{d}\mu_2/\mathrm{d}t = 2D$, or in dimensionless form, $\mathrm{d}\mu_2/\mathrm{d}t = 2$, since:

$$\frac{\mathrm{d}\mu_2}{\mathrm{d}t} = \big\langle (x-\bar{x})^2 \big| \partial_t c \big\rangle - 2\big\langle (x-\bar{x}) \big| c \big\rangle \frac{\mathrm{d}\bar{x}}{\mathrm{d}t} = \big\langle (x-\bar{x})^2 \big| \nabla^2 c \big\rangle - 2\mu_1 \frac{\mathrm{d}\bar{x}}{\mathrm{d}t} = 2\big\langle 1 \big| c \big\rangle = 2, \tag{A 8}$$

where in the last term we have integrated by parts twice and used the boundary conditions Eqs. (2.10a) and (2.10c). This corresponds to the well-known result for diffusion in one dimension, $(\Delta x)^2 = 2Dt$, with $\mu_2 \sim (\Delta x)^2$.

When the solvent velocity field u is nonzero the time-dependence of the variance is no longer linear. However, by a traditional generalization (Aris 1956; Barton 1983; Aris 1960; Mukherjee & Mazumder 1988; Chatwin 1975; Brenner & Edwards 1993) the dispersion or effective diffusivity $D_{\text{eff}}(t)$ is defined as done in Eq. (2.11) in the main text $D_{\text{eff}}(t) = \frac{1}{2}\frac{\mathrm{d}\mu_2}{\mathrm{d}t} = \frac{1}{2}\frac{\mathrm{d}M_2}{\mathrm{d}t} - M_1\,\frac{\mathrm{d}M_1}{\mathrm{d}t}$. Other works have been concerned with the skewness μ_3 of the solute distribution (Barton 1983; Camassa *et al.* 2010). More information about the distribution of c is added with each moment, however, the information contained in each moment remains valid no matter how many moments have been determined.

A.3. *The dispersion for short times*

We show here that $D_{\text{eff}}(t)$ is positive for short times $t \ll 1/\lambda_1, 1/(2\ell_{\max}\omega_{\text{o}})$. In this limit we have

$$\mathrm{e}^{\mathrm{i}(\ell-k)\omega_{\text{o}}t} - \mathrm{e}^{-(\lambda_n + \mathrm{i}k\omega_{\text{o}})t} = (\lambda_n + \mathrm{i}\ell\omega_{\text{o}})t + \mathcal{O}(t^2), \tag{A 9}$$

thus reducing Eq. (3.22) for $D_{\text{eff}}(t)$ to

$$\begin{aligned} D_{\text{eff}}(t) &\approx 1 + \mathrm{P\acute{e}}^2 \sum_{n=1}^{\infty} \sum_{\ell=-\ell_{\max}}^{\ell_{\max}} \sum_{k=-\ell_{\max}}^{\ell_{\max}} \big\langle u_k \big| f_n \big\rangle \big\langle f_n \big| u_\ell \big\rangle \, t \\ &= 1 + t\,\mathrm{P\acute{e}}^2 \sum_{n=1}^{\infty} \Big\langle \sum_{k=-\ell_{\max}}^{\ell_{\max}} u_k \big| f_n \big\rangle \big\langle f_n \Big| \sum_{\ell=-\ell_{\max}}^{\ell_{\max}} u_\ell \Big\rangle \\ &= 1 + t\,\mathrm{P\acute{e}}^2 \sum_{n=1}^{\infty} \Big| \big\langle f_n \big| u(0) \big\rangle \Big|^2, \; t \ll \frac{1}{\lambda_1}, \frac{1}{2\ell_{\max}\omega_{\text{o}}}. \end{aligned} \tag{A 10}$$

Here $u(0)$ is the total velocity field $u(t)$ evaluated at time $t = 0$. This expression becomes problematic to apply in the case where infinitely many harmonics of the velocity field is present at $t = 0$ as for the startup of the Poiseuille flow, but for flows with a maximum frequency we have shown $D_{\text{eff}}(t) > 0$.

A.4. *Numerics*

For numerical evaluations of the effective diffusivity $D_{\text{eff}}(t)$ we relied on three methods. First, using the commercial finite element package COMSOL MULTIPHYSICS version 3.5a,

we calculated $D_{\rm eff}(t)$ numerically directly from the definition Eq. (2.11) by solving for the concentration field c in the governing advection-diffusion equation (2.9) using the analytical solutions for the velocity field as input. From the obtained $c(\boldsymbol{r},t)$ we determined $M_1(t)$, $\mathrm{d}M_1(t)/\mathrm{d}t$ and $\mathrm{d}M_2(t)/\mathrm{d}t$, and from these $D_{\rm eff}(t)$. To ensure mass conservation the number of mesh elements was chosen so that the local Péclet number in each cell (as given by the velocity in the mesh element, the mesh element length and the global diffusivity) was approximately 0.5. Where possible, the available symmetries were exploited for computational efficiency. To this end the solutions of the flow problems in channels of circular cross section took advantage of the azimuthal symmetry and the solution was computed in a frame of reference traveling with the mean speed of the flow.

Second, for rectangular cross sections the problem was only solved for one quarter of the cross section in a frame of reference moving with the flow mean speed. However, due to memory limitations even these simplifications proved unfeasible for Péclet numbers exceeding $\sim$2 and aspect ratios above $\sim$2. Thus, for the results presented in Fig. 3(a) we numerically solved the axial moment equation Eq. (2.12*b*) for $c_{\rm o}$ and c_1, and from these obtained $M_1(t)$, $\mathrm{d}M_1(t)/\mathrm{d}t$, and $\mathrm{d}M_2(t)/\mathrm{d}t$, as well as $D_{\rm eff}(t)$. Time-averages of the numerical simulation results were computed by running the simulation for a full period of the base frequency after the decay of all transients, followed by numerical integration of $D_{\rm eff}(t)$ over the period.

Third, we calculated $D_{\rm eff}(t)$ based on our theoretical expression (3.22), but reduced the number of terms needed to be calculated by separating the ℓ- and k-sums and collecting complex conjugated pairs of index $\{\ell,-\ell\}$ and $\{k,-k\}$,

$$D_{\rm eff}(t) = 1 + \mathrm{P\acute{e}}^2 \sum_{n=1}^{\infty} \left\{ \frac{\langle f_n | u_0 \rangle}{\lambda_n} \left[1 - \mathrm{e}^{-\lambda_n t} \right] + 2 \sum_{\ell=1}^{\infty} \mathrm{Re}\left[\frac{\langle f_n | u_\ell \rangle}{\lambda_n + \mathrm{i}\ell\omega_{\rm o}} \left(\mathrm{e}^{\mathrm{i}\ell\omega_{\rm o} t} - \mathrm{e}^{-\lambda_n t} \right) \right] \right\} \times \left\{ \langle f_n | u_0 \rangle + 2 \sum_{k=1}^{\infty} \mathrm{Re}\left[\langle f_n | u_k \rangle \mathrm{e}^{\mathrm{i}k\omega_{\rm o} t} \right] \right\}. \tag{A 11}$$

Furthermore, The involved n-, ℓ-, and k-dependent terms are calculated and placed in lists before evaluating the sums. The latter converge quickly, and we have therefore truncated them after the first fifty terms unless stated otherwise in the text.

REFERENCES

Ajdari, A., Bontoux, N. & Stone, H. A. 2006 Hydrodynamic dispersion in shallow microchannels: the effect of cross-sectional shape. *Anal Chem* **78**, 387–392.

Aris, R 1956 On the dispersion of a solute in a fluid flowing through a tube. *P Roy Soc Lond A Mat* **235** (1200), 67–77.

Aris, R. 1960 On the dispersion of solute in pulsating flow through a tube. *P Roy Soc Lond A Mat* **259** (1298), 370–376.

Bandyopadhyay, S. & Mazumder, B. S. 1999 Unsteady convective diffusion in a pulsatile flow through a channel. *Acta Mech* **134**, 1–16.

Barton, N. G. 1983 On the method of moments for solute dispersion. *J Fluid Mech* **126**, 205–218.

Batchelor, G. K. 1967 *An Introduction to Fluid Dynamics*. Cambridge: Cambridge University Press.

Bird, R. B., Stewart, W. E. & Lightfoot, E. N. 2006 *Transport Phenomena*, 2nd edn. New York: John Wiley and Sons.

Bontoux, N., Pépin, A., Chen, Y., Ajdari, A. & Stone, H. A. 2006 Experimental characterization of hydrodynamic dispersion in shallow microchannels. *Lab Chip* **6**, 930–935.

Brenner, H. & Edwards, D. A. 1993 *Macrotransport Processes*. Boston: Butterworth–Heinemann.

Bruus, H. 2008 *Theoretical Microfluidics*. Oxford: Oxford University Press.

Bruus, H. & Stone, A. D. 1994 Quantum chaos in a deformable billiard: Applications to quantum dots. *Phys. Rev. B* **50** (24), 18275–18287.

Camassa, R., Lin, Z. & McLaughlin, R. 2010 The exact evolution of scalar variance in pipe and channel flow. *Commun Math Sci* **8** (2), 601–626.

Chatwin, P. C. 1975 On the longitudinal dispersion of passive contaminant in oscillatory flows in tubes. *J Fluid Mech* **71**, 513–527.

Chatwin, P. C. 1977 Initial development of longitudinal dispersion in straight tubes. *J Fluid Mech* **80**, 33–48.

Chatwin, P. C. & Sullivan, P. J. 1982 The effects of aspect ratio on longitudinal diffusivity in rectangular channels. *J Fluid Mech* **120**, 347–358.

Dirac, P. A. M. 1981 *The Principles of Quantum Mechanics*, 4th edn. Oxford: Oxford University Press.

Doshi, M. R., Daiya, P. M. & Gill, W. N. 1978 Three dimensional laminar dispersion in open and closed rectangular conduits. *Chem Eng Sci* **33**, 795–804.

Dutta, D., Ramachandran, A & Leighton, D. T. 2006 Effect of channel geometry on solute dispersion in pressure-driven microfluidic systems. *Microfluid Nanofluid* **2**, 275–290.

Erdogan, M. E. & Chatwin, P. C. 1967 Effects of curvature and buoyancy on laminar dispersion of solute in a horizontal tube. *J Fluid Mech* **29** (Part 3), 465–484.

Fan, L. T. & Wang, C. B. 1966 Dispersion of matter in non-Newtonian laminar flow through a circular tube. *P Roy Soc Lond A Mat* **292** (1429), 203–208.

Gleeson, J. P. 2002 Electroosmotic flows with random zeta potential. *J Colloid Interface Sci* **249** (1), 217–226.

Goddard, J. D. 1993 The Green's function for passive scalar diffusion in a homogeneously sheared continuum. *Phys Fluids A* **5**, 2295–2297.

Harris, H. G. & Goren, S. L. 1967 Axial diffusion in a cylinder with pulsed flow. *Chem Eng Sci* **22**, 1571–1576.

Jansons, K. M. 2006 On Taylor dispersion in oscillatory channel flows. *P Roy Soc Lond A Mat* **462**, 3501–3509.

Latini, M & Bernoff, AJ 2001 Transient anomalous diffusion in Poiseuille flow. *J Fluid Mech* **441**, 399–411.

Leighton, D. T. 1989 Diffusion from an intial point distribution in an unbounded oscillating simple shear flow. *PhysicoChem Hydrodyn* **11**, 377–386.

Lide, D. R. (editor-in-chief) 1995 *CRC Handbook of Chemistry and Physics*, 75$^{\text{th}}$ edn. New York, NY: CRC Press.

Mehta, M.L. 2004 *Random Matrices*, 3rd edn., *Pure and Applied Mathematics*, vol. 142. Amsterdam: Elsevier/Academic Press.

Molloy, R. F. & Leighton, D. T. 1998 Binary oscillatory cross-flow electrophoresis: Theory and experiments. *J Pharma Sci* **87**, 1270–1281.

Mortensen, N. A. & Bruus, H. 2006 Universal dynamics in the onset of a Hagen-Poiseuille flow. *Phys. Rev. E* **74** (1), 017301.

Mortensen, N. A., Olesen, L.H. & Bruus, H. 2006 Transport coefficients for electrolytes in arbitrarily shaped nano and micro-fluidic channels. *New J Phys* **8**, 37–51.

Mukherjee, A. & Mazumder, B. S. 1988 Dispersion of contaminant in oscillatory flows. *Acta Mech* **74**, 107.

Paul, S. & Mazumder, B.S. 2008 Dispersion in unsteady Couette-Poiseuille flows. *Int J Eng Sci* **46**, 1203–1217.

Probstein, R. F. 1994 *Physicochemical Hydrodynamics. An introduction*, 2nd edn. New York: John Wiley and Sons.

Sankarasubramanian, R. & Gill, W. N. 1973 Unsteady convective diffusion with interphase mass-transfer. *P Roy Soc Lond A Mat* **333** (1592), 115–132.

Skafte-Pedersen, P., Sabourin, D., Dufva, M. & Snakenborg, D. 2009 Multi-channel peristaltic pump for microfluidic applications featuring monolithic PDMS inlay. *Lab Chip* **9**, 3003–3006.

Taylor, G. I. 1953 Dispersion of soluble matter in solvent flowing slowly through a tube. *P Roy Soc Lond A Mat* **219** (1137), 186.

Taylor, H. M. & Leonard, E. F. 1965 Axial dispersion during pulsating pipe flow. *A I Ch E Journal* **11** (4), 686–689.

Thomas, A. M. & Narayanan, R. 2001 Physics of oscillatory flow and its effect on the mass transfer and separation of species. *Phys Fluids* **13** (4), 859–866.

van den Broeck, C. 1982 A stochastic description of longitudinal dispersion in uniaxial flows. *Physica A* **112**, 343–352.

Vedel, S., Olesen, L. H. & Bruus, H. 2010 Pulsatile microfluidics as an analytical tool for determining the dynamic characteristics of microfluidic systems. *J Micromech Microeng* **20**, 035026.

Vikhansky, A. & Wang, W. 2011 Taylor dispersion in finite-length capillaries. *Chem. Eng. Sci.* **66** (4), 642–649.

Watson, E. J. 1983 Diffusion in oscillatory pipe flow. *J Fluid Mech* **133**, 233–244.

Womersley, J. R. 1955 Method for the calculation of velocity, rate of flow and viscous drag in arteries when the pressure gradient is known. *J Physiol* **127**, 553–563.